Study of Double-Wall Effusion Cooling Scheme for Gas Turbine Blade Applications

Gladys Chepkirui Ngetich

Oriel College

University of Oxford

A thesis submitted for the degree of

Doctor of Philosophy

Trinity 2019

Abstract

Gladys Chepkirui Ngetich
Oriel College, University of Oxford
A thesis submitted for the degree of Doctor of Philosophy, Trinity 2019

Study of Double-Wall Effusion Cooling Scheme for Gas Turbine Blade Applications

Porous multi-wall cooling schemes such as double-wall cooling combined with effusion cooling offer a practical approximation to transpiration cooling which in turn present a potential for high cooling effectiveness. Most of the existing double-wall effusion cooling studies have been on flat plate geometries. There are varying external static pressure and secondary flow features in flow over an aerofoil which have an influence on overall cooling performance. Thus, there is need to study double-wall effusion cooling applied to an aerofoil. The main aim of this research was to extend the double-wall effusion-cooling technology research, that has long been undertaken on flat plates, onto a gas turbine blade.

In the present study, both numerical simulations and experiments were undertaken to study double-wall effusion-cooled (DWEC) turbine-representative aerofoils. The aerofoils were built from double-wall block elements that have been validated by another author. Both low porosity and high porosity circular and diamond pedestal designs were considered. A novel decoupled numerical analysis tool for preliminary cooling performance analysis of DWEC aerofoils was first developed. In this analysis method, a modified flat plate correlation from the literature was used to represent the two-dimensional distribution of film cooling effectiveness. The internal heat transfer coefficient was calculated from a validated conjugate analysis of a wall element representing an element of the aerofoil wall and the conduction through the blade solved using a finite element code in commercial CFD solver. The developed decoupled numerical analysis method was validated using results from fully coupled conjugate heat transfer (CHT) simulations. In addition, high-speed experimental tests at engine representative Mach and Reynold numbers flow conditions were carried out to study film cooling effectiveness over the full surface of three circular and six diamond pedestal DWEC blade designs using pressure sensitive paint. All the blades were tested within a range of representative modern engine coolant mass flow rate, $\dot{m}_c$ to mainstream mass flow rate, $\dot{m}_\infty$ ratios; $0.5\% < \dot{m}_c/\dot{m}_\infty < 5.5\%$.

The novel simplified numerical analysis method offered good performance approximation particularly on the suction surface of the aerofoil. In addition, compared to CHT, the novel simplified numerical analysis method reduced computational time by approximately 50 times and therefore, computationally efficient for use during preliminary design and optimization stages. High effective porosity designs exhibited better film cooling effectiveness, than the low effective porosity counterparts, but this came at an expense of internal cooling efficiency. CFD results compared well with the experiments and were able to capture similar

film effectiveness trends on both the pressure surface and the suction surface, however, inability of Reynolds-Averaged Navier–Stokes equations (RANS) models to correctly predict diffusion resulted in an overprediction of film cooling effectiveness around the vicinity of film cooling holes and an overprediction of film superposition on the suction surface.

This work has contributed knowledge of the DWEC aerofoils performance including overall cooling effectiveness predictions, internal cooling effectiveness predictions and film cooling effectiveness performance measurements. There is still much work to be done (including investigation into aerodynamic losses, weight and stresses associated with this cooling technology) to realise a practical double-wall effusion-cooled blade. The present author has included recommendations for future work.

Keywords: gas turbine cooling, effusion cooling, double-wall cooling, correlation, superposition, unit wall element, simplified numerical modelling approach, heat transfer, CHT, film cooling effectiveness, pressure sensitive paint, alternative double-wall fabrication technique

Dedication

For my Mom who dreamt of this PhD long before I did

Acknowledgements

Sincere gratitude to my supervisor. No words can fully capture my appreciation for Prof Peter T. Ireland, who has been constantly guiding and encouraging me not only in my research but also checking how I was doing in athletics and football. Thanks also to Dr. Eduardo Romero for the constant support and the biweekly meetings that pushed me to work harder.

I am eternally indebted to my family for the undying support in both good and bad times. I am also grateful to all my friends who supported me during this journey and made life at Oxford so much fun.

I joined Oxford without much prior research experience. My research life was going to be hard if not for the colleagues I met at Oxford Thermofluids Institute who I ran to every time I got stuck with MATLAB, LabVIEW, ANSYS etc. Thanks also to the entire Transpiration Cooling crew, I will not forget the good times at the quarterly meetings. I will not forget to sincerely thank the workshop staff who always went out of their way to help me during my experiments.

Sincere gratitude to the Rhodes Trust (special thanks to Mary Eaton at the Rhodes House) for the moral and financial support. Sincere gratitude also to the Engineering and Physical Sciences Research Council (EPSRC) for the program grant and the Rolls-Royce Plc. for their support.

Contents

Abstract i

Dedication iii

Acknowledgements iv

Nomenclature xv

1 INTRODUCTION 1

1.1 Introduction . . . 1
1.2 Gas Turbine Engines . . . 1
1.3 Gas Turbine Cooling . . . 3
1.3.1 Film Cooling . . . 5
1.3.2 Transpiration Cooling . . . 6
1.3.3 Effusion Cooling . . . 8
1.3.4 Advanced Turbine Blade Cooling . . . 9
1.4 Research Aims . . . 17
1.5 Thesis Contributions . . . 18
1.6 Thesis Structure . . . 19

2 LITERATURE SURVEY 21

2.1 Introduction . . . 21
2.2 Literature Review Related to a Simplified 3D Numerical Analysis of Turbine Aerofoils . . . 21
2.2.1 Simplified 3D Numerical Analysis Approach . . . 22
2.2.2 Methodologies for Predicting Film Cooling Effectiveness . . . 25
2.3 Literature Review of Fully Coupled CHT of Turbine Aerofoils . . . 26
2.3.1 Literature Review of Flow Field and Heat Transfer Characteristics of an Impingement/Effusion System . . . 30
2.4 Literature Review of Film Cooled Turbine Aerofoils . . . 31
2.5 Summary . . . 35

3 SIMPLIFIED 3D NUMERICAL ANALYSIS FOR METAL EFFECTIVENESS 37
3.1 Introduction . . . 37
3.2 Objective of the Present Numerical Simulation Work . . . 37
3.3 Details of the Test Geometry . . . 38
3.4 Numerical Simulation . . . 42
3.5 Film Cooling Effectiveness Modelling . . . 43
3.5.1 Mainstream Velocity and Density . . . 43
3.5.2 Film Cooling Effectiveness . . . 44
3.5.3 Adiabatic Wall Temperature . . . 45
3.6 External Heat Transfer Coefficient . . . 48
3.7 Conjugate Model Simulation . . . 48
3.8 Results and Discussion . . . 49
3.8.1 Film Effectiveness and Adiabatic Wall Temperature . . . 49
3.8.2 External Heat Transfer . . . 53
3.8.3 Internal Cooling Effectiveness . . . 54
3.8.4 Overall Cooling Effectiveness . . . 57
3.9 Numerical Analysis Comparison with Other Double-Wall Blades . . . 59
3.9.1 Geometrical Description . . . 59
3.9.2 DWEC Blades Numerical Analysis Results Comparison . . . 62
3.10 Conclusion . . . 66

4 FULLY COUPLED CHT SIMULATIONS 68
4.1 Introduction . . . 68
4.2 Fully coupled CHT Analysis . . . 68
4.3 Computational Setup . . . 70
4.4 Computational Mesh . . . 71
4.5 Solver and Models . . . 73
4.6 Boundary Conditions . . . 74
4.7 Results and Discussion . . . 74
4.7.1 Internal and External Flow Structures . . . 76
4.7.2 Impingement/Effusion Cooling . . . 79
4.7.3 Metal Effectiveness . . . 82
4.7.4 Blowing Ratio . . . 87
4.7.5 Adiabatic Film Cooling Effectiveness . . . 92
4.8 Conclusions . . . 96
4.9 Summary . . . 98

5 EXPERIMENTAL FACILITY AND APPARATUS **99**
5.1 Introduction . . . 99
5.2 High-Speed Single-Blade Linear Cascade . . . 99
5.3 Experimental Facility Boundary Conditions . . . 101
5.4 DWEC Test Blades . . . 102
5.4.1 Circular Pedestal Designs . . . 104
5.4.2 Diamond Pedestal Designs . . . 105
5.5 Flow Control and Measurement Devices . . . 106
5.5.1 Critical Flow Venturi Nozzle (CFVN) . . . 106
5.5.2 Orifice Plate Flow Meter . . . 109
5.5.3 Uncertainty Analysis . . . 112
5.6 Summary . . . 119

6 FILM COOLING EFFECTIVENESS EXPERIMENTS USING PRESSURE SENSITIVE PAINT **120**
6.1 Introduction . . . 120
6.2 Overview . . . 120
6.3 PSP Measurement Theory . . . 122
6.4 Experimental Test Conditions . . . 124
6.5 PSP Instrumentation and Measurement Procedure . . . 125
6.6 Errors and Uncertainties . . . 126
6.6.1 Optical-Related Errors . . . 127
6.6.2 Calibration . . . 127
6.6.3 PSP Sensitivity to Temperature . . . 127
6.6.4 Heat to Mass Transfer Analogy Limitations . . . 128
6.7 Results and Discussion . . . 128
6.7.1 Film Structure on the Pressure and Suction Surfaces . . . 128
6.7.2 Influence of Mass Flow Rates . . . 144
6.7.3 Influence of Internal Geometry . . . 145
6.7.4 Influence of the Film Cooling Hole Size . . . 148
6.8 Conclusion . . . 151
6.9 Summary . . . 152

7 SUMMARY AND CONCLUSION **154**
7.1 Summary of Major Themes and Assessment of Aims . . . 154
7.1.1 Simplified 3D numerical analysis approach . . . 154
7.1.2 Fully coupled CFD simulations . . . 155
7.1.3 Film cooling effectiveness measurement using PSP . . . 156
7.2 Conclusion . . . 158

8 RECOMMENDATIONS **160**
8.1 Explore Shaped Cooling Holes 160
8.2 Optimization 161
8.3 Flow Visualisation 161
8.4 Investigate Aerodynamic Losses 162
8.5 Investigate double-wall blade weight and the impact on turbine disc sizing . 162
8.6 Repeat simplified model analysis at other pressure ratios 162
8.7 Repeat the experiment at the same blowing ratios as the fully coupled CHT 163

Bibliography **164**

Appendix A Patent Application Number GB1806542.5; An Alternative DWEC Aerofoil Manufacturing Approach **174**

Appendix B A section of the MATLAB Code Used for Evaluating Aerofoil Metal Temperature **193**

Appendix C Film Effectiveness Parameter Variation with Streamwise Pitch and Blowing Ratio (from Murray et al. (2018)) **200**

List of Figures

1.1 The Rolls-Royce Plc. Trent 1000 turbofan gas turbine engine (Copyright: Rolls Royce Plc) . . . 2
1.2 Thermodynamic and propulsive efficiencies at cruise of some of the in-service gas turbine engines, including thrust specific fuel consumption (TSFC) and overall efficiency. Adapted from Epstein (2014) . . . 3
1.3 Increased turbine inlet temperature dramatically improves cycle power output (Han et al., 2012) . . . 4
1.4 Turbine entry temperature versus the date of entry into service (Astarita et al., 2015) . . . 5
1.5 A cut away section of a high pressure turbine blade which is cooled both internally, through enhanced serpentine passages, and externally through film cooling. Adapted from Rolls-Royce (2015) . . . 6
1.6 TET and cooling effectiveness achievable by solid, convection, film/convection and advanced cooling (adapted from Koff (2004)) . . . 7
1.7 Transpiration cooling of a concept aerofoil using a porous surface (Bunker, 2006) . . . 8
1.8 Fundamental mechanism responsible for transpiration cooling. Adapted from Polezhaev (1997) . . . 9
1.9 A schematic summary of the principle cooling technologies; film, impingement, effusion and transpiration cooling as well as the variation of effusion cooling schemes - Lamilloy®, Transply® and Poroform® (Battisti et al., 2006) 10
1.10 Allison's Lamilloy® transpiration cooling system: Pillars cast or etched into sheet material gives this triple sandwich an extended surface area over which air must pass through (Brown, 1990) . . . 11
1.11 Snowflake Lamilloy® design (Sweeney and Rhodes, 1999) . . . 13
1.12 Electroforming process to produce a Poroform concept turbine blade (Battisti et al., 2006) . . . 13
1.13 Technology impact-risk ranking of the ten challenges (Bunker, 2006) . . . 14
1.14 Key features of a double-walled effusion cooled concept turbine blade . . . 15
1.15 Secondary flow features in a turbine cascade (Sharma and Butler, 1987) . . 17

2.1 Definition of cooled multi-layered periodic unit cell (Laschet et al., 2013) . 22
2.2 Decoupled CHT numerical analysis iterative code used by (a) Andrei et al. (2014) and (b) Bonini et al. (2012) 24

3.1 Features of a double-walled effusion-cooled concept turbine blade including leading edge (LE) showerhead cooling holes, pin-fin bank and trailing edge (TE) slots as well as the external flow direction 39
3.2 CFD results showing the flow velocity distribution in the unit wall block element from Murray et al. (2017) 40
3.3 A sectioned double-wall blade with the unit wall block element showing the definition of the geometrical parameters 41
3.4 Outer skin of the blade where numerical analysis is performed 43
3.5 $\eta_c - Re$ characteristics compared to that of three simple duct cooling systems, characterized by L/D_h = 20, 40 and 60 44
3.6 Steps in the iterative code used to determine aerofoil wall temperature . . . 47
3.7 Boundary conditions for the uncooled CFD in ANSYS[1] CFX 49
3.8 Model setup in ANSYS[1] steady-state thermal module 50
3.9 Boundary conditions used for conduction calculation in ANSYS[1] steady-state thermal module 51
3.10 Film cooling effectiveness on the blade and its corresponding adiabatic wall temperature for the conditions of Table 3.2 51
3.11 External static pressure distribution around the aerofoil, including the four horizontal lines representing four coolant pressure ratios corresponding to PR= 1.00, 1.05, 1.15 and 1.25 52
3.12 Non-dimensional film flow rate per hole, film cooling effectivess, metal effectiveness and dimensionless external heat transfer coefficient as a function of the blade's dimensionless streamwise location 53
3.13 A graph of effectiveness as a function of dimensionless coolant mass flow for the C2 blade 54
3.14 The schematic illustration of the definition of the unit wall block element geometrical parameters for (a) diamond and (b) circular pedestal designs. . 56
3.15 A graph of film, internal and overall effectiveness as a function of dimensionless coolant mass flow for the DWEC circular designs; C1, C2 and C3 . 58
3.16 A graph of film, internal and overall effectiveness as a function of dimensionless coolant mass flow for the DWEC diamond designs; D1b, D2a and D3a 59
3.17 A graph of internal and overall effectiveness as a function of dimensionless coolant mass flow for both the circular (C1, C2, C3) and diamond designs; D1b, D2a, D3a 60

3.18 Overall effectiveness versus effective porosity of blades D2a, D1b, D3a, C2, C1 and C3 at the same pressure drop of 0.9 bar 61
3.19 $\eta_c - Re$ characteristics compared to that of three simple duct cooling systems, characterized by L/D_h = 20, 40, 60 and 80 63
3.20 C1, C2 and C3 overall effectiveness comparison overall effectiveness from an analytical equation of Holland and Thake (1980) 64
3.21 D1b, D2a and D3a overall effectiveness comparison with overall effectiveness from an analytical equation of Holland and Thake (1980) 65

4.1 repeating DWEC aerofoil strip 69
4.2 A simple CAD showing the mainstream, coolant and blade domains with the dimensions of the mainstream domain inlet and outlet 70
4.3 The mainstream and coolant boundary conditions 71
4.4 ANSYS[1] unstructured mesh including inflation layer and mesh refinement around the holes 72
4.5 Mesh sensitivity results showing metal temperature and coolant mass flow rate variation with mesh size 72
4.6 CFD simulation heat transfer, momentum and mass convergence status . . . 74
4.7 Pressure contours at the aerofoil midspan for the four different coolant pressure ratios corresponding to PR = 1.00, 1.05, 1.15 and 1.25 76
4.8 Mach number contours at the aerofoil midspan for the four different coolant pressure ratios corresponding to PR = 1.00, 1.05, 1.15 and 1.25 77
4.9 Mach number vectors for the four different coolant pressure ratios corresponding to PR = 1.00, 1.05, 1.15 and 1.25 77
4.10 Streamlines coloured by Mach number for the four different coolant pressure ratios corresponding to PR = 1.00, 1.05, 1.15 and 1.25 78
4.11 3D streamlines coloured by Mach number for coolant pressure ratio, PR = 1.25 78
4.12 Impingement holes, effusion holes and pedestal configuration 79
4.13 Flow structure in the form of Mach number coloured vectors, zoomed in near hole SS4 at PR corresponding to PR = 1.25 80
4.14 3D streamlines, coloured by Mach number, on both the PS and the SS walls corresponding to PR =1.25 81
4.15 Dimensionless blade temperature contour maps for the four different pressures corresponding to PR = 1.00, 1.05, 1.15 and 1.25 82
4.16 Mainstream and coolant temperature contour maps at the aerofoil midspan for the four different pressures corresponding to PR = 1.00, 1.05, 1.15 and 1.25 82

4.17 Laterally-averaged metal effectiveness distribution on both the PS and the SS at four different coolant pressure ratios corresponding to PR = 1.00, 1.05, 1.15 and 1.25. Including a comparison to the ε_m from the simplified model in Chapter 3. 83
4.18 Metal effectiveness versus dimensionless mass flow comparing the CHT results with that from the simplified analysis model 85
4.19 C2 effectiveness results compared with those of some high pressure turbine blades from Holland and Thake (1980) 86
4.20 Blowing ratio and dimensionless mass flow distribution around the aerofoil for PR = 1.25 88
4.21 Blowing ratio distribution around the aerofoil at four coolant pressure ratios - PR = 1.00, 1.05, 1.15 and 1.25 89
4.22 Discharge Coefficient from each of the PS and the SS cooling holes, corresponding to PR = 1.25, compared to the averaged C_d from an isolated wall block. 90
4.23 Flow streamlines coloured by Mach number showing the tendency of the crossflow to close off the PS film cooling holes 92
4.24 Laterally-averaged adiabatic film cooling effectiveness distribution on both the PS and the SS at four different coolant pressure ratios corresponding to PR = 1.00, 1.05, 1.15 and 1.25. Including a comparison to the ε_f from the simplified model in Chapter 3. 93
4.25 CFD laterally-averaged adiabatic film cooling effectiveness, ε_f compared to the ε_f from experiments 94

5.1 A simplified schematic diagram of the single-blade linear cascade. 101
5.2 A simplified schematic diagram of the experimental test facility key components. 102
5.3 A photograph of the test facility showing position of the key facility components 104
5.4 Schematic diagram of the test rig 105
5.5 A photograph showing how the test section was covered during PSP tests . 106
5.6 Schematic diagram showing LE and TE hole configuration as well as a sectioned DWEC blade, unit wall element and geometrical parameters 107
5.7 Film hole distribution on the C1, C2 and C3 DWEC circular blade (a) suction surface and (b) pressure surface, including (c) sectioned view 109
5.8 Film hole distribution on the D1a and D1b diamond pedestal DWEC blade (a) suction surface (b) pressure surface, including (c) sectioned view 110
5.9 Film hole distribution on the D2a and D2b diamond pedestal DWEC blade (a) suction surface and (b) pressure surface, including (c) sectioned view . . 111

5.10 Film hole distribution on the D3a and D3b diamond pedestal DWEC blade (a) suction surface and (b) pressure surface, including (c) sectioned view . . 112
5.11 (a) Shows Cylindrical-throat Venturi nozzle and (b) details of connection between quarter of torus and cylindrical throat (BSI, 2005) 114
5.12 (a) Shows the sectioned front view (b) front view (c) and detailed quarter torus, throat and the divergent section of the d = 9.3 CFVN 114
5.13 Orifice plate showing the front view and sectioned side view and some of the key features 115

6.1 PSP setup and principle of operation 121
6.2 PSP calibration curve 126
6.3 A summary of the general film structure on the PS and SS of the test blades 128
6.4 C1 film cooling effectiveness contour maps 130
6.5 C2 film cooling effectiveness contour maps 131
6.6 C3 film cooling effectiveness contour maps 132
6.7 C1, C2 and C3 individual laterally-averaged film cooling effectiveness . . . 133
6.8 C1, C2 and C3 combined laterally-averaged film cooling effectiveness . . . 134
6.9 D1a film cooling effectiveness contour maps 135
6.10 D1b film cooling effectiveness contour maps 136
6.11 D2a film cooling effectiveness contour maps 137
6.12 D2b film cooling effectiveness contour maps 138
6.13 D3a film cooling effectiveness contour maps 139
6.14 D3b film cooling effectiveness contour maps 140
6.15 Diamond pedestal D1a, D2a and D3a individual laterally-averaged film cooling effectiveness 141
6.16 Diamond pedestal D1a, D2a and D3a individual laterally-averaged film cooling effectiveness 142
6.17 Variation of static pressure distribution, from CFD, around the aerofoil compared to the coolant supply pressure $P_{o,c}$ 143
6.18 Mach number distribution on the blades obtained from CFD and using the boundary conditions presented in Table 5.1, including the streamwise hole locations 146
6.19 Recovery temperature distribution around the aerofoil 146
6.20 The flow function characteristics of all the 9 DWEC test blades 148
6.21 Diamond pedestal blade designs D1a, D1b, D2a, D2b, D3a and D3b combined laterally-averaged film cooling effectiveness 149

List of Tables

3.1 The unit wall block element dimensions from Murray et al. (2017) 40
3.2 The engine-scale operating conditions used for the numerical simulation from Colladay (1972) 44
3.3 Geometrical parameters and dimensions of the six unit wall block elements from Murray et al. (2017) used to build the midchord section of the DWEC blades 55

4.1 Geometrical parameters and dimensions of the C2 unit wall element from Murray et al. (2017) used to build the midchord section of the DWEC blade 70
4.2 Boundary conditions and initial conditions for ANSYS[1] CFX solver 75
4.3 Pressure ratios used in the CFD and experiments and their corresponding coolant mass flow rates 95

5.1 Flow conditions, blade and cascade geometry 100
5.2 A summary of the test matrix 103
5.3 The test blades design geometrical design details based on the unit wall elements from Murray et al. (2017) 108
5.4 Dimensionless streamwise location of the film hole rows 113
5.5 Uncertainty analysis for low mass flow rate measurements from Small Perturbation method of Moffat (1988) 116
5.6 Uncertainty analysis for high mass flow rate measurements from Small Perturbation method of Moffat (1988) 117
5.7 Uncertainty analysis for calibration curve parameter - P/P_{Ref} 117
5.8 Uncertainty analysis for low film effectiveness, ε_f measurements 118
5.9 Uncertainty analysis for high film effectiveness, ε_f measurements 118

Nomenclature

A	Surface area [m^2]
C	Concentration [$mol.m^{-3}$]
C_{ax}	Axial chord length [m]
C_d	Discharge coefficient [-]
C_p	Specific heat capacity [$J.kg^{-1}.K^{-1}$]
D	Diameter [m]
D_h	Hydraulic diameter [m]
E	Orifice plate expansibility factor [-]
G	Mass flux [$kg.m^{-2}.s^{-1}$]
h	Heat transfer coefficient [$W.m^{-2}.K^{-1}$]
I	Image pixel intensity [-]
k	Orifice plate isentropic exponent [-]
K	Thermal conductivity [$W.m^{-1}.K^{-1}$]
L	Length [m]
m	Metal [-]
M	Blowing ratio [-]
Ma	Mach number [-]
$\dot{m}$	Mass flow rate [$kg.s^{-1}$]
m*	Non-dimensional mass-flow [-]
N	Cooling modulus [-]
N_2	Nitrogen gas [-]
O_2	Oxygen gas [-]

P	Pressure [Pa]
Pr	Prandtl number [-]
R	Radius of the aerofoil leading edge [m]
Re	Reynolds number [-]
St	Stanton number [-]
Sx, Sz	Streamwise and spanwise pitches respectively [-]
T	Temperature [K]
u	Velocity [$m.s^{-1}$]
W	Gas molecular weight [$kg.kmol^{-1}$]
x, z	Cartesian coordinates [-]
x_{decay}	Streamwise film decay factor [-]
$z_{1/2}$	Lateral distance at which the temperature difference drops to half [m]

Greek Symbols

α_t	Turbulent thermal diffusivity [$m^2.s^{-1}$]
β	Orifice Plate diameter ratio [-]
ε	Effectiveness [-]
ε_f	Film effectiveness [-]
ε_m	Metal effectiveness [-]
ε_o	Overall metal effectiveness [-]
η_c	Convective efficiency [-]
Λ	Recovery factor [-]
μ	Dynamic viscosity [$Pa.s$]
ρ	Density [$kg.m^{-3}$]
ϕ	Unit wall element outer skin porosity [-]

Subscripts

1	Upstream of orifice plate
2	Downstream of orifice plate
∞	Mainstream
air	Air

atm	Atmospheric
ave	Average
aw	Adiabatic
B	Black
c	Coolant
ex	External
f	Film
fg	Foreign gas
in	Internal
mix	Mixture
o	Total
Ref	Reference
s	Static
w	Impenetrable wall

Abbreviations

CAD	Computer Aided Design
CCD	Charge-Coupled Device
CFD	Computational Fluid Dynamics
CFVN	Critical Flow Venturi Nozzle
CHT	Conjugate Heat Transfer
DAQ	Data Acquisition
DWEC	Double-Walled Effusion-Cooled
FEM	Finite Element Method
HTC	Heat Transfer Coefficient
IMB	Immersed Mesh Block
LE	Leading Edge
LED	Light-Emitting Diode
PR	Pressure Ratio
PS	Pressure Surface

PSP	Pressure Sensitive Paint
RANS	Reynolds-Averaged Navier–Stokes
RNG	Re-Normalisation Group
SLA	Stereolithography
SS	Suction Surface
SST	Shear Stress Transport
TBC	Thermal Barrier Coatings
TE	Trailing Edge
TET	Turbine Entry Temperature
TSFC	Thrust Specific Fuel Consumption

Chapter 1

INTRODUCTION

1.1 Introduction

This chapter aims to put the research reported in this thesis into context. It starts by providing a brief introduction to gas turbine engines. It then spells out the need for gas turbine cooling. A large part of this chapter provides an overview of four key cooling technologies that are closely related to the current research namely; film cooling, transpiration cooling, effusion cooling and some of the more advanced gas turbine cooling schemes. It then situates the current work into context and clearly states the research objectives. Section 1.6 provides a summary of what is contained in all the chapters of this thesis.

1.2 Gas Turbine Engines

Gas turbine engines are vital prime movers in the aerospace industry. The different forms of gas turbine aeroengines can be broadly classified into five categories, specifically the turbojet, turbofan, turboprop, turboshaft and propfan (Rolls-Royce, 2015). A gas turbine engine has five key sections namely; the intake section, the compressor section, combustor, the turbine section and the exhaust section. Figure 1.1 shows a Rolls-Royce Plc. Trent 1000 gas turbine engine with some of the key sections labelled. The engine works by drawing air through inlet and passing it into the compressor to be pressurized. After which (1) about 20% is ducted to be used for the engine hot-section cooling and (2) the rest is passed into

the combustor for combustion. The hot high-pressure combustion gases from the combustor are expanded through the turbine generating mechanical energy that turns the shaft that drives the fan and compressor. The gases exiting the turbine pass through the exhaust nozzle at high speed providing thrust. This combination of processes responsible for the intake, compression, combustion, expansion and exhaust cycle is called the Brayton or Joule cycle.

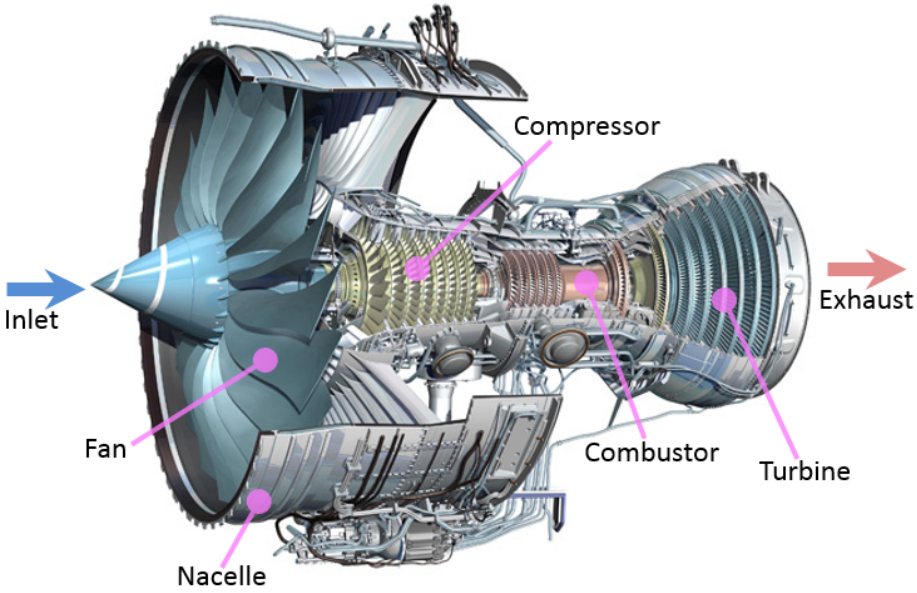

Figure 1.1: The Rolls-Royce Plc. Trent 1000 turbofan gas turbine engine (Copyright: Rolls Royce Plc)

For gas turbine engines, the primary engineering metrics include efficiency, weight, additional drag and reliability. The overall efficiency refers to efficiency with which the engine converts the power in the fuel flow to the propulsive power. The overall efficiency is a product of the thermodynamic efficiency and the propulsive efficiency. Figure 1.2 shows the thermodynamic efficiency and propulsive efficiency of some of the commercial gas turbine engines. Included in the figure also is overall efficiency and thrust specific fuel consumption (TSFC).

Since the first aircraft gas turbine engine was built in late 1940s, the overall efficiency has improved from about 10% to in excess of 40% at the present. Epstein (2014) predicts that in the next couple of decades, and given a sufficient technology investment, it is likely that the gas turbine engine will continue to see overall efficiency improvements of about 7% per decade. There are many active research programmes currently focused on various engine sections with the overarching aim of further improving efficiency. One of the high-potential

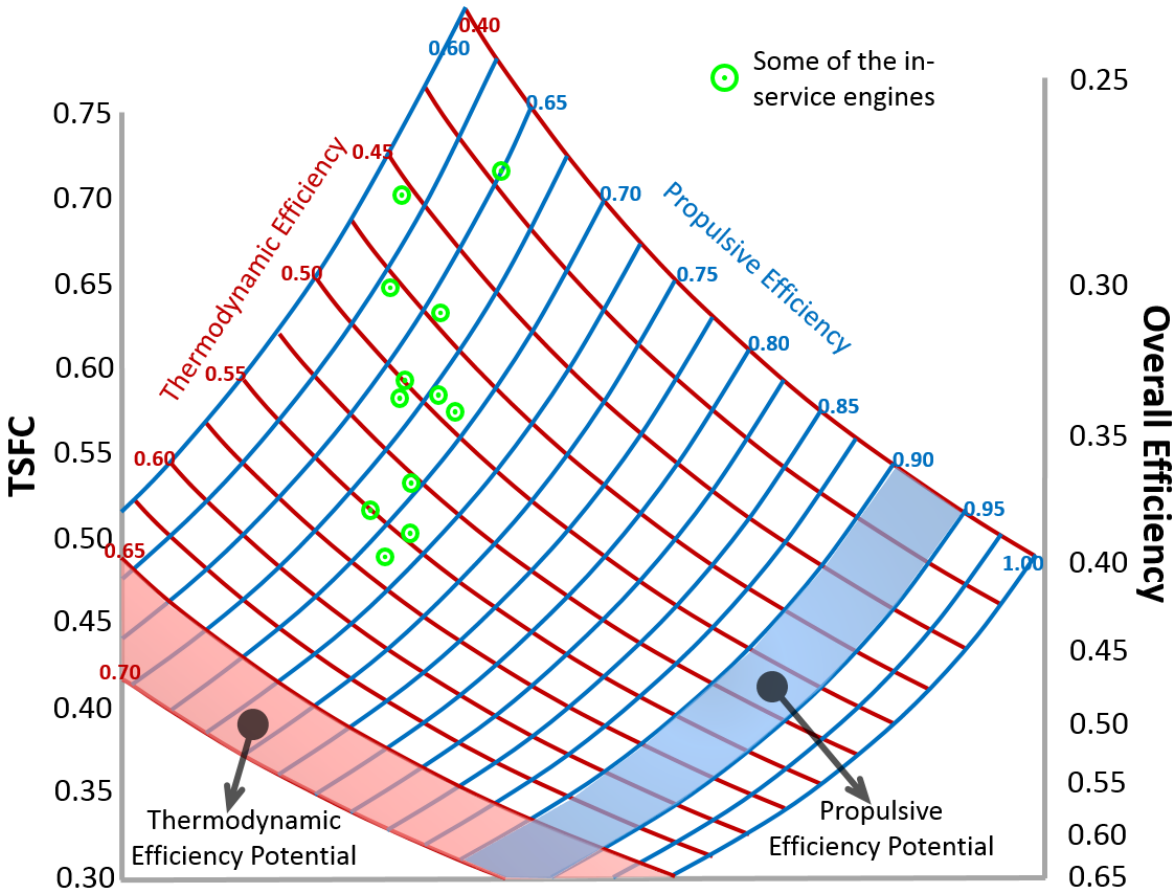

Figure 1.2: Thermodynamic and propulsive efficiencies at cruise of some of the in-service gas turbine engines, including thrust specific fuel consumption (TSFC) and overall efficiency. Adapted from Epstein (2014)

areas for further improving the engine efficiency that has received a considerable attention over the last few decades is gas turbine cooling.

1.3 Gas Turbine Cooling

The desire to build a gas turbine engine with both high efficiency and high specific power output has led to the use of very high turbine entry temperature (TET), as illustrated in Figure 1.3 (Han et al., 2012). The continuous increase in TET has resulted in an extremely harsh environment for turbine blades and other critical hot stage components. The current turbine blade alloy material's melting point is several hundred degrees below the temperature of the incoming combustion gasses. To ensure the operation of the turbine section, there is an inevitable need for cooling. From the Brayton cycle, the engine cycle efficiency increases with the increase in the TET (Han et al., 2012). Turbine blade cooling, therefore, permits the

use of high TET whilst reducing blade thermal stresses and thus prolonging the engine life.

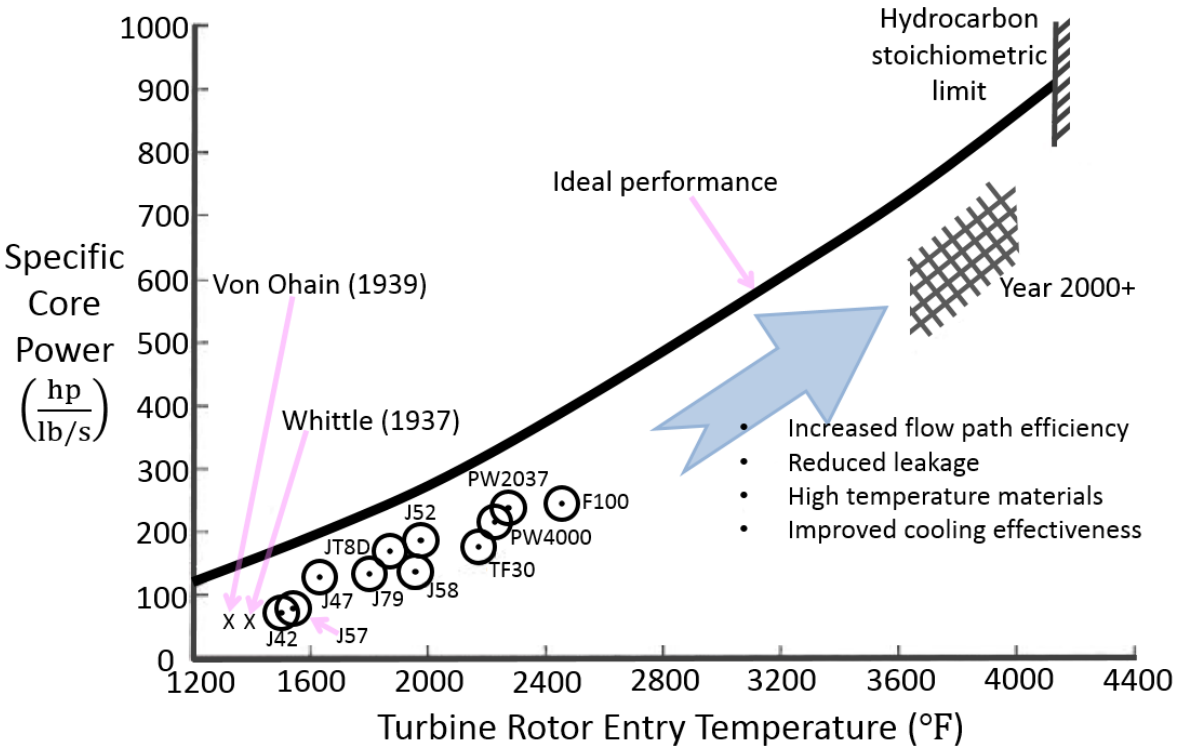

Figure 1.3: Increased turbine inlet temperature dramatically improves cycle power output (Han et al., 2012)

The concept of gas turbine cooling was first conceived in the 1960s. The most commonly applied cooling technique then was simple convection cooling. But with improvements in both manufacturing technologies and materials, sophisticated cooling technologies came into being permitting high TET. Figure 1.4 shows the TET rise (of about 10 K per year) in the Rolls-Royce jet engines from below 1000 K in 1940s to over 2000 K today. Judging from the trend observed over the years, TET is foreseen to keep rising (the stoichiometric limit being at about 2560 K, see Figure 1.3) (Han et al., 2012).

Cooling of the gas turbine blades is achieved by using high pressure air extracted from the compressor. This extraction of cooling air from the compressor for the engine hot-section leads to a direct debit in the engine thermal efficiency. Research and implementation of improved cooling techniques, therefore, is vital in reducing the amount of cooling air and improving engine efficiency. Gas turbine blades are cooled both internally and externally. The former is typically achieved by (1) passing the cooling air through several enhanced serpentine passages that are inside the blade and for the vanes (2) jet impingement and/or (3)

pin-fin cooling are used. On the other hand, external cooling is achieved by bleeding cooling air through cooling holes onto the surface of the blade forming a film of cool air that protects the blade surface from the hot mainstream gases. The external cooling process is referred to as film cooling (Han et al., 2012).

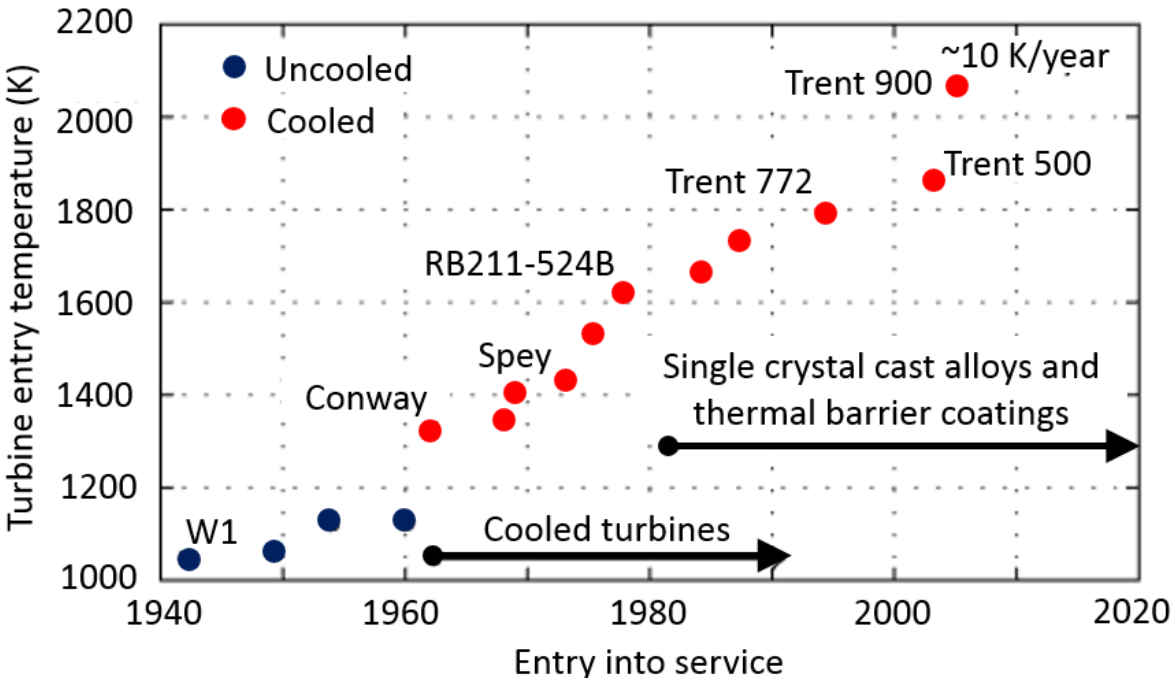

Figure 1.4: Turbine entry temperature versus the date of entry into service (Astarita et al., 2015)

1.3.1 Film Cooling

Film cooling, combined with a multi-pass system, an example is shown in Figure 1.5, has become the most common cooling method for turbine blades. In film cooling, cooling air is continuously bled from the blade internal passages through a discrete number of cooling holes onto the blade external surface. This forms a low-temperature layer of air that protects the blade from the hot mainstream gases. There have been many research studies, both experimental and computational, of film cooling with the aim of improving the state-of-art. Bunker (2006) noted that almost all the aspects of film cooling have been extensively explored. Despite this fact, the cooling air used in conventional film cooling does not reach its maximum heat sink potential and is thus considered not optimized (Bunker, 2006). For this reason, Bunker (2006) argued that there is still a chance to achieve what is called the

"ultimate discrete hole film cooling". In addition, the desire to attain a much higher engine efficiency and reduce the cooling air required has led to research into advanced cooling techniques such as transpiration cooling or those that closely approximate transpiration cooling, such as multi-wall cooling. Figure 1.6 shows the cooling effectiveness (defined as the difference between the mainstream gas temperature and metal temperature divided by the difference between the mainstream gas temperature and the coolant inlet temperature) of the combined film and convection cooling and a potential cooling effectiveness improvement that can be attained by investing in more advanced cooling technologies.

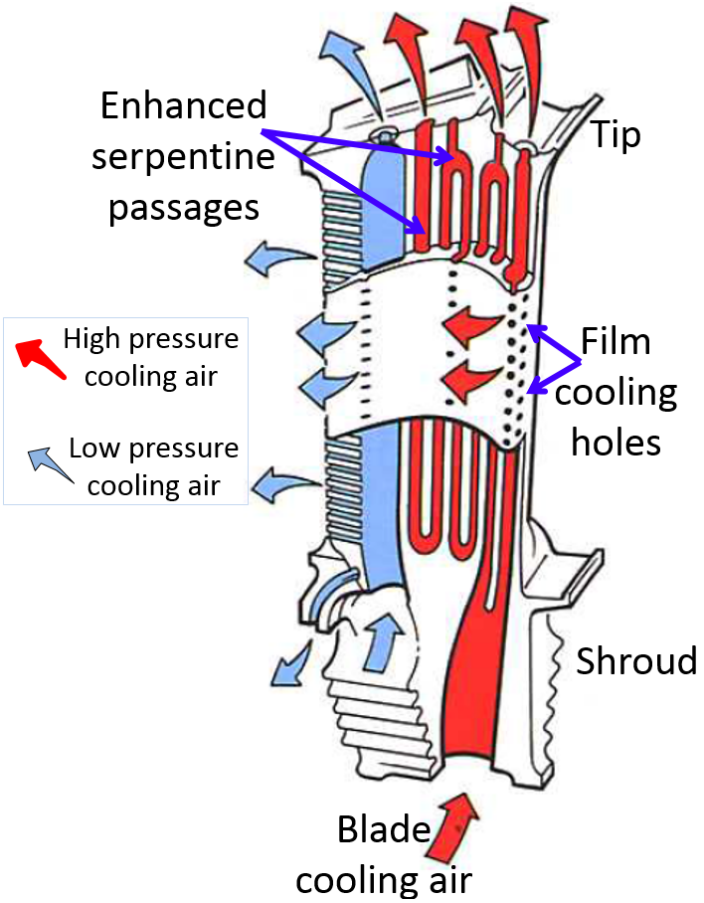

Figure 1.5: A cut away section of a high pressure turbine blade which is cooled both internally, through enhanced serpentine passages, and externally through film cooling. Adapted from Rolls-Royce (2015)

1.3.2 Transpiration Cooling

Transpiration cooling is a technique where cooling air effuses out of a porous material to the external surface forming a continuous buffer layer that blocks the hot mainstream gases

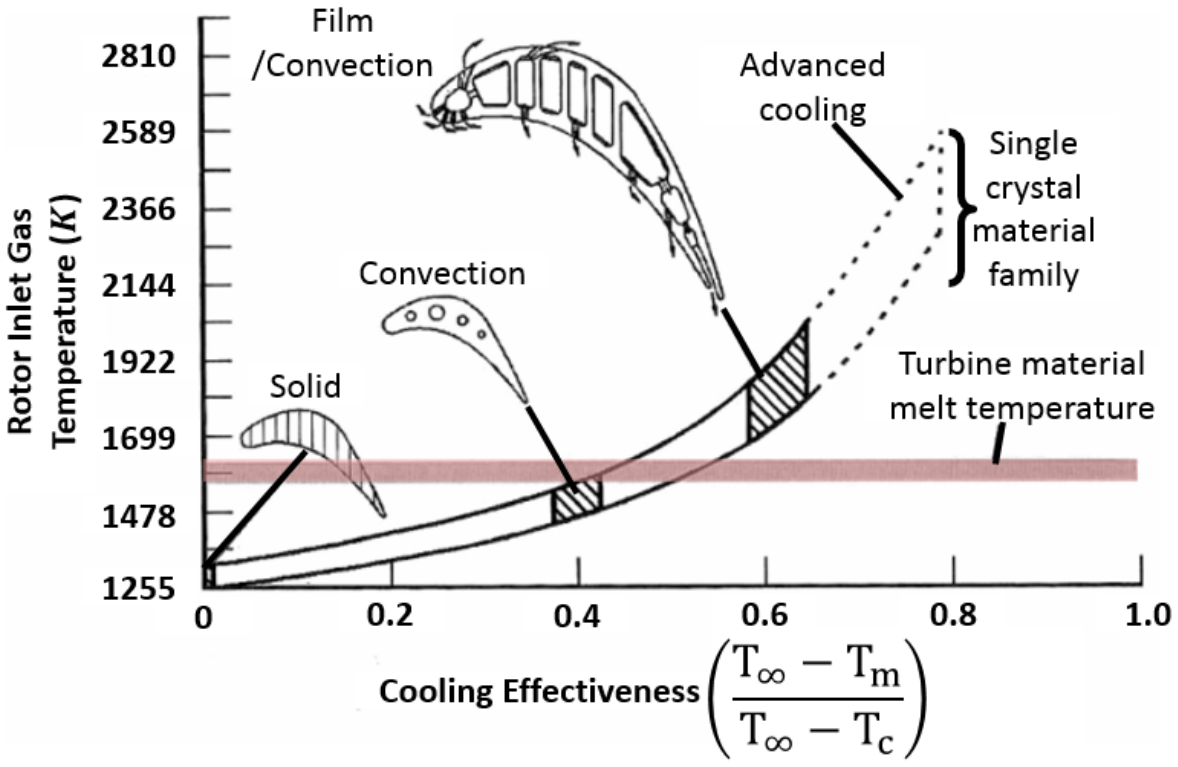

Figure 1.6: TET and cooling effectiveness achievable by solid, convection, film/convection and advanced cooling (adapted from Koff (2004))

and hence reduces the heat flux to the material. In an ideal transpiration cooling process, the cooling air extracts so much heat, uniformly, as it seeps through the vast number of tiny pores (that provides an extensive heat exchange area) so that it reaches thermal equilibrium with the wall material reaching the wall temperature by the time it exits the material. An example of a transpiration cooled aerofoil concept is shown in Figure 1.7 where the skin is a porous wall with pores which are approximately 100 μm in diameter.

The fundamental mechanism responsible for transpiration cooling is illustrated in Figure 1.8. Perhaps one of the most attractive characteristics of transpiration cooling is its ability to hardly cause any disturbance to the boundary layer, even at relatively high blowing ratios as observed by Andrews et al. (1986). Transpiration cooling is considered the ultimate cooling technique; using the least amount of cooling air whilst delivering the highest turbine efficiency (Boyce, 2011). However, the compromised structural strength of the porous material (relative to the solid material), oxidation, and the potential for blockage of the very small coolant passage by sand, dust or pollution as well as the absence of a method for accurately measuring aerothermal and mechanical stress fields have prevented practical implementation

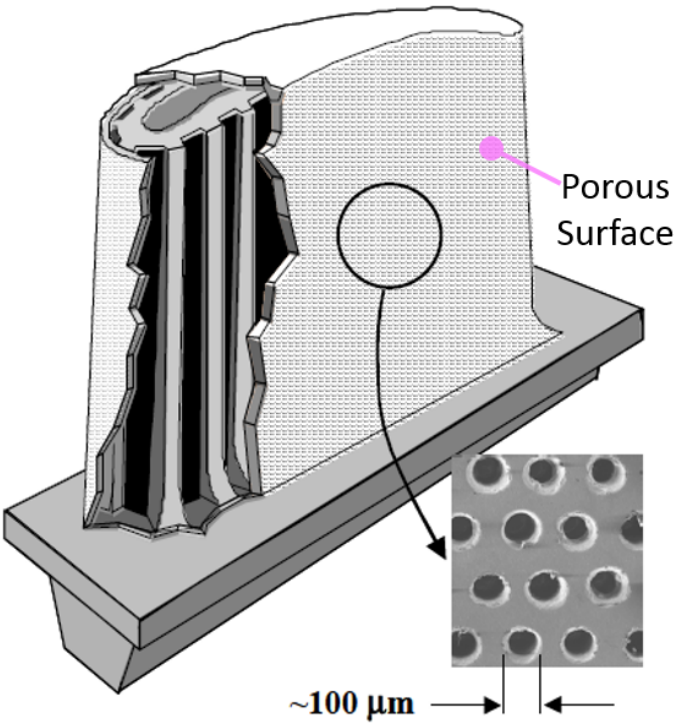

Figure 1.7: Transpiration cooling of a concept aerofoil using a porous surface (Bunker, 2006)

of this cooling method.

1.3.3 Effusion Cooling

Effusion cooling is sometimes commonly referred to as full-coverage discrete film cooling. The main difference between film cooling and effusion cooling lies in the number and size of the cooling holes employed. Effusion cooling is associated with many small-diameter, closely-packed film holes whereas film cooling is associated with relatively fewer large-diameter film holes. Consequently, the momentum and velocity of jets present in effusion cooling are lower than for film cooling.

In practice, there seems not to be a very distinct difference between systems referred to as transpiration cooling or effusion cooling in the literature. Some authors (for instance Brown (1990)) allude that any cooling system that fully utilizes the cooling air heat capacity, so that the coolant attains thermal equilibrium with the surface of the component being cooled, qualifies to be called transpiration cooling system. However, in general, the term transpiration cooling is often associated with the use of porous material whereas effusion cooling is associated with the use of a solid with a multitude of discrete small-diameter cooling holes.

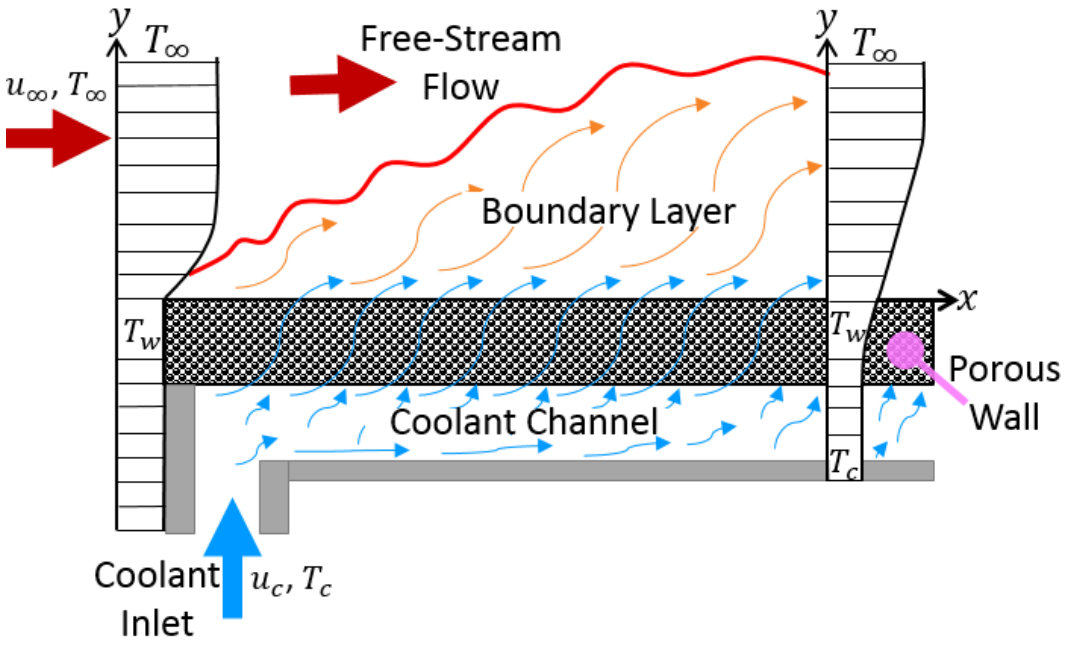

Figure 1.8: Fundamental mechanism responsible for transpiration cooling. Adapted from Polezhaev (1997)

Colladay (1972) in their analysis and comparison of three advanced gas turbine wall cooling schemes (transpiration cooling, effusion cooling and film cooling) noted that effusion cooling overall cooling performance lies somewhere in the spectrum between pure transpiration cooling and film cooling.

Figure 1.9 gives a schematic summary of the principle cooling technologies for turbine blade cooling as well as three variations of effusion cooling - Lamilloy®, Transply® and Poroform®.

1.3.4 Advanced Turbine Blade Cooling

With further advancement in manufacturing technologies, it has been possible for gas turbine researchers to realise advanced and sophisticated cooling designs by combining advanced internal cooling, film cooling, effusion cooling, impingement cooling, and other available cooling schemes. For instance, it is possible to combine effusion cooling and impingement cooling so that coolant jet flows from an aerofoil internal wall through discrete cooling holes (called impingement cooling holes) and impinge on the outer wall before flowing out through discrete effusion cooling holes. The most notable early developments incorporating effusion and impingement cooling include; Lamilloy®, as shown in Figure 1.10, and CastCool® de-

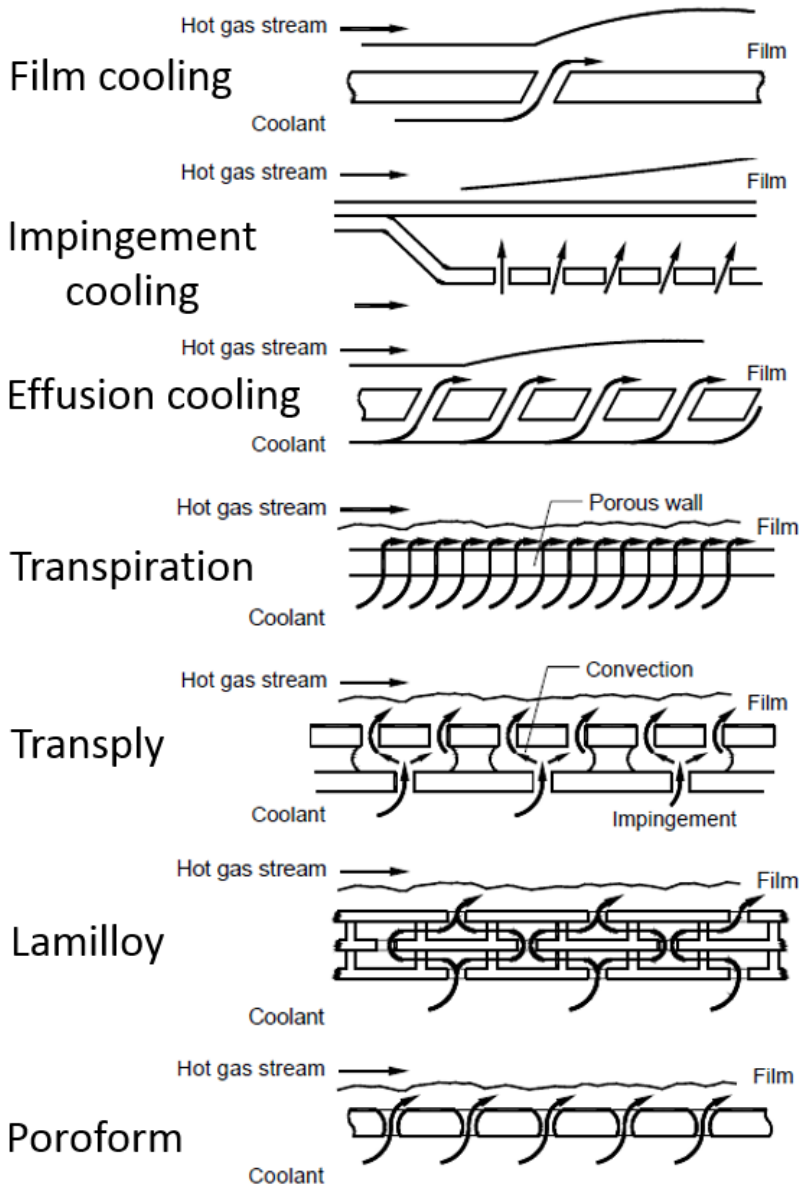

Figure 1.9: A schematic summary of the principle cooling technologies; film, impingement, effusion and transpiration cooling as well as the variation of effusion cooling schemes - Lamilloy®, Transply® and Poroform® (Battisti et al., 2006)

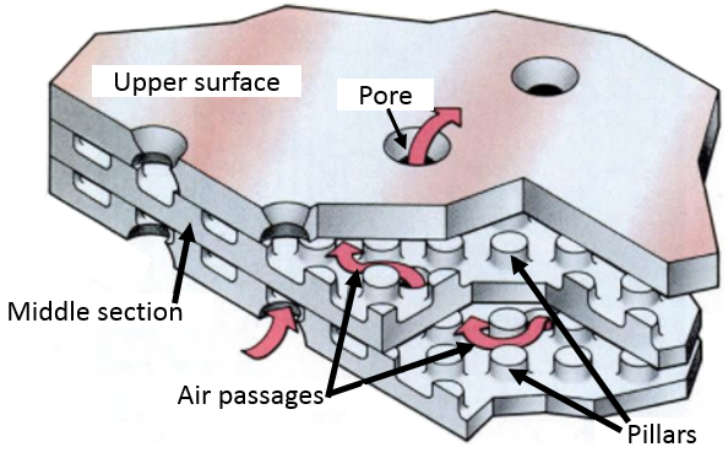

Figure 1.10: Allison's Lamilloy® transpiration cooling system: Pillars cast or etched into sheet material gives this triple sandwich an extended surface area over which air must pass through (Brown, 1990)

veloped by Allison Advanced Development Corporation.

These multi-wall porous designs allow cooling air to be bled from the impingement holes, that are staggered with respect to the film cooling holes on the outermost sheet, and as the air issues out of film holes on the outermost layer, it forms a transpiration-like film cover resulting in an excellent coolant layer on the surface of the component. Associated with these cooling schemes is significant heat pick up by the cooling air as it makes its way through a dense maze of the pillars cast/etched between the walls. Figure 1.11 shows a variation of Lamilloy® design called Snowflake (Sweeney and Rhodes, 1999).

Multi-wall porous cooling designs such as Lamilloy® and Transply® have been successfully employed for cooling gas turbine combustors. For instance, Lamilloy® combustor design was employed in several engine models including T800 turboprop engine while Transply® combustor design was developed by Rolls Royce and employed in their Spey engines (Wadia, 1988). Wassell and Bhangu (1980) analysed Transply® and concluded that Transply® permitted a significant saving in cooling air - approximately 70% compared to the conventional combustor material.

As aforementioned, transpiration cooling is considered the ultimate cooling technology for the gas turbine blades. However some of the challenges such as inadequate structural strength of the porous material, oxidation, and blockages associated with the use of porous material have barred the practical implementation of this cooling technique. The laminated

multi-wall cooling schemes are often judged to offer the most practical implementation of transpiration cooling. Just like transpiration cooling, these porous laminated double-walled systems are associated with not only superior cooling uniformity, owing to a series of highly distributed micro cooling channels, but also more efficient heat transfer as the cooling air is brought closer to the aerofoil's outer surface. In addition, due to the high internal convective efficiency associated with these cooling designs, the cooling air heat sink potential is fully utilized. As a result, the amount of air required for cooling is reduced. In broad terms, the amount of convection heat transfer depends to a larger extent on how tortuous the internal flow passages are. For instance, simple air passage layout results in a low heat transfer to the cooling air and, consequently, low internal convection effectiveness whereas a maze of interconnected flow passages result in a high internal heat transfer and hence a high convection effectiveness. Owing to the close approximation to transpiration cooling, some researchers have called these multi-wall cooling systems semi- or quasi-transpiration cooling schemes (Lefebvre, 1998).

It should be noted that in double-wall combustor designs, bulk of pressure drop takes place at the impingement plate and pressure drop across the effusion wall is minimized so as to ensure good film cooling effectiveness (Andrews et al., 1990). However, due to a large static pressure variation around a turbine blade, relative pressure drop between impingement and effusion walls becomes more complex than in combustor application. Another challenge when applying double-wall cooling to a rotor blade will be extra weight - resulting from an additional skin and a bank of pedestals. Turbine blade is attached to a turbine disc via a fir-tree root joint. Owing to high rotational velocities coupled with high temperature gradients, gas turbine rotor discs experience high mechanical and thermal stresses. The disc is generally subjected to a combination of three loads; thermal load, aerodynamic load and centrifugal load (Witek, 2006). A large proportion of centrifugal load experienced by the disc emanates from turbine blades. Therefore, turbine rotor weight has a direct impact on the stresses experienced by the turbine rotor disc.

Micro cooling, defined by Bunker (2006), is any cooling system that aims to bring cooling air as close as possible to the outer hot surface of the aerofoil using series of smaller

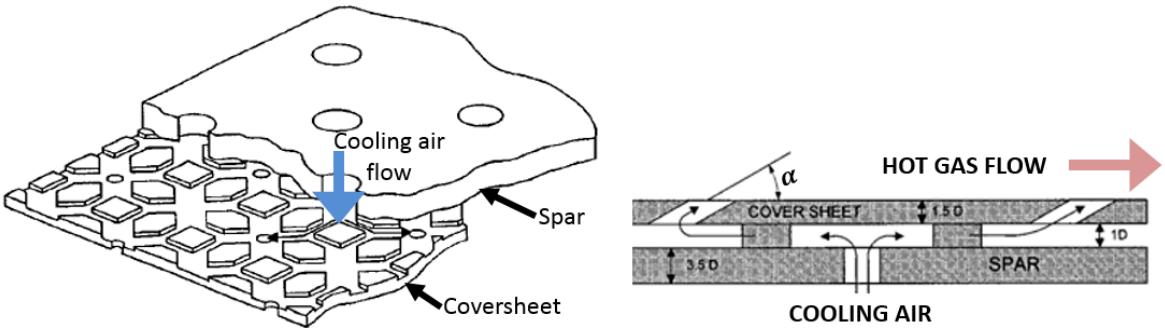

Figure 1.11: Snowflake Lamilloy® design (Sweeney and Rhodes, 1999)

highly-distributed channels and sub-channels so as to allow more efficient heat transfer. An example of a micro cooling system is the Poroform® aerofoil developed by Battisti et al. (2006) which incorporates an effusive cooling system which is manufactured through an electroforming process. In this technology, a metallic matrix (M) in Figure 1.12 is built using a blade's geometrical coordinates then indentation made on its surface to produce carefully designed imprints (S). Resin (R) is used to fill the imprints by dipping the matrix into a bath of dielectric material. The next step involves electroplating. Metal deposition (A) takes place and a metal skin grows to the required wall thickness before the blade is removed from the matrix. Metallic deposition occurs at the cathode and there is no deposition in areas where there is a dielectric discontinuity.

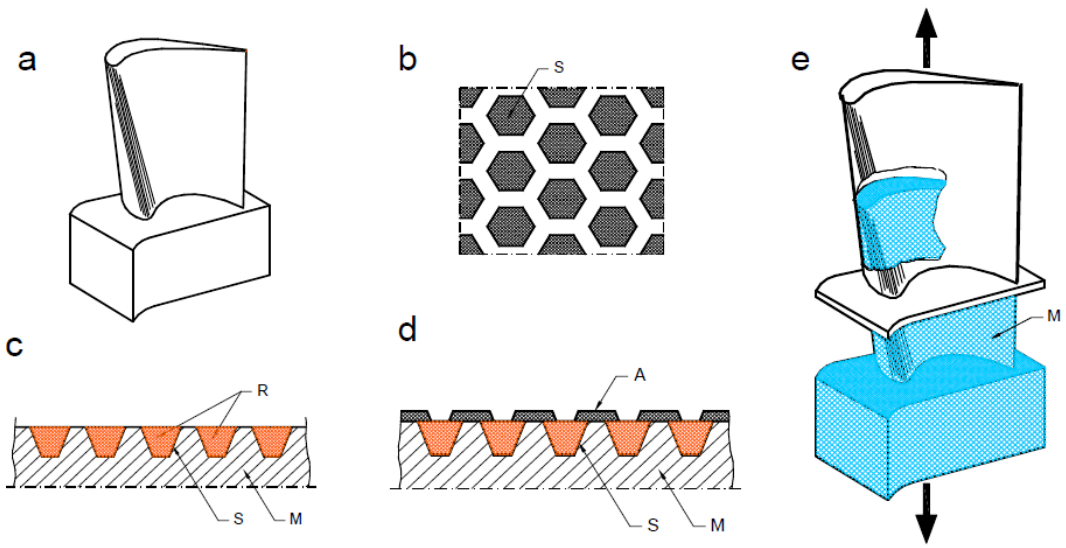

Figure 1.12: Electroforming process to produce a Poroform concept turbine blade (Battisti et al., 2006)

Despite the potential excellent cooling capabilities offered by micro channel cooling, this

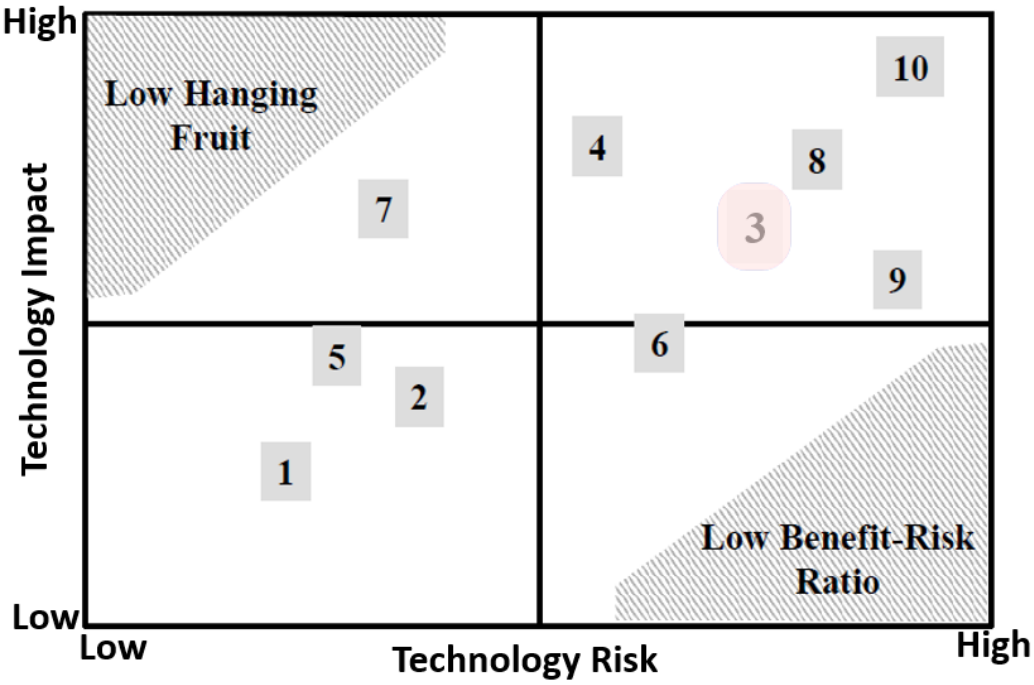

1. Uniformity of internal cooling
2. Ultimate discrete hole film cooling
3. Micro cooling
4. Reducing incident heat flux
5. Secondary flows as prime cooling
6. Micro-3D HGP surfaces
7. Thermal stress reduction
8. Controlled and adaptable cooling
9. Low emission comb-turbine systems
10. Regenerative cooling

Figure 1.13: Technology impact-risk ranking of the ten challenges (Bunker, 2006)

technology is not free from practical constraints and performance limitations. The risks of using micro-channel cooling include; unexplored thermal and fluid behaviour, the high cost of manufacture, hole plugging (if the passages are too small) by dust and sand, reduced wall strength. Bunker (2006) notes that micro cooling technology carry relatively a high technological risk (see Figure 1.13). However, if micro cooling could be successfully implemented, the technology offers a significant cooling benefit that would improve the overall engine efficiency (Bunker, 2006). With dedicated research and development, it is believed possible to design a micro-cooled system with an optimum cooling flow distribution where the amount of cooling air delivered to different regions of the aerofoil is based on the heat load characteristics. An effective cooling design would eliminate the over cooling or under cooling of the aerofoil resulting in coolant and metal temperature uniformity (Bunker, 2013).

Bunker (2005), in his extensive analysis of the '10 Remaining Hot Gas Path Challenges', lists the use of porous multi-wall (also known as micro cooling) as one of the potential not-

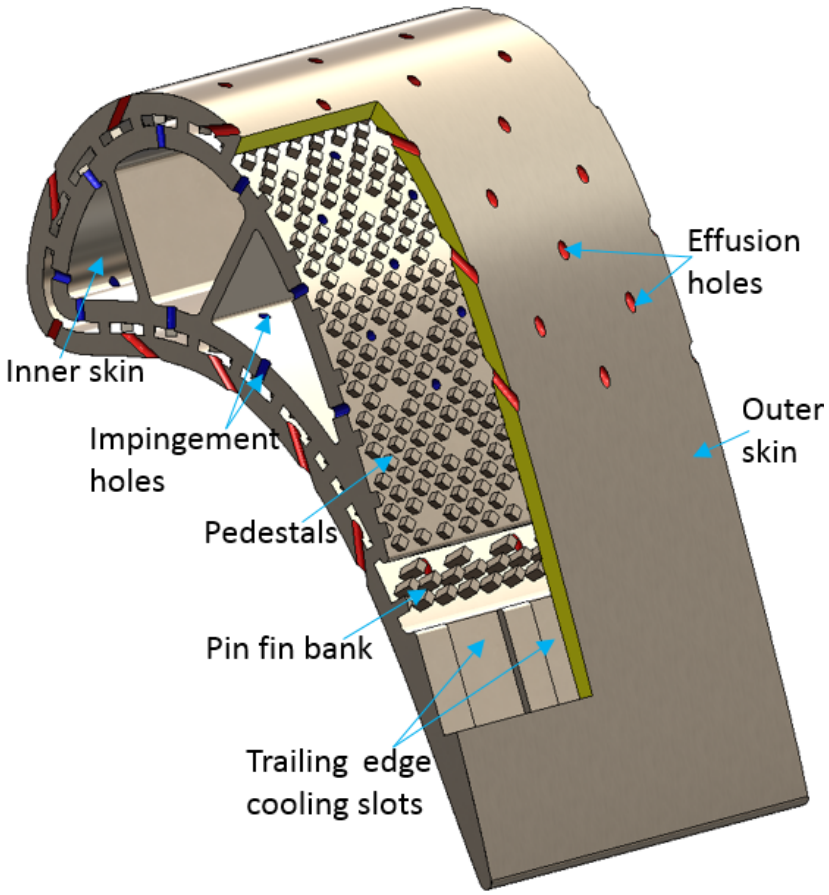

Figure 1.14: Key features of a double-walled effusion cooled concept turbine blade

fully-explored cooling areas that can take turbine cooling to a higher level of performance. A similar observation was made by Krewinkel (2013) who, after carrying out an extensive literature survey on effusion cooling, concluded that "the effects of effusion-cooling on full blades have neither been investigated very thoroughly nor are they understood very well". He reasoned that simply combining the body of basic research on effusion cooling of more basic geometries does not suffice and that the bulk of the future work should, therefore, be conducted in this field (Krewinkel, 2013).

Porous multi-wall cooling schemes such as double-wall cooling combined with effusion cooling (as shown in Figure 1.14) offer a practical approximation to transpiration cooling which, in turn, present a potential for very high cooling effectiveness. Most of the numerical and experimental research that has been conducted on flat plates, for instance recently by Murray et al. (2017), have consistently confirmed the significant cooling effectiveness potential associated with multi-wall cooling. Multi-wall cooling is arguably the next step in the

gas turbine cooling. Yet there are hardly any studies, to the best of the author's knowledge, of the double-wall effusion cooling applied to turbine aerofoils. Most of the double-wall effusion cooling research has been conducted on flat plates. Owing to the curved nature of an aerofoil, external flow over an aerofoil is associated with varying external static pressure (see Figure 3.11) and secondary flow features - Figure 1.15 (absent on flow over a flat plate geometry) which have an influence on heat transfer behaviour, film cooling performance and ultimately overall cooling performance. There is a need, therefore, for research that will extend the study of double-wall cooling technology on flat plates to a turbine-representative aerofoil.

Murray (2019) carried out experimental and numerical studies of double-wall effusion cooling performance, focusing on aerothermal and thermomechanical analysis, on thirteen diamond pedestal and seven circular pedestal geometries of wall blocks. In these wall blocks, the external and internal skins are connected via a bank of pedestals as shown in Figure 3.14. The wall block geometries were developed using design of experiments methodology whereby various geometric parameters were varied (Murray, 2019). Simplicity of pedestal shape, availability of prior data, pressure loss characteristics and ease of manufacture were major factors that informed the choice of diamond and circular pedestals (Murray, 2019).

The present author has made use of the design data and results from the double-wall blocks of Murray (2019) to build double-wall effusion cooled turbine-representative aerofoils. Both low porosity and high porosity circular and diamond pedestal designs were considered in the present study. In order to extend the work of this author, another research is underway at Oxford Thermofluids Institute at the University of Oxford (Wambersie, 2019). Wambersie (2019) research aims to experimentally and numerically study effusion cooled turbine-representative aerofoils; like the one studied here, but with effusion cooling scaled down as much as technically possible so as to approximate transpiration cooling. The research will produce film cooling effectiveness, metal cooling effectiveness and well as aerodynamic losses measurements.

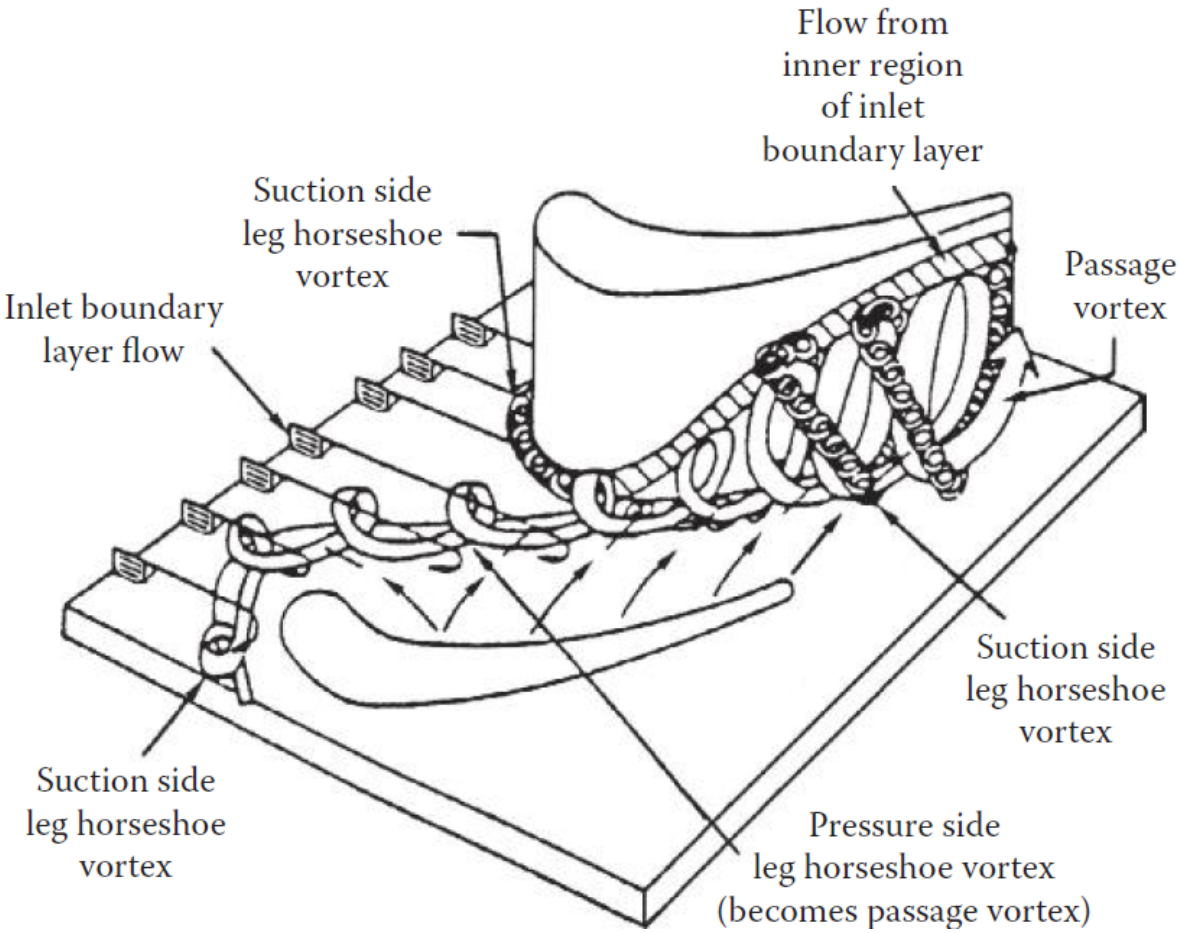

Figure 1.15: Secondary flow features in a turbine cascade (Sharma and Butler, 1987)

1.4 Research Aims

The main aim of the present work was to extend knowledge of the performance of double-wall effusion cooling from a flat plate to a gas turbine blade. In pursuing this principle aim, the following objectives formed the focus of this thesis.

1. To undertake a thorough review of literature to identify the scope of the work related to the present research.

2. To develop a novel computationally efficient numerical analysis tool for efficient analysis of a DWEC blade that would enable the interaction between key performance parameters like, mass flow rates, metal effectiveness and film effectiveness to be understood. The conventional fully meshed, 3D CHT is computationally costly and is thus not ideal where preliminary results are required to enable early design and optimization.

3. To carry out fully coupled CHT simulations using commercial CFD software to (a) validate the developed simplified numerical analysis tool (b) obtain further insight into the performance of the DWEC blades.

4. To carry out film cooling effectiveness tests to measure full surface film cooling effectiveness performance for full DWEC implementations. A detailed analysis of film cooling performance on a double-walled effusion-cooled blade is essential for both the coolant consumption optimization and assessment of the film to offer the desired levels of the turbine blade protection.

1.5 Thesis Contributions

The main scientific contributions of the current research are summarised as follows;

1. This research has developed a novel computationally efficient numerical analysis approach for analysing double-wall effusion cooled aerofoils. An existing correlation from the literature was modified and used to represent the two-dimensional distribution of film cooling effectiveness. The internal heat transfer coefficient was calculated from a validated conjugate analysis of a wall element representing an element of the aerofoil wall and the conduction through the blade solved using a finite element code in ANSYS[1]. The numerical procedure developed has permitted a rapid evaluation of the critical parameters including; film cooling effectiveness, blade temperature distribution (and hence metal effectiveness) as well as coolant mass flow distribution and consumption.

2. The present work has yielded CFD analysis of the DWEC blade. The CFD gave further insight into the DWEC cooling performance as well as a means of validating the simplified numerical analysis code for evaluating blade temperature.

3. This work has yielded a detailed film cooling performance results on the surface of the double-walled effusion-cooled turbine blades. This is the first time, to the best

[1] www.ansys.com

knowledge of the author, film effectiveness has been performed on a DWEC aerofoil. These results will be valuable in the design of the second-generation double-wall effusion-cooled turbine blades.

4. The present research has yielded three research papers: one in progress and two peer-reviewed - GT2018-76534 by Ngetich et al. (2019b) (which has also been archived in the ASME Journal of Turbomachinery - 141(1)p. 011002) and GT2019-90545 by Ngetich et al. (2019a). The author also presented the two research papers in the American Society of Mechanical Engineers (ASME) Turbomachinery Conference; GT2018-76534 in the 2018 ASME conference held in Oslo, Norway and GT2019-90545 in the 2019 ASME conference held in Phoenix, Arizona, USA.

5. The present work has produced a patent - US2019/0323359A1 (Ireland et al., 2019). The patent describes a proposal of a potential single-crystal CMSX-4 turbine blade manufacturing procedure. The invention proposes a method of fabricating effusion-cooled double-walled aerofoils. This method makes it possible to fabricate a double-walled aerofoil with a single crystal structure using the current engine blade material. The patent information has been included in Appendix A of this thesis.

The present work has stretched the double-wall cooling technology research that has long been researched on flat plates onto a turbine aerofoil. This work has contributed knowledge of DWEC aerofoils including flow structure, overall cooling effectiveness, internal cooling effectiveness and film cooling effectiveness performance. There is still much work to be done (including investigation into aerodynamic losses and stresses associated with this cooling technology) to realise a practical double-wall effusion-cooled blade. Nonetheless, the present work has made a significant step in the quest for understanding of the operation of a practical DWEC aerofoil.

1.6 Thesis Structure

This thesis is divided into nine chapters. Brief details of each chapter are described below:-

Chapter 1 Puts the current research into context by giving a brief introduction into jet engines and some of the existing jet engine cooling technologies. This Chapter identifies the existing gaps and outlines the thesis objectives as well as the work's contributions.

Chapter 2 Reviews the reports in the literature, related to the present research, and makes a case for the current research.

Chapter 3 Outlines the novel simplified numerical analysis tool that has been developed by the author for efficient performance analysis of DWEC aerofoils.

Chapter 4 Reports the fully coupled CHT simulations and results.

Chapter 5 Describes details of the experimental facility and apparatus used during PSP tests.

Chapter 6 Contains the film cooling effectiveness measurement using PSP, including PSP measurement theory and PSP results and discussion.

Chapter 7 Concludes the work done in this research and assesses the extent that the work has satisfied the thesis aims.

Chapter 8 Highlights some of the key issues to be considered for further understanding and development of the double-wall cooling technology.

Chapter 2

LITERATURE SURVEY

2.1 Introduction

This chapter reviews some of the publications that are related to the current research. Section 2.2 gives a review of studies related to the simplified numerical analysis approach, Section 2.3 covers material related to the fully coupled CHT simulations and Section 2.4 gives a review of film cooling effectiveness tests. At the end of this Chapter is a summary of the research gaps that were found in the literature survey and that formed the basis for the present research.

2.2 Literature Review Related to a Simplified 3D Numerical Analysis of Turbine Aerofoils

A fully coupled CHT simulation allows both the solution of the fluid flow and thermal fields to be determined in just one code without the need to carry out interpolation of boundary conditions between codes. However, carrying out a coupled CHT of a DWEC turbine blade presents a challenge because of the very many small-diameter cooling holes that need to be modelled. To save computational time, several authors have developed simplified numerical approaches for studying complex gas turbine cooling systems.

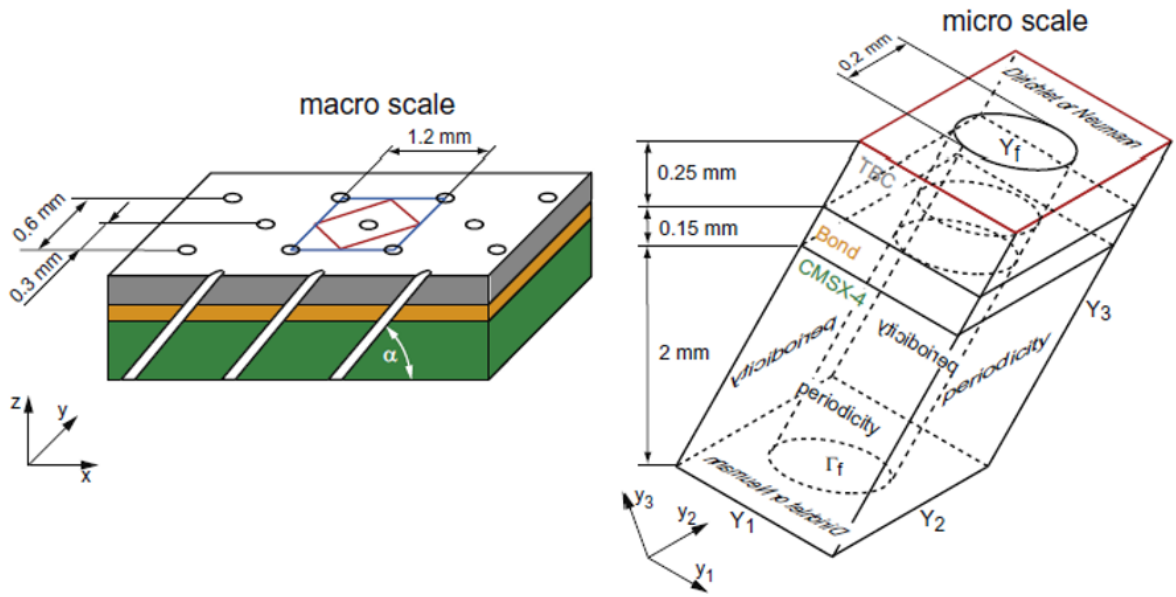

Figure 2.1: Definition of cooled multi-layered periodic unit cell (Laschet et al., 2013)

2.2.1 Simplified 3D Numerical Analysis Approach

Laschet et al. (2002), Laschet (2004) and Laschet et al. (2013) presented a 3D conjugate approach for modelling both the fluid flow and heat transfer using a homogenization method – an approach which requires that a given multi-layered model consists of the periodic repetition of a unit volume cell. This approach was used to predict the aerothermal behaviour of flat and curved multi-layered plates as well as the aerothermal behaviour of transpiration cooled plates. A CHT flow solver that depends on an implicit finite volume method in conjunction with multi-block approach was used. The domain was divided into separate blocks and the full, compressible, 3D Navier-Stokes equations were solved in each of the fluid blocks. The simulation time required to run the homogenous model was very small and the authors suggested possible future application of this technique for analysis of complex cooled gas turbine components. The limitation of this approach is that it is restricted to homogeneous models and may not be possible to be used in the analysis of a heterogeneous system where a unit volume cell cannot be simply reproduced to represent the whole domain.

Zecchi et al. (2004) developed a computationally efficient decoupled conjugate simulation tool for preliminary design stage analysis of an uncooled turbine vane. The program inputs were the hot-side and cold-side heat transfer coefficients (from flat plate correlations) and the fluid temperature. Their simulation tool permitted not only the evaluation of metal

temperature distribution but also coolant mass flow distribution on the vane. The authors compared the results from this simplified analysis approach with the experimental results of a nozzle guide vane from Hylton et al. (1983) and a satisfactory match was found.

Takahashi et al. (2005) employed a decoupled CHT to predict the 3D temperature distribution on a turbine rotor blade with rib-roughned internal cooling passages. A one dimensional flow network that used correlation for friction factors and heat transfer coefficients was employed in the internal blade passages. A 3D steady state fluid convection solution around the blade was carried out and conduction through the blade modelled by use of a finite element code.

Mendez et al. (2007) presented a simplified approach for modelling and simulating an effusion-cooled flat plate. In this approach, the number of rows was assumed to be infinitely large and a small, finite calculation domain was extracted from the plate. The calculation domain was chosen so that it contained a single hole. Periodic boundaries were specified to model an infinite plate geometry. The results obtained from their simplified approach were found to match the existing experimental results well. The authors did not report application of their approach to a turbine aerofoil.

Amaral et al. (2010) evaluated the temperature of a gas turbine blade by employing a decoupled CHT methodology which involved the use of three different solvers; (1) A Navier-Stoke solver to evaluate the non-adiabatic external flow and heat transfer, (2) a finite element analysis to obtain the thermal and stress solutions within the solid domain, and (3) a 1D aerothermal model of the cooling channels that used empirical heat transfer coefficient and friction factor formulae available in the open literature. An iterative procedure was used to exchange data at the domain boundaries between the solvers. The authors validated the results from this method against experimental test results. The authors noted that this method offered an acceptable trade-off between accuracy and computational cost. In their case, however, the blade was cooled only internally - there was no external film cooling.

Bonini et al. (2012) and Andreini et al. (2012) presented a simplified decoupled 3D CHT procedure for evaluating the performance of gas turbine blades. In their methodology, the internal cooling system was modelled using an in-house 1D thermo-fluid network solver,

external heat loads, and the external pressure distribution evaluated using three-dimensional CFD. Film cooling effectiveness was calculated using correlations for shaped and cylindrical holes developed by Colban et al. (2010) and L'Ecuyer and Soechting (1985) respectively. The effect of multiple rows of films was accounted for using the superposition approach proposed by Sellers (1963) (see Equation 2.1). Heat conduction through the metal of the blade was calculated using the three-dimensional ANSYS[1] Steady-State Thermal Module. Their CHT entailed an iterative procedure of guessing a reasonable first metal temperature, running simulations, updating the metal temperature and repeating the process until the solution converged. The predictions from their work demonstrated that decoupled CHT produced results comparable to those from experiments; with an error below 6% in the wall temperature.

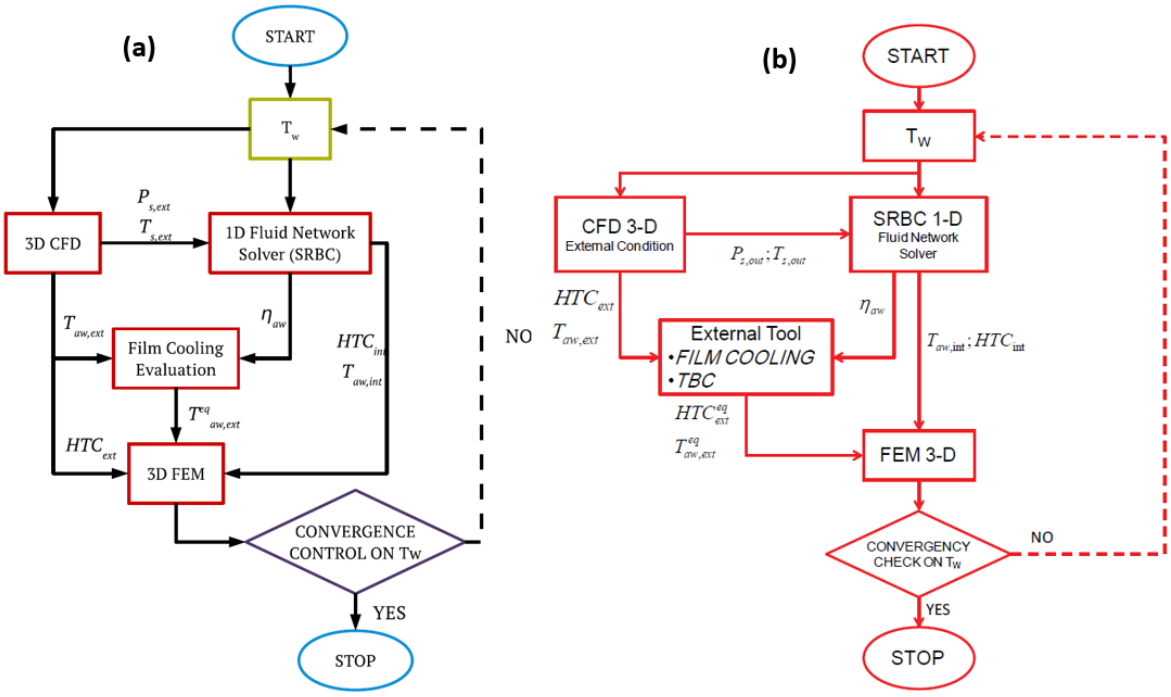

Figure 2.2: Decoupled CHT numerical analysis iterative code used by (a) Andrei et al. (2014) and (b) Bonini et al. (2012)

The decoupled 3D CHT presented by Bonini et al. (2012) and Andreini et al. (2012) was validated by Andrei et al. (2014) using both an internally cooled and film cooled gas turbine vane. The authors compared both the metal temperature and adiabatic effectiveness distribution results against those from experiments (carried out at the NASA Lewis Research Centre by Hylton et al. (1983)) and a fully 3D coupled CHT CFD analysis. The authors

[1] www.ansys.com

noted a good agreement between the decoupled CHT analysis method and the experimental data in terms of both values and trends, except on some parts of the suction surface (SS) where an under prediction of the external pressure values and hence of the heat transfer was noted.

Lad and He (2013) used Immersed Mesh Block (IMB) with an aim of solving a multiscale film cooling flow problem. The IMB approach permitted a refined mesh of a cooling hole to be immersed into a coarser mesh, on the rest of the configuration, and solved simultaneously while maintaining mass conservation. The authors employed a two-way coupling so that flow physics in and around the cooling hole interacted with the mainstream, thus the length scales of both types of flow were resolved. The IMB method permitted efficient simulation of a realistic transonic blade with a configuration consisting of up to 200 cooling holes. Jiang et al. (2016) improved the IMB method of Lad and He (2013) and applied it to investigate steady and unsteady flows in a transonic high pressure rotor blade.

Recently, Chowdhury et al. (2017) presented a detailed analytical conjugate analysis model that permits evaluation of an aerofoil surface temperature. Fluid external and internal heat transfer coefficients were calculated from correlations. Heat conduction through the aerofoil was accounted for by employing a 1D heat transfer conduction equation. With the correct boundary conditions, the authors noted that the developed analytical model was able to produce fairly accurate results- with an error of less than 10% in the metal temperature.

2.2.2 Methodologies for Predicting Film Cooling Effectiveness

Several authors have developed correlations for film effectiveness , including Colban et al. (2010) who developed a correlation specifically for both fan-shaped and cylindrical film cooling holes, Baldauf et al. (2002) for a row of cylindrical holes, and L'Ecuyer and Soechting (1985) for a row of cylindrical cooling holes.

$$\varepsilon_f = 1 - \prod_{i=1}^{N} (1 - \varepsilon_{fi}(x)) \tag{2.1}$$

Baldauf et al. (1997) carried out a comprehensive analysis of laterally averaged film cooling effectiveness. Their correlation included the influence of a full set of parameters

and was shown to demonstrate agreement with measured results. However, these researchers only considered a single row of cooling holes.

Sellers (1963) presented a simple way of predicting the film cooling effectiveness for many rows of cooling holes using correlations (or data) from single rows. Sellers (1963) approach replaces the free stream temperature for downstream rows with the adiabatic wall temperature calculated from upstream films. Sellers (1963) superposition approach can be generalised to any number of rows as shown experimentally by Murray et al. (2018), see equation 2.1. There are many reviews of film cooling effectiveness in the literature (for example Goldstein (1971)) but few deal with effusion cooling applied to turbine aerofoils or predict the two-dimensional distribution of effectiveness downstream of the cooling hole.

2.3 Literature Review of Fully Coupled CHT of Turbine Aerofoils

A fully coupled CHT simulation is a numerical simulation where the solution of the fluid flow thermal fields and the solution of the solid temperature is determined in just one code without the need to perform interpolation of boundary conditions between fluid and solid solver codes. Fully coupled CHT simulations, although more accurate compared to decoupled analysis approaches, are computationally expensive.

There is vast number of CHT simulations that have been applied to study various aspects of the turbine blade cooling. In this review, only the fully coupled CHT analysis studies that are closely related to film/effusion cooling on a gas turbine blade are considered. A section of interesting CHT studies of the turbine nozzle guide vane and turbine end wall have also been included.

Early CHT work on film cooled turbine aerofoil was undertaken by Bohn et al. (1997) and Bohn (1995). Heidmann et al. (2003) presented a CHT analysis method where the fluid solution was obtained using the Glenn-HT multiblock heat transfer code (the code is described in details by Gaugler and Lee (2001)) while the solid temperature was found using a Boundary Element Method (BEM). The BEM was directly coupled to the flow solver and

the solution achieved without iteration. Heidmann et al. (2003) used this CHT procedure to study a film cooled turbine vane. Kassab et al. (2003) later extended this same CHT procedure to a gas turbine blade. The authors noted that the use of the BEM saved computational time as no volumetric grid within the solid was required - the surface grid already available from the fluid solver sufficed.

Facchini et al. (2004) carried out CHT simulations of a radially cooled gas turbine vane, the NASA-C3X (Hylton et al., 1983), using the commercial CFD simulation software - STAR-CD. They employed $k-\varepsilon$ turbulence model. They modelled the static pressure, external temperature and heat transfer coefficient distribution along the vane. Their numerical results compared well with the experimental results from Hylton et al. (1983). They noted, however, that the numerical HTC when transition was not accounted for severely overestimated HTC values especially near the vane's leading edge (LE). It should be noted that the vane was only cooled internally, and there was no film cooling.

Luo and Razinsky (2007) carried out CHT of the same radially cooled vane, as Facchini et al. (2004), using the same CFD STAR-CD tool but used the V2F turbulence model to study aerodynamic and thermal properties of the turbine vane. The V2F ($\overline{v^2}-f$) is a turbulence model similar to the standard $k-\varepsilon$ model but incorporates near-wall turbulence. The numerical results generally matched the experimental results - with a discrepancy of 10 K at the midspan and 30 K in the peak error region. They noted high temperature downstream of LE on the SS (attributed to the transitioning boundary layer) just like Facchini et al. (2004).

The same nozzle guide vane test case used by Facchini et al. (2004) and Luo and Razinsky (2007) was used by Ledezma et al. (2008). Furthermore, Ledezma et al. (2008) used the commercial ANSYS[1] software for the CHT analysis. They further compared three turbulence models - $k-\omega$, $k-\varepsilon$ and SST in an effort to find out which model was the best. They found a good agreement with the experimental results when using $k-\omega$ and SST turbulence models. Ledezma et al. (2008) carried out a CHT analysis of the same internally cooled NASA-C3X vane but with the addition of film cooling. The numerical results matched the experimental results satisfactorily except on the LE near the SS where the the boundary

[1] www.ansys.com

layer transition was not captured by the turbulence model causing an over prediction of the HTC and wall temperature. Ames (1998) and Dyson et al. (2012) also noted that Reynolds-averaged Navier–Stokes equations (RANS) models failed to correctly predict film cooling effectiveness near the stagnation leading edge region of an aerofoil. In addition, RANS models failed to correctly predict coolant jet separation and diffusion causing enhanced film effectiveness levels in the vicinity of the film cooling holes.

Sipatov et al. (2009) carried out a CHT analysis of a turbine rotor blade using ANSYS[1] CFX. They employed the SST turbulence model. In their analysis, the effect of stator-rotor interaction was included.

A detailed CHT analysis of a turbine end wall using steady state RANS in ANSYS[1] was performed by Lynch et al. (2011). They modelled exit flow field, HTC and film effectiveness. They also compared the performance of two different turbulence models - realizable $k-\varepsilon$ and SST $k-\omega$. They found that both turbulence models failed to capture the physics of endwall contouring. Endwall contouring is a design feature included at the blade tip and hub as a way of controlling passage flow (Han et al., 2012).

Ho et al. (2012) employed ANSYS[1] CFX with the RNG $k-\varepsilon$ turbulence model to perform CHT studies on an internally-cooled gas turbine stator. Their CHT thermal effectiveness results compared well (with a 4% discrepancy) with experimental results obtained using thermocouples.

Mick et al. (2013) employed the SST turbulence model available in ANSYS[1] CFX in their CHT analysis to determine the temperature distribution on a turbine blade. Their turbine blade was only cooled through internal convection and there was no film cooling. They extended their research to investigate the influence of radiation on the blade temperature distribution. It was further observed that the surface temperature was strongly affected by the characteristics of the cooling system and the radiation effects on surface temperature were almost negligible.

A thorough CHT analysis of a film cooled gas turbine blade was carried out by Moritz et al. (2013). Their analysis focused only on the LE of the blade with the aim of improving the LE cooling holes configuration. For their CHT, they employed the CHTflow solver de-

veloped at the Institute of Steam and Gas Turbines at the RWTH Aachen University. They concluded that the CHT technique is applicable for reasonable prediction of the 3D temperature field for complex cooling configurations encountered in some turbine blades.

Ho et al. (2014) performed similar CHT studies as Ho et al. (2012) but; (1) using a turbine rotor blade instead of a stator and (2) using the SST turbulence model instead of RNG $k-\varepsilon$ turbulence model. Ho et al. (2014) compared their CHT results with experimental results obtained using Silicon Carbide chip at three different blade spans. Their CHT results were in a good agreement with the experimental results except at the midspan LE where maximum temperature discrepancy of 46 K was noted. The turbine blade was only cooled internally without films.

The CHT study of Ho et al. (2014) was later extended onto a film-cooled turbine rotor blade by Ho et al. (2016). Ho et al. (2016) employed ANSYS[1] CFX with the SST turbulence model to perform CHT studies on a film-cooled turbine rotor blade. The midchord temperature values from CHT were in agreement within 20 K (except at the LE and the SS near LE) with the experimental thermocouple temperature data.

Tsukamoto et al. (2014) employed ANSYS[1] CFX and SST turbulence model to carry out CHT analysis of surface temperatures on an internally cooled turbine rotor blade. Their CHT temperature distribution profile compared well with the experimental temperature profile (obtained using a pyrometer) except at the midchord region on the pressure surface (PS) where a temperature discrepancy of 50 K was noted. In addition, they found that the CHT analysis underestimated the flow mixing effects generated by the rib tabulators.

A comprehensive CHT study of a nozzle guide vane with internal cooling, showerhead cooling, one SS row and TE slots is presented by Kusterer et al. (2016). The CHT analysis was achieved using STAR-CCM+ CFD tool and turbulence modelled using SST $k-\omega$ model. The numerical nozzle wall temperature results matched the experimental results.

In summary, the present author is able to conclude that most of the CHT studies of turbine vanes and blades in the literature have only considered either (1) internally-cooled aerofoils or (2) conventional convection cooled aerofoils combined with film cooling. There is a lack of CHT studies in the open literature that have modelled a double-wall effusion cooled

aerofoil.

2.3.1 Literature Review of Flow Field and Heat Transfer Characteristics of an Impingement/Effusion System

Impingement cooling has been demonstrated by many researchers to be an effective way to cool a surface with locally high heat transfer rates. Impingement/effusion system could also be used to deliberately increase or decrease coolant pressure before entering the film holes and thereby altering the blowing ratios around an aerofoil to desired levels. This review focuses on studies that have undertaken research of an impingement/effusion system with an aim of understanding flow field and heat transfer characteristics.

Rhee et al. (2003) observed high heat transfer regions near coolant jet stagnation zones. Additional heat transfer peaks were observed at the midway regions due to interaction between the wall jets. They also observed a fairly symmetrical heat transfer distributions since the spent air was discharged through effusion cooling holes.

Bunker et al. (2014) observed that for a large array of impingement jets, the interaction of accumulating spent impingement fluid with impingement jets is detrimental - the accumulating cross flow decreased the peak heat transfer coefficient from the impingement jet. The detrimental effect of the accumulating spent jet fluid has also been observed by other researchers - Nam et al. (2003) and Hong et al. (2007).

To mitigate the detrimental effects of the accumulating crossflow, Hong et al. (2007) used shaped pedestals in the channel and noted a reduced crossflow deflection in the presence of the pedestals. Nam et al. (2003) noted that presence ribs/pedestals/pins in the channel helped to realise a uniform heat transfer. When Nam et al. (2003) studied crossflow without ribs in the channel, they observed that regions of high heat transfer at stagnation points were deflected and bended towards the downstream direction by the crossflow. As a result, heart-shaped regions of low heat transfer were formed between the effusion cooling holes because the jets were swept by the cross flow and sucked by the effusion cooling holes. However when rib turbulators were introduced, the heart-shaped regions of low heat transfer disappeared.

Son et al. (2001) found zones of re-impingement due to interaction of the spent impingement fluid. These re-impingement zones were found to contribute to a local increase in heat transfer on the impingement plate downstream surface. Cho et al. (2008) found that the heat transfer coefficients at these midway region where re-impingement takes place were as high as those at the stagnation zones.

Funazaki et al. (2001) observed stripe-shaped regions of high heat transfer emerging between two neighbouring jets impinging on the plate. They attributed this to the interaction between two spent impingement jets emanating from two neighbouring impingement jets. Bernard et al. (1999) and Cho and Rhee (2000) made a similar observation. They noted that the spent jets rolled up and moved upwards after interaction, in what the authors termed as a 'fountain effect'. At the same time, two counter-rotating vortices appeared under the 'fountain' and impinged on the plate causing the stripe-shaped regions of high heat transfer. Horse-shoe vortices caused high heat transfer regions near the junction between the pin and the target plate.

Cross flow is detrimental to the impingement/effusion system performance. Some of the ways to mitigate the negative effects of the cross flow inside the impingement/effusion system passages include introducing; (1) periodic discharge holes on the target plate to discharge the spent impingement air. (2) Ribs/pins/pedestals that will not only enhance uniform heat transfer but also prevent the spent impingement fluid from being swept away.

2.4 Literature Review of Film Cooled Turbine Aerofoils

This review focuses on reports of studies of film effectiveness and flow structures on the pressure and suction surfaces of turbine aerofoils. It particularly focuses on experimental studies that have used mass transfer analogies such as Pressure Sensitive Paint (PSP). However, a few selected numerical or analytical studies and those that did not use mass/heat transfer analogy have been included for completeness.

Takeishi et al. (1992) used gas chromatography with carbon dioxide as a tracer gas in a low-speed stationary cascade to investigate film cooling effectiveness (which is defined as $(T_\infty - T_{aw})/(T_\infty - T_{c,ex})$) on a rotor blade with different showerhead and aerofoil cooling hole con-

figurations. From their tests, they observed that the centreline (a straight line in streamwise direction and cutting through the centre of the hole) film effectiveness measured downstream of cooling holes decayed faster on the PS compared to the SS. The authors attributed this difference to the strong lateral mixing which causes different roles of concave and convex curvature on boundary layer stability. They also observed that the PS region closer to the leading edge had low film effectiveness compared to regions further downstream. This was attributed to the lower blowing ratios in the PS region closer to the leading edge. The blowing ratio, M is defined as shown in Equation 2.2.

$$M = \frac{u_c \rho_c}{u_\infty \rho_\infty} \tag{2.2}$$

Ito et al. (1978) used gas chromatography similar to Takeishi et al. (1992) to investigate the effect of rotor blade curvature on film cooling in a 6-blade low-velocity cascade. The test aerofoil included a single row of cooling holes on both the PS and SS. It was observed that the largest suction surface effectiveness was achieved at blowing ratios of 0.5 to 0.7. When the blowing ratio was further increased above 0.7, effectiveness was seen to drop owing to the jet penetration into the boundary layer. On the pressure side, low blowing ratios resulted in low effectiveness. However, at high blowing ratio, the near tangential jets tend to strike the concave surface downstream resulting in high effectiveness.

The influence of surface curvature has been numerically and experimentally investigated by many researchers (Berhe and Patankar (1999), Kasagi et al. (1987), Folayan and Whitelaw (1976)) with the general conclusion being that the concave (pressure) surface is generally difficult to cool compared to the convex (surface) surface especially at low blowing ratios.

Goldstein and Chen (1985) used gas chromatography on a rotor blade but their study, which was conducted in a low-velocity linear cascade, investigated the phenomena near the blade end wall. A single row of cooling holes was used. They observed that the concave (pressure) surface film cooling was not significantly affected by the presence of the end wall. On the suction surface, however, there was a significant region close to the end wall over which the film cooling jet had been essentially swept away from the surface by the presence of the passage vortex (Gao et al. (2008) observed this same phenomenon in their PSP film

cooling effectiveness investigation on a full-coverage film cooled gas turbine blade).The authors further observed that the dimensions over which the influence of the end wall was significant depended on the blade geometry and the incoming flow conditions.

Narzary et al. (2012) investigated film cooling effectiveness at relatively high blowing ratios in a linear cascade using PSP. The tests were carried out on a high-pressure turbine blade with 2, 3 and 4 rows of cooling holes on the suction surface, leading edge and pressure surface respectively. They observed that there was a large improvement on the pressure surface and moderate improvements of the suction surface film cooling effectiveness when blowing ratio was raised from 1.2 to 1.7 and 1.1 to 1.4 respectively, with no significant improvements thereafter. The peak film effectiveness was recorded at momentum flux ratio of coolant to mainstream ($\rho_c {u_c}^2 / \rho_\infty {u_\infty}^2$) = 1.15 and 0.75 on pressure and suction surface respectively.

Gao et al. (2008) and Gao et al. (2009) also used PSP to study film effectiveness on an SLA high-pressure rotor blade with 2 rows on the suction surface and 4 rows of cooling holes on the pressure surface. The film effectiveness on the suction surface was noted to be higher than that of the pressure surface except in the regions affected by the secondary vortices. Moderate blowing ratios resulted in higher film effectiveness immediately downstream of the film cooling hole. Further downstream of the cooling holes, higher blowing ratios covered a wider surface area. This same observation was made by Garg (2000) after carrying out a numerical analysis.

Rallabandi et al. (2010) employed the PSP technique to study film effectiveness on a rotor blade at high blowing and density ratios of up to 4 and 2.5 respectively in a low-speed 5-passage wind tunnel. The blade had 2 rows on both the pressure and suction surface in addition to 3 showerhead cooling holes. They noted that, owing to higher velocity and acceleration on the suction surface, the film coolant traces (corresponding to high effectiveness) were generally longer in comparison to the pressure side films. They further observed that there was more coolant accumulation downstream for the pressure surface than on the suction surface. This was attributed to the fact that, in their blade design, the rows of cooling holes on the suction surface were located further physically apart compared to rows on the pressure surface. They also observed that the suction and pressure surfaces had different film

effectiveness levels at different blowing ratios. Suction side film was seen to adhere to the surface at blowing ratios, M below 0.5, then the jet begins to lift off at M = 0.75 and completely lift off as the blowing ratio was further increased, there was no effectiveness trace at M = 2.0. A similar trend was observed on the pressure surface. However, the jet lift-off occurred at a higher blowing ratio (M greater than 1.0). At M = 4.0, only a modest effectiveness trace was observed near the cooling hole exit due to jet lift-off. But, the jet reattached at a region further downstream near the trailing edge. This tendency of pressure surface jet to reattach (jet reattachment was absent on the suction surface) was attributed to the concave shape of the pressure surface. It should be noted that the two surfaces had different cooling hole configurations; compound and simple angled holes on the pressure and suction surface respectively.

Mhetras et al. (2012) also employed PSP to investigate film effectiveness although on a high-pressure rotor blade in a three-blade linear cascade facility. The blade had 3 showerhead holes, 6 and 4 pressure and suction surfaces respectively. They observed that (1) higher blowing ratio benefited the pressure surface more than the suction surface as increasing the blowing ratios gave higher film effectiveness levels on the pressure side while the suction side effectiveness levels were observed to remain almost unaffected. (2) On the suction surface, long and distinct coolant traces were observed whereas short and smeared out traces were observed on the pressure surface. On both surfaces, the coolant was deflected towards the mid-span particularly on the suction surface. (3) Showerhead cooling hole ejection affected the film distribution only up to the third row on both surfaces implying that there was hardly any film cooling additive effect from the showerhead cooling holes. (4) The effectiveness levels near the leading edge were observed to be low due to lack of coolant accumulation and traces from each film hole could be observed.

Recently, Gurram et al. (2016) successfully employed PSP to study film cooling effectiveness of trailing edge slots of a high-pressure rotor blade in a stationary single-blade high-speed flow blow down cascade at the University of Oxford.

Cutbirth and Bogard (2001) employed quite a different measurement technique. These authors used an infrared camera, to carry out an experimental study with the aim of invest-

igating the influence of parameters like density ratio on the local effectiveness. They used a turbine vane with 6 rows of showerhead cooling holes. Their study did not look at the pressure and suction surfaces of the vane. Nevertheless, they observed that the coolant jets separated from the leading edge - even at low blowing ratios. Their work revealed the significance of the internal cross-flow from the finite feed passage on the slot film effectiveness.

Ahn et al. (2006), Takeishi et al. (1992) and Dring et al. (1980) attempted to extend the film effectiveness study on a rotor blade by using the mass/heat transfer analogy in a rotating facility with the main aim being to study effects of rotation on film cooling effectiveness. Dring et al. (1980) used ammonia and Ozalid paper[3] in a low-speed rotating facility to obtain surface flow visualisation as well as local film cooling effectiveness on both the pressure and suction surfaces (each surface had a single row of cooling holes) of a high-pressure rotor blade. These authors compared their data with that of a flat plate. The authors noted that, owing to the effects of both the curvature and radial flow, the film on the pressure surface was found to decay faster. In general, the film cooling effectiveness results from the rotating cascade closely matched those from linear cascade - particularly on the suction surface. However, the pressure side film cooling effectiveness from the rotating cascade was observed to be much lower than that from the linear cascade. The authors explained that this difference was due to the radial flow and strong mixing that is present in the rotating facility.

In summary, there exist many film cooling effectiveness studies on turbine aerofoils. However, there are hardly any studies in the open literature on film cooling effectiveness investigation on a double-walled aerofoil with full-coverage film cooling.

2.5 Summary

From the extended literature survey that has been conducted, it is evident that; (1) out of all the simplified numerical approaches that have been developed, there seems to be no approach that has been specifically designed for the numerical analysis of a DWEC turbine aerofoil. (2) No data are available for a full conjugate CHT of a DWEC turbine aerofoil. (3) There

[3]Ozalid paper consists of chemical components, mainly diazos; which are light sensitive and react with ammonia gas leaving traces of varying darkness on the paper (Friedrichs and Hodson, 1994).

are hardly any studies in the open literature that have attempted to investigate film cooling effectiveness on a double-walled aerofoil with full-coverage film cooling. Chapter 3, Chapter 4 and Chapter 6 of this thesis will outline the research conducted by the author in an attempt to close these research gaps.

The next chapter will present the novel simplified numerical analysis tool that has been specifically designed for time efficient analysis of the cooling performance of a DWEC turbine aerofoil.

Chapter 3

SIMPLIFIED 3D NUMERICAL ANALYSIS FOR METAL EFFECTIVENESS

3.1 Introduction

In an effort to minimize the numerical simulation time required for the early stage of a design, many authors have developed computationally cheap numerical methods to study some of the complex gas turbine cooling schemes, as detailed in the literature review in Chapter 2. Chapter 3 describes in detail a novel simplified numerical approach that was developed by the author for analysis of a DWEC aerofoil. Most of this chapter gives the procedure followed to devise the simplified numerical method. Section 3.8 contains numerical results including a detailed discussion of external HTC, internal cooling effectiveness and overall cooling effectiveness. Section 3.9 then summarises results from six DWEC blades that were analysed using the developed numerical analysis approach.

3.2 Objective of the Present Numerical Simulation Work

The present numerical simulation work aimed to build on the concept of the decoupled 3D CHT approach presented by Bonini et al. (2012) and Andreini et al. (2012) (refer to the

literature survey provided in Chapter 2 for more details) to a DWEC gas turbine blade so as to develop a computationally efficient conjugate approach that can be used to produce an assessment of the performance of the complex DWEC blade (whose key features are shown in Figure 1.14 in Chapter 1). The Goldstein (1971) correlation was employed to represent film cooling effectiveness for a single hole and the film superposition approach of Sellers (1963) used to model the 2D distribution of film cooling effectiveness of arrays of cooling holes. The suitability of this approach was confirmed for multiple rows of films by Murray et al. (2018). The internal heat transfer coefficient was evaluated from conjugate analyses of a unit wall block element and the conduction through the blade was simulated using the finite element code in ANSYS[1] Steady-State Thermal module. The developed numerical analysis was used to analyse the cooling performance of three circular and three diamond pedestal DWEC blade designs. The developed novel simplified numerical analysis approach will be a valuable tool for DWEC turbine blade redesign and optimization. Figure 3.1 shows a concept double-wall turbine blade with a cooling design for the leading edge and trailing edge.

3.3 Details of the Test Geometry

A practical double-wall blade cooling concept is shown in Figure 3.1 and comprises three main regions with different cooling designs.

- The leading edge (LE) cooling is achieved through a combination of impingement jets from the inner skin and showerhead cooling holes through the outer skin.
- The mid-chord region is cooled both internally (through impingement jets from the inner skin and convective heat transfer in the array of pedestals) and externally by an array of effusion cooling holes.
- Early and late trailing edge (TE) cooling is achieved using a pin-fin bank and TE slots respectively. The present study focuses on the double-wall mid-chord region of the blade.

[1] www.ansys.com

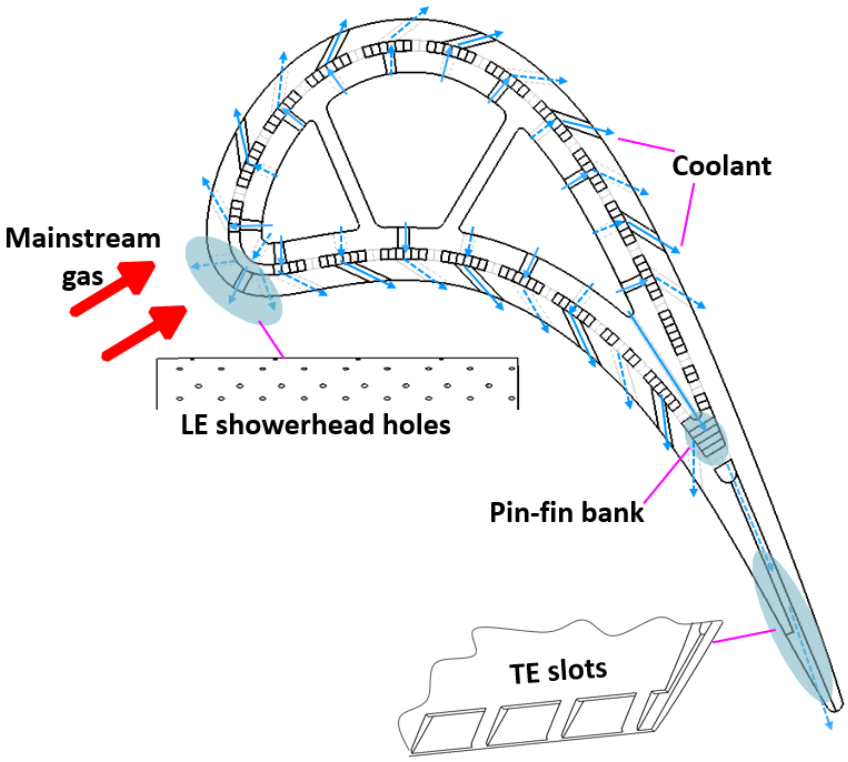

Figure 3.1: Features of a double-walled effusion-cooled concept turbine blade including leading edge (LE) showerhead cooling holes, pin-fin bank and trailing edge (TE) slots as well as the external flow direction

The pedestal height, diameter, spacing as well as impingement and effusion cooling holes sizes and spacing are set to match that of a specified wall block element. Each of the wall block elements studied by Murray et al. (2017) has distinct aerothermal characteristics (such as convective efficiency, discharge coefficient and mass flow rate). A sample CFD result of a unit wall block element showing the flow velocity distribution is as shown in Figure 3.2. It should be noted that the presented CFD result in Figure 3.2 has film holes inclined at 90° to the external surface. The 90° angle of inclination permitted an application of periodic boundary conditions during the CFD simulation (Murray et al., 2017). The CFD results from the 90° film holes were then interpolated onto 30° inclined film holes (refer to Murray et al. (2017) for more details). To demonstrate how the numerical analysis approach developed herein works, one of the best-performing wall block elements named Geometry 3 (from Murray et al. (2017)) but herein referred to as C2, was used. The extent of the mid-chord region of the aerofoil is made up of 88 of these wall block elements.

To simplify the analysis, the C2 wall block element (whose geometrical parameters and

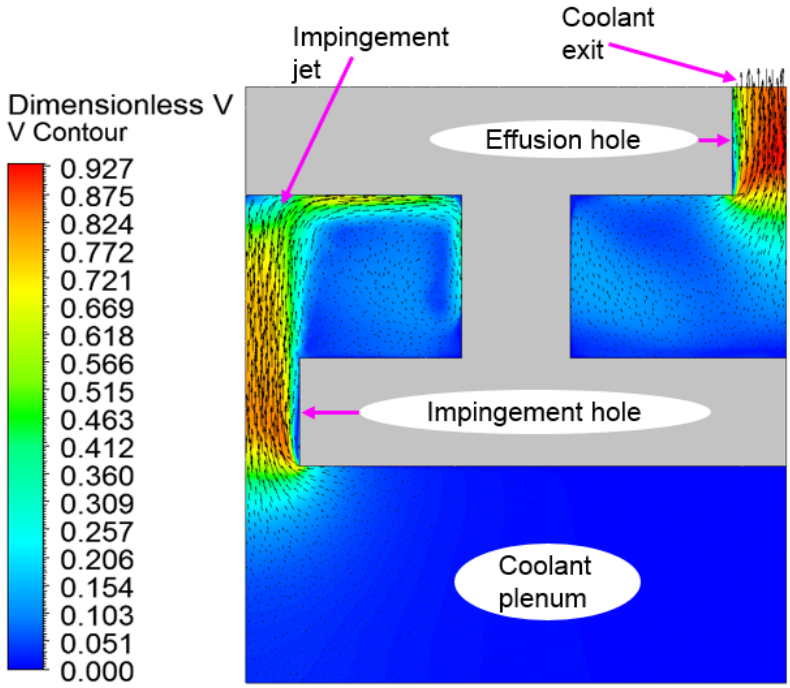

Figure 3.2: CFD results showing the flow velocity distribution in the unit wall block element from Murray et al. (2017)

Table 3.1: The unit wall block element dimensions from Murray et al. (2017)

Geometry number	Passage height, L_P (mm)	Pedestal diameter, D_P (mm)	Pedestal spacing, L_1 (mm)	Effusion, D_f and impingement hole diameter, D_i (mm)	Streamwise, S_x and Spanwise, S_z Effusion Hole Spacing (mm)	Dimensionless Streamwise, S_x/D_f and Spanwise pitch, S_z/D_f	Unit Wall Outer Skin Porosity, ϕ (%)
C2	1.5	1.0	1.5	1.0	10	10	3.14

dimensions are as shown in Figure 3.3 and Table 3.1 respectively) was used in the whole of the mid-chord region. However, owing to varying flow structure, static pressure distribution and heat load around a turbine blade, it will be necessary, in future of double-wall blade designs, to employ different wall block elements around the blade. For instance, employing a wall block element with a low-mass flow in the transonic region of the suction surface where coolant ejection onto the surface is undesirable because of the aerodynamic losses. Cylindrical cooling holes with 1 mm diameter and inclined at an angle of 30° to the external surface of the blade were modelled in a staggered pattern on the blade surface, as shown in Figure 3.4. This design, with equal spanwise and streamwise pitches of 10 diameters, resulted in a total of 12 staggered rows of cooling holes; 7 on the suction side and 5 on the

pressure surface.

$$Nu = ARe^{B} \tag{3.1}$$

Where A = 0.07 and B = 0.80

Murray et al. (2017) carried out an elaborate conjugate CFD while performing aero-thermal and thermomechanical analysis of seven different geometries of unit wall block elements. Each of the elements comprised a small domain with square sides equal to half the streamwise pitch between the effusion holes. In this wall block element, the external and internal skins were connected via a bank of pedestals, see Figure 3.3. To carry out numerical analysis in the present study, the internal heat transfer coefficient of the unit wall block element calculated from the conjugate CFD (from Murray et al. (2017)) was correlated using a power law, Equation 3.1. Therefore, for a given *Re* and with known values of constants *A* and *B* it is possible to evaluate the *Nu* and hence internal heat transfer coefficient for a specific wall block element geometry installed in the aerofoil.

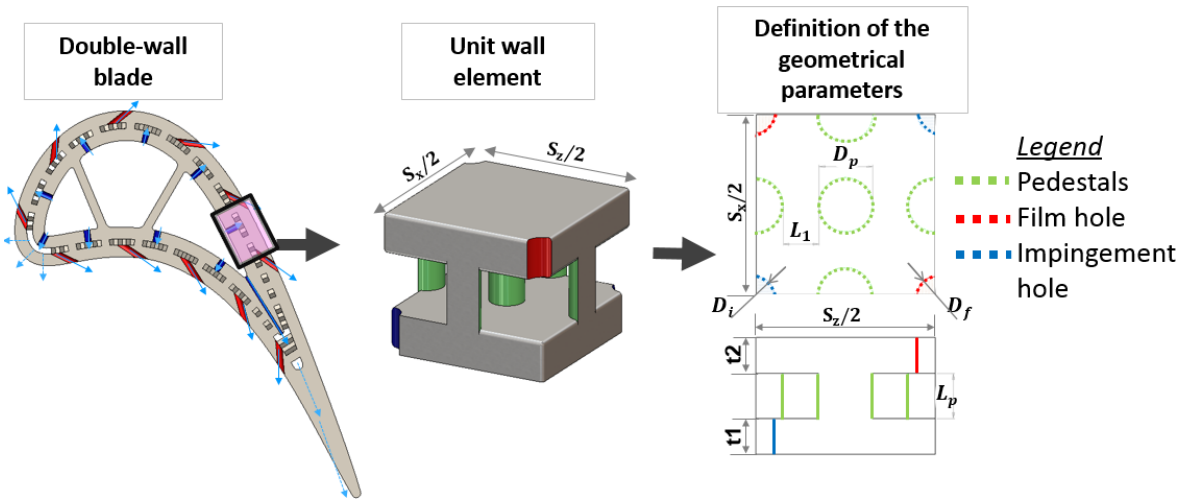

Figure 3.3: A sectioned double-wall blade with the unit wall block element showing the definition of the geometrical parameters

The wall block element analysis also yielded an effective discharge coefficient which was subsequently used by the author to predict the coolant flow rate through the effusion holes on the aerofoil, using Equation 3.2. The ideal coolant mass flow rate, $\dot{m}_{c,ideal}$ is calculated assuming an isentropic one-dimension expansion from the coolant total pressure inside the

blade to the static pressure local to the cooling hole exit. In the present work, the discharge coefficient was correlated from the conjugate analysis of Murray et al. (2017) for average aerofoil cross-flow but later work has correlated C_d with blowing ratio.

$$\dot{m}_{c,actual} = C_d \dot{m}_{c,ideal} \tag{3.2}$$

To evaluate the internal heat transfer coefficient in the blade, $h_{i,blade}$, a heat balance was carried out between the block and the blade resulting in Equation 3.3 where A_{blade} is the internal surface area occupied by the wall block element on the blade and η_c is the convective efficiency (temperature increase of the coolant, from coolant supply to film cooling hole exit, divided by the maximum temperature increase possible) of the wall block element. Figure 3.5 gives a graph of η_c variation with Re for the wall block element used in the present study.

$$h_{i,blade} = \frac{\dot{m}_{c,actual} C_{p,c} \eta_c}{A_{blade}} \tag{3.3}$$

3.4 Numerical Simulation

As aforementioned, the conjugate model in the present study adopted a decoupled approach which modelled the blade in three separate steps; internal heat load modelling, film cooling (external heat load) modelling, and a conjugate simulation of the whole domain. In practice, the outer skin of the aerofoil which is effusion cooled is connected to the internal impingement plate via a bank of pedestals forming a double-skin system, as shown in Figure 1.14. In the present analysis, the blade temperature was predicted in the aerofoil wall (modelled as 1 mm thick) but account for impingement cooling and the pedestals by increasing the internal heat transfer coefficient.

The internal and external heat load modelling is described in detail in the following Section 3.5 and Section 3.6.

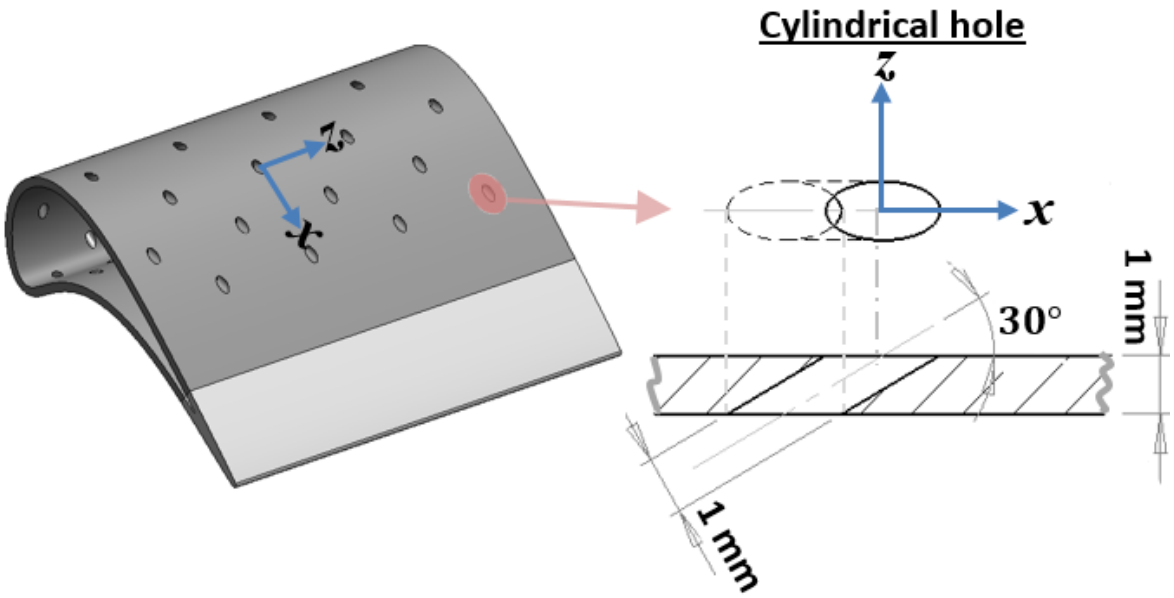

Figure 3.4: Outer skin of the blade where numerical analysis is performed

3.5 Film Cooling Effectiveness Modelling

A MATLAB[2] script, refer to an excerpt in Appendix B, was written to compute both the adiabatic wall temperature and the film cooling effectiveness at every grid point on the blade. The following subsections describe how each of the inputs necessary for the film cooling evaluation was obtained.

$$T_{r,\infty} = T_{s,\infty} + \Lambda(T_{o,\infty} - T_{s,\infty}) \tag{3.4}$$

3.5.1 Mainstream Velocity and Density

The mainstream Mach number and velocity were evaluated from the local static pressure assuming an isentropic flow. The blade profile used is similar to the one used by Gurram et al. (2016) for blade trailing edge studies which was scaled from an engine representative shape. It should be noted that this same blade profile but scaled approximately twice the engine scale was used in the Chapter 6 film cooling effectiveness studies. The engine-representative conditions used by Colladay (1972), summarized in Table 3.2 were used in this numerical analysis. The mainstream density was evaluated from the ideal gas equation. The recovery

[2] www.matlab.com

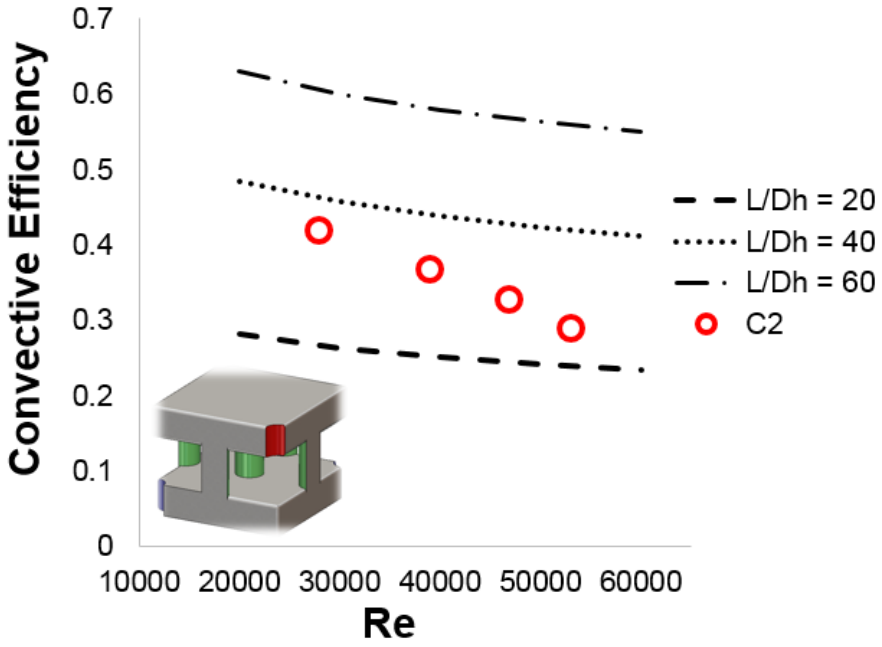

Figure 3.5: $\eta_c - Re$ characteristics compared to that of three simple duct cooling systems, characterized by L/D_h = 20, 40 and 60

temperature, evaluated using Equation 3.4, was evaluated from the specified total gas temperature and was used as the effective gas temperature. An estimate of a turbulent boundary layer flow recovery factor formula ($\Lambda = \sqrt[3]{Pr}$) proposed by Eckert (1956) was used.

Table 3.2: The engine-scale operating conditions used for the numerical simulation from Colladay (1972)

Operating Conditions		
Parameter	Value	Units
Coolant inlet total temperature	811	K
Mainstream gas total temperature	2200	K
Mainstream gas total pressure	40	bar
Mainstream gas inlet Mach number	0.26	–
Mainstream gas outlet Mach number	0.72	–
Mainstream gas flow rate per passage	1.8	kg/s

3.5.2 Film Cooling Effectiveness

The effectiveness of the coolant film diminishes with increasing distance downstream of the cooling hole exit. There have been a vast number of studies, both experimental and numerical, that have been undertaken to measure film effectiveness under a variety of conditions.

From these data, film effectiveness has been correlated with several variables which include; downstream position, coolant and mainstream Re, hole shape and diameter, mainstream gas-coolant density ratio, and specific heat ratio. In the present study, the correlation developed by Goldstein (1971), Equation 3.5, which has an addition of the lateral coordinate, z (see the spatial coordinates shown in Figure 3.4) was used.

$$\varepsilon_f = \frac{Mu_\infty D}{8\alpha_t(x/D + x_{decay})} exp(-0.693(z/z_{1/2})^2) \tag{3.5}$$

The aerofoil external surface was divided into a number of elements. The values of the mainstream gas parameters, such as density, velocity, and static pressure vary from one grid point to another. A MATLAB[2] code was written to compute the film cooling effectiveness at each of these grid points. The values of x_{decay} (streamwise film decay factor), α_t (turbulent thermal diffusivity) and $z_{1/2}$ (spanwise distance at which the temperature difference drops to half) vary with the blowing ratio and streamwise pitch, see Appendix C. It was possible to calculate the required values at any given blowing ratio and streamwise pitch by performing a linear interpolation using the detailed film effectiveness results compiled by Murray et al. (2018) and Baldauf et al. (1999) obtained through combination of a CFD and experiments on a flat plate, see Appendix C.

For this case of effusion cooling, where there are many rows of cooling holes on the blade surface, film cooling effectiveness at each of the successive downstream rows of cooling holes is strongly influenced by the film coming from the upstream rows. In this study, Sellers (1963) superposition approach (see Equation 2.1 in Chapter 2) was employed to evaluate the composite film effectiveness of the downstream rows.

3.5.3 Adiabatic Wall Temperature

The temperature increase of the coolant, from coolant supply to film cooling hole exit, divided by the maximum temperature increase possible is defined as the convective efficiency, η_c. This parameter is a function of cooling modulus, N, see Equation 3.6 (Holland and Thake, 1980). For a duct with hydraulic diameter, D_h and length, L the cooling modulus, N is given as $N = {}^{4StL}/_{D_h}$. The temperature rise of the coolant as it flows through the wall

of the component being cooled is a key feature of all cooling systems that aim to achieve a transpiration-like performance ((Andrews and Asere, 2013), (Andrews et al., 1985)).

The mainstream gas recovery and coolant inlet temperatures were used as boundary conditions. The temperature of the coolant at the exit of each cooling hole, $T_{c,ex}$, is not known but depends on the wall temperature, coolant temperature, internal heat transfer coefficient and the wetted surface area of the internal cooling system.

$$\eta_c = 1 - exp(-N) \tag{3.6}$$

$$\eta_c = 1 - exp(-0.12Re^{-0.2}L/D_h) \tag{3.7}$$

$$T_{c,ex} = T_{c,in} + \eta_c(T_m - T_{c,in}) \tag{3.8}$$

$$T_{aw} = T_{r,\infty} - \varepsilon_f(T_{r,\infty} - T_{c,ex}) \tag{3.9}$$

$$Re = \frac{u_c \rho_c D}{\mu_c} \tag{3.10}$$

Assuming a fully developed turbulent pipe flow and using Dittus-Boelter's expression relating Nu and Re ($Nu = 0.023Re^{0.8}Pr^{0.33}$), then Equation 3.6 can be re-written so that the η_c becomes a function of only L/D_h (Equation 3.7) and Re. Figure 3.5 shows η_c plotted as a function of Re (evaluated from Equation 3.10) comparing the convective efficiency of the wall block element in this study with three simple duct cooling systems, characterized by L/D_h. From the graph, it is evident that the wall block element possesses very high convective efficiency corresponding to that of a circular pipe with length, L in the range of $20 < {}^{L}/_{D_h} < 40$. It should be noted that the η_c of C2 drops more rapidly with Re compared to that of the plain duct. This indicates that the η_c drop off rate (the η_c drop off rate is governed by the negative power of Re in Equation 3.7) is lower than that expected in a unit wall block element.

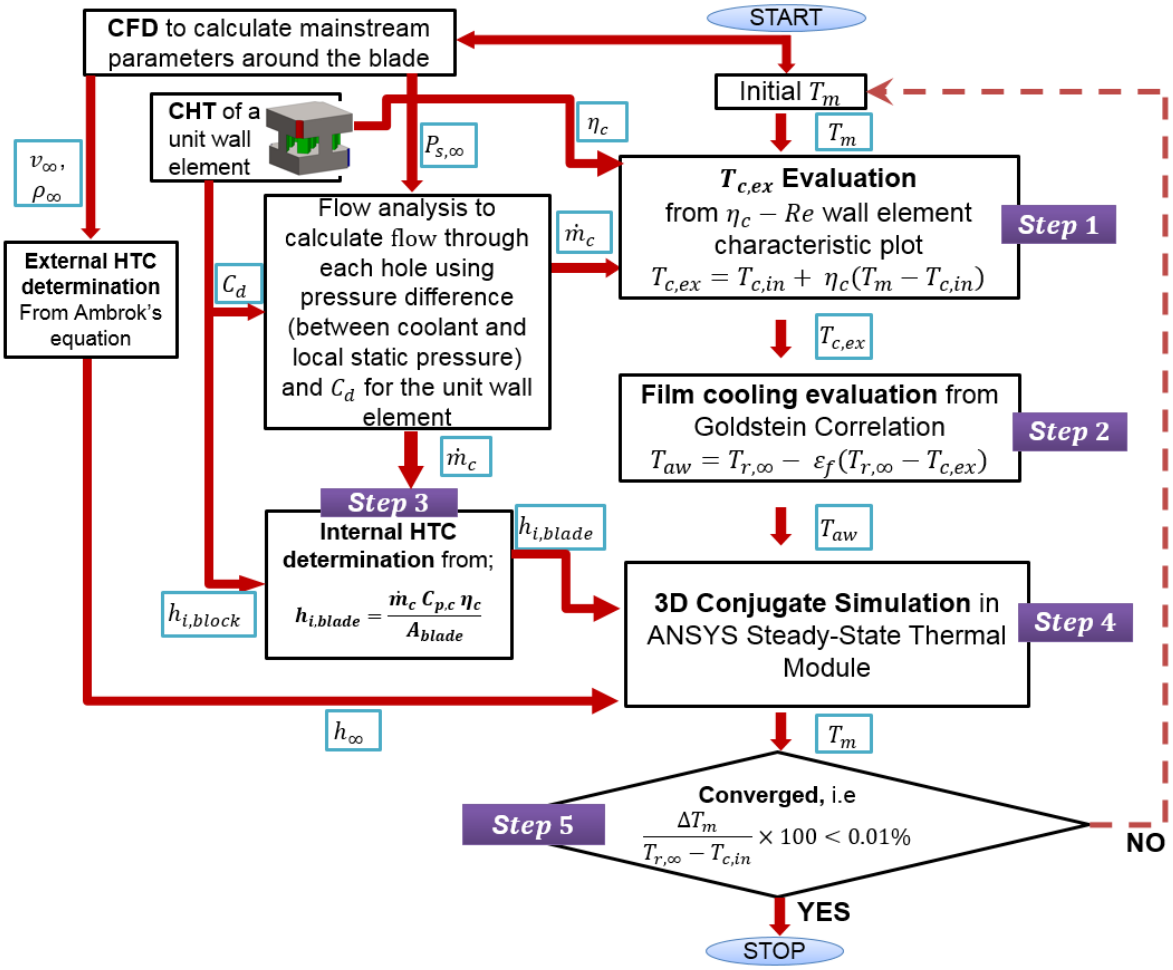

Figure 3.6: Steps in the iterative code used to determine aerofoil wall temperature

An iterative process for calculating T_m (the program logic is illustrated in Figure 3.6) was necessary owing to the interdependent nature of the metal temperature distribution, the amount of heat picked up by coolant as it flows through the internal passages, the adiabatic temperature decay downstream of the cooling hole, the hot-side and cold-side heat transfer coefficients. Equation 3.8 was employed to evaluate the coolant exit temperature, $T_{c,ex}$, which supplies the film. An initial guess for the metal temperature distribution, T_m (chosen to be a uniform value which was the average of the gas and the coolant inlet temperature) was set.

The η_c corresponding to a given wall block element geometry and Re, determined from a flow analysis, was read from the $\eta_c - Re$ database from which $T_{c,ex}$ was determined. The calculated $T_{c,ex}$ was then used in Equation 3.9 to evaluate adiabatic wall temperature, T_{aw}. The calculated T_{aw} was exported to ANSYS[1] Steady-State Thermal Analysis and conjugate simulations executed, as explained in Section 3.7, from which volume-average metal temperature,

T_m, was evaluated. This new updated temperature was then fed into the iteration loop and the iteration process executed till convergence. Convergence was met when $^{\Delta T_m}/(T_{r,\infty} - T_{c,in})$ was below 0.01%. To accelerate convergence in the subsequent cases, the initial metal temperature was set to be the converged metal temperature of the preceding case. On average, up to four iterations were required for convergence in all the cases studied. Some section of the MATLAB[2] code that was written by this author to compute the blade metal temperature is included in Appendix B.

3.6 External Heat Transfer Coefficient

A simple integral approach was used to determine the external heat transfer coefficient around the aerofoil in the presence of varying free stream velocity. Specifically, Ambrok's procedure for a turbulent boundary layer, Equation 3.11, described in Kays and Crawford (1993) was used. This procedure of determining external HTC was applied to all regions of suction and pressure surfaces except at the aerofoil's leading edge. The leading edge was modelled as a two-dimensional cylinder.

$$St = 0.0287 Pr^{-0.4} \frac{(T_{surface} - T_{r,\infty})^{0.25} \mu^{0.2}}{[\int_0^x (T_{surface} - T_{r,\infty})^{1.25} (u_\infty \rho_\infty) dx]^{0.2}} \tag{3.11}$$

3.7 Conjugate Model Simulation

A 3D Fourier's law module included in ANSYS[1] 16.2 - Steady-State Thermal module was used for the conjugate simulation. The blade was meshed using ANSYS[1] meshing software and mesh refinement undertaken near the cooling holes to minimize discretization errors.

The T_{aw} and external heat transfer coefficient (external heat load) as well as internal heat transfer coefficient (from Equation 3.3) and coolant inlet temperature (internal heat load) were imported into ANSYS[1] FEM module and interpolated on the external and internal surfaces of the blade respectively. The summary of this process is shown in Figure 3.8. Steps 2, 3 and 4 in Figure 3.8 correspond to the steps in the program logic (Figure 3.6). Figure 3.9 shows a simplified diagram showing boundary conditions for the finite element

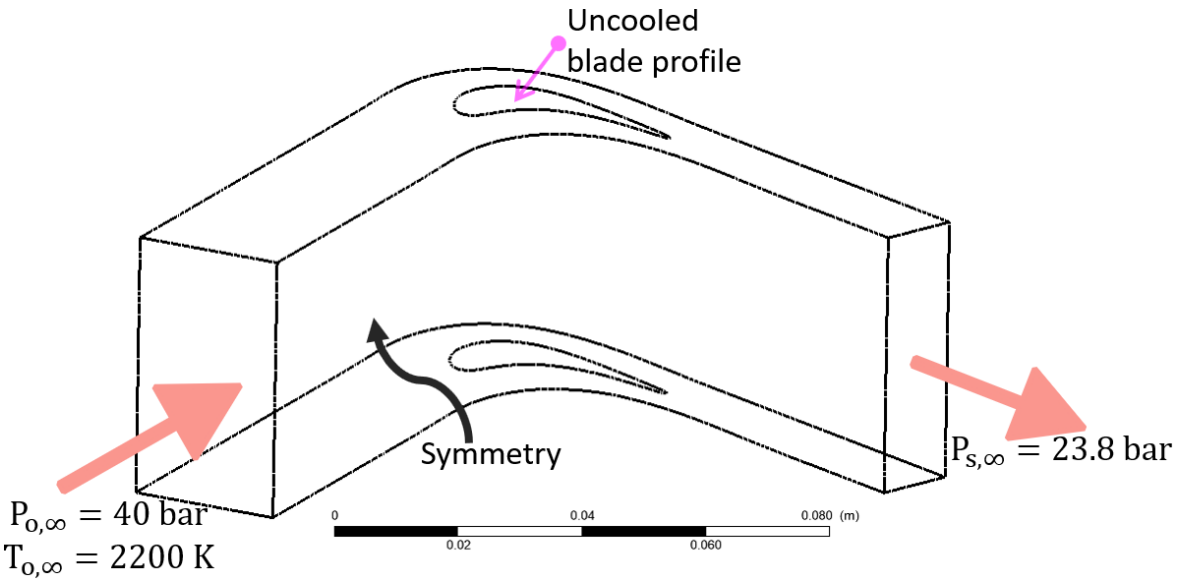

Figure 3.7: Boundary conditions for the uncooled CFD in ANSYS[1] CFX

analysis. A freestream total pressure of 40 bar and an exit Mach number of 0.72 (see Table 3.2 and Figure 3.7) were considered in this analysis. The results are documented graphically under Section 3.8.

3.8 Results and Discussion

3.8.1 Film Effectiveness and Adiabatic Wall Temperature

The Goldstein (1971) correlation was used to predict the film effectiveness for each row of holes which enabled the adiabatic wall temperature to be predicted in a procedure outlined in Figure 3.6. The approach introduced by Sellers (1963), which superposes the effect of rows of the film, was used to account for the accumulation of film effectiveness. To the authors' knowledge, this is the first time the two dimensional film distribution has been superposed using the method of Sellers (1963) on an aerofoil. The approach, after comparison with experimental data, was shown to be successful by Murray et al. (2018) for flat plate test geometries. It should be noted that a flat-plate streamwise film decay factor (x_{decay}) was used in the present analysis. It is expected that curvature may have an influence on x_{decay}. However, the aerofoil here was built using a series of unit wall blocks and thus a flat-plate x_{decay} was taken to be a good approximation. Figure 3.10 shows the film effectiveness,

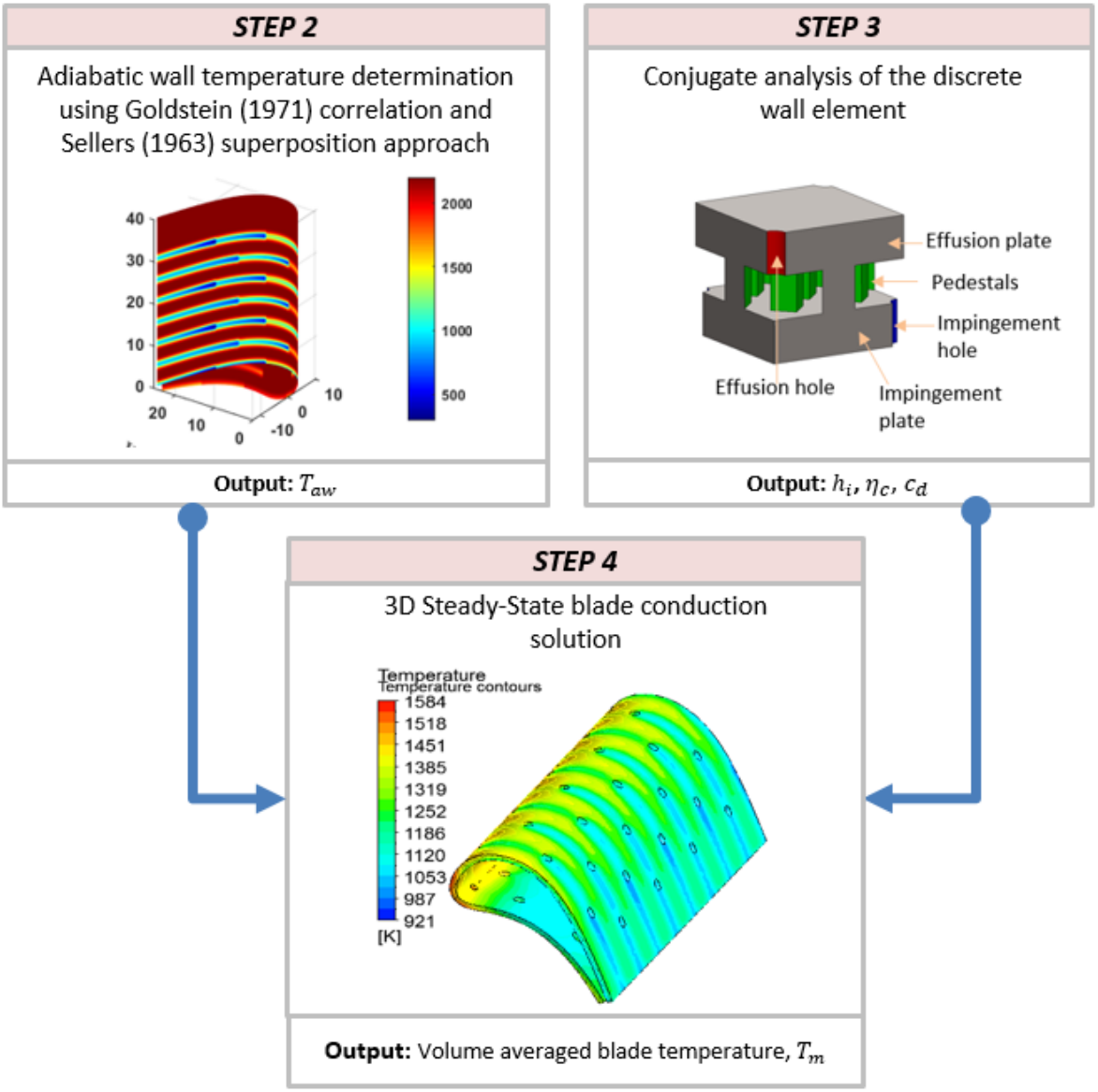

Figure 3.8: Model setup in ANSYS[1] steady-state thermal module

and its corresponding adiabatic wall temperature distributions on the external surface of the aerofoil.

A similar film cooling effectiveness trend can be seen on both the pressure and suction surface of the blade. On both the pressure and suction surfaces, the metal effectiveness increases from leading to trailing edge. This is because; (a) the film effectiveness builds up downstream as more coolant is injected into the successive rows of films and (b) the internal heat transfer coefficient increases as the coolant flow through the wall block increases as the pressure difference between the coolant and static pressure increases.

It is interesting to note that the film cooling effectiveness, ε_f, on the pressure surface

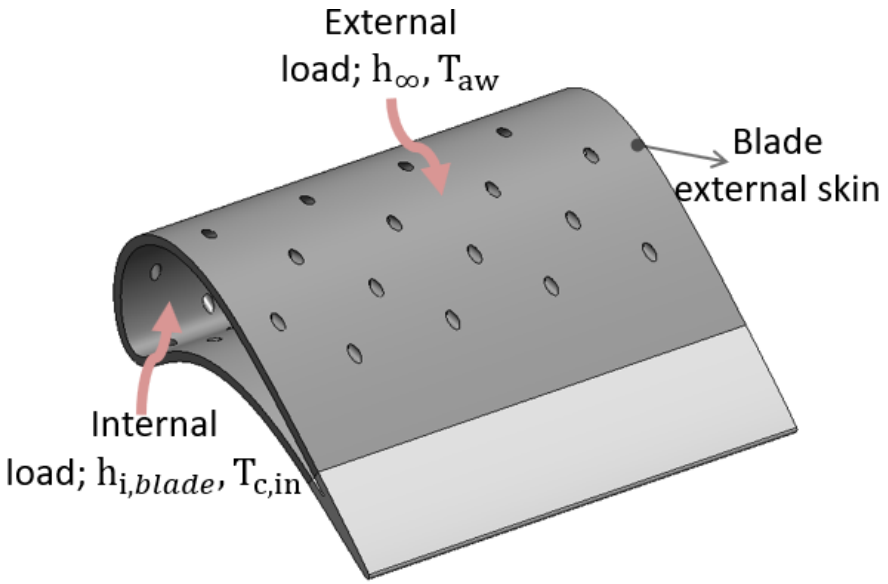

Figure 3.9: Boundary conditions used for conduction calculation in ANSYS[1] steady-state thermal module

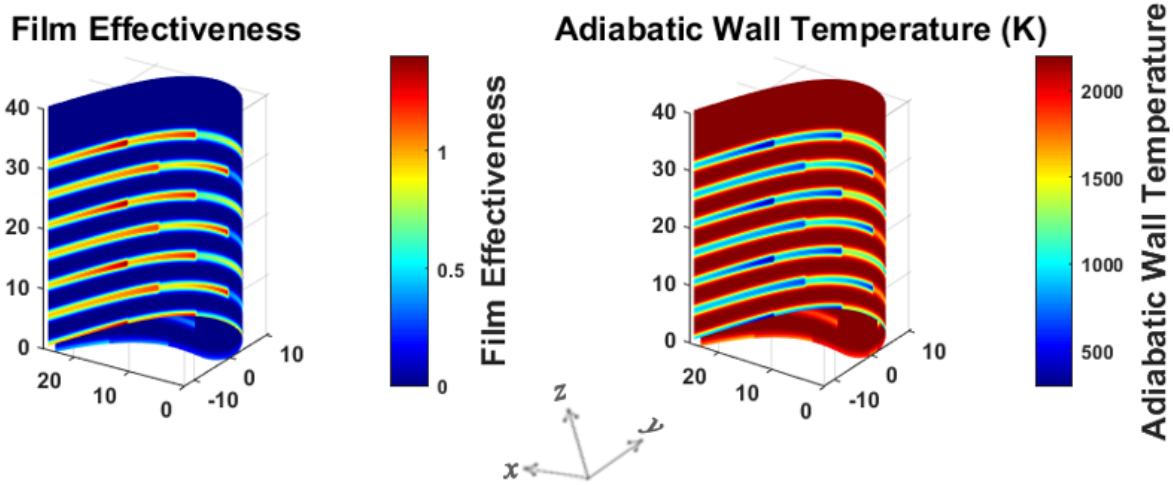

Figure 3.10: Film cooling effectiveness on the blade and its corresponding adiabatic wall temperature for the conditions of Table 3.2

is significantly lower than the level on the suction surface. This bias is known to occur in real turbine designs which include aerofoil curvature and passage secondary flows. The correlation used in the present work is the Goldstein (1971) equation which is based on flat plate data and makes no allowance for curvature or vortices. The different ε_f levels on pressure and suction surfaces is caused by the difference in the mainstream velocity between the two surfaces. Presently, the blowing ratio is also different on the PS and SS. Figure 3.11 shows external static pressure distribution around the aerofoil, including four horizontal dotted lines representing four total coolant inlet pressures; $P_{o,c}/P_{o,\infty}$, PR = 1.00, 1.05, 1.15 and

1.25 used for the numerical simulations in Chapter 4.

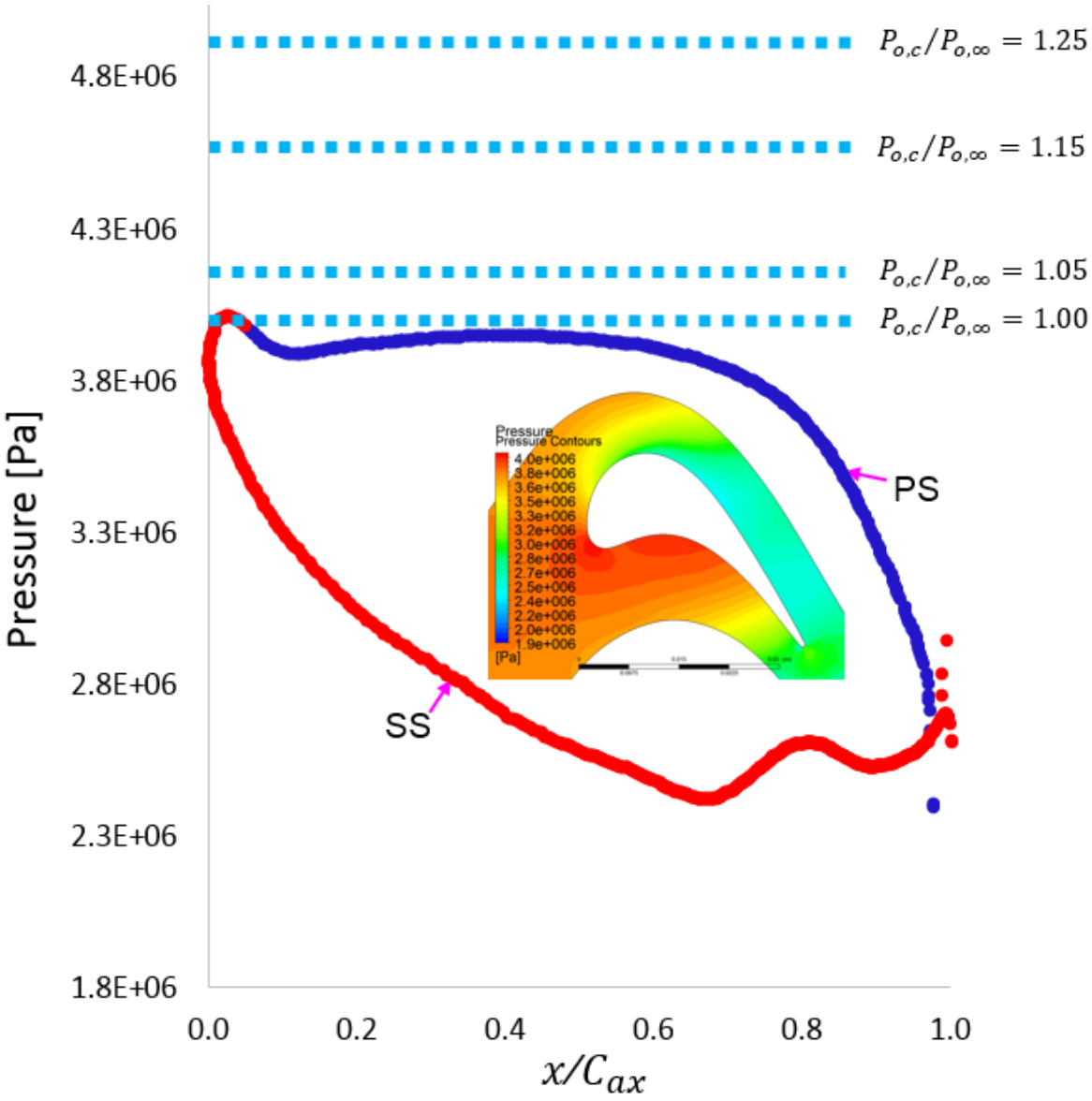

Figure 3.11: External static pressure distribution around the aerofoil, including the four horizontal lines representing four coolant pressure ratios corresponding to PR= 1.00, 1.05, 1.15 and 1.25

Figure 3.12 shows the variation of non-dimensional spanwise-averaged film flow rate per hole (obtained by dividing coolant flow rate through each hole by the mean coolant flow rate) as well as film cooling and metal effectiveness as a function of dimensionless streamwise distance, for a total coolant pressure of 40 bar (PR = 1.00). A total coolant pressure corresponding to PR = 1.00, in this simplified analysis, resulted in engine-realistic blowing ratios, M on the pressure surface and the suction surface of the blade ranging from $0.6 < M < 1.7$ as shown in Figure 3.12

There is undoubtedly higher coolant mass flow on the suction surface compared to pressure surface - approximately three times the mean PS level for the cooling holes in the vicinity of the transonic mainstream flow. This high flow rate is undesirable as it causes additional aerodynamic losses (Denton, 1993). In the future, the design of the DWEC blade will require a well-thought means of reducing the amount of coolant ejected into the high-loss regions of the suction surface.

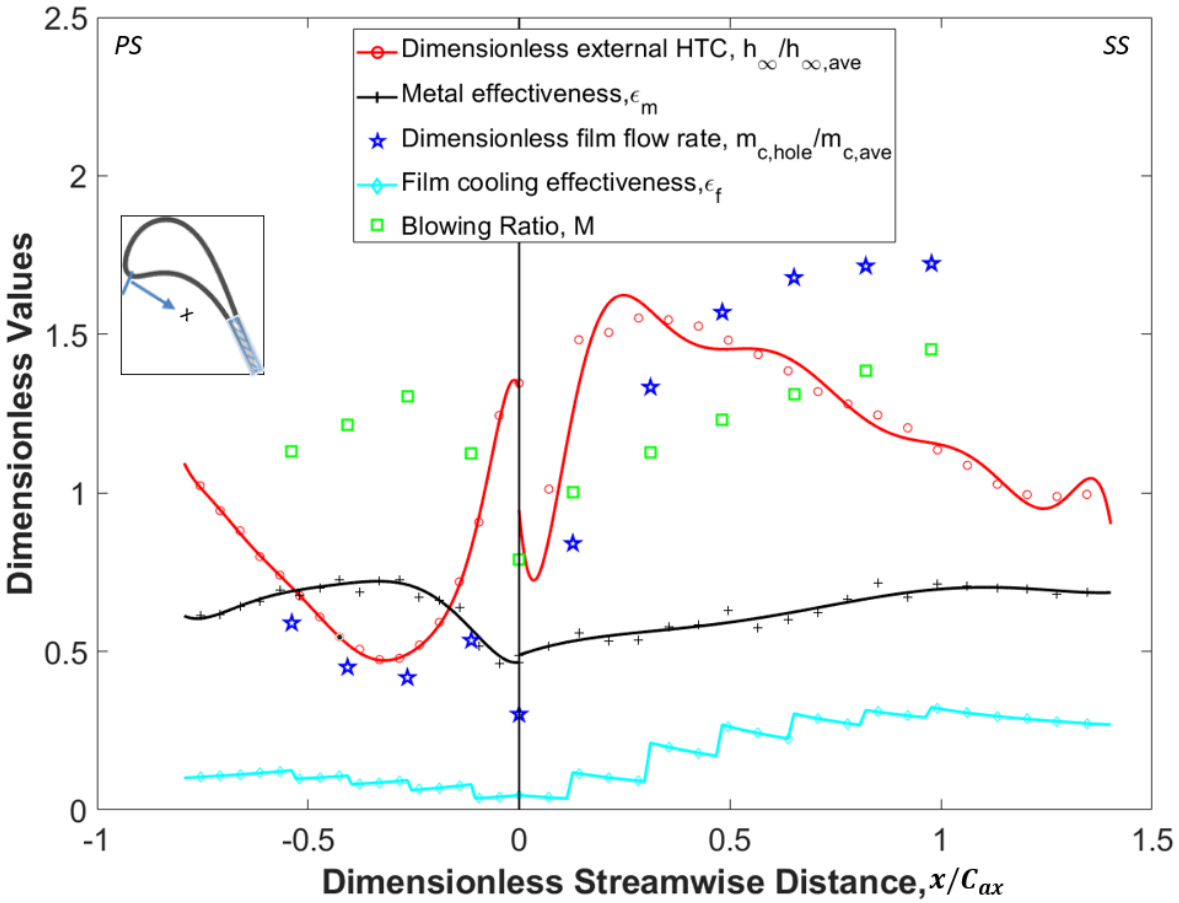

Figure 3.12: Non-dimensional film flow rate per hole, film cooling effectivess, metal effectiveness and dimensionless external heat transfer coefficient as a function of the blade's dimensionless streamwise location

3.8.2 External Heat Transfer

As aforementioned, the external heat transfer coefficient, h_∞, around the aerofoil was calculated from the Ambrok's procedure described in Kays and Crawford (1993). The values of h_∞ obtained were nondimensionalized using an averaged heat transfer coefficient over the whole surface, $h_{\infty,ave}$. The resulting graph is included in Figure 3.12. The highest heat load

occurs in the vicinity of the leading edge where stagnation takes place. The suction surface experiences a rapid fall in the heat transfer coefficient in the laminar region of the boundary layer before a sharp rise in the transition region and finally a gradual fall towards the trailing edge. On the pressure surface, there is a gradual fall in the h_∞ from the leading edge to almost the half of the downstream distance followed by a gradual rise towards the trailing edge.

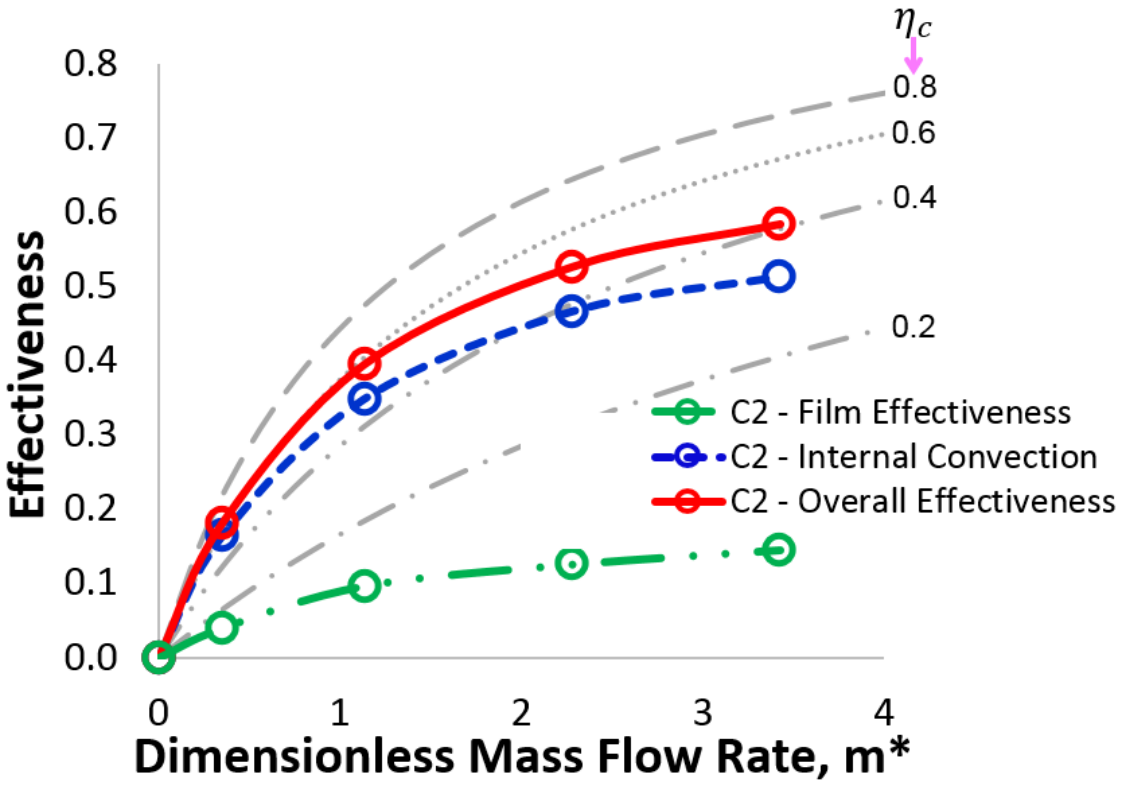

Figure 3.13: A graph of effectiveness as a function of dimensionless coolant mass flow for the C2 blade

3.8.3 Internal Cooling Effectiveness

The success of the internal cooling system arises from the high heat transfer coefficients caused by the combination of the pedestals and the impingement jets. To evaluate the value of internal convection cooling, the model was adjusted to remove the benefits of film cooling (that is, ε_f was set to zero). The boundary condition temperature, on the external surface, while carrying out the conjugate simulation of the blade, was set to the mainstream recovery gas temperature, $T_{r,\infty}$, not the adiabatic wall temperature, T_{aw}. The resulting volume-

averaged metal temperature was subsequently used in Equation 3.12 to calculate the internal cooling effectiveness. The spatially averaged internal cooling effectiveness is plotted against non-dimensional coolant mass flow rate in Figure 3.13.

Table 3.3: Geometrical parameters and dimensions of the six unit wall block elements from Murray et al. (2017) used to build the midchord section of the DWEC blades

Geometry Number / Geometrical Parameter	D1b	D2a	D3a	C1	C2	C3
Passage Height, L_P (mm)	0.5	1.5	1.5	1.0	1.5	1.3
Pedestal Edge Length, L_2 (mm)	0.5	0.5	0.5	--	--	--
Pedestal Diameter, D_P (mm)	--	--	--	1.0	1.0	1.5
Pedestal Spacing, L_1 (mm)	0.5	0.5	1.5	1.5	1.5	1.0
Effusion hole diameter, D_f (mm)	0.5	1.0	1.0	1.0	1.0	0.8
Impingement hole diameter, D_i (mm)	0.5	0.5	0.5	1.0	1.0	0.8
Streamwise, S_x and Spanwise, S_z Effusion Hole Spacing (mm)	5.7	5.7	11.3	10.0	10.0	10.0
Dimensionless Streamwise, S_x/D_f and Spanwise pitch, S_z/D_f	11.3	5.7	11.3	10.0	10.0	13.3
Unit Wall Outer Skin Porosity, ϕ (%)	2.5	9.8	2.5	3.1	3.1	1.8
Discharge Coefficient, C_d	0.5	0.2	0.2	0.5	0.5	0.5
Effective Porosity, $\phi \times C_d$	1.3	1.9	0.4	1.7	1.7	1.0

$$\varepsilon_m = \frac{T_{r,\infty} - T_m}{T_{r,\infty} - T_{c,in}} \tag{3.12}$$

$$\varepsilon_m = \frac{m^* \eta_c}{1 + m^* \eta_c} \tag{3.13}$$

$$m^* = \frac{\dot{m}_c C_{p,c}}{h_\infty A_{ex}} \tag{3.14}$$

The results show that the overall effectiveness of the double-walled effusion cooled system is dominated by the internal convective heat transfer. Figure 3.13 makes clear the significant contribution from internal convection to overall cooling effectiveness, with the internal cooling contributing approximately 80% to the overall cooling effectiveness. This contribution is found to be even higher at low m^*. The high internal convection is attributed to the use of impingement cooling, the significant internal surface area of the impingement plate and the inclusion of pedestals, which contribute to the high internal heat transfer coefficient, calculated from Equation 3.3. The grey-dashed lines, calculated with different values of convective efficiency as a parameter, show the cooling efficiency curves of $\eta_c = 0.2$, 0.4, 0.6 and 0.8 calculated from Equation 3.13 for a range of values of m^*. The internal cooling from this study corresponds to a convective efficiency of approximately $\eta_c = 0.5$ particularly at low m^* values (m^* was calculated from Equation 3.14). This reflects the convective efficiency results of its unit building wall block element shown in Figure 3.5.

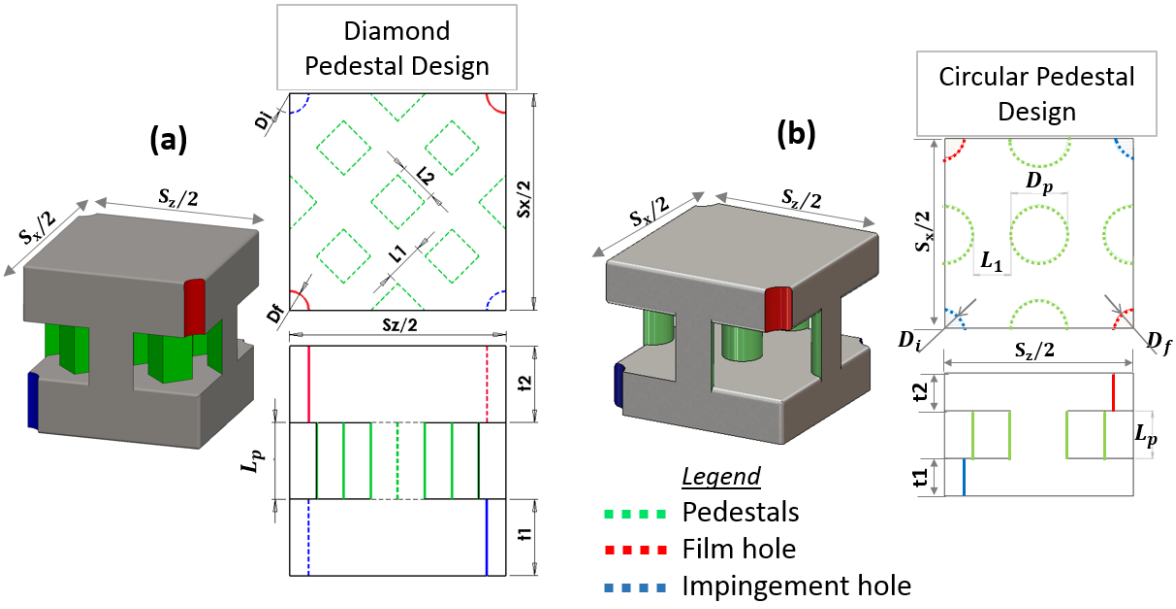

Figure 3.14: The schematic illustration of the definition of the unit wall block element geometrical parameters for (a) diamond and (b) circular pedestal designs.

Colladay (1972) reports that a high internal convection is always beneficial and it has a potential to cut down on coolant air requirements. From their analysis and comparison of wall cooling schemes for advanced gas turbine applications, they found out that an increase in the internal convection efficiency resulted in a reduced amount of cooling air required to maintain a given wall temperature. For instance, a full-coverage (effusion) cooling system with an internal convective efficiency of 0.6 required a m^* of 2.1 to maintain a wall temperature of 1255 K. But when the internal convective efficiency dropped to 0.2, m^* needed to maintain the same wall temperature increased by over 60% to about 3.4. This same observation has been echoed by Holland and Thake (1980) in their analysis of high pressure turbine blade cooling. Andrews and Asere (2013) and Andrews et al. (1985) have observed that, for any cooling scheme to offer cooling performance that closely approximates that of transpiration cooling, internal convection cooling must be improved, whilst maintaining good film cooling effectiveness levels.

This balance between internal convection and film cooling for combustor liner geometries is also reported by Andrews et al. (1986). They carried out an experimental investigation on a flat plate geometry to assess the relative performance of effusion and transpiration cooling. In their case, however, there was a greater contribution to overall cooling from film cooling as there was no large internal surface area, and correspondingly high effective internal heat transfer coefficient, influencing the internal cooling.

3.8.4 Overall Cooling Effectiveness

In this case, both the internal convection and film cooling were taken into consideration. To evaluate the overall metal effectiveness, the conjugate simulation was performed with the external load h_∞ and T_{aw} . It should be noted that the procedure followed to calculate the internal cooling and overall cooling effectiveness was similar to that described in 3.8.3 except that the input temperature for the blade's external surface in the code was the mainstream effective gas temperature, $T_{r,\infty}$ for 3.8.3 while in the latter it was the adiabatic wall temperature, T_{aw}. A simulation at one pressure ratio took about 30 minutes to be completed. On the other hand, a fully coupled conjugate heat transfer, CHT simulation (that will be discussed

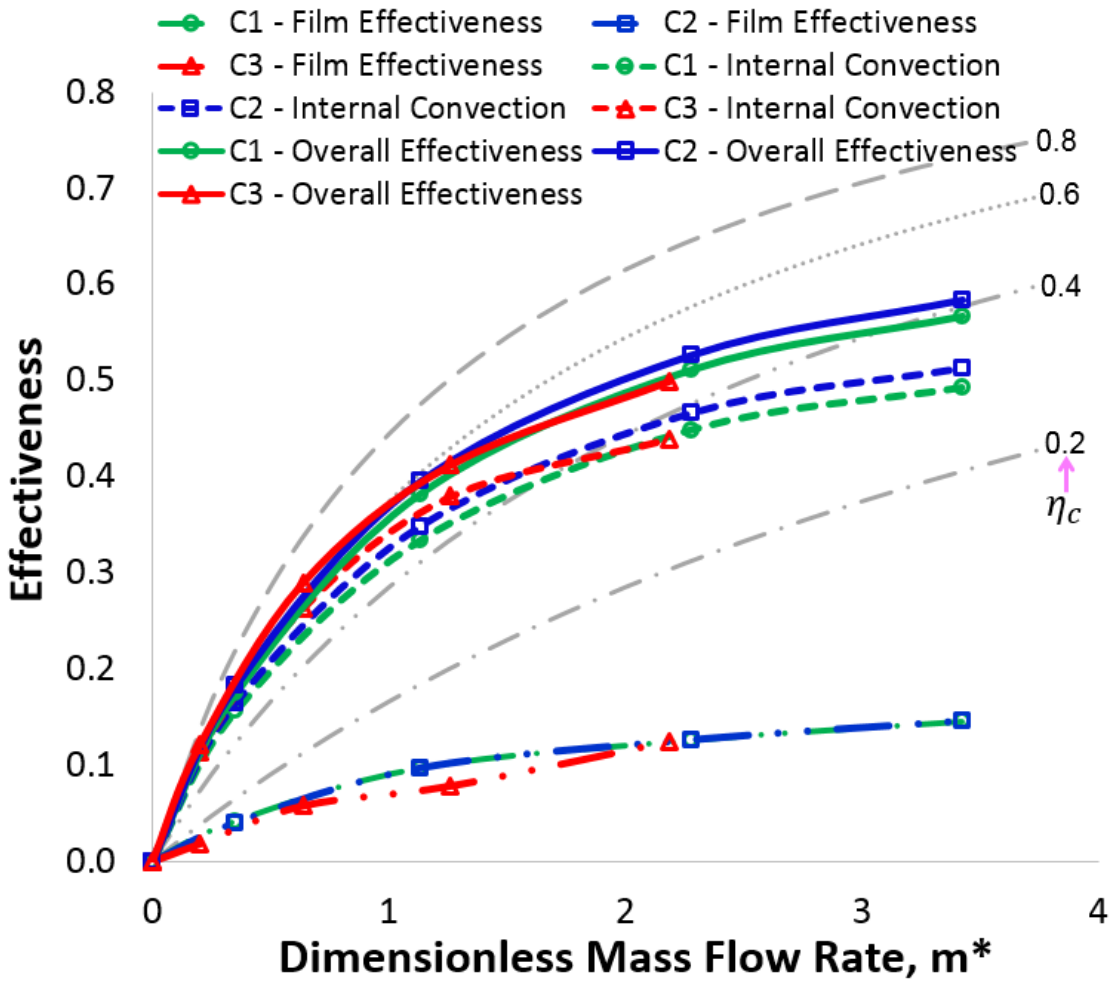

Figure 3.15: A graph of film, internal and overall effectiveness as a function of dimensionless coolant mass flow for the DWEC circular designs; C1, C2 and C3

in Chapter 4) on a periodic DWEC aerofoil strip required over 25 hours for simulation at any given pressure ratio to be completed.

The overall metal effectiveness graph is plotted alongside film and internal cooling effectiveness, Figure 3.13. Both the overall effectiveness and effectiveness from the internal cooling are within η_c range of 35% to 60%, reflecting the efficiency results from the unit cell (shown in Figure 3.5).

The progressive decrease in η_c with m^* in Figure 3.15, Figure 3.16 and Figure 3.17 was attributed to the rapid drop of η_c with *Re* of the unit wall blocks (afore discussed in Section 3.5.3 of this Chapter).

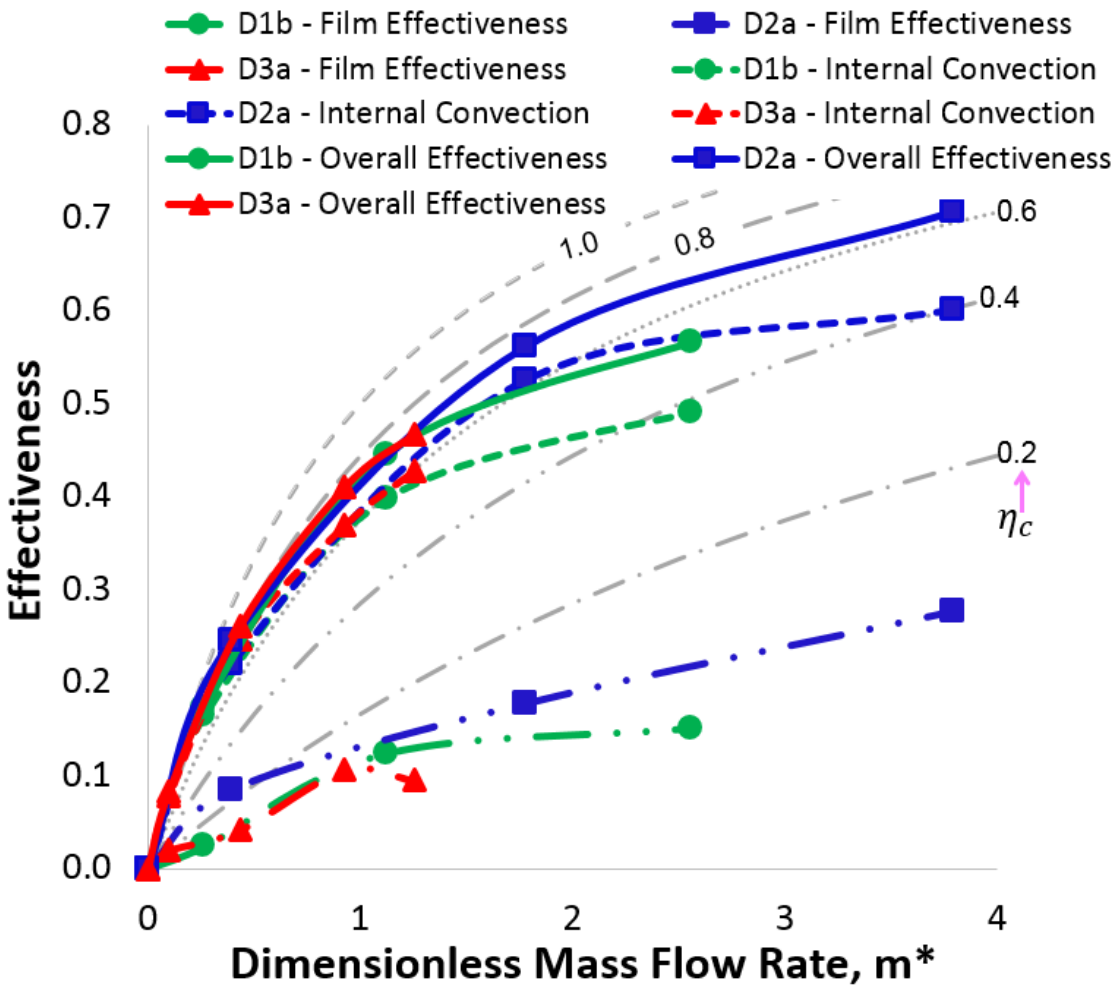

Figure 3.16: A graph of film, internal and overall effectiveness as a function of dimensionless coolant mass flow for the DWEC diamond designs; D1b, D2a and D3a

3.9 Numerical Analysis Comparison with Other Double-Wall Blades

3.9.1 Geometrical Description

As afore described, Murray (2019) carried out experimental and numerical studies of double-wall effusion cooling performance, including aerothermal and thermomechanical analysis, on thirteen diamond designs and seven circular pedestal geometries of double-wall blocks. The wall block geometries were developed using design of experiments methodology whereby various geometric parameters were varied (Murray, 2019). The authors chose diamond and circular pedestals based on simplicity of pedestal shape, availability of prior data, pressure loss characteristics and ease of manufacture.

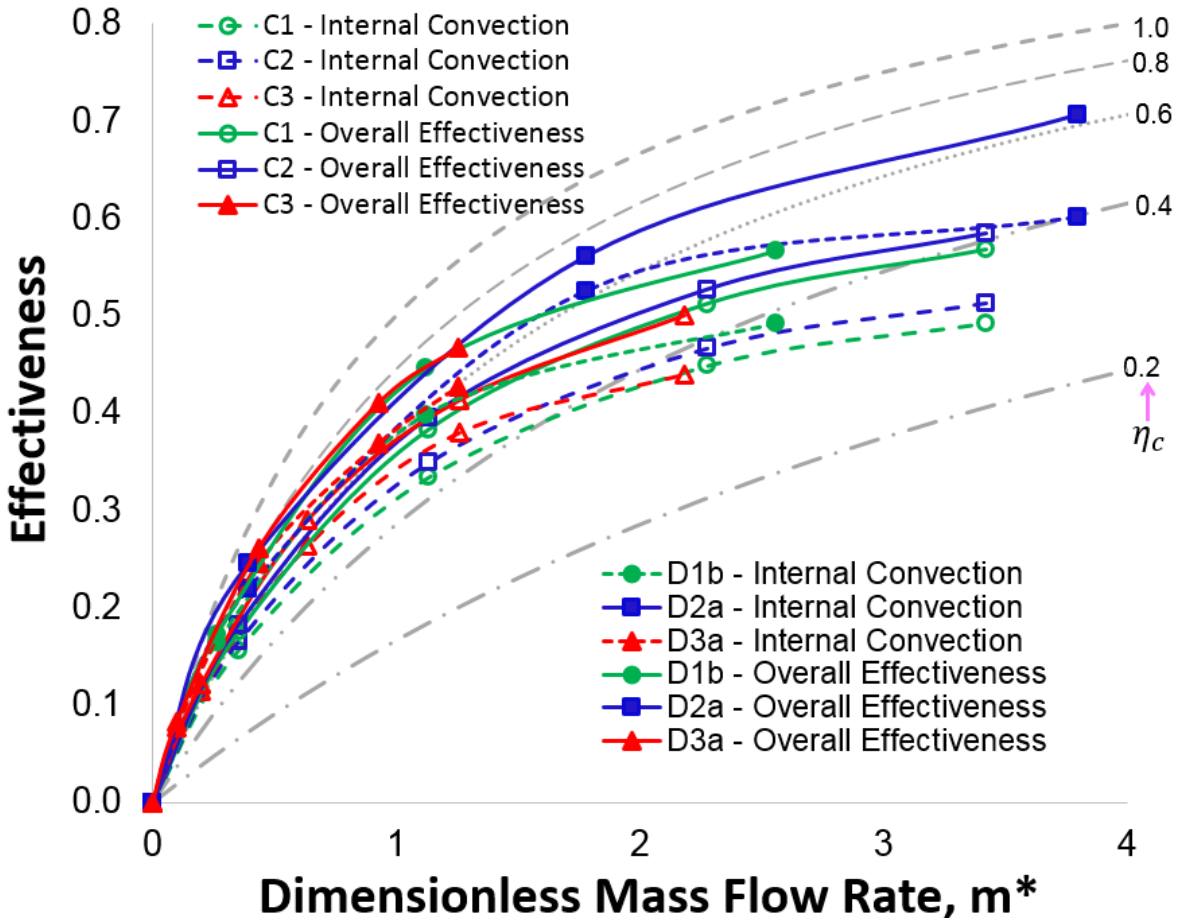

Figure 3.17: A graph of internal and overall effectiveness as a function of dimensionless coolant mass flow for both the circular (C1, C2, C3) and diamond designs; D1b, D2a, D3a

In this study, one high porosity diamond pedestal blade design, D1 and one low porosity diamond pedestal blade design, D3 were considered. Similarly, one high porosity circular pedestal blade design, C1 and one low porosity circular pedestal blade design, C3 were considered. For comparison, baseline diamond pedestal blade design, D2 and circular pedestal blade design, C2 were also included in the present research.

In addition to the numerical analysis of the best-performing circular pedestal baseline design, C2, the developed simplified numerical analysis approach was also applied to five additional DWEC blades - two circular (C1 and C3) and three diamond (D1b, D2a and D3a) pedestal DWEC blade designs. The names have been selected to be consistent with the nomenclature used in Chapter 6. For any particular diamond pedestal design, the difference between names which end with the letters a or b is the size of the effusion hole diameter; specifically 1.0 mm or 0.5 mm respectively. So that D1b, for instance, has exactly the same design features as D1a except the size of the effusion hole diameter. The circular pedestal

designs have circular pedestals while the diamond pedestal designs have diamond pedestals connecting the inner and outer skins in the mid-chord region of the DWEC blade.

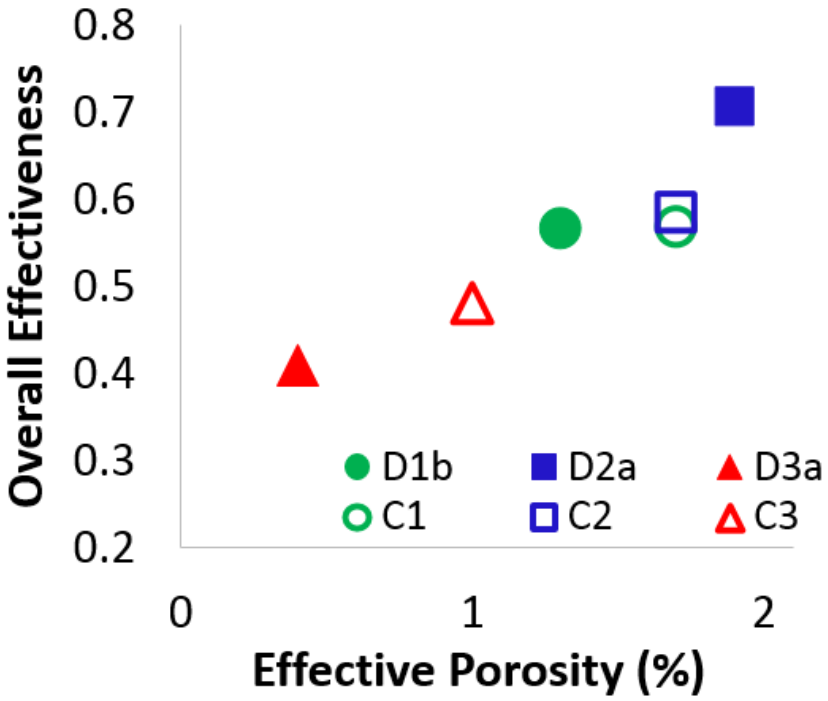

Figure 3.18: Overall effectiveness versus effective porosity of blades D2a, D1b, D3a, C2, C1 and C3 at the same pressure drop of 0.9 bar

A summary of the geometrical parameters and dimensions of six unit wall block elements from Murray et al. (2017) used to build the midchord section of the DWEC blades is given in Table 3.3. Table 3.3 also gives the geometric porosity, ϕ, discharge coefficients, C_d, and effective porosity. The unit wall block element outer skin geometric porosity gives a measure of how much of the outer skin is open. The unit wall block element outer skin porosity was evaluated by dividing the area occupied by the film hole on a unit wall block element by the area of the unit wall block element external surface, as shown in Equation 3.15. Murray et al. (2017) noted that the geometric porosity did not sufficiently capture the levels of internal blockage on flow associated with double-wall cooling and thereby defined another parameter - effective porosity (which is product of the porosity, ϕ and C_d).

$$\phi = \frac{\pi D_f^2}{2 S_x S_z} \tag{3.15}$$

3.9.2 DWEC Blades Numerical Analysis Results Comparison

The numerical analysis procedure outlined in the earlier sections of this Chapter were followed in analysing all the five DWEC blades.

Figure 3.15 gives a comparison of the film cooling effectiveness, internal convection effectiveness and overall effectiveness for the three circular DWEC blade designs, C1, C2, C3. While Figure 3.16 give the comparison of the film cooling effectiveness, internal convection and overall convection of the three diamond DWEC blade designs, D1b, D2a and D3a. Figure 3.17 combines the effectiveness results of both the circular and diamond pedestal designs.

The only difference between C1 and C2 is the length of the pedestal, as shown in Table 3.3. The greater spacing between the inner and outer skins and, therefore, the length of the pedestals in C2 contributed to extra surface area and, consequently, enhancing internal heat transfer boosting both the internal convection and the overall cooling effectiveness compared to C1. A similar observation was noted in the diamond pedestal designs - the blade with the big internal wetted area (like D2a) exhibited better internal convection and overall effectiveness. D2a is seen to consistently have the best internal convection and overall effectiveness performance, of all the five blades - C1, C2, C3, D1b and D3a across all the tested m^*.

Murray et al. (2017) experimentally and numerically studied the double-wall elements, used to build the mid chord section of the DWEC blades studied here. They found that, at the same pressure drop across the double-wall, the overall effectiveness increased with the increase in the effective porosity (effective porosity is defined here as a product of outer skin porosity, ϕ - 3.15, and C_d). This was attributed to the fact that, for the same pressure drop, there is more coolant flow in the design with high effective porosity. A similar trend was observed here. The overall effectiveness of the six blades at the same pressure drop of 0.9 bar can be ranked in the following descending order; D2a, C2, C1, D1b, C3 and D3a, reflecting the effective porosities rank, as shown in Figure 3.18. It is worth noting that when the designs were compared at the same mass flow rates, the low porosity designs showed superior performance than the high porosity ones. This was captured in Figure 3.19, where the low porosity designs like D3a exhibited superior cooling efficiency compared to high

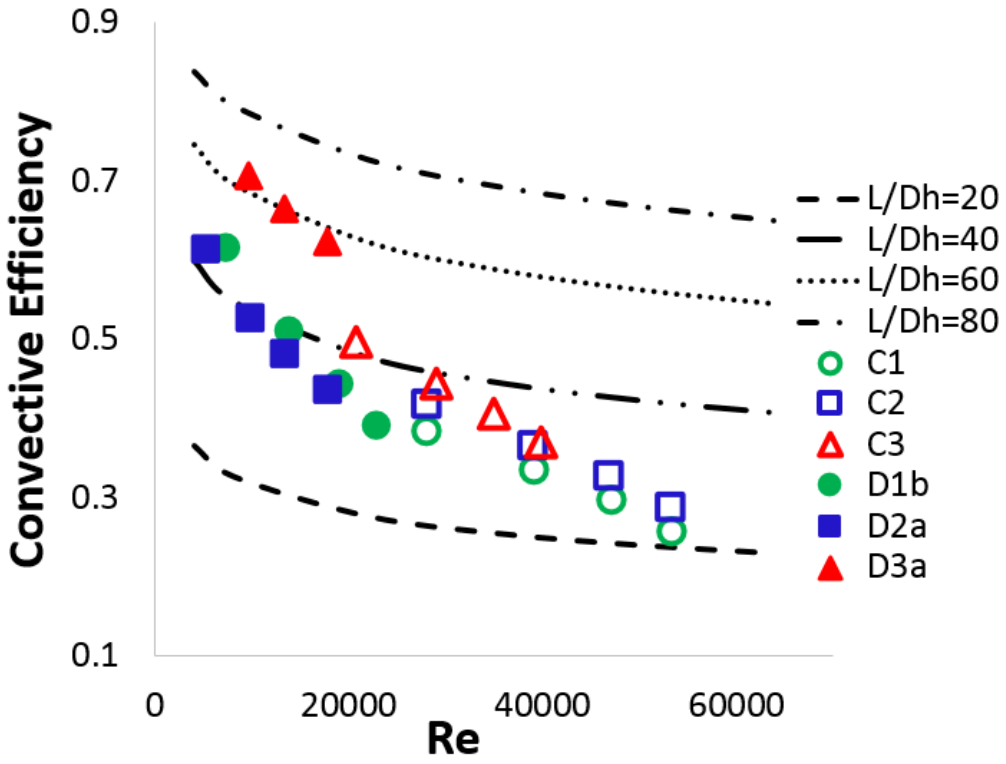

Figure 3.19: $\eta_c - Re$ characteristics compared to that of three simple duct cooling systems, characterized by L/D_h = 20, 40, 60 and 80

porosity designs such as D2a. This is because the low porosity blade geometries caused the coolant to slow down allowing it to extract a lot of heat from the blade before flowing out. On the other hand, the coolant in the more porous blades was expelled before utilizing its full heat sink capacity resulting in lower convective efficiency.

It should be noted that the DWEC blade internal convection cooling and overall cooling effectiveness performance should reflect that of the corresponding unit wall element. This was used as the first check to confirm the accuracy of the developed analysis approach. The internal convection and overall cooling effectiveness lie within within η_c range of 35% to 60%, reflecting the efficiency results from the corresponding unit wall elements, whose characteristics are shown in Figure 3.19. The η_c data used to plot Figure 3.19 were obtained from Murray et al. (2017).

$$\varepsilon_m = \frac{m^* \eta_c + \varepsilon_f (1 - \eta_c)}{1 + \eta_c (m^* - \varepsilon_f)} \tag{3.16}$$

Equation 3.13 applies only for a convection-cooled model (Holland and Thake, 1980).

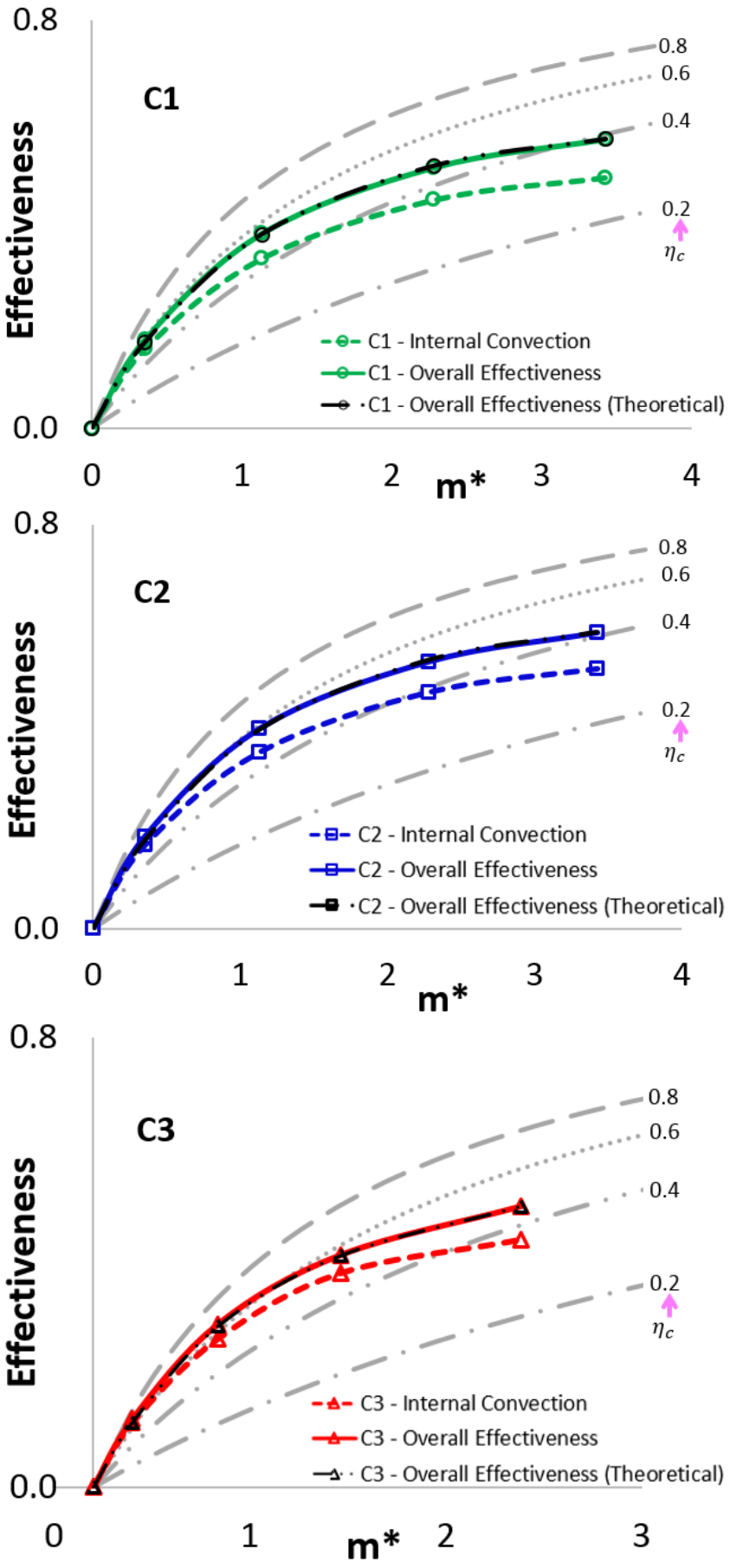

Figure 3.20: C1, C2 and C3 overall effectiveness comparison overall effectiveness from an analytical equation of Holland and Thake (1980)

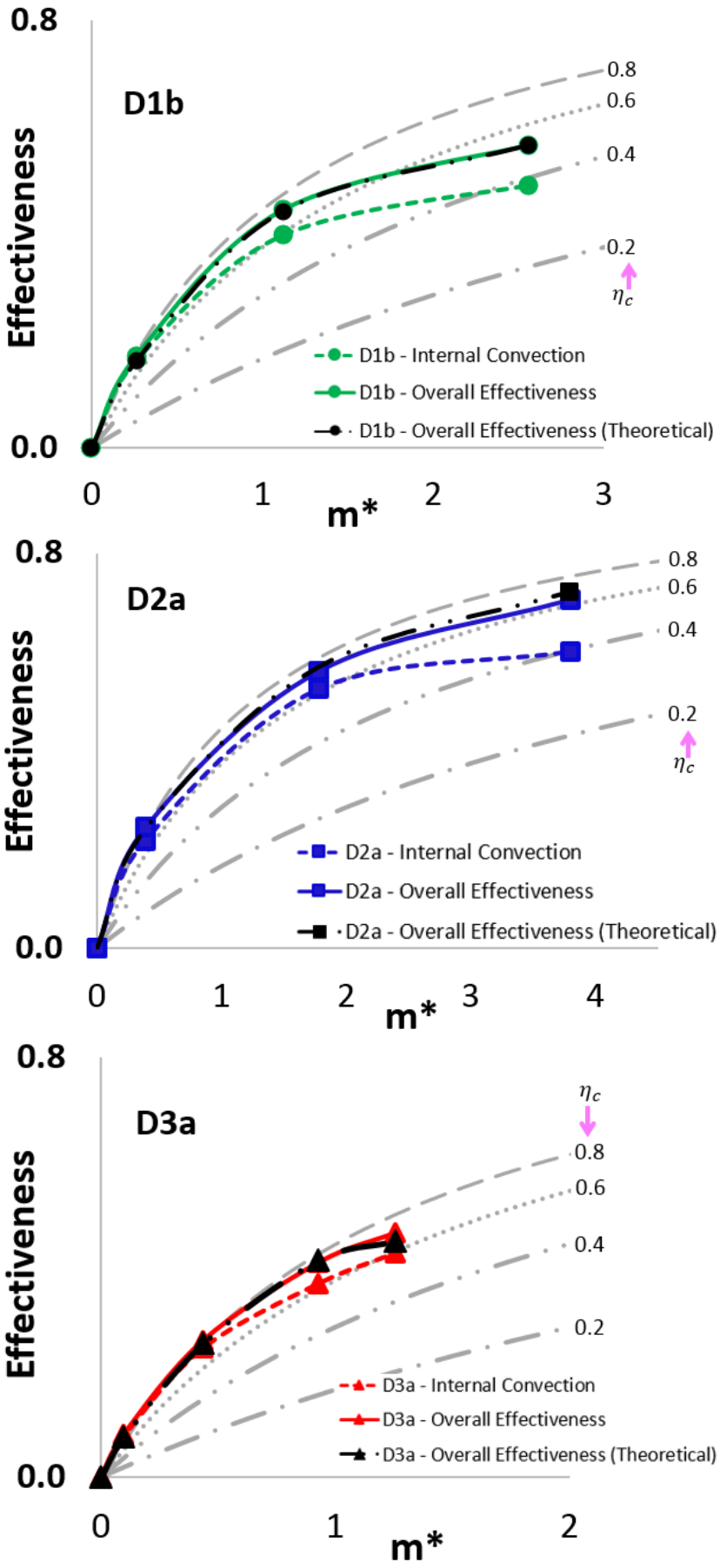

Figure 3.21: D1b, D2a and D3a overall effectiveness comparison with overall effectiveness from an analytical equation of Holland and Thake (1980)

Holland and Thake (1980) extended Equation 3.13 so as to factor in both convection cooling and film cooling - the resulting equation is shown in Equation 3.16. Equation 3.16 was used to evaluate theoretical overall metal effectiveness for all the six DWEC blade designs - C1, C2, C3, D1b, D2a and D3a. ε_f in the Equation 3.16 was estimated by taking a average of ε_f on both the PS and the SS surfaces. m^* was evaluated from Equation 3.14 and η_c computed as has been described in Section 3.5 and averaged. The theoretical effectiveness was then compared to the overall effectiveness evaluated from the simplified numerical analysis approach developed by the author in this thesis. The results have been included in Figure 3.20 and Figure 3.21. Generally, the overall effectiveness from the developed numerical analysis approach matches that calculated from theoretical Equation 3.16 developed by Holland and Thake (1980). There was, however, some slight discrepancies in all the blade designs across all the tested m^*. The percentage error between the overall effectiveness values was seen to reduce with increasing m^*. In all the test designs, and across all the m^*, the percentage error was below 8% - with the largest percentage error, of 7.2%, seen in design D3a at $m^* = 0.1$.

3.10 Conclusion

A computationally efficient numerical approach which permits an assessment of the performance of a complex double-walled effusion cooled turbine blade has been developed. The modified Goldstein (1971) correlation was used to predict the film effectiveness for each row of holes and the film superposition downstream of the rows obtained using the Sellers (1963) approach. The internal heat transfer coefficient was evaluated from a validated unit wall block element conjugate analysis and the conduction through the blade was simulated using the finite code available in ANSYS[1] Steady-State Thermal module. The numerical simulation approach has permitted analysis of DWEC blades allowing key performance parameters like film cooling effectiveness, internal cooling effectiveness, overall cooling effectiveness and coolant mass flow rate to be evaluated. The developed novel numerical analysis approach, compared to a fully coupled CHT simulation, reduced computational time by approximately 50 times. Therefore, it was found to be a simplified computationally efficient tool that could be used in the preliminary and optimisation stages of a DWEC turbine blade

design.

The internal cooling was found to contribute a larger proportion to the overall cooling effectiveness of the DWEC blade and this was attributed to a very large internal surface area brought about by a combination of impingement cooling and a large internal surface area contributed by the pedestals. The impressive internal cooling performance of the DWEC blade is key if DWEC system is to closely approximate that of transpiration cooling, as has been observed by Andrews and Asere (2013) and Andrews et al. (1985).

The numerical analysis tool developed was also used to analyse a total of six DWEC rotor blades. The validated unit wall elements data, from Murray et al. (2017), were used for the analysis. The simplified numerical tool allowed a comparison of the blades. The main aim of this research was to devise a simplified numerical analysis tool for analysing the complex DWEC blade. It should be noted that influence of various geometrical parameters like the cooling holes size, shape and pedestal shape and size was not exhaustively investigated. To enable redesign and optimization of the DWEC aerofoils, further research is, therefore, recommended to thoroughly investigate the influence of the DWEC geometrical parameters like pedestal spacing, shape, and size, cooling holes spacing, shape, and sizing on the cooling performance of the DWEC.

The next chapter - Chapter 4 will provide details on the CHT simulations undertaken to further analyse the DWEC turbine aerofoil.

Chapter 4

FULLY COUPLED CHT SIMULATIONS

4.1 Introduction

This chapter contains details of the fully coupled CHT simulation that was carried out to further analyse and understand the DWEC turbine aerofoil. Most of the CHT studies on turbine vanes and blades in the open literature have only considered either internally-cooled aerofoil or internally-cooled and film cooled aerofoils. There are hardly any CHT studies in the open literature that have been conducted on a double-wall effusion cooled aerofoil. This chapter outlines the fully coupled CHT analysis, using the commercial CFD software - ANSYS[1], that was conducted on the DWEC aerofoil. Section 4.3 describes the computational setup, Section 4.4 gives details of the computational mesh used, Section 4.5 contains details of the solver and Section 4.6 describes the boundary conditions used. The CHT numerical results and discussion are given in Section 4.7. At the end is the summary of this Chapter.

4.2 Fully coupled CHT Analysis

A fully coupled CHT simulation is a numerical simulation where the solution of the fluid flow and solution of the solid is determined in just one code without the need to perform

[1] www.ansys.com

interpolation of boundary conditions between the fluid and solid solver codes. Fully coupled CHT simulations are computationally expensive. Thus, in cases where preliminary numerical analysis of a complex cooling system, like the DWEC aerofoil, is required to permit redesign and optimization, a de-coupled simplified numerical analysis procedure is necessary. Such a simplified numerical analysis approach was developed in the course of this research and has been outlined in details in Chapter 3 of this thesis.

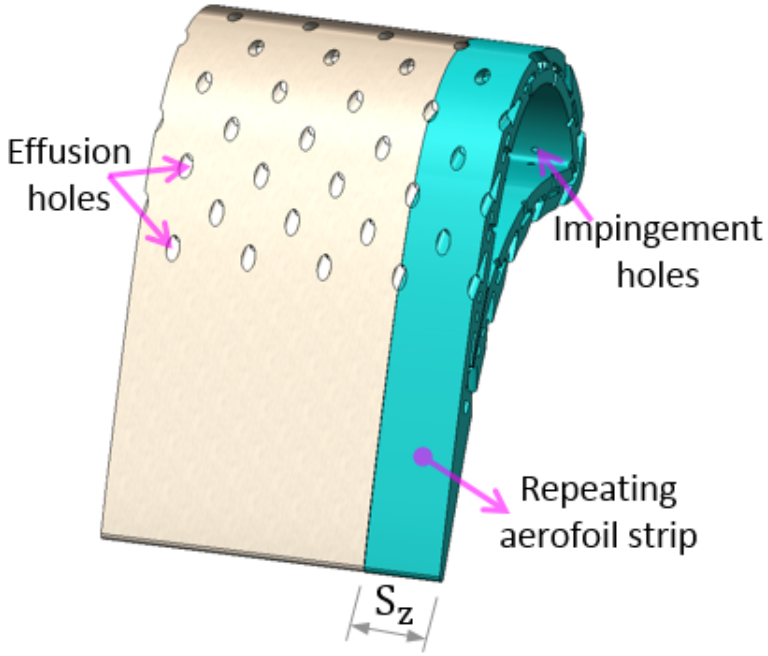

Figure 4.1: repeating DWEC aerofoil strip

Most of the CHT studies on turbine vanes and blades in the literature (a detailed literature survey of some of the CHT studies related to this study has been detailed in Section 2.3 in Chapter 2) have only considered either internally-cooled aerofoils or internally-cooled and film cooled aerofoils. To the best knowledge of this author, there are no CHT studies in the open literature that have been conducted on a double-wall effusion cooled aerofoil. The following sections contain details of the fully coupled CHT simulations carried out during this research to further analyse and understand the flow structure and cooling performance of the DWEC turbine aerofoil. A circular pedestal design, C2, was used for the CHT analysis.

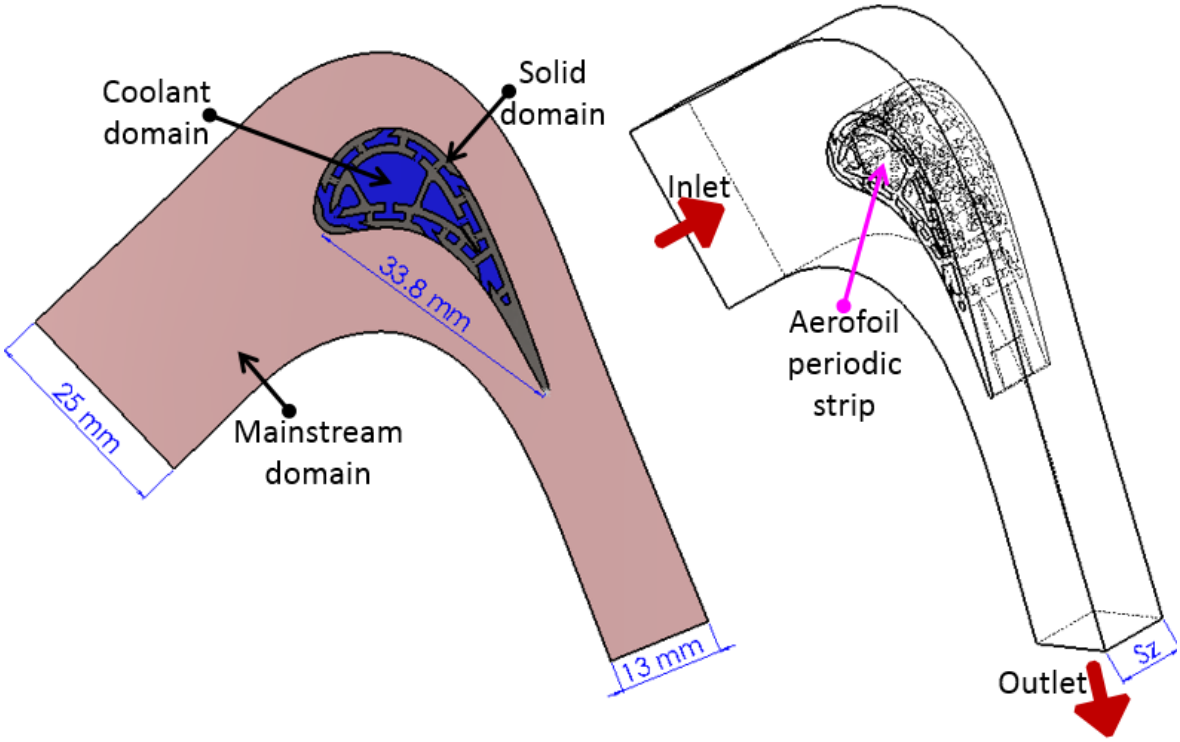

Figure 4.2: A simple CAD showing the mainstream, coolant and blade domains with the dimensions of the mainstream domain inlet and outlet

4.3 Computational Setup

The DWEC aerofoil under investigation is two dimensional and therefore the features have a repeating pattern in spanwise direction. Thereby, to reduce the computational mesh size and computational time, CHT simulation was performed on a repeating DWEC aerofoil strip - shown in Figure 4.1.

Table 4.1: Geometrical parameters and dimensions of the C2 unit wall element from Murray et al. (2017) used to build the midchord section of the DWEC blade

Geometry Number	Passage Height, L_P (mm)	Pedestal Diameter, D_P (mm)	Pedestal Spacing, L_1 (mm)	Effusion hole diameter, D_f (mm)	Impingement hole diameter, D_i (mm)	Streamwise, S_x and Spanwise, S_z Effusion Hole Spacing (mm)	Dimensionless Streamwise, S_x/D_f and Spanwise pitch, S_z/D_f
C2	1.5	1.0	1.5	1.0	1.0	10.0	10.0

The mainstream domain has a rectangular cross-section of 25 mm x S_z mm at inlet and 13 mm x S_z mm at the exit. Note that the domain width is uniform and is equal to S_z which

corresponds to the spanwise effusion hole spacing, shown in the last column of Table 4.1. Figure 3.14 gives the definition of the geometrical parameters. Figure 4.2 gives a simple CAD showing the mainstream, coolant and blade domains with the dimensions of the mainstream domain inlet and outlet. Note that the cascade used here for the CFD simulations is the same as the one used for the PSP tests (described in details in Chapter 5) but at engine scale. The rig scale is approximately twice engine scale. Figure 4.3 gives a summary of the mainstream domain and coolant domain inlet and outlet boundary conditions.

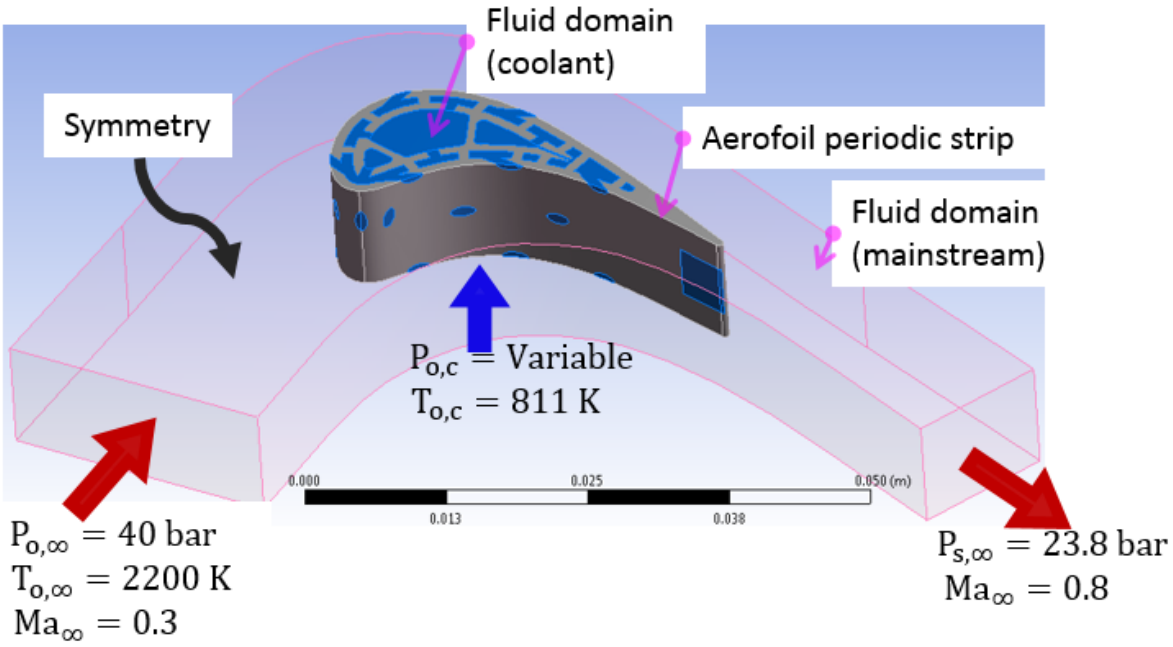

Figure 4.3: The mainstream and coolant boundary conditions

A circular pedestal DWEC design C2 was used in the CFD simulations carried out in this Chapter. As as aforementioned in Chapter 3, the blade name has been given so as to be consistent with the naming used elsewhere in this thesis. A summary of the geometrical parameters and dimensions of the unit wall elements from Murray et al. (2017) used to build midchord section of the DWEC blade is given in Table 4.1.

4.4 Computational Mesh

Due to the complex geometry of the DWEC aerofoil, the unstructured tetrahedral ANSYS[1] mesh was used. Inflation layers in the fluid were added to improve the accuracy of the simulation of the viscous boundary layer near the blade surface mesh, see Figure 4.4. Mesh re-

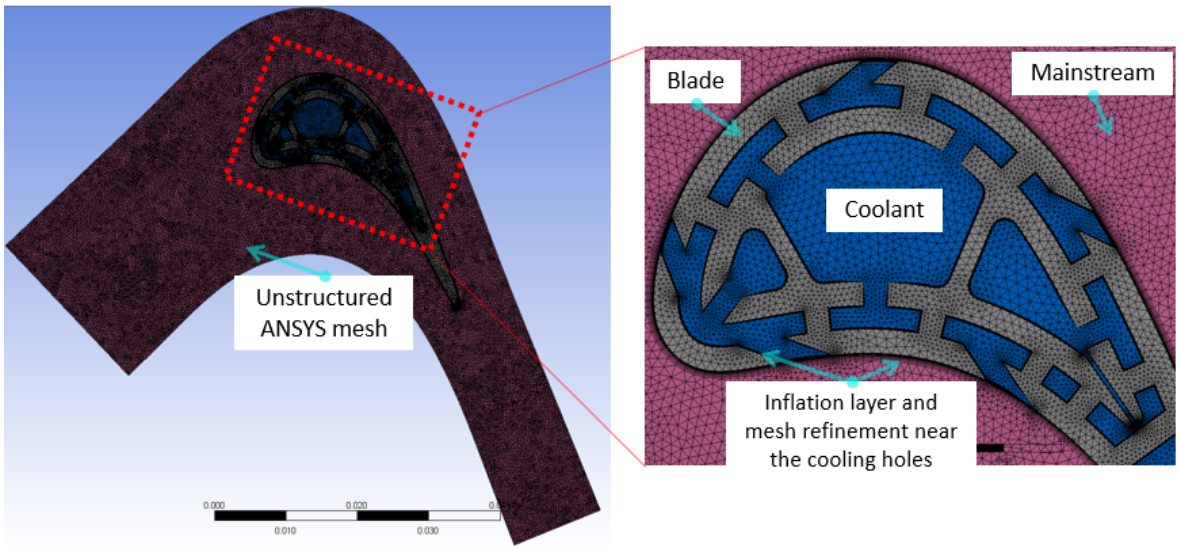

Figure 4.4: ANSYS[1] unstructured mesh including inflation layer and mesh refinement around the holes

finement near the cooling holes was also undertaken. Mesh sensitivity study was undertaken to enable selection of an optimum mesh size that resulted in reasonably accurate simulation results without excessive computational time. The mesh was refined until there was no much difference in the simulation results. Volume-averaged metal temperature, T_m (normalised by diving by the coolant inlet temperature, $T_{c,in}$) and coolant mass flow rate, $\dot{m}_c$ were used to evaluate mesh independence. The mesh sensitivity study results were as shown in Figure 4.5.

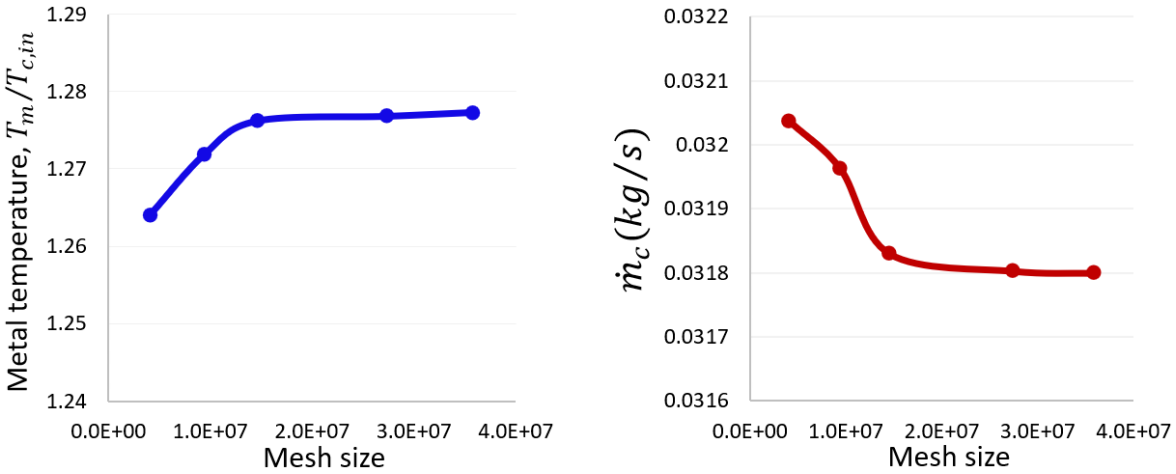

Figure 4.5: Mesh sensitivity results showing metal temperature and coolant mass flow rate variation with mesh size

In order to eliminate the need for interpolation, conformant mesh was used. The main-

stream and coolant domain had a total of 25,365,060 mesh elements while the solid domain resulted in a total of 2,013,213 mesh elements. The mesh quality was judged based on the mesh quality parameters such as orthogonal quality, aspect ratio, and skewness as outlined in the ANSYS manual (ANSYS, 2013).

4.5 Solver and Models

The CFD simulations were undertaken using the commercial student-version CFD software ANSYS[1] CFX version 16.2. Total energy model available in ANSYS[1] CFX was enabled for heat transfer setup. Air in both the coolant and mainstream domains was modelled as an ideal gas. Whereas the solid domain material was set as pure Nickel. A summary of the solver details is given in Table 4.2.

The pressure-based formulation of the steady RANS equations and the energy equation were solved with second-order discretization of all variables. Turbulence was modelled by the SST turbulence model with an automatic wall function. The SST turbulence model has been shown by many researchers in literature ((Menter et al., 2003), (Menter and Esch, 2001), (Esch, 2003), (Dyson et al., 2014), (Mick et al., 2013)) to give more accurate numerical results in turbomachinery applications. Medium turbulence intensity of 5% was employed in the present simulation. High level of turbulence causes an increase in temperature over an aerofoil surface. In addition, onset of boundary layer transition is influenced by the level of turbulence (Mayle, 1991). Considering Re based on the distance from the aerofoil leading edge, and using flat plate critical Re (500,000), it was estimated that in the present simulation transition onset takes place at approximately $x/C_{ax} = 0.25$.

A second-order discretization scheme was used. High resolution was selected for both the turbulence numerics and advection scheme. Simulation convergence was judged on root mean square residual levels of mass and momentum, heat transfer and turbulence dropping below $1e-4$. In order to aid solution convergence, initialization was done by setting an automatic static pressure and temperature distribution in fluid domain. Figure 4.6 shows an example of the convergence trajectory for the simulations with PR = 1.25.

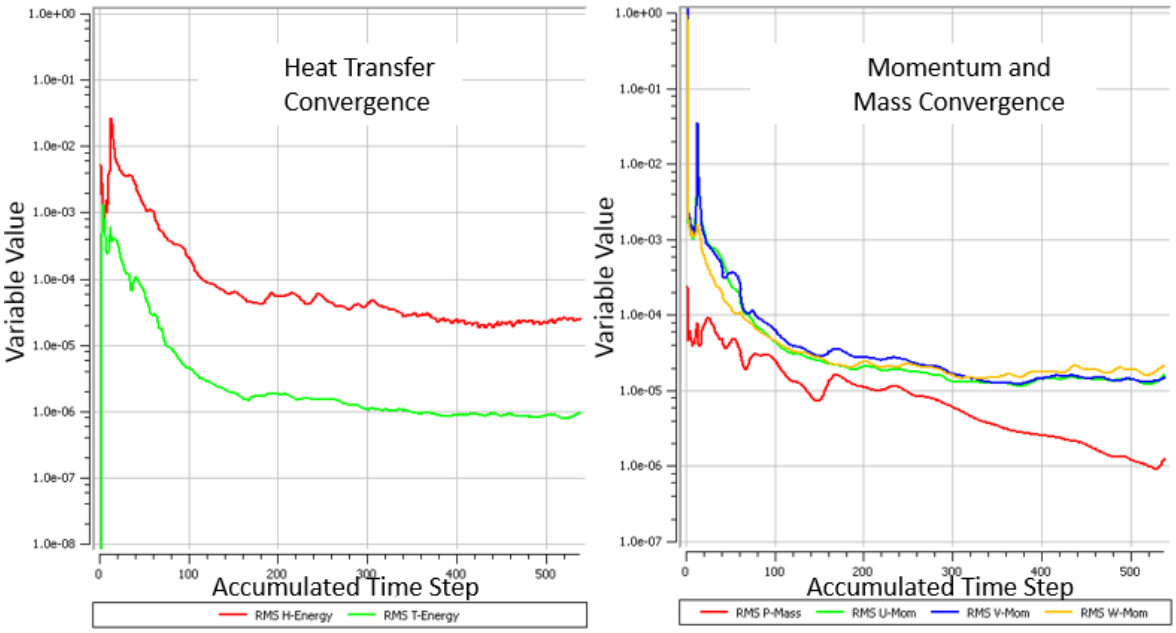

Figure 4.6: CFD simulation heat transfer, momentum and mass convergence status

4.6 Boundary Conditions

The engine-scale boundary conditions used for the CFD simulations are shown in Table 4.2. With these boundary conditions, the inlet and exit Mach number of 0.3 and 0.8 respectively and an overall ratio of the inlet total pressure, $P_{o,\infty}$ to the exit static pressure $P_{s,\infty}$, of 1.6 were achieved. Figure 4.3 gives a schematic diagram showing a summary mainstream and coolant inlet and outlet boundary conditions.

In order to cover a range of engine-realistic blowing ratios, CFD simulations were carried out at four total coolant inlet pressure ratios; $P_{o,c}/P_{o,\infty}$, PR = 1.00, PR = 1.05, PR = 1.15 and PR = 1.25. The lowest pressure ratio, PR = 1.00 was included in this analysis so as to permit a direct comparison of CHT results with those from the simplified analysis method in Chapter 3. A summary of the mainstream and coolant domain boundary conditions is given in Table 4.2.

4.7 Results and Discussion

CHT simulations using the commercial ANSYS[1] CFX CFD software has permitted valuable insight into the cooling performance and flow structure of the DWEC turbine aerofoil. From

Table 4.2: Boundary conditions and initial conditions for ANSYS[1] CFX solver

Input	Value
Analysis Type	Steady State
Fluid Domain Material	Air Ideal Gas
Solid Domain Material	Pure nickel
Heat Transfer	Total Energy
Turbulence Model	SST
Turbulence Intensity	Medium (5%)
Wall Function	Automatic
Mainstream Flow Conditions:	
Total Pressure	40 bar
Exit Static Pressure	23.8 bar
Total Temperature	2200 K
Inlet Mach Number	0.3
Outlet Mach Number	0.8
Coolant Flow Conditions:	
Total Pressure, $P_{o,c}/P_{o,\infty}$	1.00, 1.05, 1.15 and 1.25
Total Temperature	811 K
Advection Scheme	High Resolution
Timescale Control	Auto Timescale
Turbulence Numerics	High Resolution

the CFD simulations, it was possible to get information about internal and external fluid flow structures as well as overall metal effectiveness, adiabatic film cooling effectiveness and blowing ratio. A circular DWEC design C2 was considered and simulations carried out at four total coolant inlet pressures corresponding to PR = 1.00, 1.05, 1.15 and 1.25. The four PR, with respect to the external static pressure distribution on the aerofoil, are represented using horizontal dotted lines in Figure 3.11 in Chapter 3. Figure 3.11 shows the mainstream flow static pressure distribution around the aerofoil.

The following subsections give the results of the CFD simulations in form of post-processed images and graphs from CFX post and a discussion of the results. Subsection 4.7.1, Subsection 4.7.2, Subsection 4.7.3, Subsection 4.7.4, Subsection 4.7.5 give results and discussion of the flow internal and external structure, impingement/effusion cooling, metal effectiveness, blowing ratio and adiabatic film cooling effectiveness respectively.

4.7.1 Internal and External Flow Structures

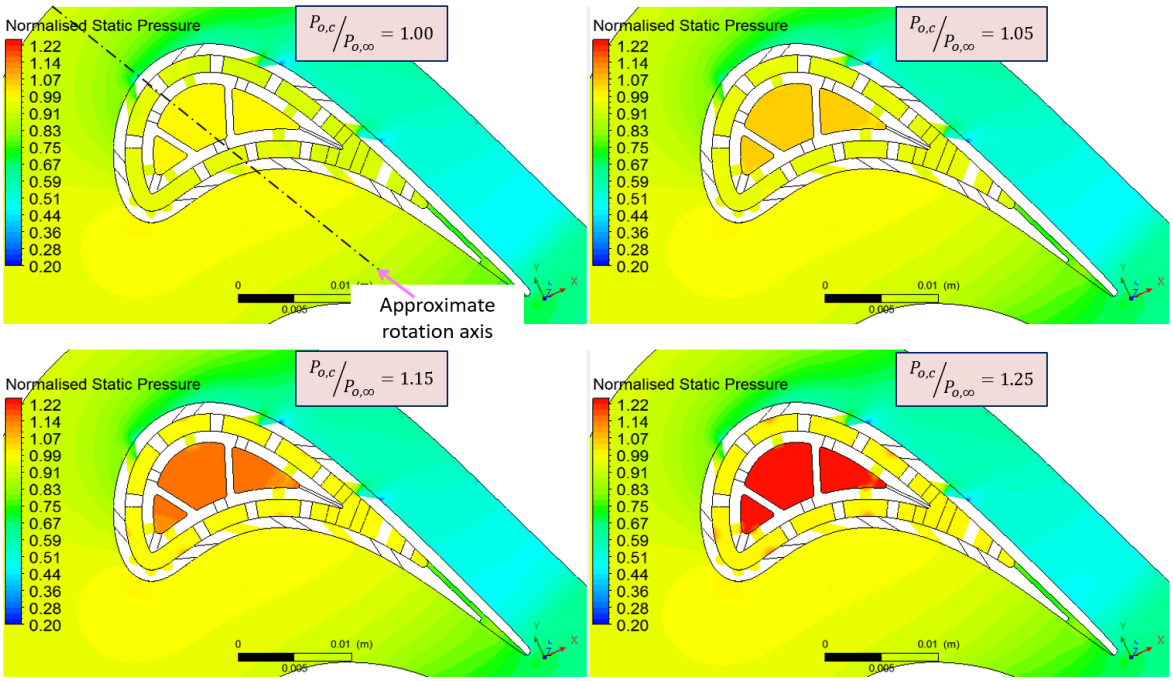

Figure 4.7: Pressure contours at the aerofoil midspan for the four different coolant pressure ratios corresponding to PR = 1.00, 1.05, 1.15 and 1.25

The cooling air and external mainstream flow characteristics were visualised using static pressure contours in Figure 4.7, Mach number contours in Figure 4.8, Mach number coloured vectors in Figure 4.9 and streamlines coloured by Mach number in Figure 4.10. Figure 4.11 shows 3D coolant and mainstream streamlines coloured by Mach number for PR = 1.25. The pressure contours and Mach number contours were drawn on a plane at the midspan of the aerofoil. The images have deliberately focused on the region near the aerofoil surface so that the flow structure near the cooling holes can be clearly visualised. The static pressure in the contours has been normalised by dividing it by the mainstream inlet total pressure, $P_{o,\infty}$.

The highest external static pressure was at the vicinity of the aerofoil LE stagnation point.

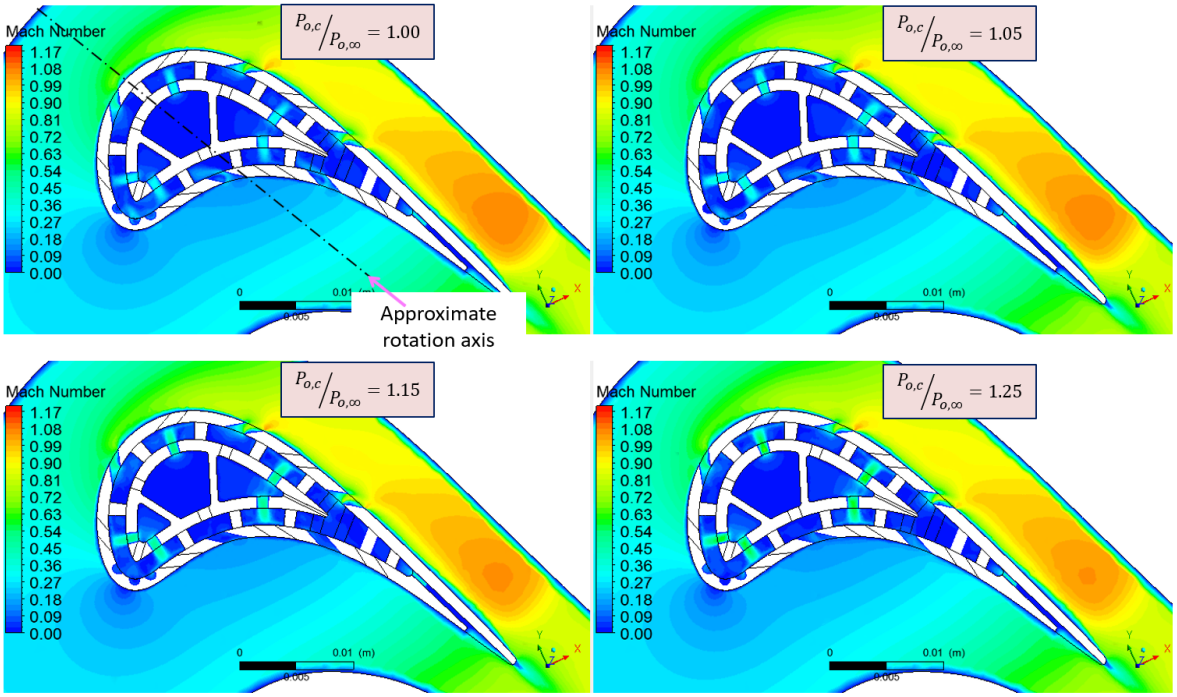

Figure 4.8: Mach number contours at the aerofoil midspan for the four different coolant pressure ratios corresponding to PR = 1.00, 1.05, 1.15 and 1.25

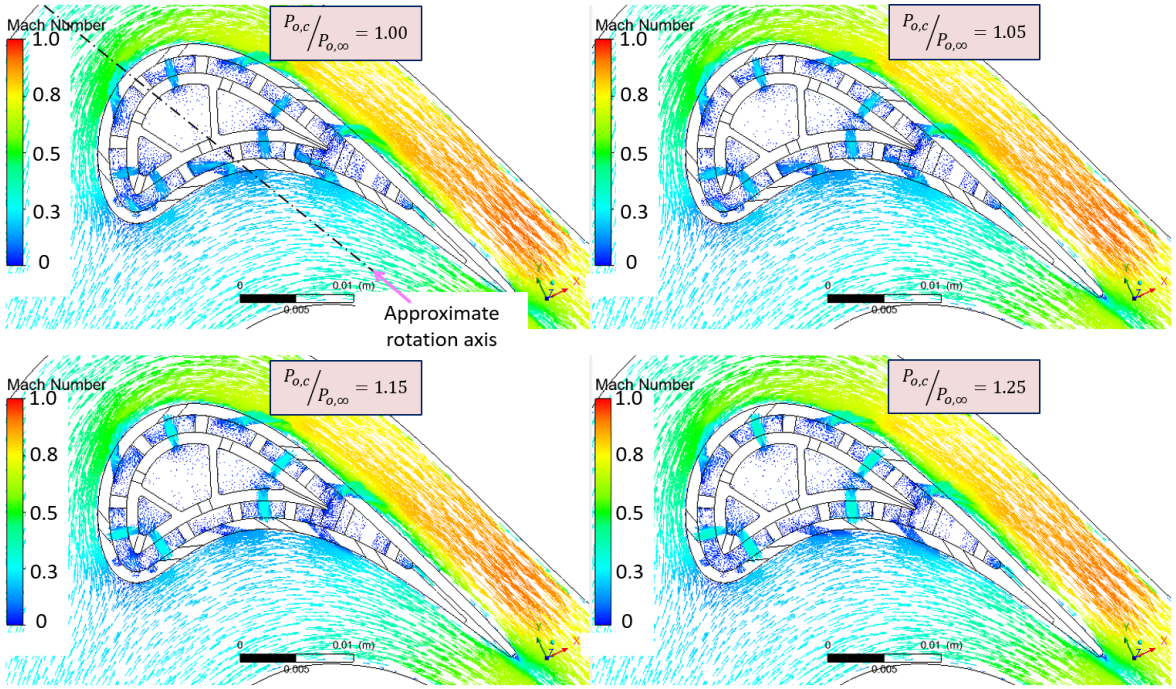

Figure 4.9: Mach number vectors for the four different coolant pressure ratios corresponding to PR = 1.00, 1.05, 1.15 and 1.25

The static pressure then reduced rapidly on the SS near the LE and continued to gradually drop for most part of the SS, with the lowest external static pressure observed at the blade exit throat, as shown in Figure 3.11. On the PS, the external static pressure dropped slightly

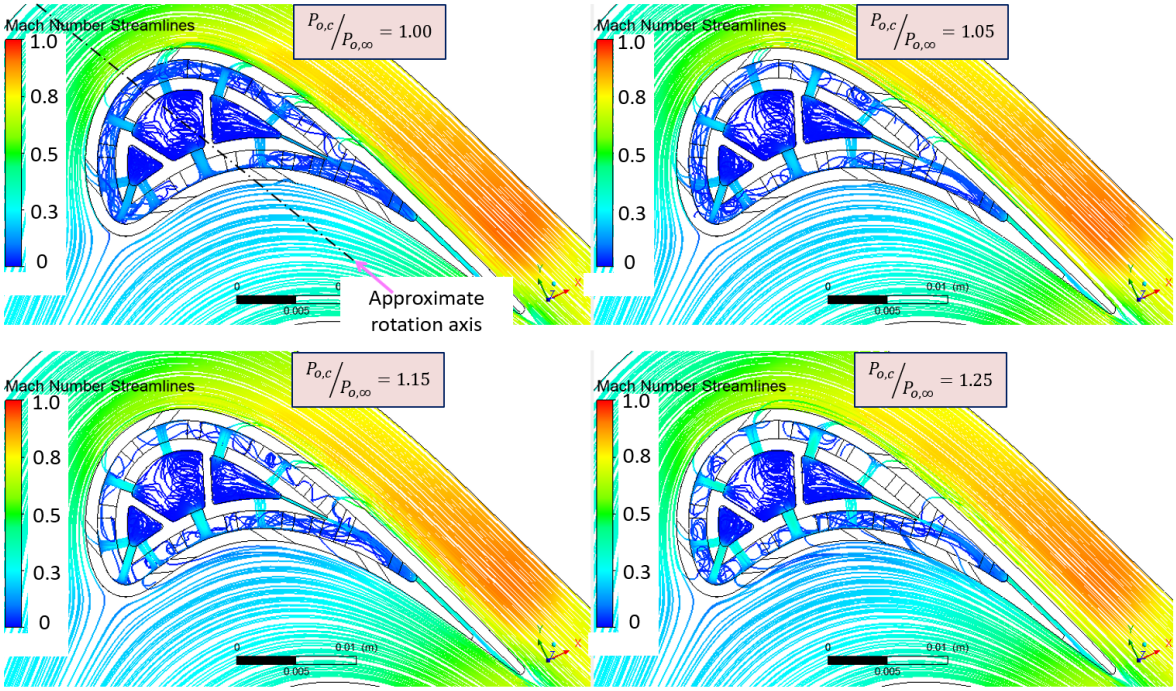

Figure 4.10: Streamlines coloured by Mach number for the four different coolant pressure ratios corresponding to PR = 1.00, 1.05, 1.15 and 1.25

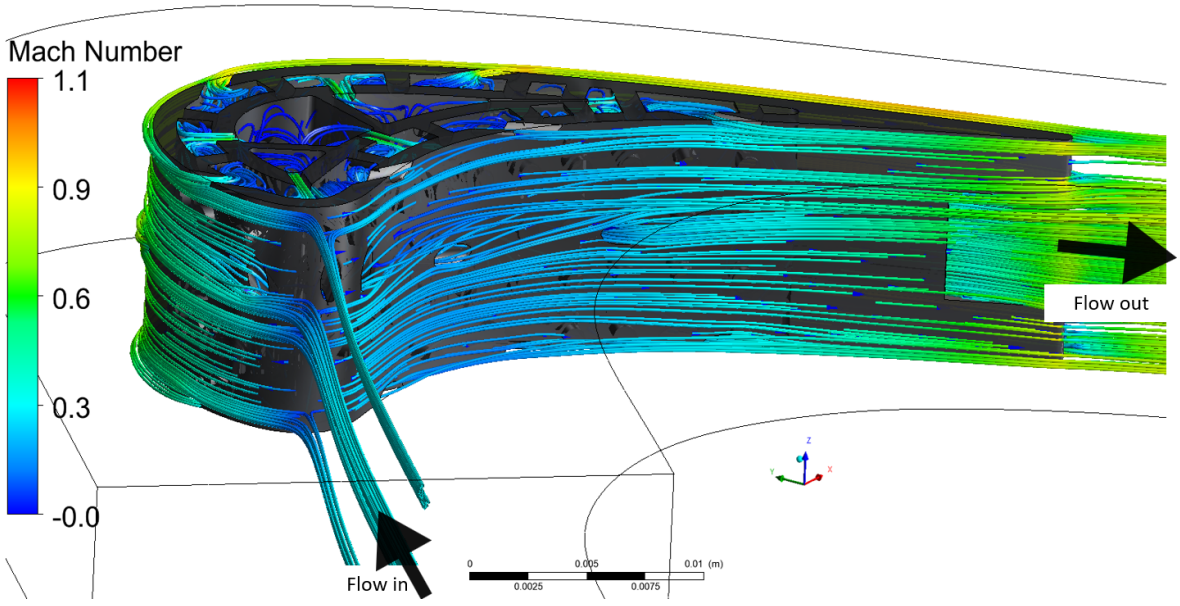

Figure 4.11: 3D streamlines coloured by Mach number for coolant pressure ratio, PR = 1.25

on the PS near the LE but then remained almost constant up to about 70% of the axial chord before plummeting at the vicinity of the TE.

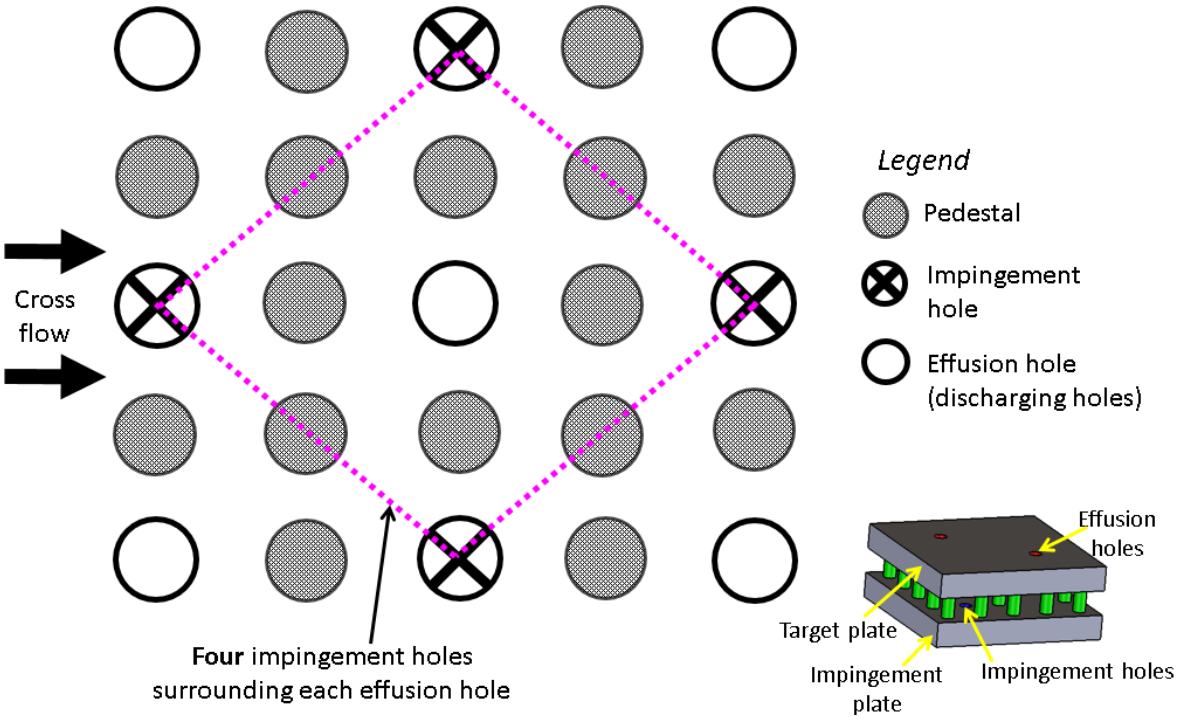

Figure 4.12: Impingement holes, effusion holes and pedestal configuration

4.7.2 Impingement/Effusion Cooling

Impingement cooling has been demonstrated by many researchers to be an effective way to cool the surface with locally high heat transfer rates [(Metzger and Bunker, 1990), (Rhee et al., 2003), (Son et al., 2001), (Bunker et al., 2014), (Murray et al., 2017)]. Impingement/effusion system could also be used to deliberately increase or decrease coolant pressure before entering the film holes and thereby altering the blowing ratios around an aerofoil to desired levels (Bunker et al., 2014). A review of some studies that have researched flow structure and heat transfer characteristics of impingement/effusion cooling systems have been included in the Literature Survey in Chapter 2.

To minimize the negative effects of the cross flow inside the impingement/effusion channel in the current design, the impingement/effusion cooled double-wall mid chord region (which is the focus of this research) has both the discharge effusion cooling holes on the outer skin and pedestals between the impingement and effusion plate. Figure 4.12 shows a configuration of the impingement holes, effusion (discharge) holes and pedestals within the impingement/effusion cooled double-wall region of the blade. The analysis here focused on the impingement/effusion configuration on the aerofoil midchord section and aimed to

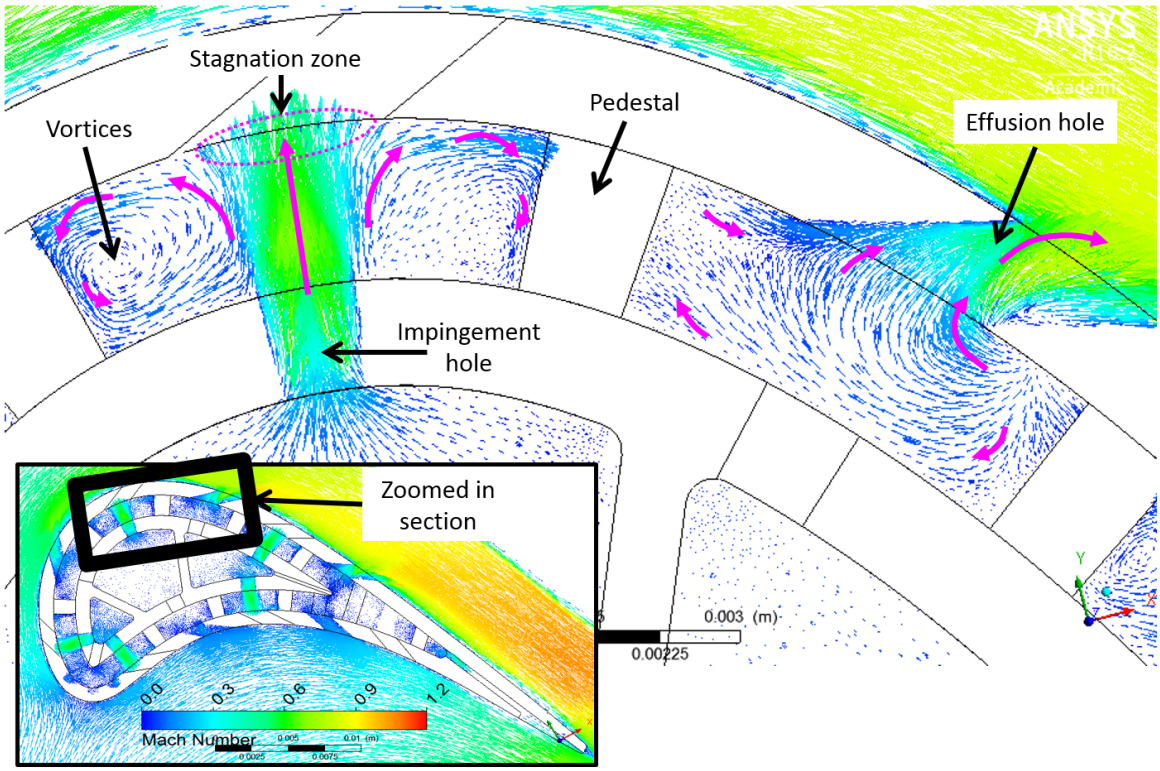

Figure 4.13: Flow structure in the form of Mach number coloured vectors, zoomed in near hole SS4 at PR corresponding to PR = 1.25

show the structure of the impingement jet as it impinges on the outer curved target plate and subsequent interactions with the jets emanating from neighbouring impingement holes. Figure 4.13 shows a flow structure in the form of Mach number coloured vectors, zoomed in from Figure 4.9. The impingement jet from the impingement hole impinges on the inner walls of the outer target surface, at relatively high velocity - as shown in Figure 4.13. The jet then splits, rolls up hitting the walls of the nearby pedestals. There were vortices formed as the spent impingement fluid rolled up. The spent impingement fluid then flowed downwards along the walls of the pedestals towards the impingement plate. The fluid was finally discharged through the nearest effusion hole (located one row of pedestals away both in streamwise and spanwise directions - as shown in Figure 4.12) on the outer effusion wall.

There were zones of jet re-impingement (as illustrated in Figure 4.14) resulting from an interaction of spent impingement flow from neighbouring impingement holes. Owing to the presence of the pedestals in the channel, the spent impingement flow stroke the pedestal and split into two jets resulting in two re-impingement zones on the opposite sides of the pedestal, as shown in Figure 4.14. After the re-impingement, the resulting flow was then

accelerated towards the nearest effusion hole and discharged.

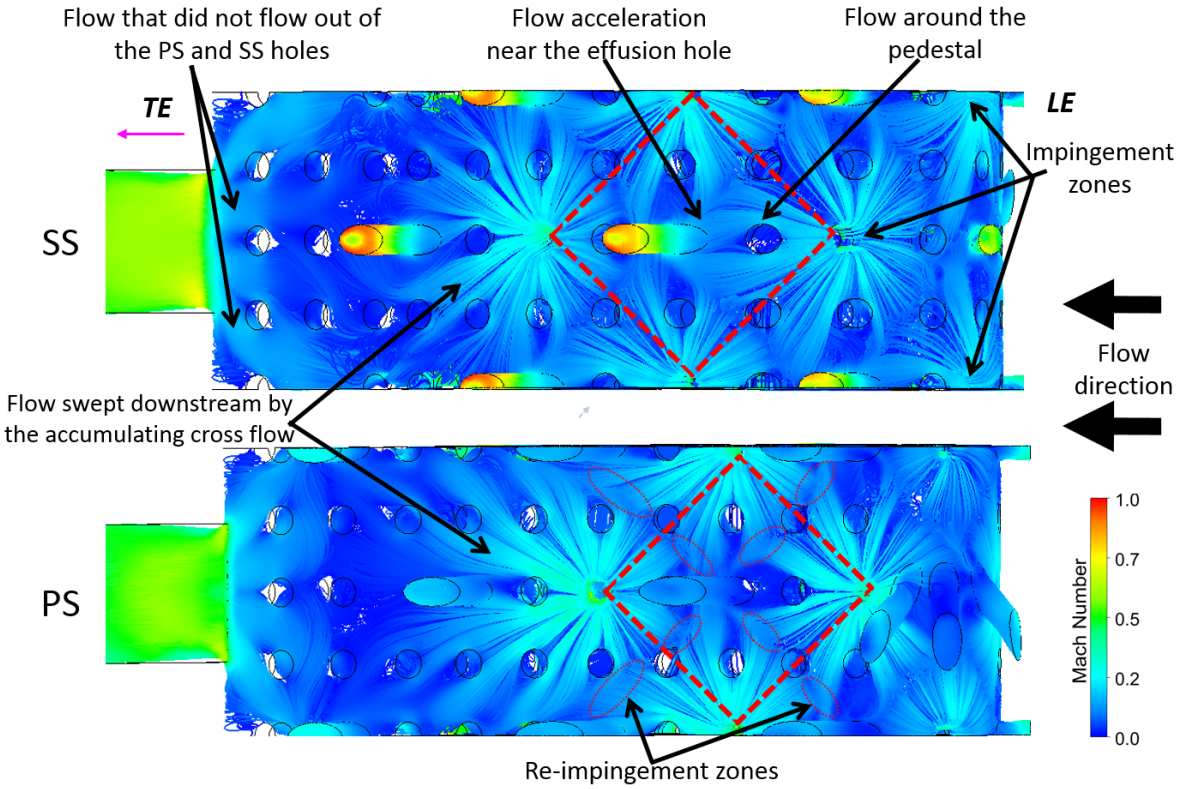

Figure 4.14: 3D streamlines, coloured by Mach number, on both the PS and the SS walls corresponding to PR =1.25

To further analyse the flow structure of the double-wall impingement/effusion midchord section of the blade, 3 dimensional streamlines coloured by Mach number were visualised on both the SS and the PS walls - see Figure 4.14. On both surfaces, the spread of the impingement jet after impinging on the effusion wall differed in streamwise direction. Near the LE, the spent jet spread more uniformly around the impingement stagnation point. However, further downstream towards the TE, the spent impingement flow did not spread uniformly around the stagnation point; the jet spread more in the downstream direction of the impingement stagnation point than on the upstream. This was attributed to the fact there was less cross flow at the region near the LE. But further downstream on both the PS and the SS, the cross flow continued to accumulate and became stronger downstream towards the TE. Consequently, sweeping away the spent impingement flow towards the TE.

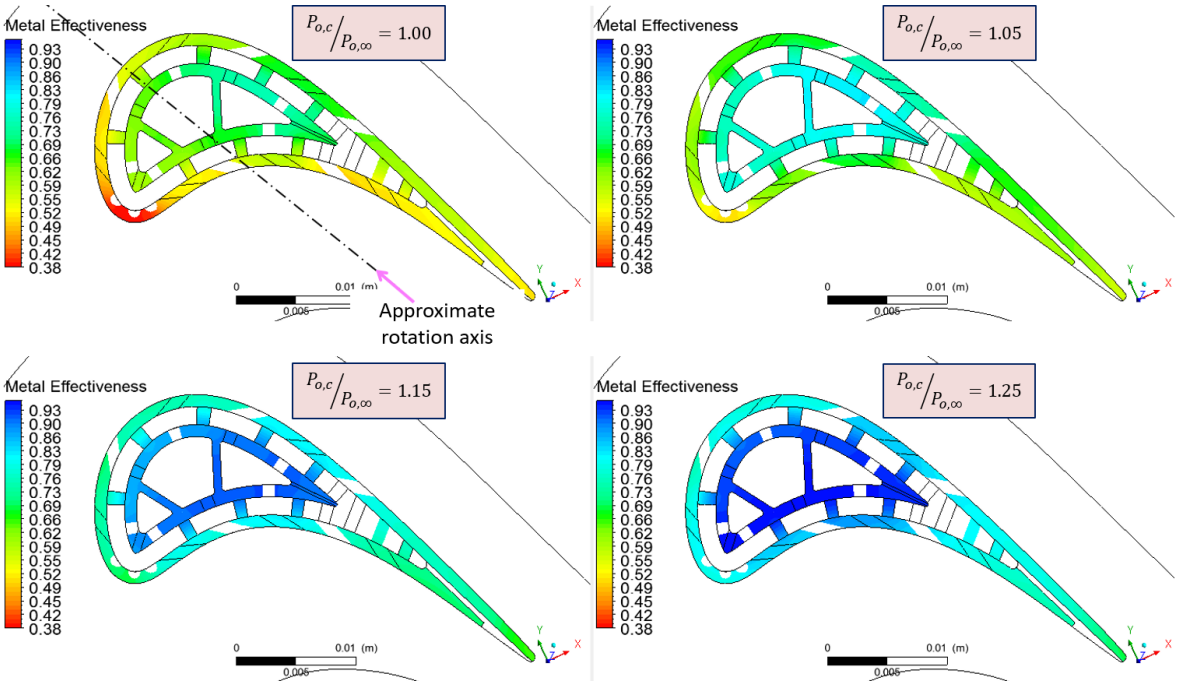

Figure 4.15: Dimensionless blade temperature contour maps for the four different pressures corresponding to PR = 1.00, 1.05, 1.15 and 1.25

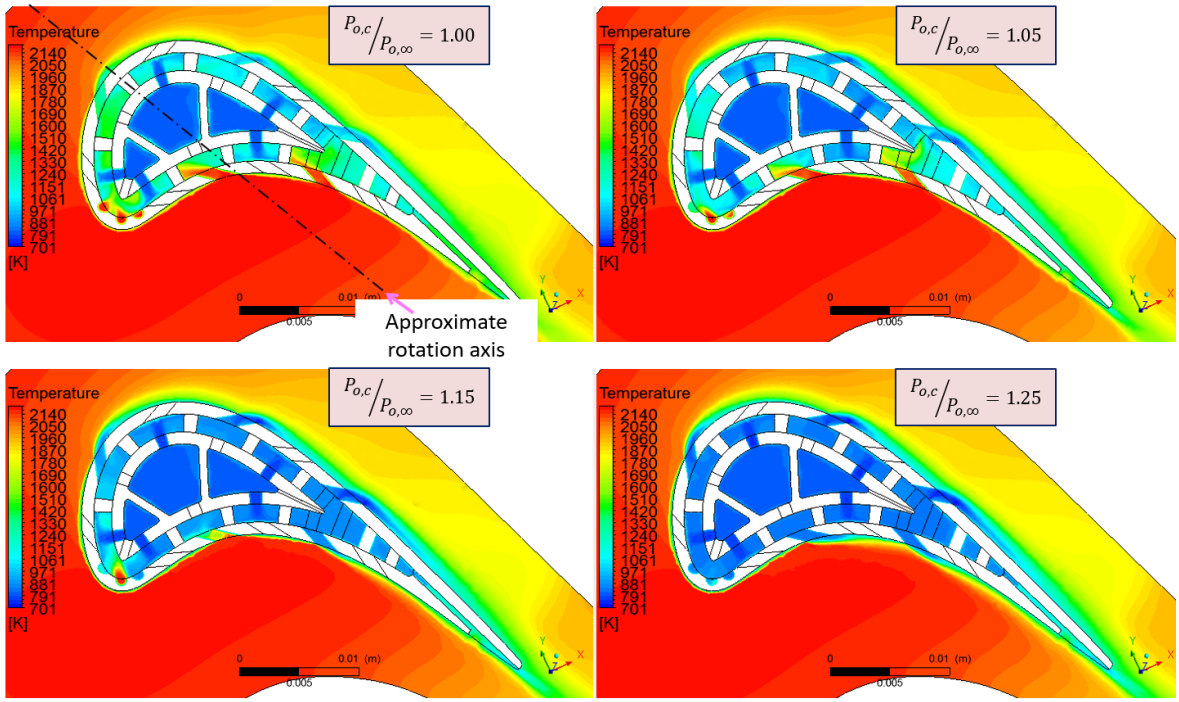

Figure 4.16: Mainstream and coolant temperature contour maps at the aerofoil midspan for the four different pressures corresponding to PR = 1.00, 1.05, 1.15 and 1.25

4.7.3 Metal Effectiveness

The metal temperature is presented in the form of metal effectiveness defined in Equation 3.12. As earlier described in Section 4.6, CFD simulations were carried out at four different

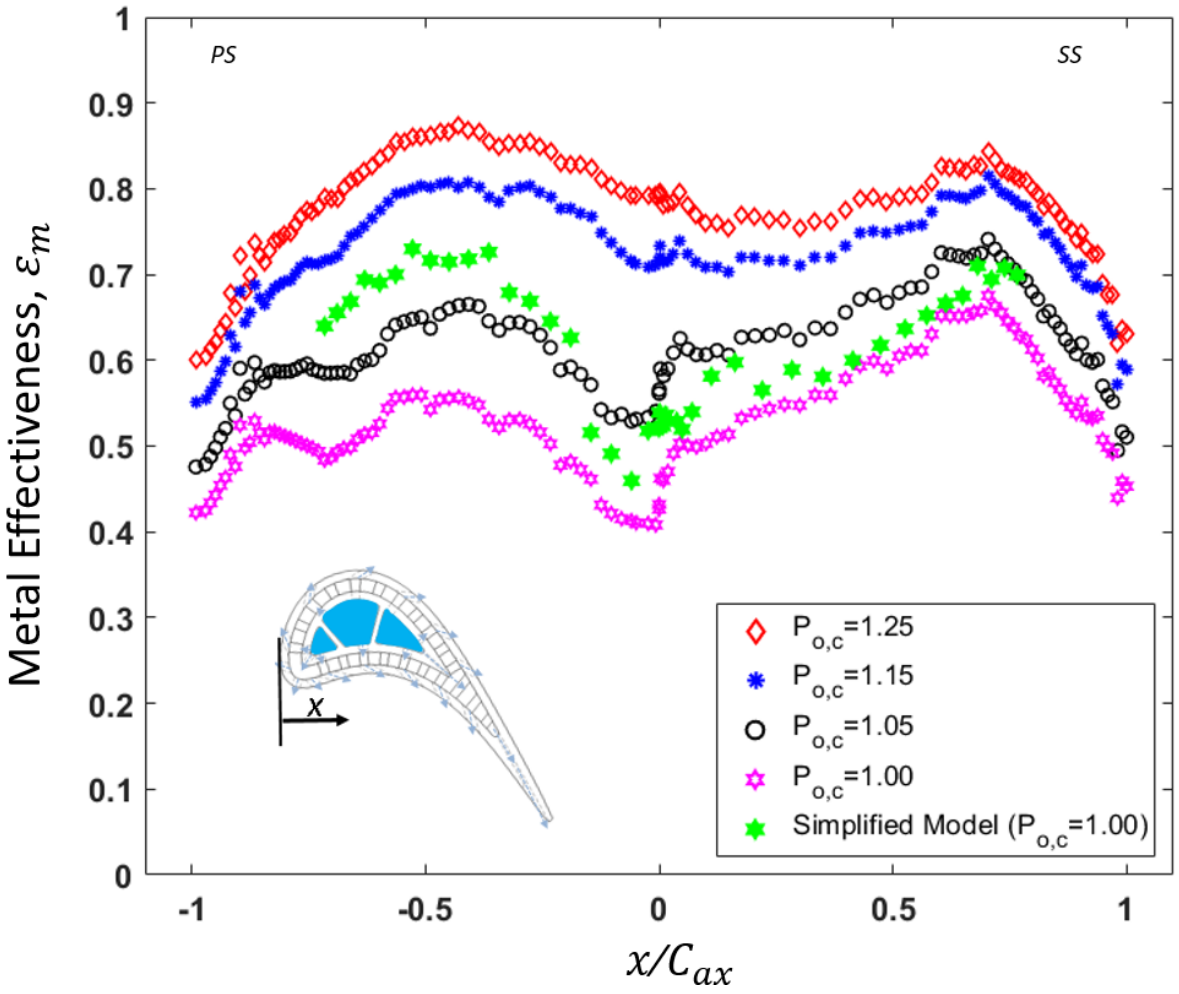

Figure 4.17: Laterally-averaged metal effectiveness distribution on both the PS and the SS at four different coolant pressure ratios corresponding to PR = 1.00, 1.05, 1.15 and 1.25. Including a comparison to the ε_m from the simplified model in Chapter 3.

coolant inlet pressure ratios corresponding to PR = 1.00, 1.05, 1.15 and 1.25. Figure 4.15 shows the metal effectiveness contours of the blade, at the four different coolant pressure ratios, drawn on a plane located at the aerofoil midspan while Figure 4.16 shows temperature distribution on both the coolant and mainstream domains.

As expected, ε_m on both the SS and the PS improved with the increase in PR, and hence $\dot{m}_c$, as illustrated in Figure 4.17. Figure 4.17 shows a graph of laterally-averaged ε_m at four different coolant pressure ratios corresponding to PR=1.00, 1.05, 1.15 and 1.25. From Figure 4.17, the general ε_m trend on both the SS and the PS is that metal effectiveness is lowest around the LE and the TE regions of the aerofoil. The lowest metal effectiveness on both the LE and the TE is attributed to the fact that the LE is located at the mainstream flow stagnation point where vortices are formed that augment heat transfer. On the other

hand, the TE has a narrow shaped geometry and is exposed to a fully turbulent hot gas path. The metal effectiveness on both the SS and the PS, and across all the four different coolant pressure ratios, was low around the LE region of the blade. It then progressively increased downstream reaching a maximum approximately 70% and 50% of axial chord on the SS and the PS respectively. After attaining the maximum, ε_m on both surfaces dropped rapidly to the lowest value at the TE. The rapid drop in the ε_m after 70% and 50% axial chord on the SS and the PS respectively was attributed to the fact that the coolant plenum ended approximately 70% axial chord on the SS and 50% axial chord on the PS. Thus, downstream locations did not benefit from high $P_{o,c}$ compared to the upstream locations which were proximate to the coolant plenum.

It was expected that, owing to high HTC inherent on the PS (the PS has significantly high pressure margin, see Figure 3.11, and hence low blowing ratios), ε_m on the PS to be generally lower than ε_m on the SS for any given $P_{o,c}$. It is interesting to note that this was only true at low PR - for instance, the case of PR = 1.00 and PR = 1.05 in the Figure 4.17). At higher PR, ε_m was generally higher on the PS compared to the SS, for instance the highest value of ε_m at PR = 1.25 was 0.87 (at approximately 40% axial chord) on the PS. This trend was attributed to the fact that as PR was increased, and since the $P_{s,\infty}$ is much lower on the SS than the PS - as illustrated in Figure 3.11, the blowing ratio on the SS was much higher than that on the PS causing coolant jet to lift off the SS and consequently resulting in lower cooling performance. The influence of blowing ratio on the blade cooling performance has been discussed in Subsection 4.7.4.

$$\varepsilon_m = \frac{T_{o,\infty} - T_m}{T_{o,\infty} - T_{c,in}} \tag{4.1}$$

The ε_m from CHT simulation undertaken here was compared to that from the simplified analysis model outlined in Chapter 3. The comparison was done at PR = 1.0. The ε_m from the CHT simulation and from the simplified model show the same trend on both the SS and the PS; low ε_m at the vicinity of the LE and progressive improvement downstream. It should be noted, as earlier described in Chapter 3, that the simplified analysis model considered only the double-wall midchord region of the aerofoil - up to 87% axial chord on the SS and 80%

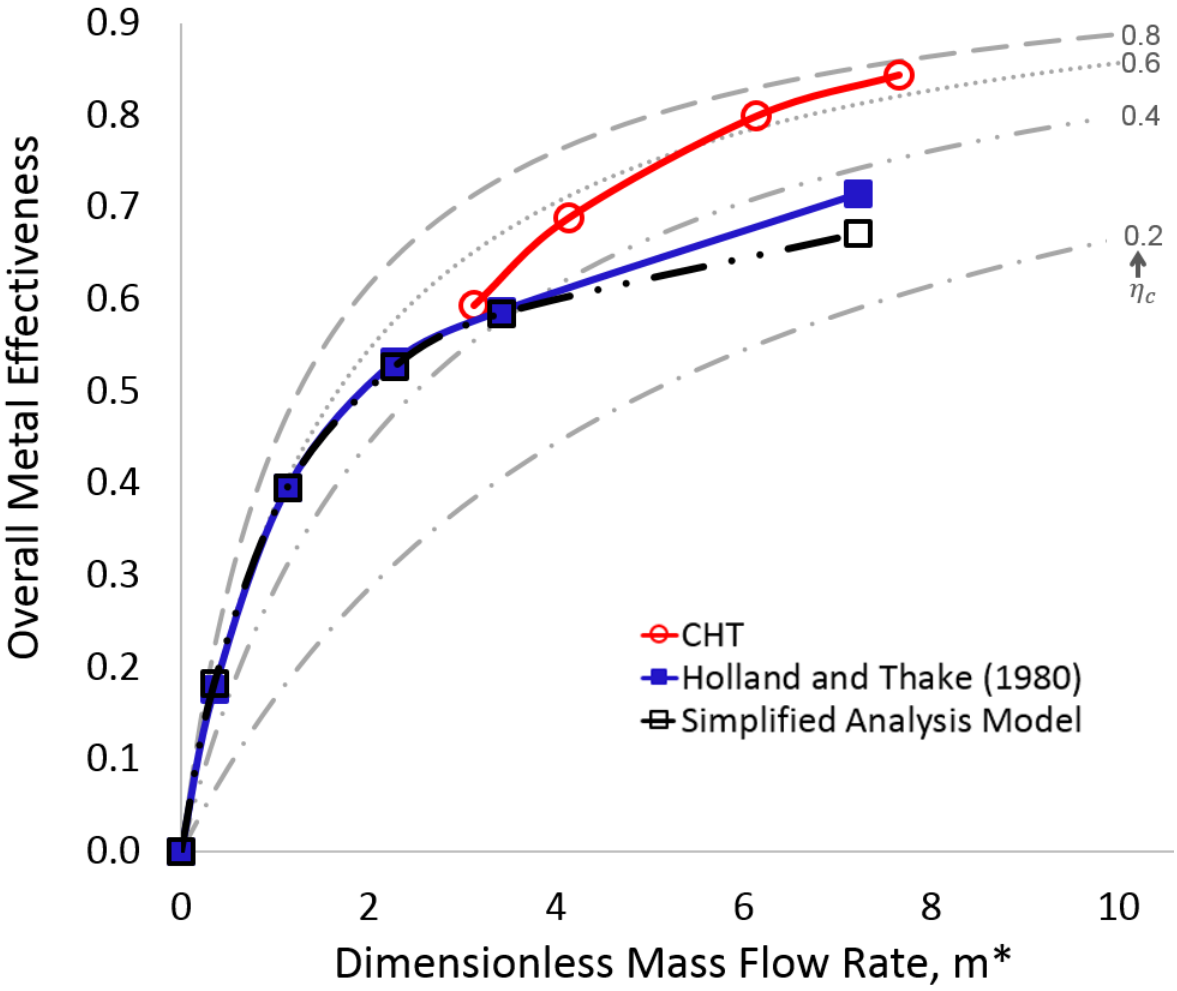

Figure 4.18: Metal effectiveness versus dimensionless mass flow comparing the CHT results with that from the simplified analysis model

axial chord on the PS. On the SS, the ε_m from the simplified model compared quite well with the ε_m from the CHT simulation. On the PS however, there was a big discrepancy between the ε_m from the CHT and that from the simplified analysis model; with the simplified model over predicting the ε_m. The largest discrepancy was observed at 35% PS axial chord where the percentage error was 28%. The reason why the simplified model overpredicted ε_m on the PS was attributed to the fact that discharge coefficient, C_d from Murray et al. (2017) isolated wall block was found to over predict PS C_d and thus mass flow rates. A detailed discussion of the C_d and a comparison of the SS holes, the PS holes and the isolated wall block C_d has been included in Subsection 4.7.4 of this Chapter.

Figure 4.18 shows a graph of overall metal effectiveness, ε_m, versus dimensionless mass flow, m^* of the CHT undertaken in this chapter and simplified analysis model outlined in

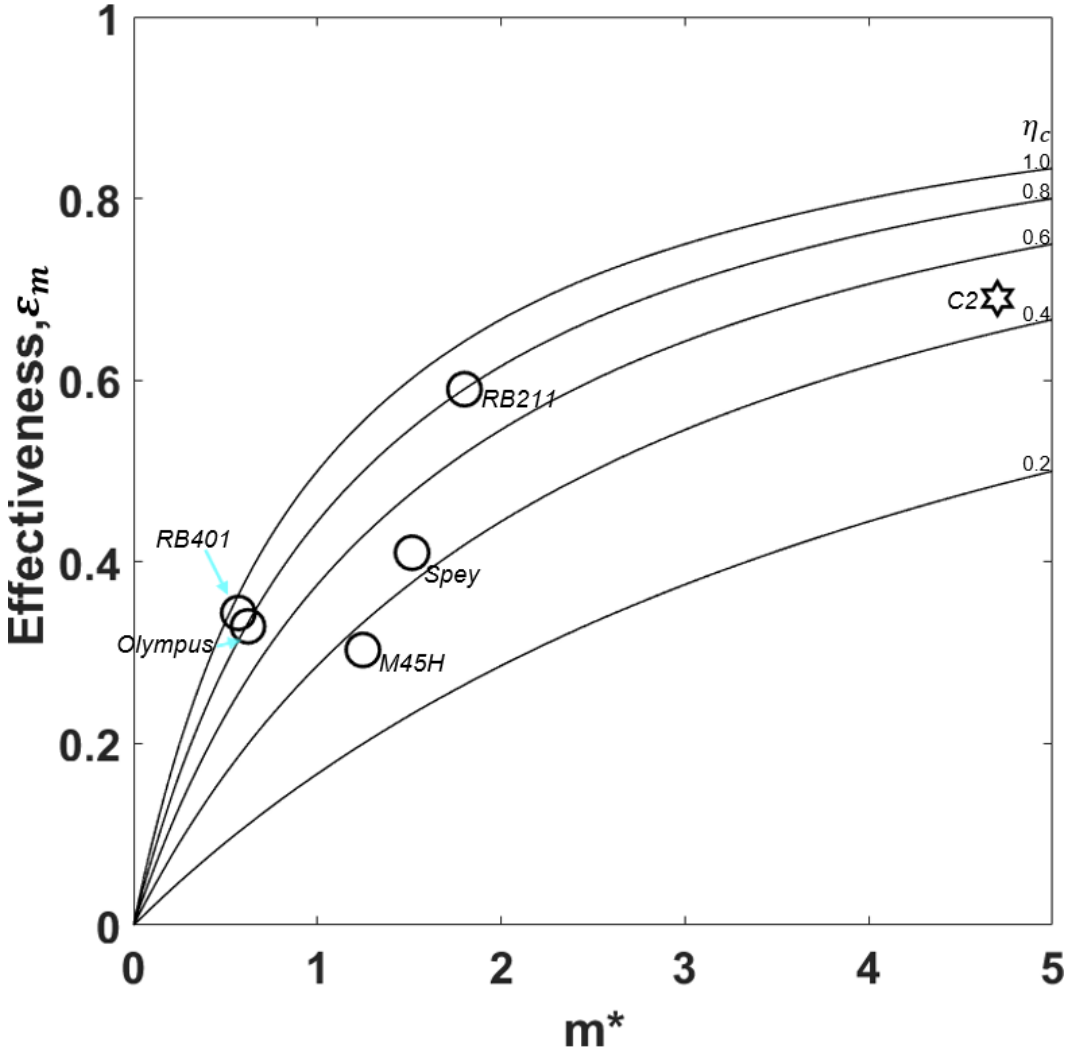

Figure 4.19: C2 effectiveness results compared with those of some high pressure turbine blades from Holland and Thake (1980)

Chapter 3. ε_m was evaluated from equation 4.1, where T_m was volume-averaged metal temperature. m^* was evaluated using Equation 3.14. The grey-dashed lines, calculated with different values of convective efficiency as a parameter, show the cooling efficiency curves of η_c = 0.2, 0.4, 0.6 and 0.8 calculated from Equation 3.13 for a range of values of m^*. The ε_m from CHT metal effectiveness was found to be higher than ε_m from the simplified analysis model at higher mass flow rates - $m^* > 3$. There was a notable difference between the ε_m from CHT and that from the simplified analysis model. This difference was attributed to the difference in the aerofoil geometry. To simulate a more realistic aerofoil, LE showerhead holes and TE slots were incorporated in the CHT double-wall aerofoil. This resulted in a lower overall volume-averaged metal temperature and hence a much elevated

cooling performance. Whereas, only the double-wall midchord section was considered when undertaking the metal temperature analysis using the simplified model in Chapter 3.

The ε_m from the simplified analysis model was also compared to the ε_m computed from an analytical equation, Equation 3.16 in Chapter 3, developed by Holland and Thake (1980). As has been described in Chapter 3, Holland and Thake (1980) extended Equation 3.13 (for a convection-cooled blade) so as to factor in both convection cooling and film cooling - Equation 3.16. ε_f in the Equation 3.16 was evaluated by taking an average of ε_f on both the PS and the SS. m^* was evaluated from Equation 3.14 and η_c computed following the procedure outlined in Section 3.5 of Chapter 3. There was a fairly accurate match between the ε_m from the theoretical equation of Holland and Thake (1980) and ε_m from the simplified analysis model, with the highest discrepancy between the two being 4% at $m^* = 9.2$.

The metal effectiveness results of C2 corresponding to a m*=4.7 from Figure 4.18 were extracted for comparison with the effectiveness results from some of the turbine blades available in the open literature in Holland and Thake (1980), the comparison results are shown in Figure 4.19. It should be noted that the circular pedestal blade design, C2 analysed in this Chapter has much lower overall metal effectiveness compared to diamond pedestal designs such as D2 - see Figure 3.17. It is expected that, at the same mass flow rate, better performing DWEC blade designs, for instance diamond pedestal blade design, D2, will be placed higher than C2 on the graph in Figure 4.19.

4.7.4 Blowing Ratio

Blowing ratio, M, is defined as the ratio of coolant flow mass flux to mainstream mass flux, and is defined in Equation 2.2. It is an important parameter that directly affects film cooling effectiveness of a cooling scheme design.

To evaluate the blowing ratio, the mainstream velocity and density were measured just outside of the cooling holes. The coolant side mass flux through each of the cooling holes was obtained by dividing the coolant mass flow rate by the cross sectional area of the film cooling hole. Figure 4.20 shows the blowing ratio distribution around the aerofoil corresponding to PR = 1.25. At this PR = 1.25, the pressure was high enough to force the coolant

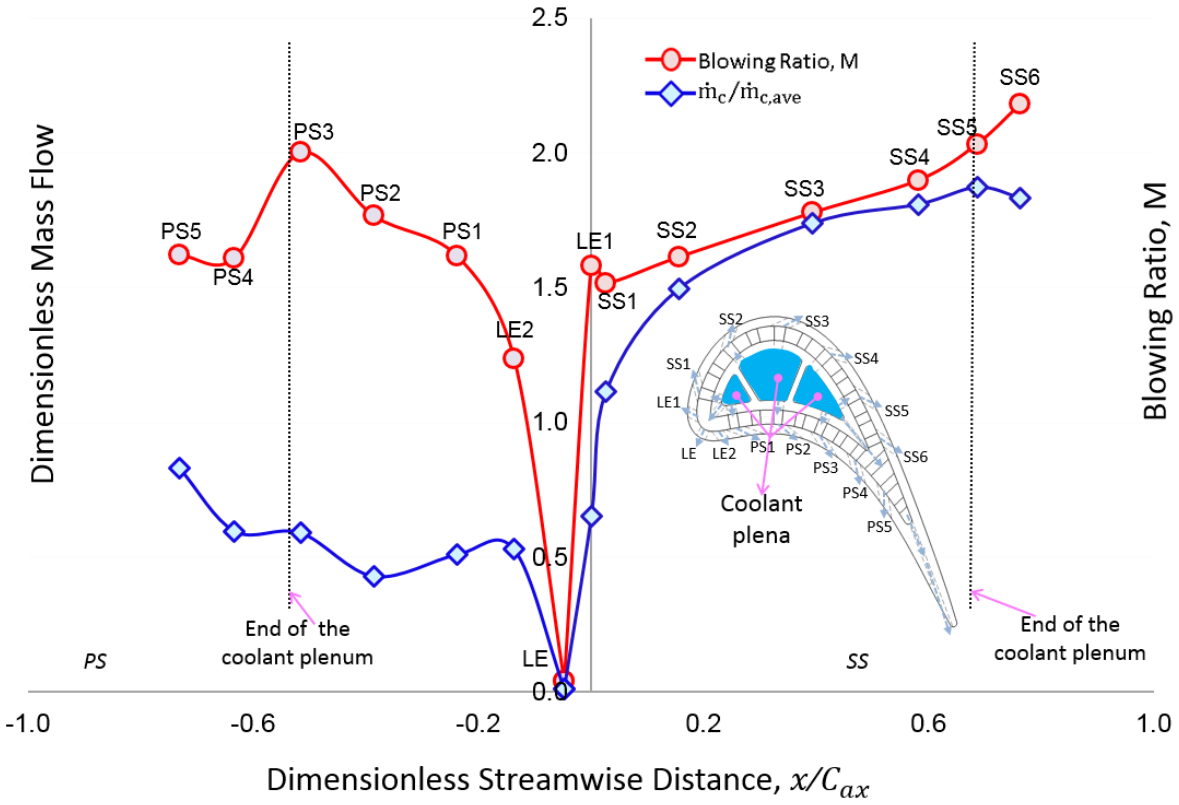

Figure 4.20: Blowing ratio and dimensionless mass flow distribution around the aerofoil for PR = 1.25

out of all the cooling holes, including the PS holes and the LE showerhead holes (albeit mass flow through the LE holes on the LE showerhead was almost zero). Figure 4.20 also includes the dimensionless mass flow, $\dot{m}_c/\dot{m}_{c,ave}$ corresponding to PR = 1.25. The dimensionless mass flow was computed by dividing the mass flow rate through each cooling hole by the average mass flow rate, $\dot{m}_{c,ave}$. The average mass flow rate was evaluated by dividing the total mass flow rate through the PS and the SS holes by the total number of holes on both the PS and the SS.

Both the SS and the PS show a similar trend - low blowing ratio in the vicinity of the LE (with almost no flow at the LE hole) then a gradual increase downstream up to PS3 on the PS and SS6 on the SS. Because of the nature of the external static pressure distribution around the aerofoil, as depicted in Figure 3.11, it was expected that blowing ratio of PS4 and PS5 should be greater than that of PS3. However, it was not the case since the coolant plenum ended at approximately 52% PS axial chord; just downstream of PS3, as illustrated in Figure 4.20. Thus, PS4 and PS5 did not have the high inlet coolant pressure that PS3 and

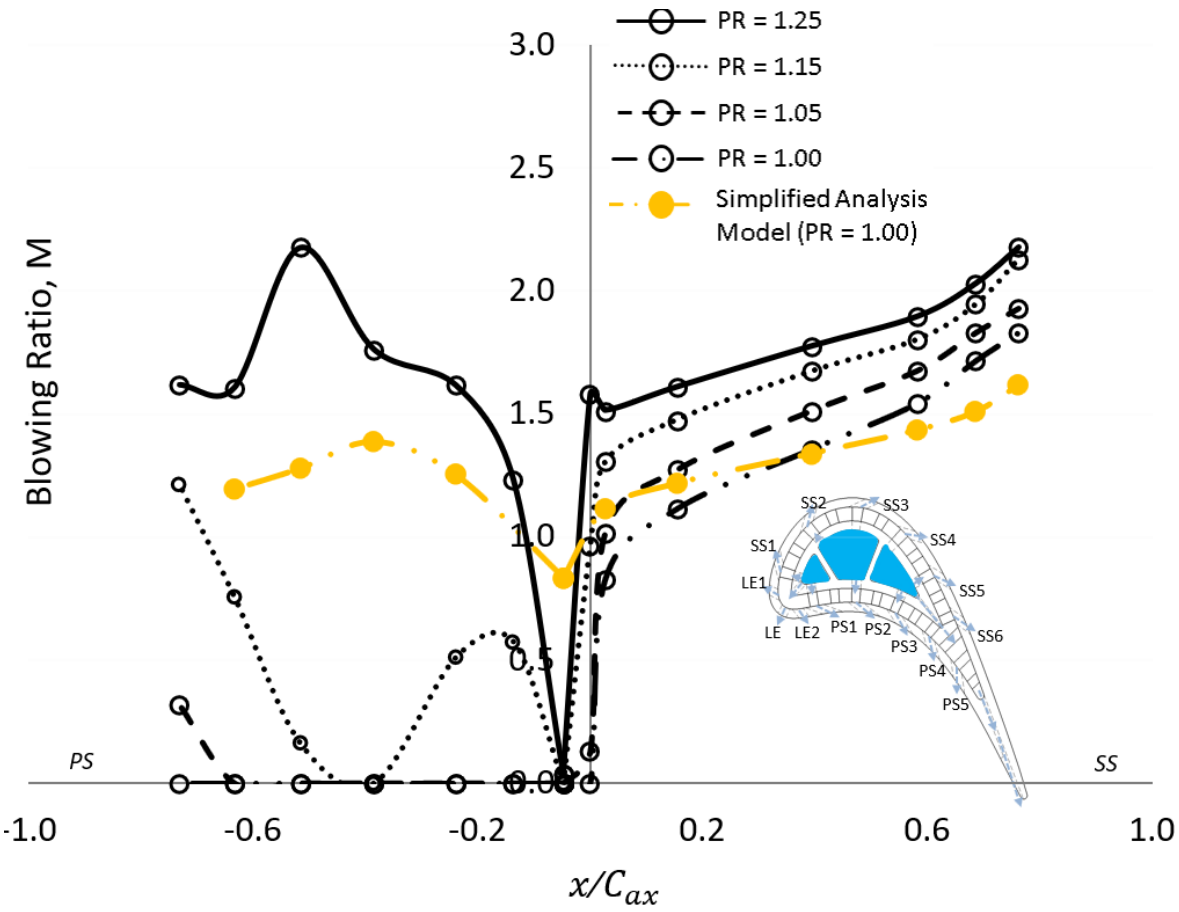

Figure 4.21: Blowing ratio distribution around the aerofoil at four coolant pressure ratios - PR = 1.00, 1.05, 1.15 and 1.25

other upstream PS holes had. The same applies to the SS holes - the coolant plenum ended at approximately 70% SS axial chord. But unlike the PS, the relatively high pressure margin on the SS caused the coolant flow through holes SS5 and SS6 (located downstream of the streamwise location where the coolant plenum ends) to still flow out at fairly high blowing ratios, with SS5 and SS6 attaining blowing ratios higher than the other upstream SS holes.

Figure 4.21 gives a comparison of blowing ratios at the four coolant pressure ratios corresponding to PR = 1.0, 1.05, 1.15 and 1.25. As aforementioned, the relatively lower external static pressure on the SS compared to the PS, shown in Figure 3.11, caused a significantly high pressure margin on the SS, resulting in high blowing ratio values on the SS holes. For all the tested PR, it was only LE1 on the SS, at the lowest PR = 1.0, that failed to allow coolant to flow through. The PS holes, however, suffered from low pressure margin - with no PS hole managing to allow cooling air to flow through at the lowest PR = 1.0. As the PR was increased, for instance at PR = 1.15, only the PS holes located at the vicinity of the highest

external static pressure - LE and PS2 that did not allow coolant to flow out. These two PS holes - LE and PS2 were observed to consistently exhibit the lowest blowing ratio across all the tested PR. There was a significant improvement, particularly on the PS2 and PS3, as the PR was increased to 1.25. At PR = 1.25, coolant was observed to flow out through all the PS and the SS cooling holes.

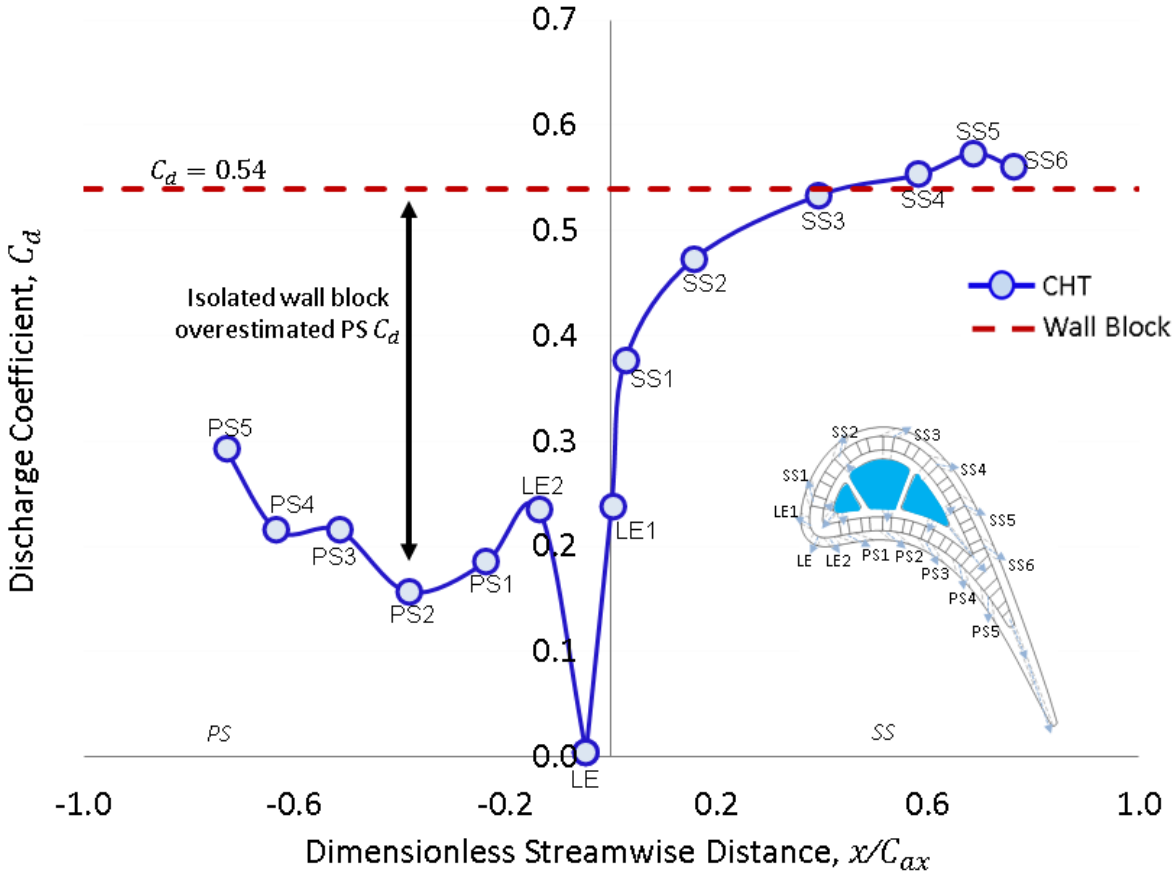

Figure 4.22: Discharge Coefficient from each of the PS and the SS cooling holes, corresponding to PR = 1.25, compared to the averaged C_d from an isolated wall block.

To compare the blowing ratio, M from CHT study undertaken here with the M from the simplified analysis model in Chapter 3, M corresponding to PR = 1.0 has been included in Figure 4.21. As aforementioned, the blowing ratio was evaluated from Equation 2.2. The coolant mass flux - numerator in Equation 2.2 was evaluated by dividing the mass flow rate by the cross sectional area of the cooling hole. The actual mass flow rate was taken as the product of discharge coefficient, C_d, and the ideal mass flow rate (calculated assuming an isentropic one-dimension expansion from the coolant total pressure inside the blade to the static pressure local to the cooling hole exit). On the SS, the C_d from the isolated wall

block predicted mass flow rate, and hence the blowing ratio, reasonably well - with the highest discrepancy in blowing ratio being 12%. On the other hand, the simplified model overestimated the C_d and hence the blowing ratio of the PS holes.

To confirm the overestimation of the PS C_d by the simplified analysis model, data from the CHT analysis undertaken here were used to calculate C_d of each of the PS and the SS cooling holes. The C_d was evaluated by dividing actual mass flow rate through the cooling hole by the ideal mass flow rate - Equation 3.2. The ideal mass flow rate was evaluated assuming an isentropic one-dimension expansion from the coolant total pressure inside the blade to the static pressure local to the cooling hole exit. Figure 4.22 shows the C_d of each of the PS and the SS cooling holes at coolant pressure ratio corresponding to PR=1.25. For comparison, an average C_d of Murray et al. (2017) wall block was included in Figure 4.22. From Figure 4.22, it is evident that the C_d from the simplified analysis model overestimated C_d of the PS holes; with the highest discrepancy of up to 71%. On the other hand, on the SS, there was a fairly accurate match between the CHT C_d and the simplified analysis model C_d, with the highest error being 7% on the double-wall midchord section of the aerofoil. The simplified analysis model was able to predict SS3 C_d with the highest accuracy; with only 1% discrepancy between the CHT C_d and wall block C_d. The overestimation of the C_d on the PS by the simplified analysis model seem to imply that the C_d from the simplified analysis model may not be used directly on the PS to estimate mass flow rate, and blowing ratio.

The drop of C_d on the PS compared to the SS can be attributed to capping mechanism. Capping mechanism, also referred to 'pinching' effect (Rowbury et al., 2001), has also been observed by other researchers to occur on the PS film cooling holes on an aerofoil where the external crossflows act as a lid partially blocking the PS film cooling holes. Rogers and Hersh (1976) has called this 'lid model' and they have showed that the external crossflow restricts the emerging flow from a cooling hole as would a lid attached to the upstream edge of an orifice. Hay and Benmansour (1983) and Gritsch et al. (1998) also noted a decreased C_d with external crossflow for streamwise inclined holes. The capping mechanism was demonstrated in Figure 4.23 - which was zoomed in from Figure 4.10 for the case of PR = 1.25. Figure 4.23 shows the tendency of the mainstream crossflow to close off the PS film cooling holes

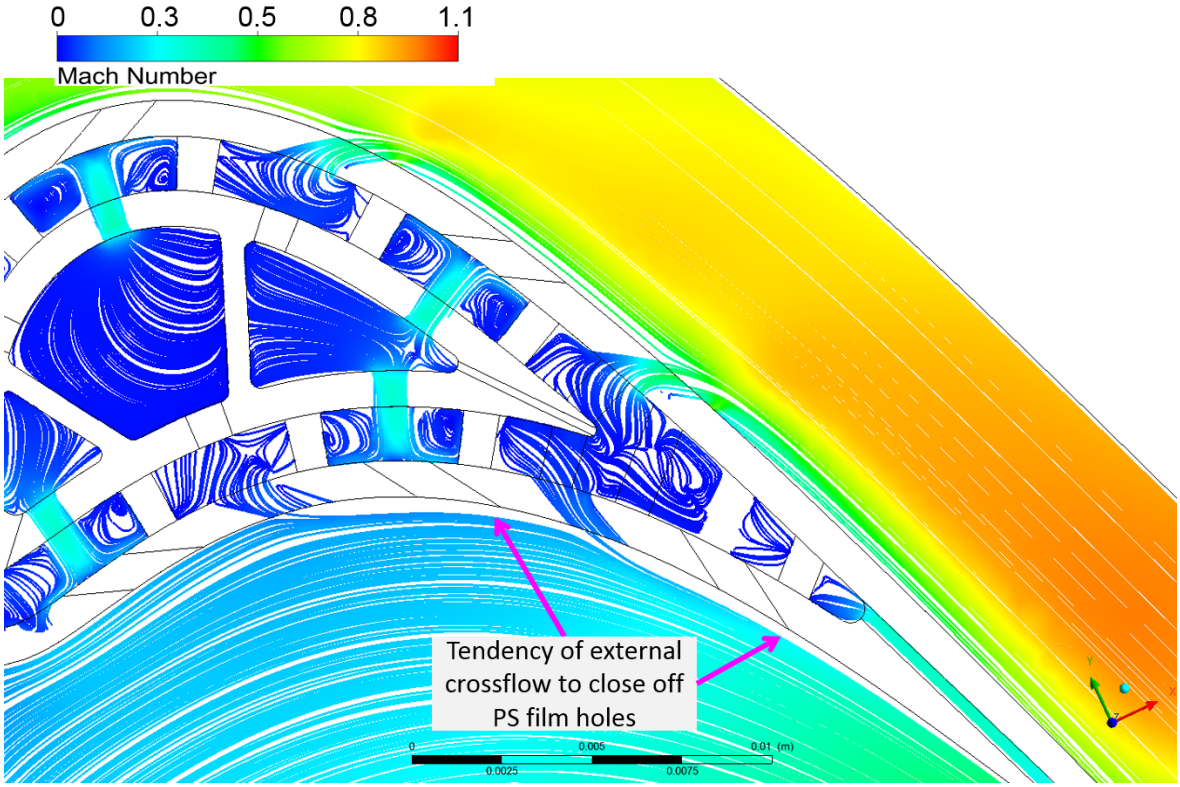

Figure 4.23: Flow streamlines coloured by Mach number showing the tendency of the crossflow to close off the PS film cooling holes

and hence limiting the coolant mass flow through the cooling holes. The capping mechanism was not observed on the SS film cooling holes.

4.7.5 Adiabatic Film Cooling Effectiveness

Film cooling effectiveness is a key performance parameter in any cooling scheme. To evaluate adiabatic film cooling effectiveness, ε_f CFD simulations in ANSYS[1] CFX were undertaken following the afore outlined procedure in Sections 4.3, 4.4, 4.5 and 4.6 of this Chapter. In this case, however, the solid domain was simulated as a low thermal conductivity plastic. A Polystyrene material available in the ANSYS[1] CFX material library (with a thermal conductivity of 0.033 $^{W}/_{m.K}$ (ANSYS, 2013)) was used. A low thermal conductivity solid material permitted adiabatic wall temperature, T_{aw}, to be measured near the external surface of the aerofoil. Adiabatic film cooling effectiveness, ε_f was then evaluated using Equation 4.2. To evaluate recovery temperature, $T_{r,\infty}$, in Equation 4.2, another CFD simulation in ANSYS[1] CFX was undertaken with only the mainstream flow - with no coolant flow. Coolant temper-

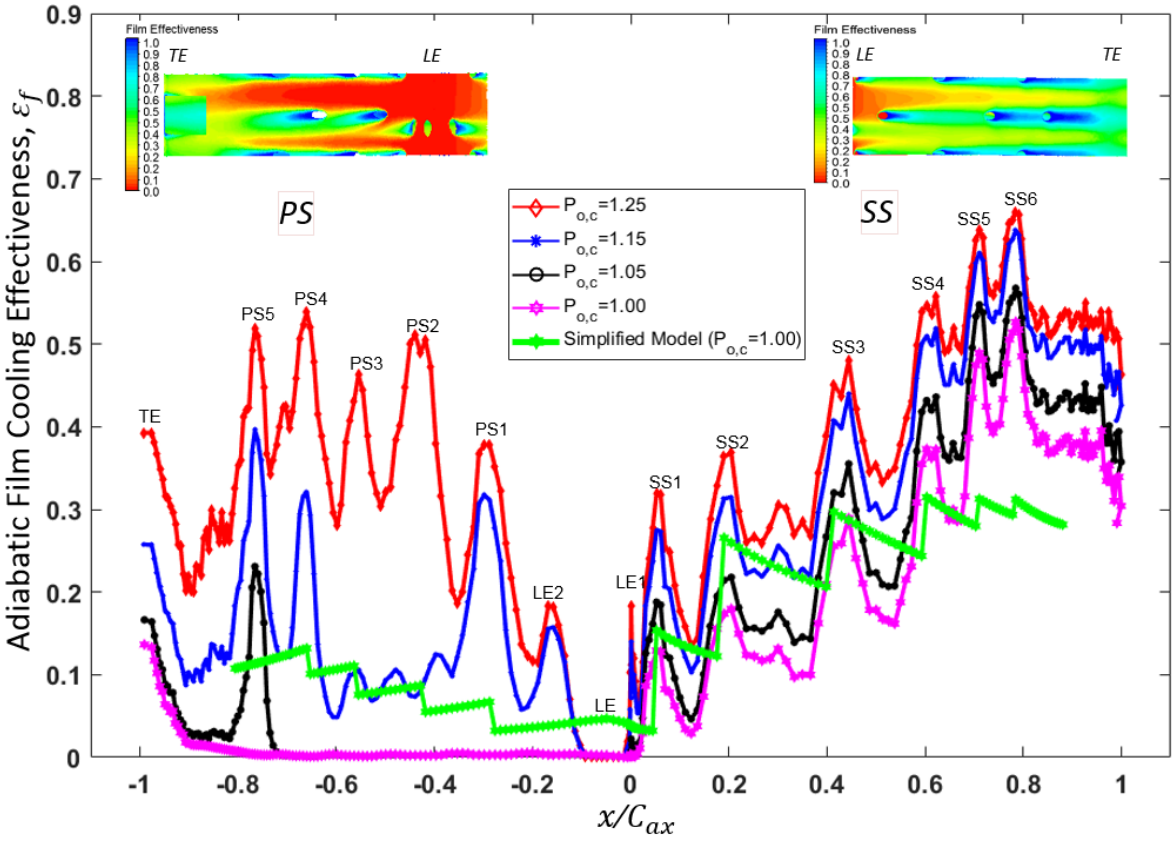

Figure 4.24: Laterally-averaged adiabatic film cooling effectiveness distribution on both the PS and the SS at four different coolant pressure ratios corresponding to PR = 1.00, 1.05, 1.15 and 1.25. Including a comparison to the ε_f from the simplified model in Chapter 3.

ature at the exit of the cooling hole, $T_{c,ex}$, was taken to be approximately equal to the coolant temperature at the coolant plenum inlet, $T_{c,in}$.

Adiabatic film cooling effectiveness was evaluated for four different coolant pressure ratios corresponding to PR = 1.00, 1.05, 1.15 and 1.25 as shown in Table 4.2. Figure 4.24 shows laterally (spanwise) averaged adiabatic film cooling effectiveness.There was an apparent strong relationship between blowing ratio and the adiabatic film cooling effectiveness. At low PR, relatively low pressure margin on the PS caused low blowing ratios and hence low film cooling effectiveness on the PS. On the other hand, at the same low PR, relatively high pressure margin on the SS caused relatively high blowing ratios and consequently, better film cooling effectiveness. In addition, increasing PR, and hence blowing ratio, caused ε_f improvement on both the PS and the SS. As the PR was increased further, very high blowing ratios on the SS resulted in film lift off from the surface. Consequently, there was an insignificant ε_f improvement on the SS when PR was raised from PR = 1.15 to PR = 1.25. On the

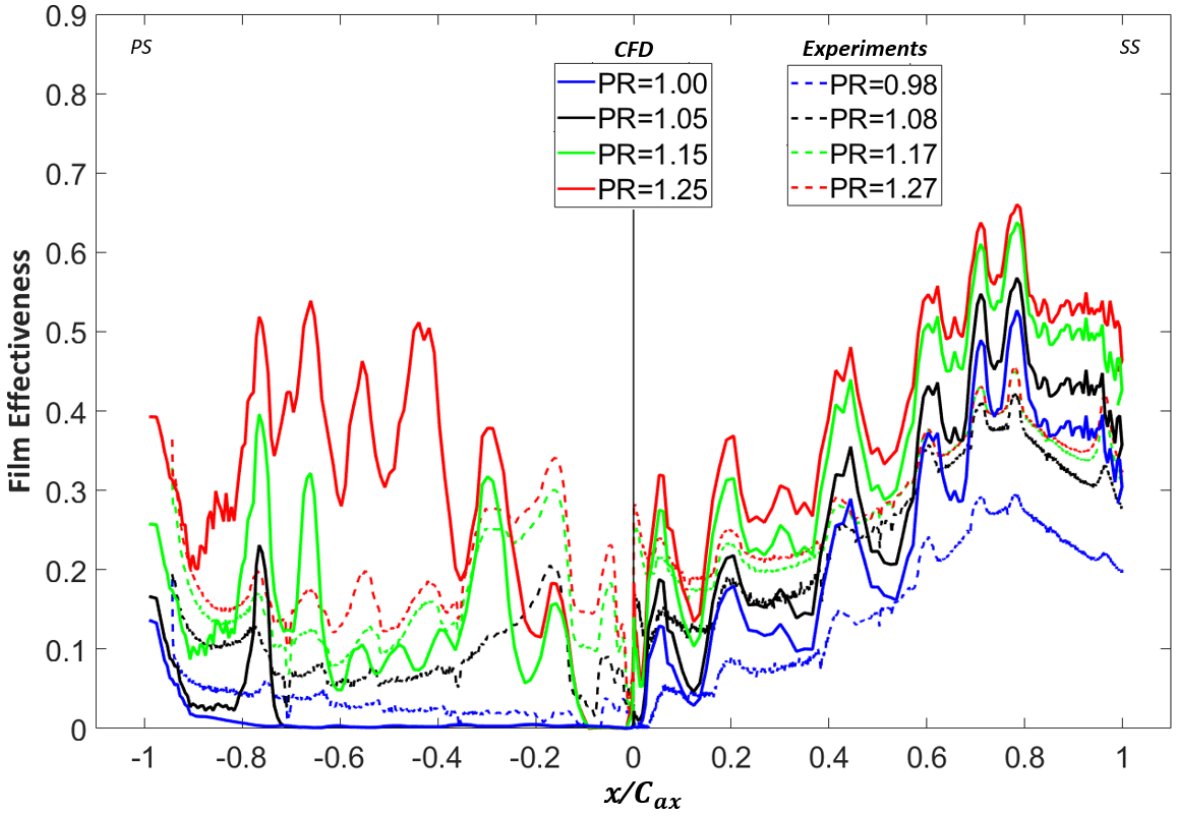

Figure 4.25: CFD laterally-averaged adiabatic film cooling effectiveness, ε_f compared to the ε_f from experiments

PS, however, higher blowing ratios as a result of PR increase, for instance from PR = 1.15 to PR = 1.25, caused a very significant improvement on the ε_f - as illustrated in Figure 4.24.

$$\varepsilon_f = \frac{T_{r,\infty} - T_{aw}}{T_{r,\infty} - T_{c,ex}} \tag{4.2}$$

The SS was found to suffer coolant jet lift off due to the high blowing ratios, resulting in poor ε_f performance unlike the PS which showed better performance at high blowing ratios. This observation is in line with the observation made by Rallabandi et al. (2010) when they experimentally studied the performance of a turbine blade at relatively high blowing ratios. They found out that the SS holes suffered greatly from coolant jet lift off at high blowing ratios, unlike the PS holes. In their studies, they found that the coolant jets began to lift off the SS beyond M $>$ 0.75 whereas on the PS, the coolant jets were still attached at M far greater than 1.00, and a complete lift off was only apparent at M = 4.0. The present author, through film cooling effectiveness tests detailed in Chapter 6, made the same observation; that the SS films were found adhere to the surface at low blowing ratios but suffered jet lift

Table 4.3: Pressure ratios used in the CFD and experiments and their corresponding coolant mass flow rates

	CFD		Experiments	
Case	PR	$\dot{m}_c/\dot{m}_\infty$ (%)	PR	$\dot{m}_c/\dot{m}_\infty$ (%)
1	1.00	3.7	0.98	1.6
2	1.05	4.6	1.08	3.4
3	1.15	6.2	1.17	4.5
4	1.25	7.8	1.27	5.5

off at relatively higher blowing ratios.

As previously discussed, the data from the isolated wall block employed during the simplified analysis outlined in Chapter 3 did not accurately predict C_d, and hence coolant mass flow rates and blowing ratios, see Figure 4.22. Consequently, the simplified analysis model over predicted the PS film cooling effectiveness. The simplified analysis model was only able to accurately predict SS film at the vicinity of SS3 to a reasonable accuracy - since the simplified model was able to accurately predict C_d, and hence blowing ratio of SS3.

The laterally-averaged adiabatic film cooling effectiveness, ε_f results from the CFD undertaken here were compared to the experimental ε_f results from Chapter 6 of this thesis. Four cases of total coolant pressure corresponding to PR = 0.98, 1.08, 1.17 and 1.27 from experiments were considered for comparison - as shown in Figure 4.25. Both the CFD and the experiments captured similar ε_f trends on both the PS and the SS: (1) better ε_f with increasing coolant mass flow rates, (2) PS ε_f poorer, than SS, at low PR but gets better at higher PR, (3) almost no film superposition on the PS unlike the SS.

CFD compared quite well with the experiments at moderate PR - for instance the case of PR=1.05 on the SS and PR=1.15 on the PS. At low and high PR, however, there were higher discrepancies between CFD and experimental results.

In general, CFD showed much higher ε_f values than experiments. This was thought to be caused, in part, by the difference in density ratio, ρ_c/ρ_∞. The experiments (see more details in Chapter 6) used nitrogen as coolant and air as mainstream and hence producing a density ratio of about 1.0. Whereas the CFD, given the flow conditions in Table 4.2, produced a density ratio of about 2.0 - approximately twice that from the experiments. The difference in density ratio was also reflected in difference in coolant mass flow, $\dot{m}_c/\dot{m}_\infty$ between the CFD and the experiments at almost similar PR, see Table 4.3. Coolant mass flow rate, $\dot{m}_c$ and mainstream mass flow rate, $\dot{m}_\infty$ were measured at coolant inlet section and mainstream flow inlet section respectively.

The CFD also predicted much higher ε_f at the vicinity of film cooling holes. Reynolds-Averaged Navier–Stokes equations (RANS) have been shown by other researchers (Gritskevich and Hohenstein, 2017) to have difficulties in accurately predicting ε_f near cooling hole exit. RANS models do not correctly predict coolant jet separation immediately downstream of the cooling holes [(Ames, 1998) and (Dyson et al., 2012)]. In addition, due to poor prediction of coolant diffusion by RANS models, film superposition on the SS was more pronounced in the CFD than in the experiments.

4.8 Conclusions

A fully coupled CHT analysis, using the commercial ANSYS[1], has been carried out on a circular pedestal DWEC turbine aerofoil. A strip from the blade span was extracted so as to reduce the computational time. Meshing was achieved using an ANSYS[1] unstructured mesh. The SST turbulence modelling available in ANSYS[1] CFX was employed. To the best knowledge of the author, this is the first time the analysis of the wall blocks have been extended onto an aerofoil. This research has also compared the performance of an isolated wall block subjected to a uniform external static pressure distribution and that which has been applied onto an aerofoil (to form a DWEC aerofoil) subjected to a varying external static pressure distribution. The general conclusion was that, the simplified analysis model predicted C_d, and subsequently other parameters such as mass flow rates, on the SS with reasonable accuracy but overestimated parameters on the PS - for instance of up to 71% on

C_d prediction. The implication of this is that, the isolated wall block data may be used to predict aerofoil SS performance but not the PS.

In addition, it was further noted that:

- Metal effectiveness improved with the increase in the coolant inlet total pressure, and hence the mass flow rates. The LE is located at the mainstream flow stagnation point where vortices are formed that augment heat transfer and the TE has a narrow shaped geometry and is exposed to a fully turbulent hot gas path causing both the LE and the TE regions of the aerofoil to exhibit low metal effectiveness, compared to the rest of the aerofoil surfaces, for all of the test PR. Simplified analysis model and isolated wall block $\varepsilon_m - m^*$ comparison showed a drop in the metal effectiveness performance of the isolated wall block when used on the aerofoil with a varying external static pressure.

- 3D streamlines visualised using Mach number provided some information about the flow interaction on the impingement/effusion cooled midchord section of the aerofoil. Showing the impingement jet impinging on the inner walls of the outer target surface at relatively high velocity, spent jet split and vortices and spent jet interaction resulting in re-impingement.

- Blowing ratio increased with an increase in PR on both the PS and the SS. Owing to a relatively low external static pressure, and hence relatively higher pressure margin on the SS, blowing ratio of the SS holes was generally higher than that of the PS holes at any given PR. The low pressure margin on the PS made it difficult for the coolant to flow out of the PS holes particularly at low PR - it was only at the highest PR=1.25 that the coolant was able flow out of all the PS holes. On the other hand, the high pressure margin on the SS caused the coolant to flow out of the SS holes, even at the lowest PR=1.0.

- As expected, the adiabatic film cooling effectiveness improved on both the PS and the SS with an increase in PR, and hence blowing ratio. At high blowing ratios, SS exhibited low film cooling effectiveness as a result of jet lift off. Whereas on the PS, better film cooling effectiveness was evident at high blowing ratios.

- Despite the difference in density ratio between the CFD and the experiment, CFD results compared well with the experiments and were able to capture similar ε_f trends on the PS and the SS. Inability of RANS models to correctly predict coolant diffusion led to ε_f over prediction around the vicinity of the film cooling holes and over prediction of film superposition on the SS.

4.9 Summary

This Chapter has described details of the fully coupled CHT simulation that was carried out to further analyse the DWEC. A circular DWEC aerofoil, C2, was considered for the simulations. To reduce the computational time, a strip from the blade span was extracted for use during the simulations. Meshing was achieved using ANSYS[1] unstructured mesh. SST turbulence modelling available in ANSYS[1] CFX was employed. The results and detailed discussion including internal and external flow structure, metal effectiveness, blowing ratio and adiabatic film cooling effectiveness have also been presented in this chapter.

The following chapter, Chapter 5, will provide details of the experimental facility and apparatus used for the film cooling effectiveness tests.

Chapter 5

EXPERIMENTAL FACILITY AND APPARATUS

5.1 Introduction

This Chapter describes in detail the experimental facility and apparatus used during the film cooling effectiveness tests. The experimental facility used for the film cooling effectiveness tests is the high-speed linear single-blade linear cascade that was designed and built by Wong (2018) for the LE and the TE studies. The present author was responsible for some alterations that were undertaken to achieve the desired test conditions for the current research. Section 5.2 gives the details of experimental facility, Section 5.3 gives details of the test facility operating conditions and Section 5.4 gives design details of the DWEC test blades. Section 5.5 gives design details of the CFVN and orifice plate that were used for measuring and controlling the coolant mass flow rate during tests.

5.2 High-Speed Single-Blade Linear Cascade

The experimental test facility used for the film cooling effectiveness tests (film effectiveness tests using PSP is given in details in the next chapter - Chapter 6) were carried out in a linear single-blade high-speed blowdown test facility. The test section inner surface walls were contoured to follow the mid-span streamline pattern midway between two adjacent turbine

rotor blades.

Table 5.1: Flow conditions, blade and cascade geometry

Approximate Scale Factor	2.0	**Inlet $\mathbf{P_{o,\infty}}$**	1.9 bar
Blade Axial Chord Length, C_{ax}	66.8 mm	**Exit Area**	32.5 mm x 100 mm
Inlet Area	57.6 mm x 100 mm	**Exit Flow Angle**	65.8°
Inlet Flow Angle	43.4°	**Exit $\mathbf{P_{s,\infty}}$**	1.2 bar
Inlet Ma	0.3	**Exit Ma**	0.7
Inlet Re	1.2×10^6	$\dot{\mathbf{m}}_\infty$	622 g/s
Test Section Pressure Limit, $P_{o,c}/P_{s,\infty}$	2.7		

The blade passage has a rectangular cross-section with a constant width (of 100 mm) throughout. The test section inlet area was 57.6 mm x 100 mm and reduced to 32.5 mm x 100 mm at the exit. Most parts of the test section were built from Perspex to permit maximum visibility of the test blade during PSP tests. To ensure both good structural integrity and optical access during the tests, the test section walls were built from a 20 mm thick Perspex (Wong, 2018). Both the engine Mach number and *Re* were matched during the tests. See Table 5.1 for a summary of the operating conditions, blade, and cascade geometry. Schematic diagrams of the stationary linear cascade with some details of the test facility and the test facility key components are shown in Figure 5.1 and Figure 5.2 respectively. Figure 5.3 shows a photograph of the test facility with the position of some of the key facility com-

ponents identified - its corresponding schematic diagram is as shown in Figure 5.4. Figure 5.5 shows a photograph of the rig test section with a cover used during PSP tests. The cover was used to block background light noises during the film effectiveness tests.

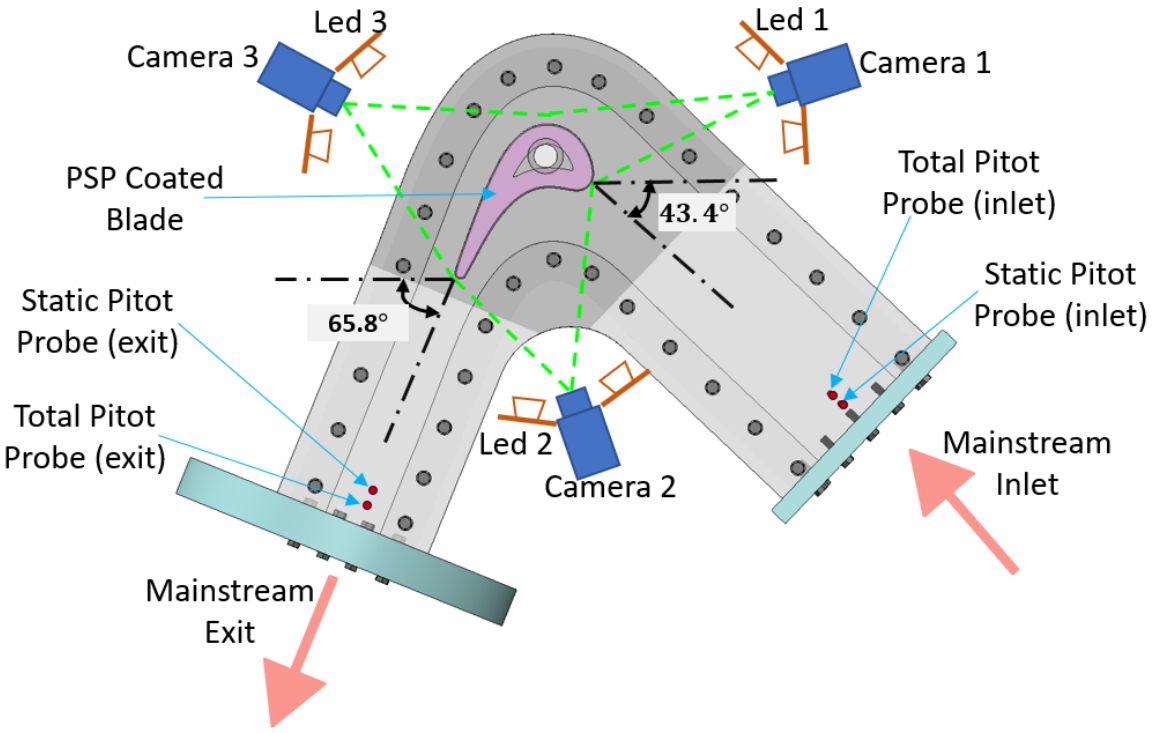

Figure 5.1: A simplified schematic diagram of the single-blade linear cascade.

5.3 Experimental Facility Boundary Conditions

The mainstream flow was supplied from a 400 Psig compressed air supply at ambient temperature. To ensure that the design flow conditions were realised at the test section, the compressed air flows through a regulator, an orifice plate and a honeycomb flow straightener before flowing into the test section. The compressed air then exhausts into the atmosphere through a butterfly valve. The inlet conditions were; Mach number of 0.3, and Re, based on the mainstream inlet velocity and passage height, equal to 1.2×10^6. An overall ratio of the inlet total pressure, $P_{o,\infty}$, to the exit static pressure $P_{s,\infty}$, of 1.6 was achieved. The coolant mass flow rate was altered by adjusting the inlet coolant total pressure, $P_{o,c}$. A summary of the test matrix is as shown in Table 5.2.

To continuously monitor the inlet velocity, pitot total and static pressure probes were

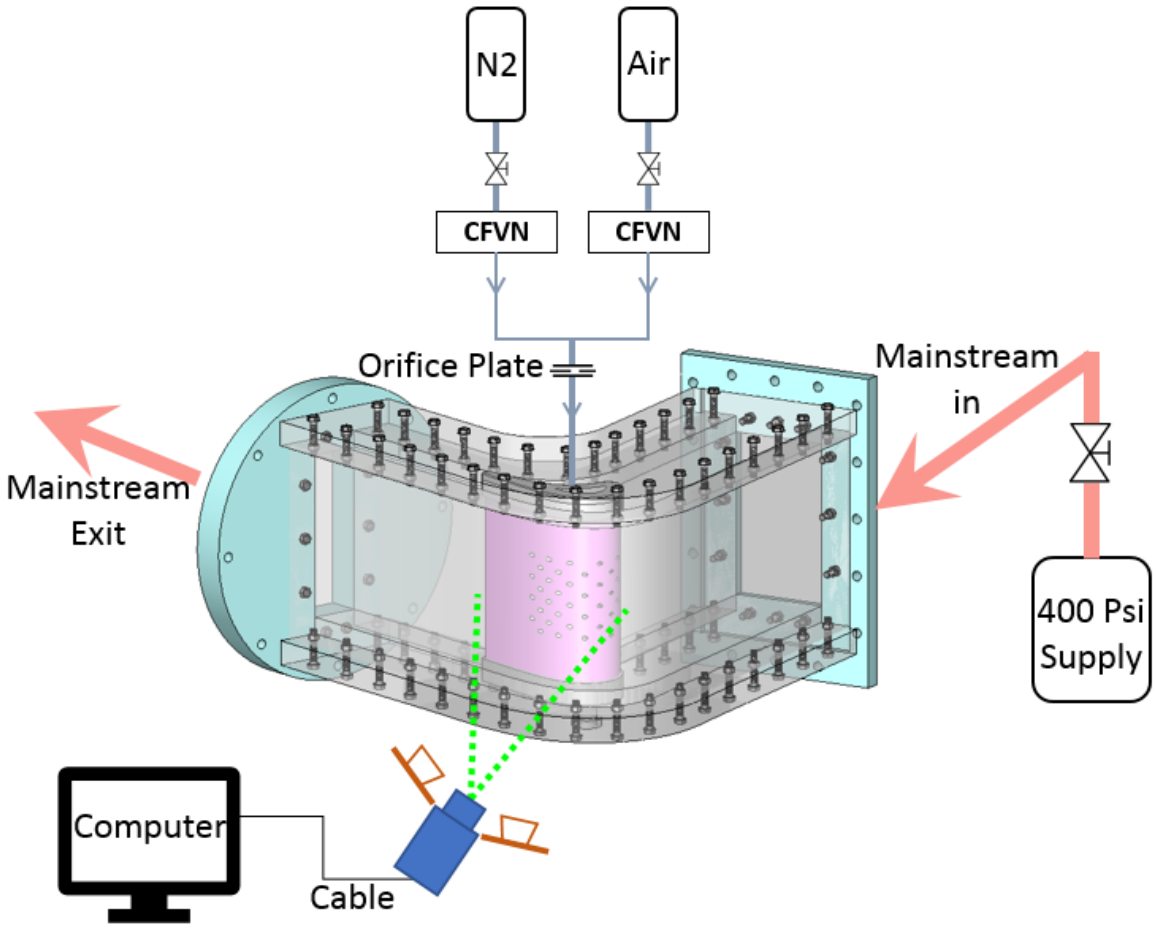

Figure 5.2: A simplified schematic diagram of the experimental test facility key components.

mounted upstream of the cascade. Both the pressure and temperature measurement systems were connected to National Instruments data acquisition (DAQ) cards installed in the workstation and measurements was logged via LabVIEW. The cooling air and nitrogen gas were supplied from 100 Psi reservoir and two compressed oxygen-free nitrogen 230 Psi gas cylinders respectively. Two CFVN and orifice plates were used to control the flow and the composition of the coolant. The coolant flowed through a long pipe to ensure mixing before the coolant arrives at the test section.

5.4 DWEC Test Blades

All of the test blades were made through Stereolithography, SLA. The blades have a constant area coolant feed passage with the tip end blocked with an end plate and the other hub end connected to the coolant supply. All of the cooling holes were cylindrical with a streamwise

Table 5.2: A summary of the test matrix

Blade	Test Number	$\dot{m}_c$ (g/s)	$\dot{m}_c/\dot{m}_\infty$ (%)	Pressure Ratio, $P_{o,c}/P_{o,\infty}$	Blade	Test Number	$\dot{m}_c$ (g/s)	$\dot{m}_c/\dot{m}_\infty$ (%)	Pressure Ratio, $P_{o,c}/P_{o,\infty}$
D1a	1	8	1.2	1.00	D3a	1	3	0.5	0.98
	2	10	1.5	1.03		2	5	0.8	1.15
	3	16	2.5	1.15		3	7	1.1	1.44
	4	20	3.2	1.30					
	5	27	4.3	1.51	D3b	1	3	0.5	0.95
						2	5	0.8	1.15
						3	7	1.1	1.42
D1b	1	8	1.2	1.00					
	2	10	1.5	1.03	C1	1	10	1.6	0.98
	3	16	2.5	1.20		2	16	2.6	1.04
	4	20	3.2	1.31		3	21	3.4	1.12
	5	27	4.3	1.56		4	28	4.5	1.27
D2a	1	8	1.2	0.98	C2	1	10	1.6	0.98
	2	10	1.5	1.04		2	16	2.6	1.02
	3	16	2.5	1.27		3	21	3.4	1.08
	4	20	3.2	1.52		4	28	4.5	1.17
						5	34	5.5	1.27
D2b	1	8	1.2	1.05	C3	1	10	1.6	1.09
	2	10	1.5	1.17		2	16	2.6	1.20
	3	16	2.5	1.43		3	21	3.4	1.36
	4	20	3.2	1.69					

inclination angle of 30° to the surface. The cutback-with-straight-lands TE slots (as shown in Figure 5.6) studied by Gurram et al. (2016) were used for TE cooling geometry for all of the test blades. Since the focus of this study is on the double-walled mid-chord section of the blade, the LE and the TE cooling holes configuration was kept the same in all the test blades. In order to avoid any tip and hub end-wall secondary flows, cooling features were constructed for a width equal to 60% of the blade span. Note that all the mid-chord region of all the test blades were built from the validated unit wall elements that were studied by Murray et al. (2017). For this initial study, each blade was built from one particular unit wall element.

All of the blade designs used a staggered pedestal arrangement. Impingement holes,

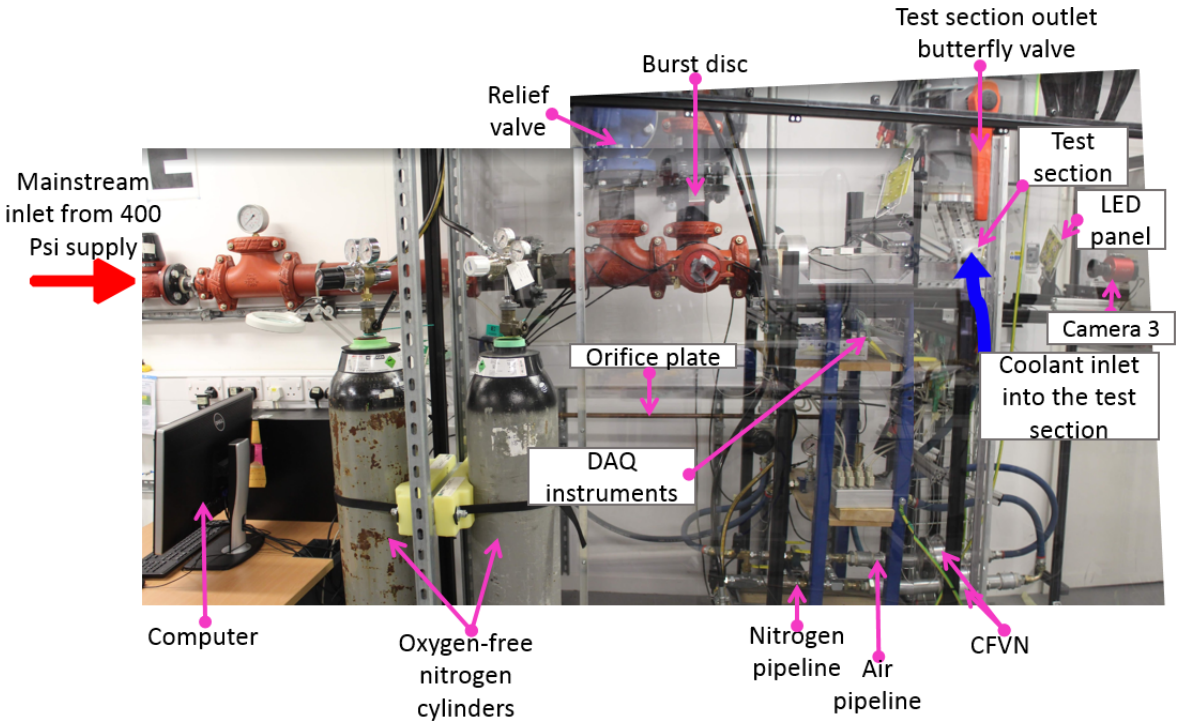

Figure 5.3: A photograph of the test facility showing position of the key facility components

attached to the inner skin, were also staggered with respect to the effusion holes on the outer skin. The passage height is essentially the distance between the inner and outer skin. Note that both the outer and inner skin have equal thicknesses which was kept constant for all the designs. Therefore, to alter the cooling passage height, the inner skin is moved in or out (the outer skin is not altered in order to maintain the original aerofoil external profile). Figure 5.6 shows a schematic diagram giving details of the LE and the TE hole configuration as well as the double-wall blade. The unit wall element geometry and definition of the geometrical parameters are as shown in Figure 3.14 and Table 5.3 respectively. The detailed design features for all the test pieces are as summarised in Table 5.3. The circular pedestals designs have circular pedestals while the diamond pedestal designs have diamond pedestals connecting the inner and outer skins in the mid-chord region of the DWEC blade.

5.4.1 Circular Pedestal Designs

In the circular pedestal designs, the LE showerhead cooling was achieved by employing a typical showerhead cooling holes configuration with three rows of compound angle cylindrical holes. Figure 5.7 shows a schematic diagram of film holes distributions on both the

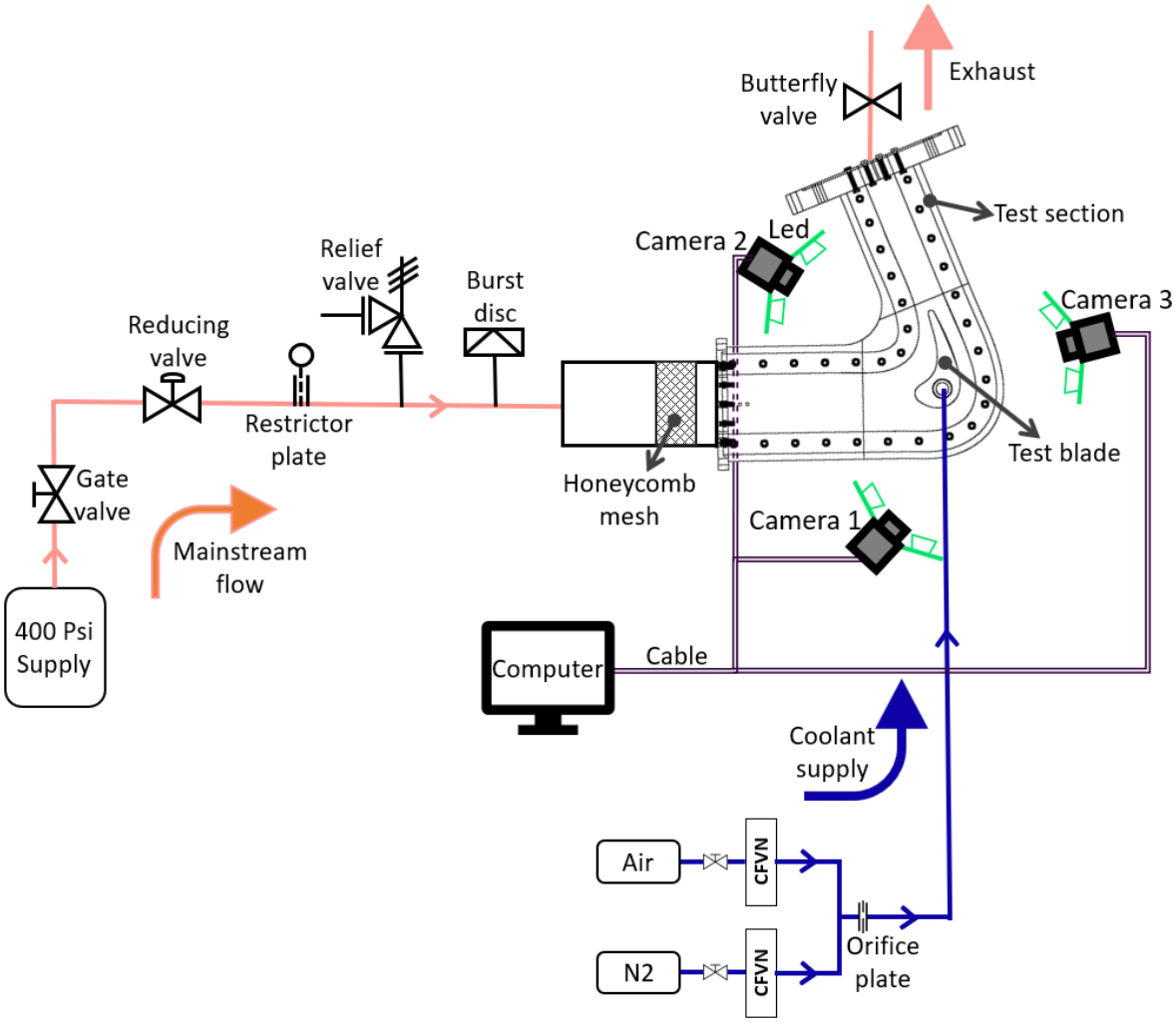

Figure 5.4: Schematic diagram of the test rig

PS and the SS of the circular DWEC blade. Table 5.4 gives the exact dimensionless streamwise locations of the rows of film holes on the blade. Note that the streamwise film hole row location is the same for all the three circular pedestal blade geometries.

5.4.2 Diamond Pedestal Designs

As aforementioned, there were a total of six diamond-pedestal DWEC blade designs tested - D1a, D1b, D2a, D2b, D3a, and D3b. It should be noted that, for any particular diamond pedestal design, the only difference between blades which include the letters a and b in the name is the size of the effusion hole diameter; 2.3 mm and 1.15 mm respectively. So that D1b, for instance, has exactly the same design features as D1a except for the size of the effusion hole diameter. It should be noted that the LE showerhead cooling holes configuration was used in

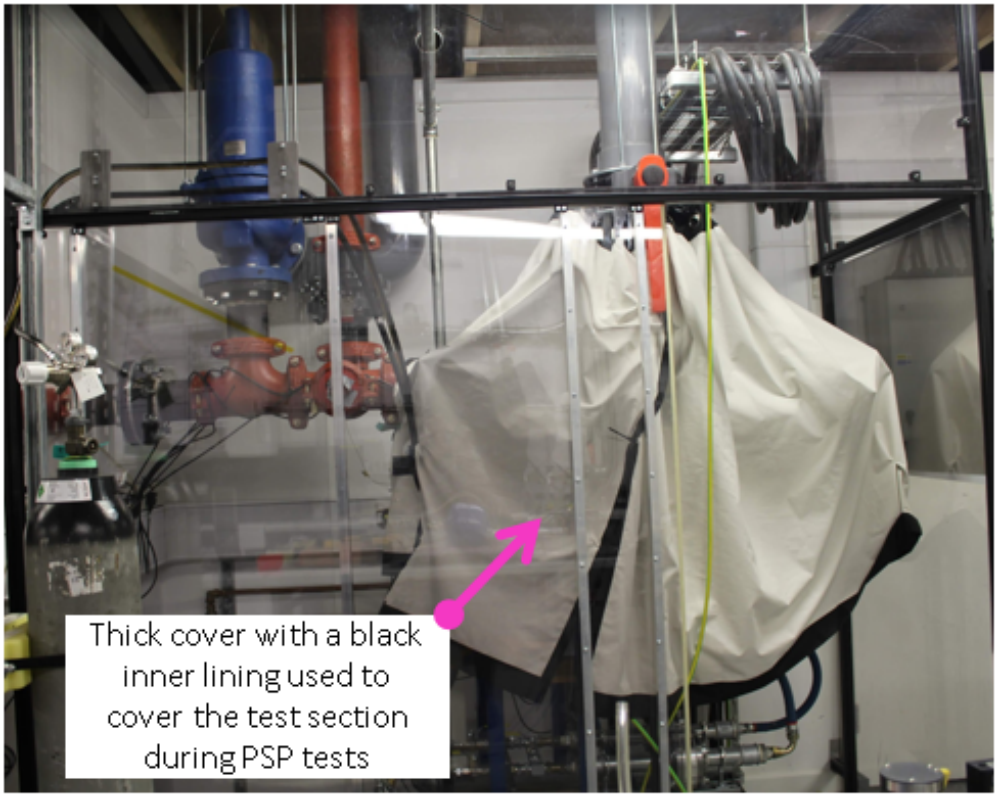

Figure 5.5: A photograph showing how the test section was covered during PSP tests

circular pedestal designs and not the diamond DWEC blade designs. The diamond pedestal designs had a simple one row of cylindrical cooling holes on the LE. Figure 5.8, Figure 5.9, and Figure 5.10 show schematic diagrams of film holes distribution on both PS and SS of the D1, D2, and D3 diamond pedestal DWEC blades respectively. Table 5.4 gives the exact dimensionless streamwise locations of the rows of film holes on the blades.

5.5 Flow Control and Measurement Devices

The coolant mass flow rate was controlled using CFVN and measured using an orifice plate. Both the CFVN and the orifice plate were installed in the coolant pipeline upstream of the blade, as shown in Figure 5.4.

5.5.1 Critical Flow Venturi Nozzle (CFVN)

Critical Flow Venturi Nozzles are sometimes referred to as sonic nozzles. Their main advantages over other flow meters include; excellent repeatability, a differential pressure measure-

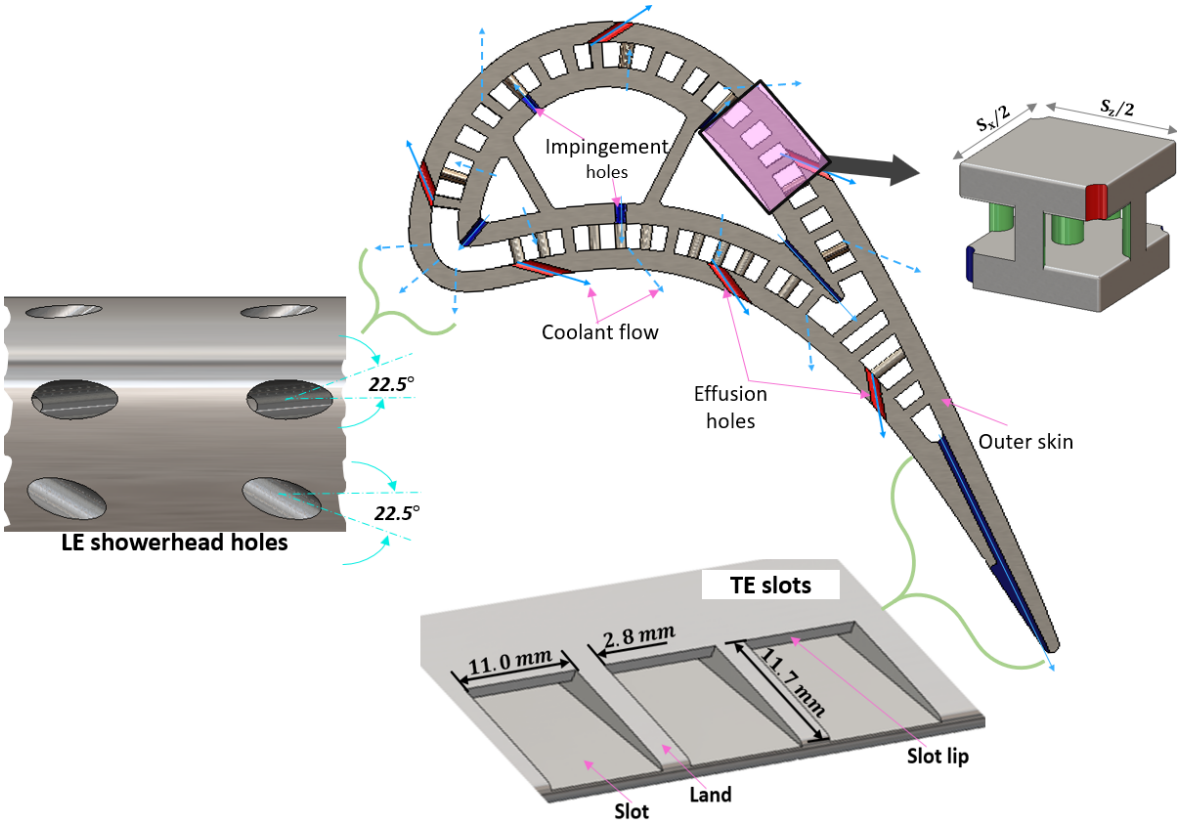

Figure 5.6: Schematic diagram showing LE and TE hole configuration as well as a sectioned DWEC blade, unit wall element and geometrical parameters

ment is not required, there are no moving parts, the flow rate is not affected by downstream flow disturbances and the mass flow varies linearly with inlet pressure. The following sub-sections give details of how the CFVN devices were designed and installed.

Design Considerations

The CFVN design was based on BS EN ISO 9300:2005 (BSI, 2005). A cylindrical-throat venturi nozzle that conformed to the Figure 5.11 as per the standards was chosen. The inlet plane of the nozzle is that plane which is tangential to the inlet contour of the CFVN and perpendicular to the nozzle centre-line. The convergent section of the CFVN inlet was designed as a quarter of a torus tangential on one end to the inlet plane and the cylindrical throat on the other end. The length of the cylindrical throat and the radius of curvature of the quarter of torus are all equal to the throat diameter. The parts were visually inspected to ensure that the connection between the cylindrical throat and the divergent section was free from any defects. The divergent section, with length greater than the throat diameter,

Table 5.3: The test blades design geometrical design details based on the unit wall elements from Murray et al. (2017)

Geometry Number	Passage Height, L_P (mm)	Pedestal Edge Length, L_2 (mm)	Pedestal Diameter , D_P (mm)	Pedestal Spacing, L_1 (mm)	Effusion hole diameter, D_f (mm)	Impingement hole diameter, D_i (mm)	Streamwise, S_x and Spanwise, S_z Effusion Hole Spacing (mm)	Dimensionless Streamwise, S_x/D_f and Spanwise pitch, S_z/D_f
D1b	1.15	1.15	--	1.15	1.15	1.15	13.0	11.3
D1a	1.15	1.15	--	1.15	2.30	1.15	13.0	5.7
D2b	3.45	1.15	--	1.15	1.15	1.15	13.0	11.3
D2a	3.45	1.15	--	1.15	2.30	1.15	13.0	5.7
D3b	3.45	1.15	--	3.45	1.15	1.15	26.0	22.6
D3a	3.45	1.15	--	3.45	2.30	1.15	26.0	11.3
C1	2.3	--	2.30	3.45	2.30	2.30	23.0	10.0
C2	3.45	--	2.30	3.45	2.30	2.30	23.0	10.0
C3	2.85	--	3.45	2.30	1.73	1.73	23.0	13.3

comprised a frustum of a cone with a half-angle of 3.5°.

Installation Requirements

The CFVN were installed in accordance with BS EN ISO 9300:2005 (BSI, 2005) guidelines for an upstream pipeline with a circular cross-section. The inlet conduit, D, was designed to be more than $4d$ (where d is the CFVN cylindrical throat diameter). The length of the circular upstream pipeline was set to be more than $3D$ as per the guidelines. The downstream circular pipeline was designed to be more than $2D$. This ensured that the outlet conduit did not restrict the flow. A total pressure probe and a thermocouple were installed on the upstream conduit at a distance $1.0D$ and $2.0D$ respectively. The downstream static pressure probe was installed on the outlet conduit at a distance $0.5D$ from the exit plane of the divergent section.

A total of four CFVN - two with d = 6 mm and two with d = 9.3 mm were designed and installed in the coolant flow pipeline. Two matched diameter CFVNs - one on the nitrogen line and the other on the air line were used for each experiment. The larger and smaller

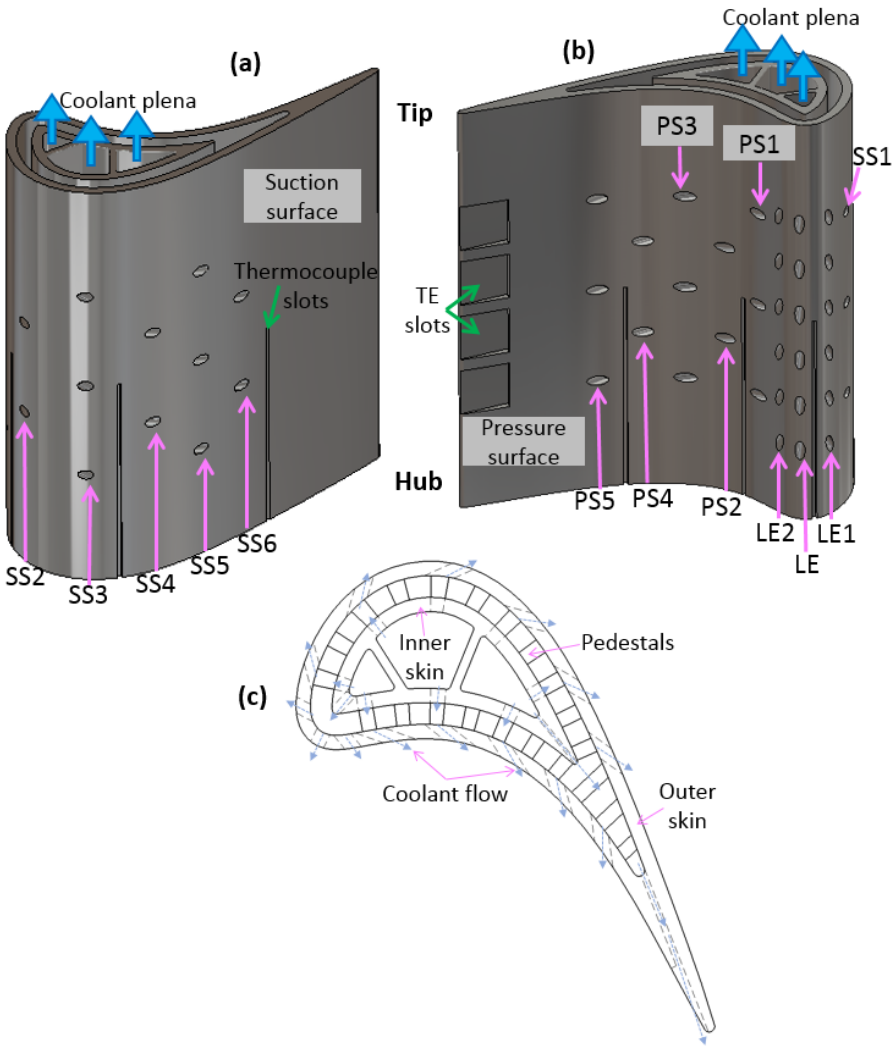

Figure 5.7: Film hole distribution on the C1, C2 and C3 DWEC circular blade (a) suction surface and (b) pressure surface, including (c) sectioned view

diameter CFVN were switched depending on the desired mass flow rate. Figure 5.12 shows a sectional view, front view and features of the quarter torus throat and divegent section of the $d = 9.3$ mm CFVN.

5.5.2 Orifice Plate Flow Meter

The orifice plate used for coolant flow measurements corresponded to a thin plate with a hole, diameter d, installed inside a pipe, diameter D.

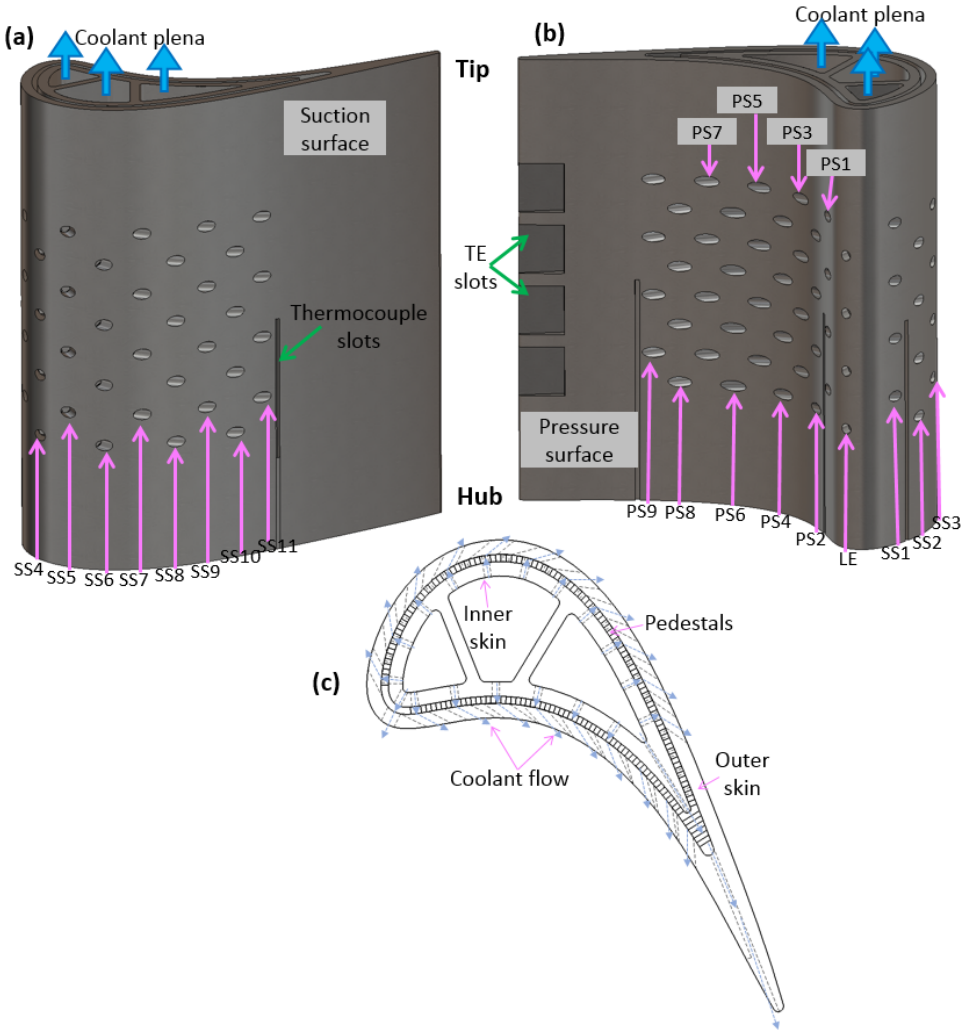

Figure 5.8: Film hole distribution on the D1a and D1b diamond pedestal DWEC blade (a) suction surface (b) pressure surface, including (c) sectioned view

Installation Requirements

An orifice plate with a D and D/2 tappings was used. The design specifications for this type of orifice plate requires the upstream pressure tapping and downstream pressure tapping to be installed at $L_1 = l_1/D = 1$ and $L_2' = l_2'/D = 0.47$ respectively. Two orifice plates with d = 5 mm and d = 13.7 mm were designed and installed. During tests, the big and small diameter orifice plates were swapped depending on the coolant flow rate being measured. The orifice plate installation along the coolant pipeline in the test facility is as shown in Figure 5.2 and Figure 5.3. Figure 5.13 shows the details of the orifice plate.

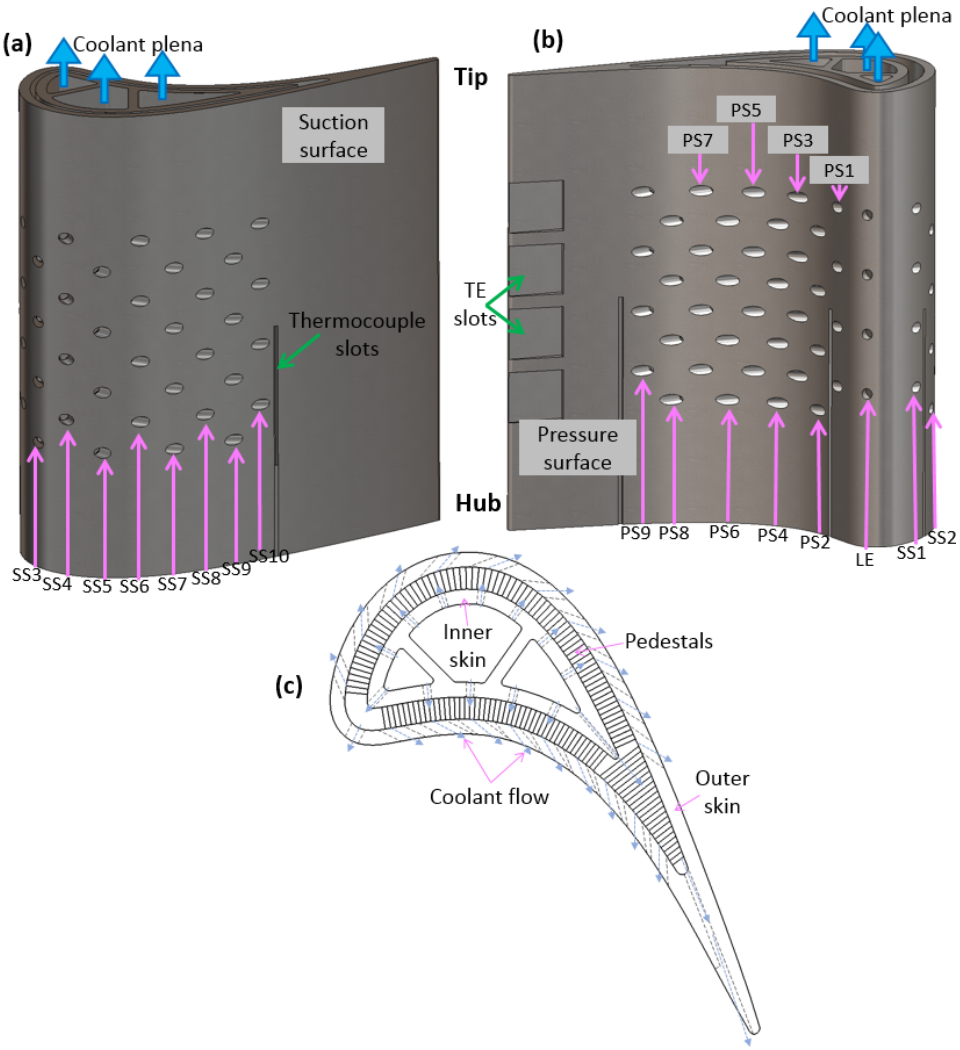

Figure 5.9: Film hole distribution on the D2a and D2b diamond pedestal DWEC blade (a) suction surface and (b) pressure surface, including (c) sectioned view

Discharge Coefficient

The Reader-Harris/Gallagher equation specified in ISO 5167-1 standard (ISO, 1991) was used to evaluate the discharge coefficient associated with flow through the orifice plate.

Expansibility Factor

The expansibility factor was evaluated using Equation 5.1 which is defined in the ISO standard ISO 5167-1 (ISO, 1991). Pressures p_1 and p_2 were carefully monitored, in LabVIEW, during tests to ensure that p_2/p_1 was always above or equal to 0.75 as Equation 5.1 is only applicable for $p_2/p_1 \geqslant 0.75$.

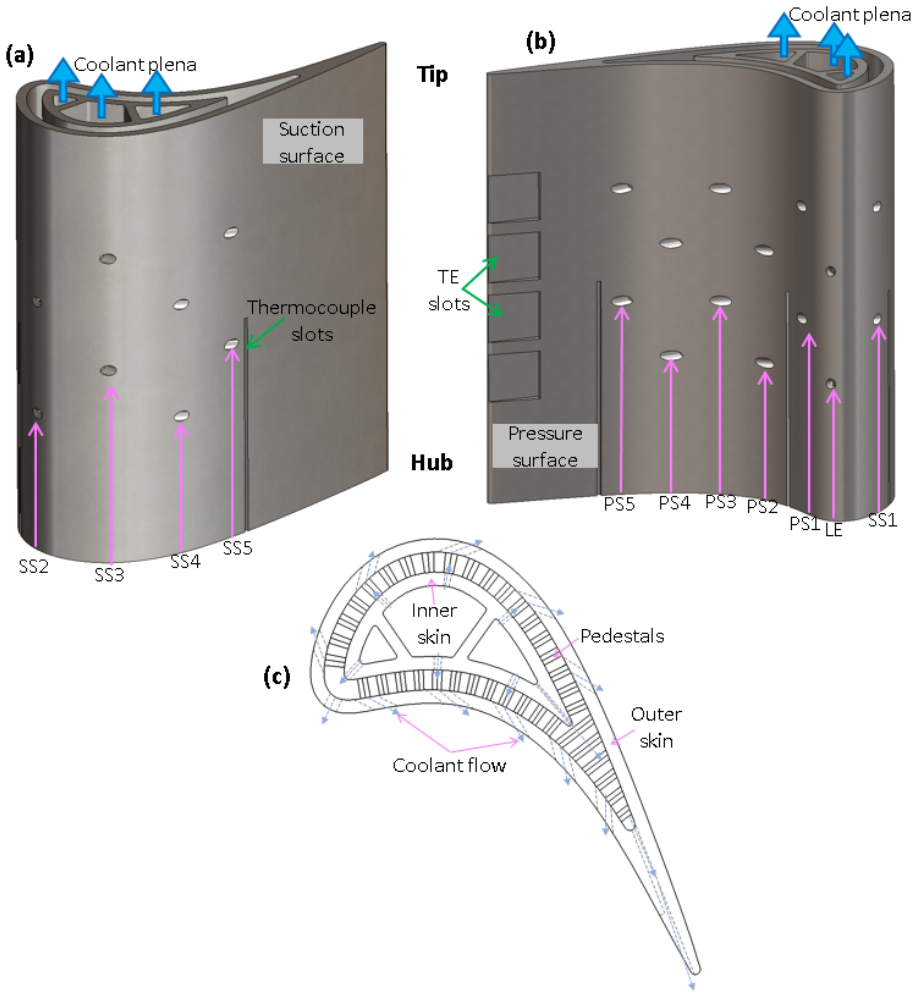

Figure 5.10: Film hole distribution on the D3a and D3b diamond pedestal DWEC blade (a) suction surface and (b) pressure surface, including (c) sectioned view

$$E = 1 - \left(0.41 + 0.35\beta^4\right)\frac{p_1 - p_2}{kp_1} \tag{5.1}$$

Mass Flow Rate Calculation

The mass flow rate through the orifice plate was calculated using Equation 5.2.

$$\dot{m}_c = C_d E \frac{\pi d^2}{4}\sqrt{\frac{2\rho(p_1 - p_2)}{1-\beta^4}} \tag{5.2}$$

5.5.3 Uncertainty Analysis

The uncertainties inherent in the experimental calculation of mass flow rate discharge coefficient were calculated using the small perturbation method of Moffat (1988). In the Moffat

Table 5.4: Dimensionless streamwise location of the film hole rows

Rows	x/C_{ax}			
	C1, C2, C3	D1a, D1b	D2a, D2b	D3a, D3b
LE	0.05	0.05	0.05	0.05
LE1	0.00	--	--	--
LE2	0.14	--	--	--
PS1	0.24	0.17	0.19	0.19
PS2	0.38	0.27	0.29	0.38
PS3	0.52	0.36	0.37	0.53
PS4	0.63	0.45	0.45	0.65
PS5	0.73	0.53	0.52	0.76
PS6	--	0.60	0.59	--
PS7	--	0.67	0.65	--
PS8	--	0.72	0.71	--
PS9	--	0.77	0.76	--
SS1	0.03	0.01	0.01	0.01
SS2	0.16	0.05	0.07	0.15
SS3	0.39	0.12	0.15	0.41
SS4	0.58	0.21	0.28	0.61
SS5	0.69	0.33	0.41	0.72
SS6	0.76	0.44	0.53	--
SS7	--	0.54	0.61	--
SS8	--	0.61	0.67	--
SS9	--	0.67	0.72	--
SS10	--	0.71	0.76	--
SS11	--	0.75	--	--

(1988) Small Perturbation method, each input parameter to the data reduction code used to evaluate the results is examined. Sequential perturbations to each one of those parameters are then introduced and the individual uncertainty contribution is measured.

R and X_i refer to the calculated result and input parameter of interest respectively (Moffat, 1988). The uncertainty from one single parameter on the calculated result is then expressed as in Equation 5.3

$$\delta R_{X_i} = \frac{\partial R}{\partial X_i} \delta X_i \tag{5.3}$$

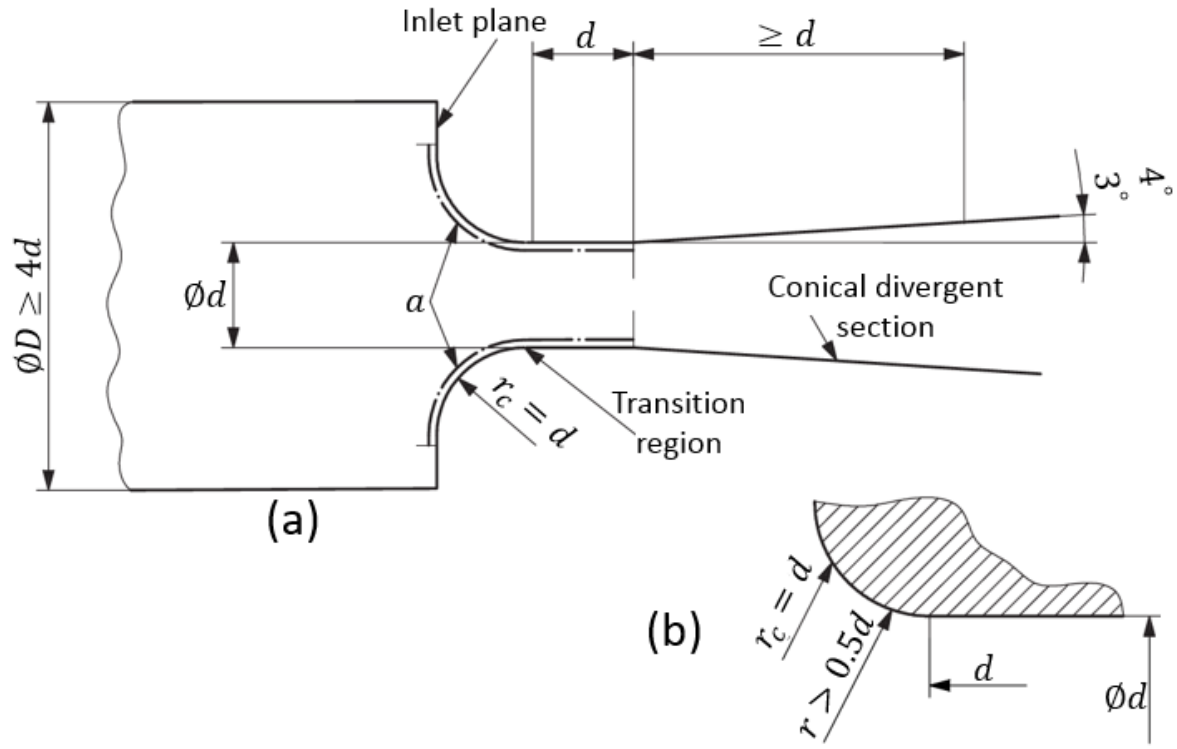

Figure 5.11: (a) Shows Cylindrical-throat Venturi nozzle and (b) details of connection between quarter of torus and cylindrical throat (BSI, 2005)

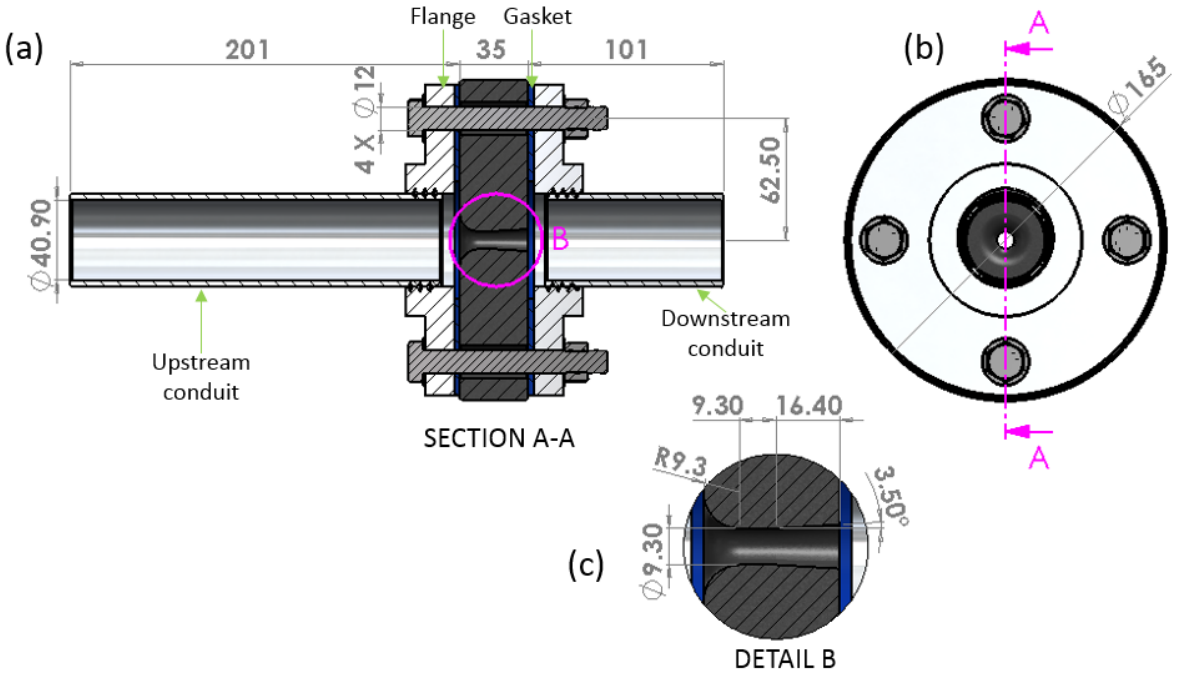

Figure 5.12: (a) Shows the sectioned front view (b) front view (c) and detailed quarter torus, throat and the divergent section of the d = 9.3 CFVN

Where δX_i and δR_{X_i} refer to levels of uncertainty for each parameter. The partial derivative of R with respect to X_i; $\partial R/\partial X_i$ is the sensitivity coefficient for the result R with respect

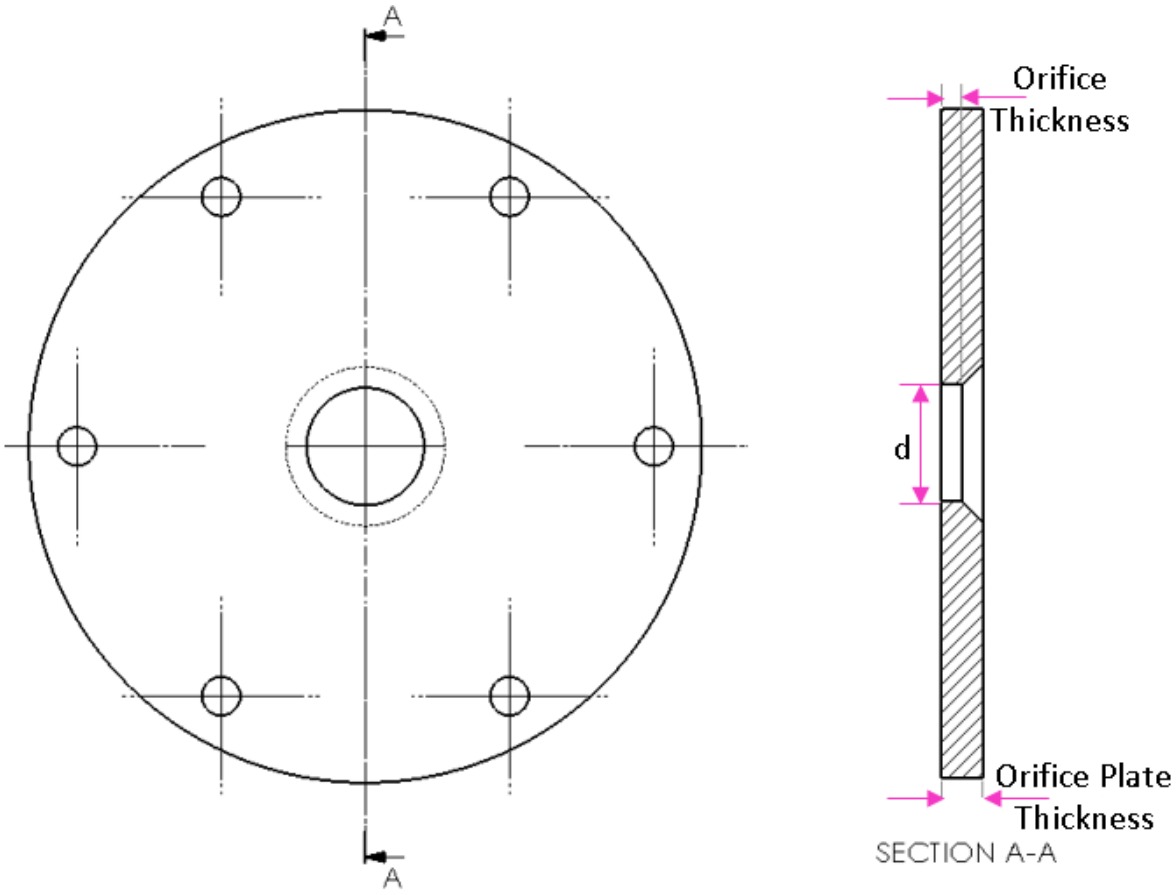

Figure 5.13: Orifice plate showing the front view and sectioned side view and some of the key features

to the measurement X_i (Moffat, 1988). It is common to express uncertainty in dimensionless terms - by dividing Equation 5.3 by the base value to form Equation 5.4. The base value is obtained using the original measured values for all the parameters.

$$\frac{\delta R_{X_i}}{R_o} = \frac{\partial R}{\partial X_i}\frac{\delta X_i}{R_o} \tag{5.4}$$

The mass flow rate is a function of more than one parameter, therefore, in order to combine all the individual uncertainties into one overall average uncertainty, Root Square Mean (RSS) method was used as shown in Equation 5.5

$$\delta R = \sqrt{\sum_{i=1}^{N}\left(\frac{\partial R}{\partial X_i}\frac{\delta X_i}{R_o}\right)^2} \tag{5.5}$$

The worst case uncertainty, Equation 5.6, was evaluated by summing up the absolute values of all individual uncertainties.

Table 5.5: Uncertainty analysis for low mass flow rate measurements from Small Perturbation method of Moffat (1988)

Parameter	Typical Values	δX_i	$\partial R/\partial X_i$	$(\partial R/\partial X_i)(\delta X_i/R_o)$
Hole Diameter [m]	0.014	0.00005	1.496	0.0093
Pipe Diameter [m]	0.020	0.00005	-0.210	-0.0013
Differential Pressure [Pa]	1209	60	0.000003	0.0248
Upstream Orifice Pressure [Pa]	205102	60	0.00000002	0.0001
Orifice Temperature [K]	295	1	0.00001	-0.0017
Discharge Coefficient [-]	0.650	0.004	0.012	0.0062
Mass Flow Rate Base Value [kg/s]	0.008			
			RSS Error	2.7%
			Worst Case	4.2%

$$\delta R_{worstcase} = \sum_{i=1}^{N} \left| \frac{\partial R}{\partial X_i} \frac{\delta X_i}{R_o} \right| \tag{5.6}$$

A central difference scheme, Equation 5.7, was employed to numerically solve the partial derivatives in Equation 5.3 and Equation 5.4.

$$\frac{\partial R}{\partial X_i} = \frac{R(X_i + \delta X_i) - R(X_i - \delta X_i)}{2\delta X_i} \tag{5.7}$$

Both the minimum and maximum values were considered for the mass flow rate uncertainty analysis. Table 5.5 and Table 5.6 show the contributions of individual parameters to the uncertainty level for low and high mass flow rates respectively. The representative uncertainty, RSS error, of the mass flow rate was between 1.2% and 2.7%. The worst case uncertainty of the mass flow rate was between 2.1% and 4.2%.

Film cooling effectiveness uncertainty was evaluated using the afore described small per-

Table 5.6: Uncertainty analysis for high mass flow rate measurements from Small Perturbation method of Moffat (1988)

Parameter	**Typical Values**	δX_i	$\partial R/\partial X_i$	$(\partial R/\partial X_i)(\delta X_i/R_o)$
Hole Diameter [m]	0.014	0.00005	6.357	0.0093
Pipe Diameter [m]	0.020	0.00005	-0.891	-0.0013
Differential Pressure [Pa]	19292	60	0.000001	0.0016
Upstream Orifice Pressure [Pa]	273798	60	0.0000001	0.0001
Orifice Temperature [K]	295	1	-0.0001	-0.0017
Discharge Coefficient [-]	0.613	0.004	0.055	0.0065
Mass Flow Rate Base Value[kg/s]	0.034			
			RSS Error	1.2%
			Worst Case	2.1%

Table 5.7: Uncertainty analysis for calibration curve parameter - P/P_{Ref}

Parameter	Typical Values	δX_i	$\partial R/\partial X_i$	$(\partial R/\partial X_i)(\delta X_i/R_o)$
P_{atm} [Pa]	101450	100	0.000	0.000
$P_{surface,test}$ [Pa]	10449	0.004	0.000	0.000
$\dot{m}_{c,air}$ [kg/s]	0.009	0.027	0.315	0.017
$\dot{m}_{c,N2}$ [kg/s]	0.009	0.027	0.611	0.034
P/P_{ref} [-]	0.492			
			RSS Error	3.8%
			Worst Case	5.1%

Table 5.8: Uncertainty analysis for low film effectiveness, ε_f measurements

Parameter	Typical Values	δX_i	$\partial R/\partial X_i$	$(\partial R/\partial X_i)(\delta X_i/R_o)$
$I_{air,ratio}$	1.28	0.006	0.960	0.051
$I_{N2,ratio}$	1.17	0.008	1.051	0.069
ϵ_f	0.12			
			RSS Error	8.6%
			Worst Case	12.1%

Table 5.9: Uncertainty analysis for high film effectiveness, ε_f measurements

Parameter	Typical Values	δX_i	$\partial R/\partial X_i$	$(\partial R/\partial X_i)(\delta X_i/R_o)$
$I_{air,ratio}$	1.15	0.003	-0.276	-0.0010
$I_{N2,ratio}$	0.46	0.002	0.694	0.0016
ϵ_f	0.78			
			RSS Error	0.2%
			Worst Case	0.3%

turbation method of Moffat (1988). Uncertainty in producing calibration curve (see Figure 6.2) was evaluated as follows: (1) uncertainty in calibration curve x-axis parameter, P/P_{Ref} was calculated at $P/P_{Ref} = 0.49$. There are four parameters that influenced P/P_{Ref}: reference atmospheric pressure, P_{atm}, oxygen partial pressure during test, P, air mass flow rate, $\dot{m}_{air}$ and nitrogen mass flow rate, $\dot{m}_{N2}$. Small perturbation was applied to these parameters and

RSS as well as worst case uncertainties were evaluated as shown in Table 5.7. RSS error was found to be 3.8% while worst case error was 5.1%. (2) uncertainty in calibration curve y-axis parameter, $I_{ratio}(=(I_{ref}-I_B)/(I-I_B))$ was calculated at $P/P_{Ref} = 0.49$. At $P/P_{Ref} = 0.492$, I_{ratio} was 0.69 and uncertainty was 1.2%.

Film cooling effectiveness uncertainty varied; low ε_f produced high uncertainty while high ε_f produced low uncertainty. Therefore, uncertainty in ε_f was evaluated at both low and high ε_f, as shown in Table 5.8 and Table 5.9 respectively. At low ε_f of 0.12, uncertainty was found to be 8.6% (RSS error) and 12.1% (worst case error) whereas at high ε_f of 0.78, uncertainty was found to be 0.2% (RSS error) and 0.3% (worst case error).

5.6 Summary

The details of the stationary single-blade linear cascade running at the engine realistic Mach number and *Re* has been described. This Chapter gave details of the test facility operating conditions as well as the design details of the DWEC blades that were used for PSP tests in Chapter 6. This Chapter also describes the design details of critical flow venturi nozzle and orifice plate meter including the CAD designs and installation procedure. The orifice plate meter mass flow calculation equation, mass flow rate uncertainty analysis as well as film cooling effectiveness uncertainty analysis are included in this chapter.

The next chapter - Chapter 6 - gives details of the film cooling effectiveness tests using PSP in the test facility which has been described in this chapter.

Chapter 6

FILM COOLING EFFECTIVENESS EXPERIMENTS USING PRESSURE SENSITIVE PAINT

6.1 Introduction

This chapter presents a detailed investigation into the film cooling effectiveness performance over the full surface of a double-wall effusion-cooled high-pressure turbine rotor blades using pressure sensitive paint, PSP. The tests were carried out in the high-speed linear cascade, running at the engine realistic Mach number and Re flows, described in Chapter 5. Section 6.3 gives details of the PSP methodology and Section 6.7 presents the test results in form of film effectiveness contour maps and laterally-averaged film cooling effectiveness. A detailed discussion of the results is given in Section 6.7. Conclusions are given at the end of the chapter.

6.2 Overview

A detailed measurements of film cooling performance for double-walled effusion-cooled blades is useful for both coolant consumption optimization and assessment of the success of the cooling designs at delivering the desired levels of the turbine blade film cooling ef-

fectiveness. Pressure Sensitive Paint, PSP is a commonly used method for evaluating film cooling effectiveness. The technique has been employed in studies of many different cooling configurations (flat plates, curved surfaces, rotor blades, and vanes) and under a wide range of test conditions (low to high-speeds, cold to hot flows) for engine combustor, turbine vane and rotor representative conditions. Some of the advantages the method possesses include; (1) PSP permits an accurate and spatially continuous film cooling effectiveness map over the whole component surface without disturbing the flow. (2) Lateral heat conduction related errors are eliminated and hence a clean and well-defined film effectiveness is achievable.

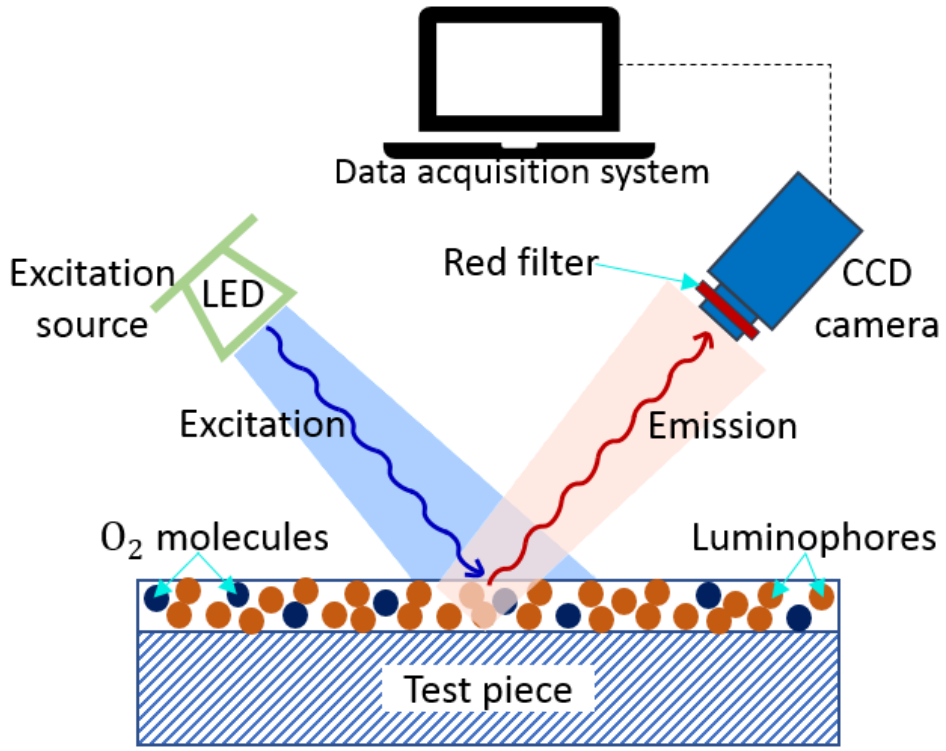

Figure 6.1: PSP setup and principle of operation

In this study, the PSP method was used to investigate the film cooling effectiveness of three large-scale circular pedestal and six diamond pedestal double-wall blade designs with varying pedestal size and spacing, and cooling hole size and spacing in a high-speed stationary single-bladed linear cascade operating at engine-representative Mach and Reynolds numbers flows. To simulate different blowing ratios (and putting into consideration the test section safety limit) all the samples were tested within a range of typical modern engine coolant mass flow, $\dot{m}_c$, to mainstream flow, $\dot{m}_g$, ratios as detailed in the Table 5.2. The film effectiveness results are presented in the form of film effectiveness contour maps and their

corresponding laterally (spanwise) averaged plots. In order to get an insight into the blade internal cooling and the influence of the different blade internal cooling features on the film cooling effectiveness and overall cooling effectiveness, the simplified numerical analysis approach, presented in Chapter 3, was applied to the test.

6.3 PSP Measurement Theory

PSP coatings constitute a compound that emits light when illuminated by a suitable source. When excited by ultraviolet light, the electrons in the oxygen-sensitive molecule change energy from the base to high-energy levels. When the molecules return to their original energy state, a longer-wavelength (red) light is emitted whose intensity is inversely proportional to the partial pressure of oxygen; a phenomenon called oxygen quenching (Je-Chin and Akhilesh, 2010). The emitted light is captured by a scientific grade cooled charge-coupled device (CCD) camera equipped with a red pass filter that filters out the exciting blue light, as shown in Figure 6.1. The intensity of the emitted light is related to the partial pressure of oxygen surrounding the PSP coated test surface using the Stern-Volmer Equation - Equation 6.1 (Tianshu et al., 2001).

$$\frac{I_{Ref} - I_B}{I - I_B} = A(T) + B(T)\frac{P_{O_2}}{P_{O_2,Ref}} \tag{6.1}$$

Where I_{Ref} is the reference intensity image captured at atmospheric conditions with the excitation lights on and without coolant and mainstream flow. The corresponding atmospheric pressure and atmospheric oxygen partial pressure are given by P_{Ref} and P_{O_2Ref} respectively. The so called black intensity image, I_B, is recorded with no illumination, no coolant flow and no mainstream flow, and the image I recorded with lights on, coolant flow on and mainstream flow on. $A(T)$ and $B(T)$ are the Stern-Volmer constants (Tianshu et al., 2001).

PSP is carefully sprayed on the whole surface of the test component (a white base paint is sprayed on the surface before applying PSP for SLA test pieces) with about four to eight coats over the area of interest. Four to eight layers ensure that the paint layer is thick enough

to offer ample cover of the test surface and not so thick that the paint peels off under flow. Oxygen-deficient gas, such as nitrogen, is used as a coolant. The oxygen-deficient gas reduces the local concentration of oxygen near the wall in regions of finite film cooling effectiveness. PSP senses this alteration in the concentration.

For a given configuration, four tests are required to determine the film cooling effectiveness distribution. For each of the tests, several images are acquired, and an average is taken to minimize instrumentation noise.

1. The Black image, I_B, is captured without the excitation LED light and with no mainstream and without coolant flow. Extraneous illumination, such as the room lights, is minimised.

2. The Reference Test image, I_{Ref}, is captured with the excitation LED lights switched on and at their normal operating temperature. There is no mainstream nor coolant flows for this case.

3. The Air Injection Test image, I_{air}, is captured with the excitation LED switched on. The mainstream is at test flow conditions and the coolant is flowing at the required blowing ratio. During this test, the resulting oxygen partial pressure and concentration fields are $P_{O_2,air}$ and $C_{O_2,air}$ respectively.

4. The Oxygen-deficient coolant injection test image, I_{fg}, is captured with the excitation LED on. The mainstream is on and oxygen deficient gas flows at the set desired blowing ratio. During this test, the resulting oxygen partial pressure and concentration fields are $P_{O_2,fg}$ and $C_{O_2,fg}$ respectively.

The analogy between heat and mass transfer enables Equation 6.2 to be written.

$$\varepsilon_f = \frac{T_{aw} - T_\infty}{T_c - T_\infty} \approx \frac{C_w - C_\infty}{C_c - C_\infty} \tag{6.2}$$

To apply the mass transfer analogy, Equation 6.2 is rearranged to form an equivalent expression but based on partial pressures of oxygen. During the Air Injection Test 3 and oxygen deficient gas injection Test 4, the concentrations are; $C_{O_2,air}$ ($= C_{O_2,\infty}$), and is a

constant value, and $C_{O_2,fg}$ respectively. In the latter case, the light emitted is of higher intensity since injection of the oxygen deficient gas reduces the local mass concentration of oxygen. During this oxygen deficient gas injection test, oxygen concentration, $C_{O_2,c} = 0$. Thereby, Equation 6.2 can be rewritten as in Equation 6.3.

$$\varepsilon_f \approx \frac{C_w - C_\infty}{C_c - C_\infty} = \frac{C_{O_2,fg} - C_{O_2,air}}{C_{O_2,c} - C_{O_2,air}} = 1 - \frac{C_{O_2,fg}}{C_{O_2,air}} \tag{6.3}$$

Equation 6.2 can be rewritten as in Equation 6.3 first in terms of mass fraction and then in terms of molecular weight and partial pressures to form Equation 6.4 (Je-Chin and Akhilesh, 2010).

$$\varepsilon_f = 1 - \frac{1}{1 + \left[\frac{P_{O_2,air}/P_{O_2,Ref}}{P_{O_2,fg}/P_{O_2,Ref}} - 1\right]\frac{W_{fg}}{W_{air}}} \tag{6.4}$$

6.4 Experimental Test Conditions

The PSP tests were carried out in the stationary single-blade high-speed flow blowdown test facility, described in Chapter 5. The mainstream flow was supplied from a 400 Psig compressed air supply at ambient temperature. To ensure that the design flow conditions were realised at the test section, the compressed air was passed through a regulator, an orifice plate, and a honeycomb flow straightener before flowing into the test section.

The cooling air and nitrogen gas were supplied from a 100 Psig lab utility and two compressed oxygen-free nitrogen 230 Psi gas cylinders respectively. Two CFVN and orifice plate (their design details have been outlined in Chapter 5) were used to control the flow and the composition of the coolant. The coolant flowed through a long pipe to facilitate mixing before it was fed into the test section. A detailed description of the experimental test facility, including its key features, can be found in Chapter 5.

All the samples were tested within a range of typical modern engine coolant mass flow rate, $\dot{m}_c$ to mainstream mass flow rate, $\dot{m}_g$ ratios as detailed in the Table 5.2. Table 5.2 also contains a column of pressure ratio, of each test blade at every test mass flow rate, calculated by diving the inlet coolant total pressure, $P_{o,c}$, by the cascade exit static pressure, $P_{s,\infty}$.

6.5 PSP Instrumentation and Measurement Procedure

UniFIB[4] PSP used for the current study, has an excitation range of 380-520 nm and an emission range of 620-750 nm. The blades were coated with a white base coat and then carefully sprayed with four coats of Uni-FIB PSP with an airbrush. The four coats ensured that the paint layer was thick enough to offer ample cover on the test surface and not too thick that the paint peeled off. The excitation of the PSP coat was achieved using a panel of 400 nm LED lights. The emitted light intensity distribution from the PSP was then recorded using a monochrome, cooled CCD camera fitted with a 610 nm long pass filter. Three cameras, one for the whole of the PS and two for the SS (see the schematic diagram of the test section setup in Figure 5.1 in Chapter 5), were used to view the complete blade surface. The film cooling effectiveness data from each individual camera were post-processed and combined to form a complete picture of the variation of film effectiveness over the blade surfaces. Two CFVN (one in the air pipeline and the other in the nitrogen pipeline, as shown in Figure 5.2 in Chapter 5) and an orifice plate flow meter were used to adjust, control, and measure the coolant flow rates.

PSP coated test pieces were calibrated in-situ to minimize bias errors. The calibration was performed in two steps. For $P/P_{Ref} > 1$, the test section was pressurised with air at ambient temperature and 26 calibration readings were taken between 0.9 bar(g) and 0 bar(g) to cover the range of air pressures experienced on the blades during tests. Two reference images were taken - one before the start of the calibration and one at the end. An I_{Ref} image for each calibration image was obtained by interpolating between the two reference images. The interpolation allowed the minor photodegradation effects of the PSP to be accounted for. To achieve $P/P_{Ref} < 1$, air and nitrogen were mixed in different proportions and about eight calibration images, including their corresponding reference images, were recorded. A dark image, I_B, was taken at the end of the calibration.

For each of the aforedescribed calibration images, 30 TIFF (tagged image file format) intensity images were captured by the camera at a rate of 5 frames per second. During post

[4]From Innovative Scientific Solutions Inc., ISSI Supplied by Aircraft Research Association Limited, Bedford, UK

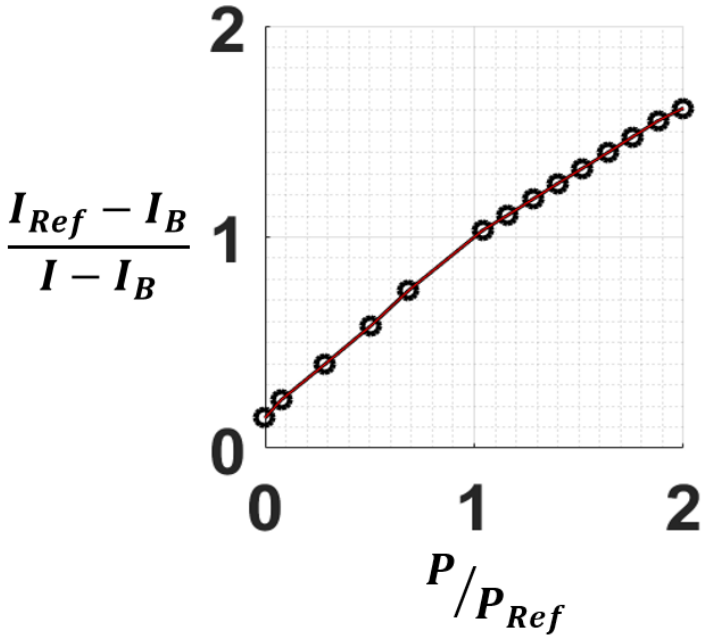

Figure 6.2: PSP calibration curve

processing, these images were averaged to give a mean intensity image. A calibration curve was prepared using the collected intensity images and the pressure data. Figure 6.2 shows an example of a calibration curve obtained during one of the blades calibration process. During the film effectiveness tests, each experiment involved taking four intensity measurements - black, reference, air and N_2 to capture I_B, I_{Ref}, I_{air}, and I_{N_2} respectively as described above. After, the film effectiveness was evaluated using Equation 6.4. A MATLAB[2] code was written by the author to convert the pixel intensities into pressure using the calibration curve and then into film cooling effectiveness. Section 6.3 of this chapter gives further details of the image intensity capture process and film effectiveness calculations.

6.6 Errors and Uncertainties

Uncertainty in film cooling effectiveness was evaluated following the Small Perturbation method of Moffat (1988) that has been described in Chapter 5. The greatest uncertainty in film cooling effectiveness measurements was found to be greatest at low ε_f and least at high ε_f. At low ε_f of 0.12, uncertainty was found to be 8.6% (RSS error) and 12.1% (worst case error) whereas at high ε_f of 0.78, uncertainty was found to be 0.2% (RSS error) and 0.3%

[2]www.matlab.com

(worst case error).

The possible sources of errors and how they were minimized are discussed in the Subsections 6.6.1, 6.6.2, 6.6.3 and 6.6.4.

6.6.1 Optical-Related Errors

A total of 30 images were recorded during each test. The images were then averaged to eliminate errors stemming from random camera noise and minor fluctuations in excitation light intensity. Furthermore, the excitation lights were switched on for about 30 minutes prior to testing to ensure that the light intensity stabilized before tests. A black (no-excitation, no flow) image was used to cancel out any constant offset camera noise. Unwanted reflections in the image intensities were subtracted during post processing of the data. An image intensity of an uncooled patch was averaged and subtracted from both the I_{air} and I_{N_2} during post processing in the MATLAB[2] code.

6.6.2 Calibration

In order to minimize bias errors, the test pieces were calibrated in-situ. To improve calibration accuracy, many pressure conditions, and corresponding image intensities, were recorded during calibration; typically more than 25. These images were used to compute the best fit polynomial, see Figure 6.2. The calibration was done on the day of the tests so that errors due to PSP photodegradation were minimized. In addition, during the post processing of the calibration images, the drop in intensity of the LED was factored in. As aforementioned, two reference images were taken - one before the start of the calibration process and one at the end. An I_{Ref} image for each calibration image was obtained by interpolating between the two reference images.

6.6.3 PSP Sensitivity to Temperature

The reference and black images were captured immediately after the tests were completed. Care was taken to ensure that N_2 and air were always at the same temperature during tests.

6.6.4 Heat to Mass Transfer Analogy Limitations

The mass transfer analogy holds only when the turbulent Lewis number is equal to 1. The flows in this experiment were turbulent and thus this was a good approximation.

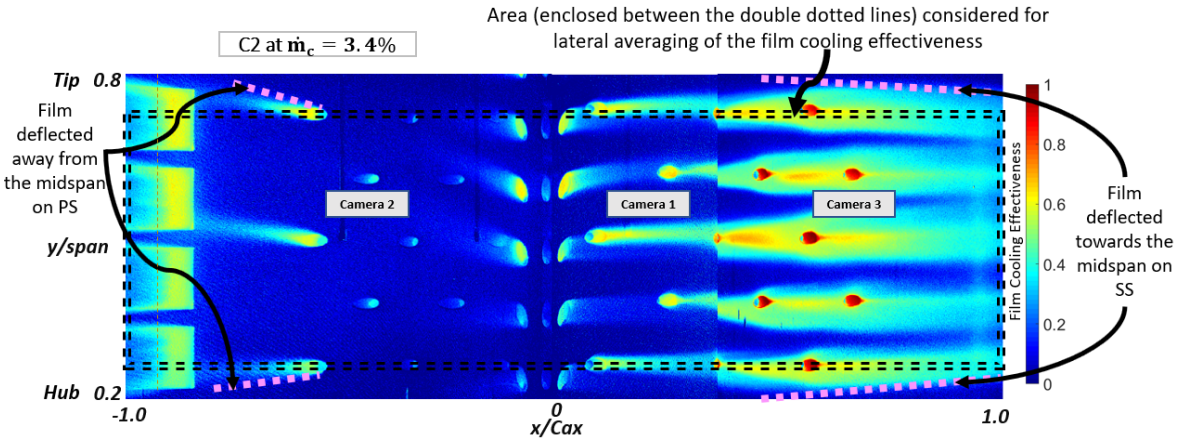

Figure 6.3: A summary of the general film structure on the PS and SS of the test blades

6.7 Results and Discussion

The following Subsections 6.7.1, 6.7.2, 6.7.3 and 6.7.4 present the post-processed film cooling effectiveness data from the PSP tests and a detailed discussion of the results.

6.7.1 Film Structure on the Pressure and Suction Surfaces

The film effectiveness levels and distribution over the aerofoil surface varied over the blade geometry as well as with coolant flow rate. Passage vortices (emanating from the pressure-side LE and travelling towards the suction surface and towards the passage exit) are known to be the predominant vortex structure (Langston (1980)). Figure 6.3 gives a summary of the film effectiveness results (a case of C2 at $\dot{m}_c = 3.4\%$ has been used as an example) that have been post-processed from the raw images captured by the three cameras and combined into one map representing the whole blade surface. It should be noted that the streamwise distances between the cooling holes on the pressure and suction surfaces are the same. For the exact dimensionless streamwise locations of the rows of film holes on both circular and diamond pedestal DWEC blade designs, refer to Table 5.4. Figures 6.4, 6.5, 6.6, Figure 6.7

and Figure 6.8 show the film cooling effectiveness contour maps, individual and combined laterally-averaged film effectiveness respectively for all the three circular DWEC blades, C1, C2, and C3, at different test mass flow rates. While Figure 6.9 and 6.10 give the film effectiveness contour maps for diamond pedestal blade designs D1a and D1b, Figure 6.11 and Figure 6.12 give the film effectiveness contour maps for the blades D2a and D2b, and Figure 6.13 and Figure 6.14 give the film effectiveness contour maps for the blades D3a and D3b at different test coolant mass flows. The individual laterally-averaged film effectiveness for all the six diamond pedestal blade designs (D1a, D1b, D2a, D2b, D3a, and D3b) are presented in Figure 6.15 and Figure 6.16 . The combined laterally-averaged film effectiveness for all the six diamond pedestal blade designs will be discussed later in this section under Subsection 6.7.4.

For all the blades, a general trend is evident. Films are short and smeared out on the pressure surface whereas they are long and extended on the suction surface. The tendency of long and extended film streaks to exist on the SS has also been noted by Mhetras et al. (2012) and Rallabandi et al. (2010). The passage vortices spiralling motion on the SS forces the coolant jets on the SS cooling holes to deflect towards the blade midspan. The jet deflection towards the midspan on the SS and away from midspan on the PS has been observed experimentally by other researchers (Mhetras et al., 2012) and in numerical simulations, (Garg, 2000).

The SS for all of the blades show a good film coalescence with laterally averaged film cooling effectiveness reaching the highest value of about 0.4 for circular pedestal blades C1 and C2, and 0.65 for the diamond pedestal design D1a. There is hardly any film coalescence on the double-wall midchord PS, see a case of circular pedestal designs Figure 6.7. It was found, however, that on the PS, downstream film coalescence seemed to get better as the size of the film hole is reduced (more on the influence of film hole size on film effectiveness is discussed later in this section under the subsection 6.7.4).

Of all the test blades for all of the tested mass flow rates, the highest value of film cooling effectiveness on the PS is seen at the TE. With the less porous designs, such as the circular pedestal blade design C3 and diamond pedestal designs D1b, D2b, and D3b exhibiting the highest laterally averaged film effectiveness (see Figure 6.8 and Figure 6.16). The good film

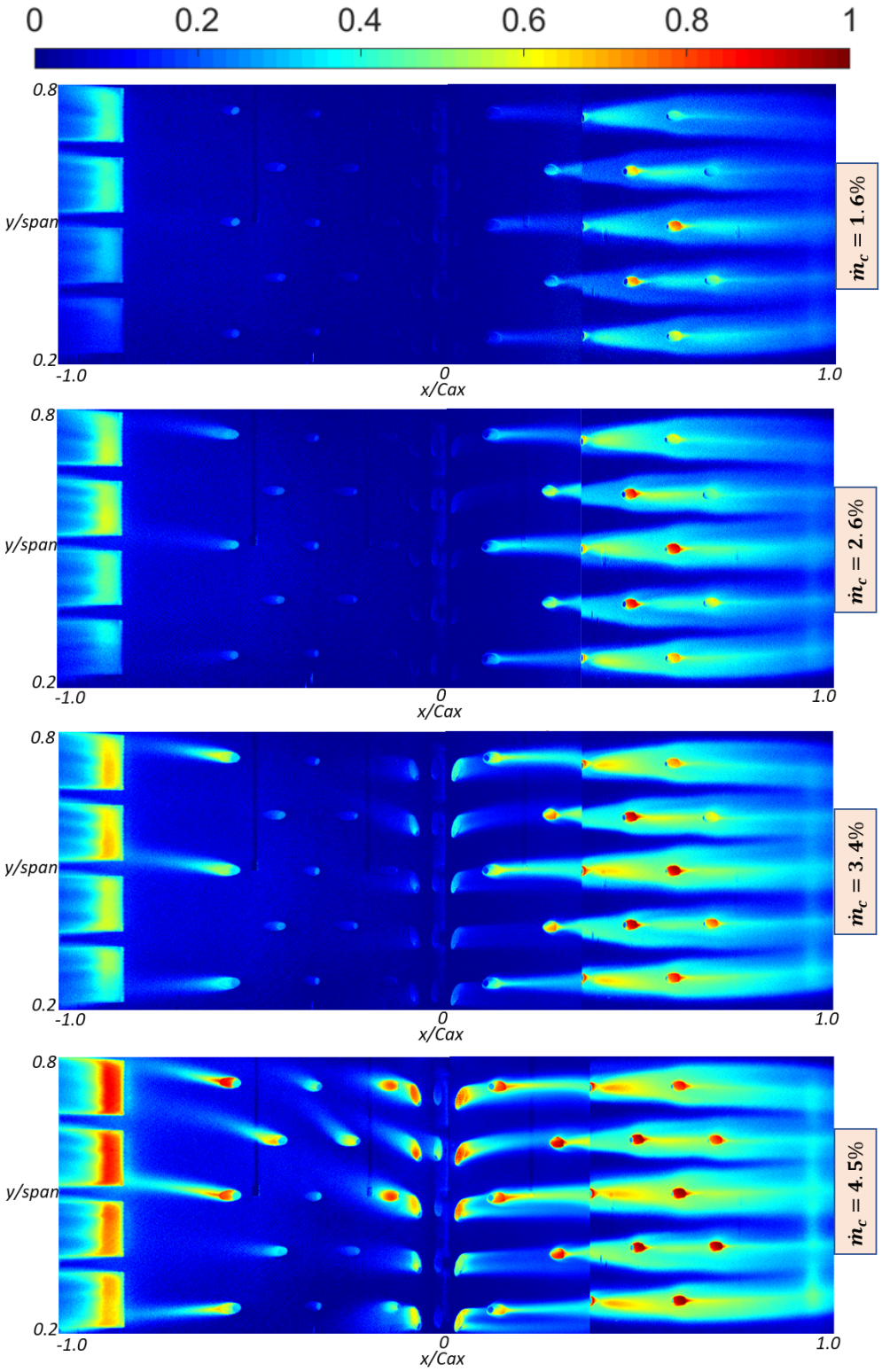

Figure 6.4: C1 film cooling effectiveness contour maps

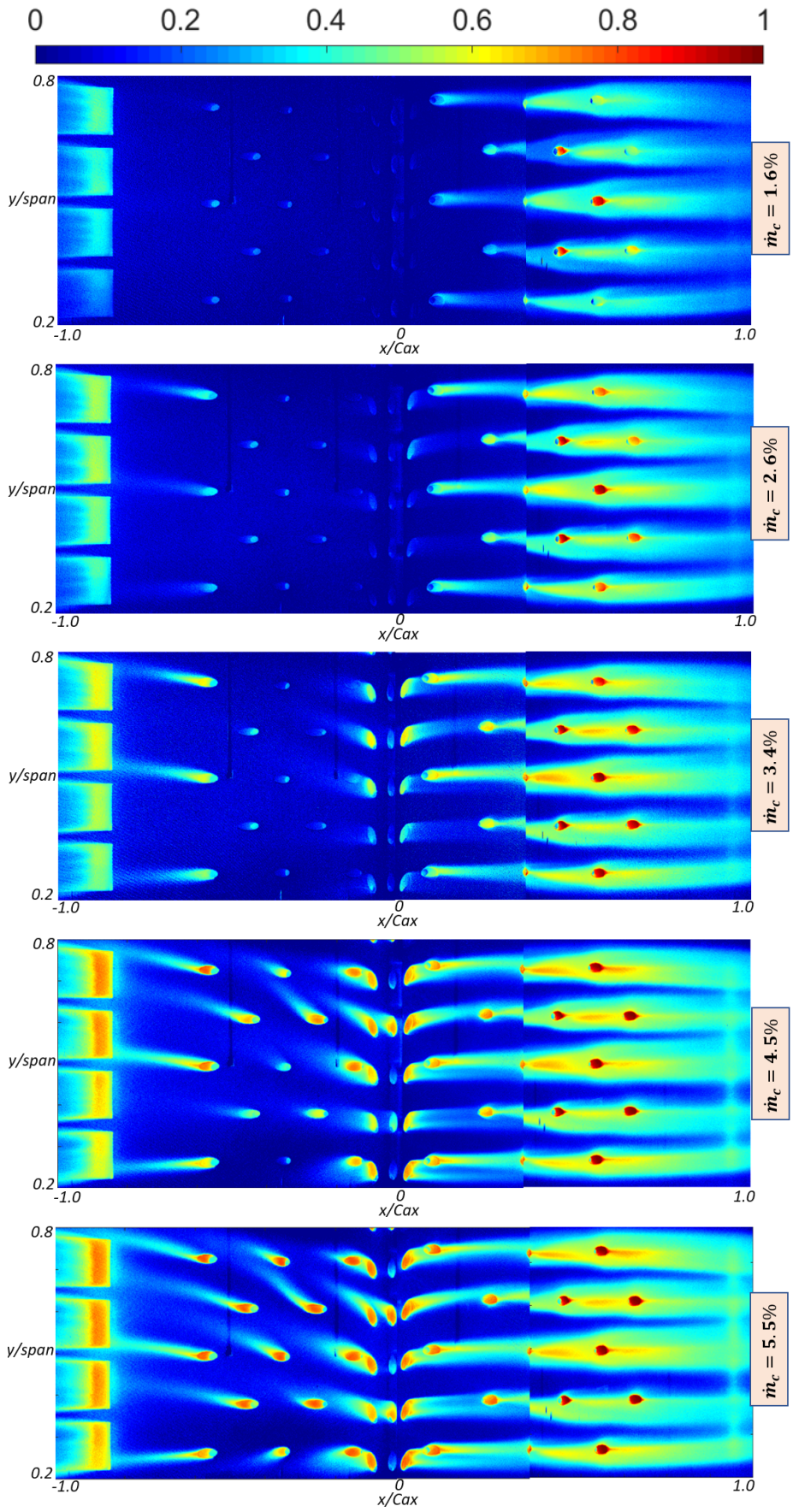

Figure 6.5: C2 film cooling effectiveness contour maps

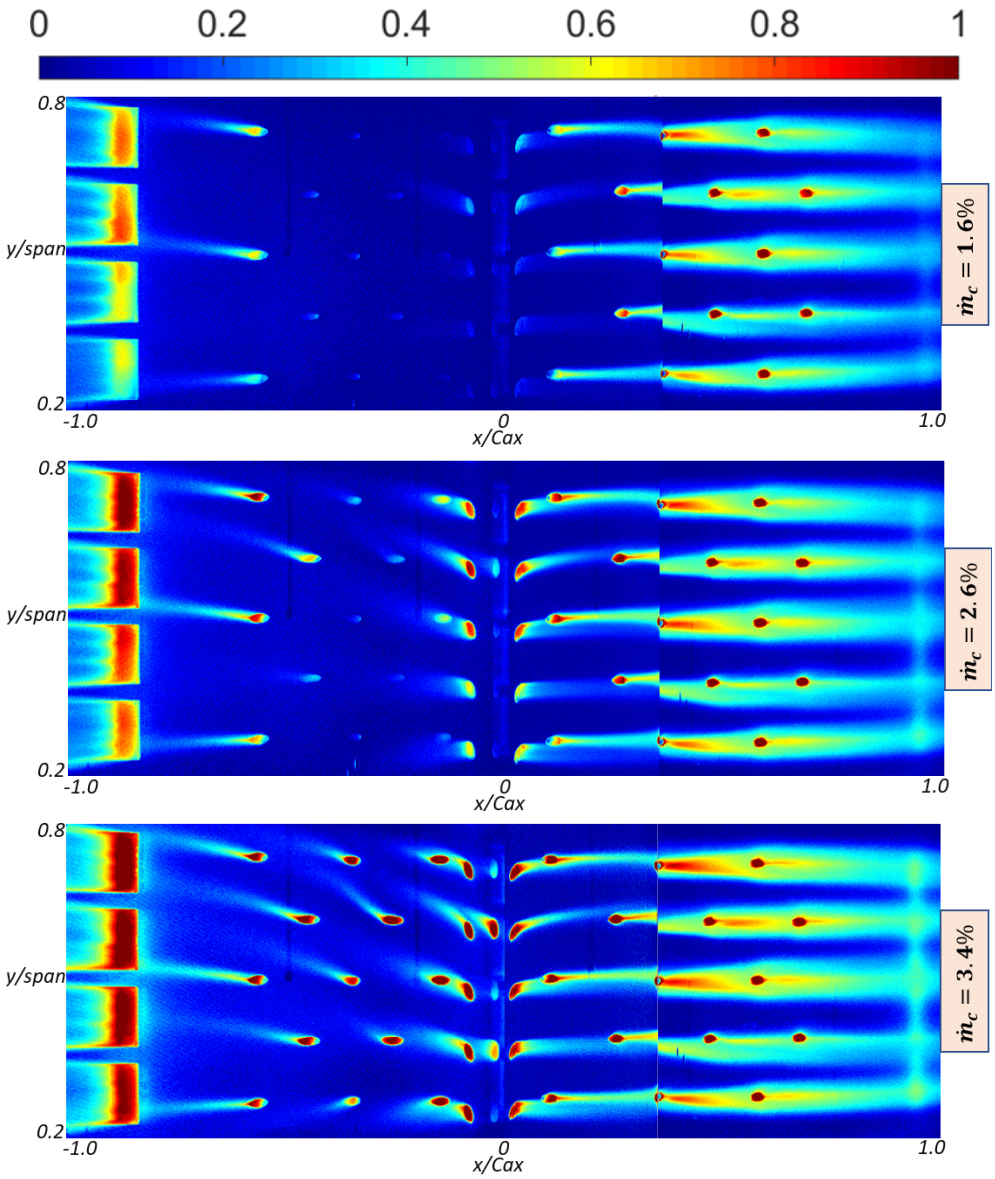

Figure 6.6: C3 film cooling effectiveness contour maps

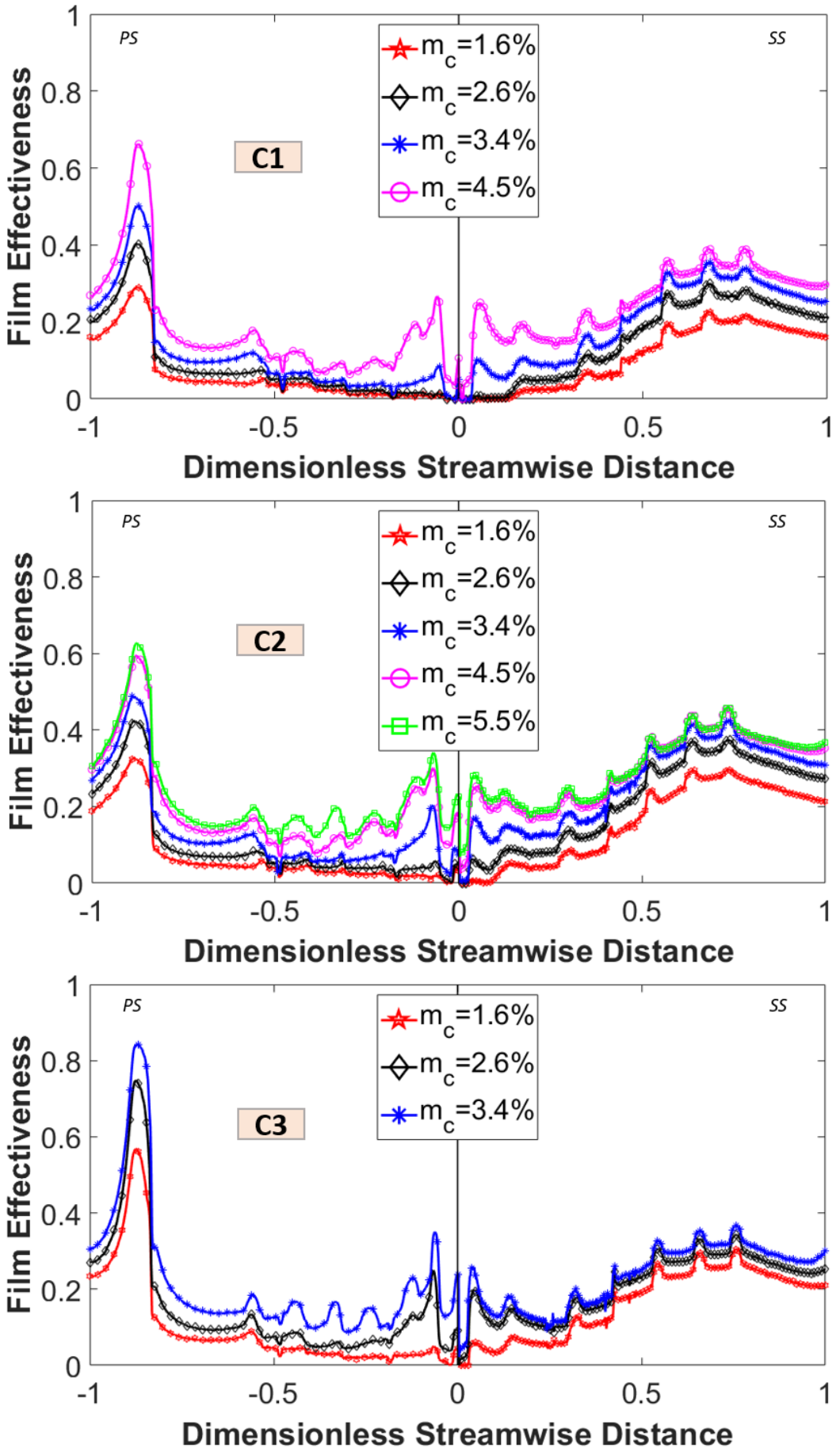

Figure 6.7: C1, C2 and C3 individual laterally-averaged film cooling effectiveness

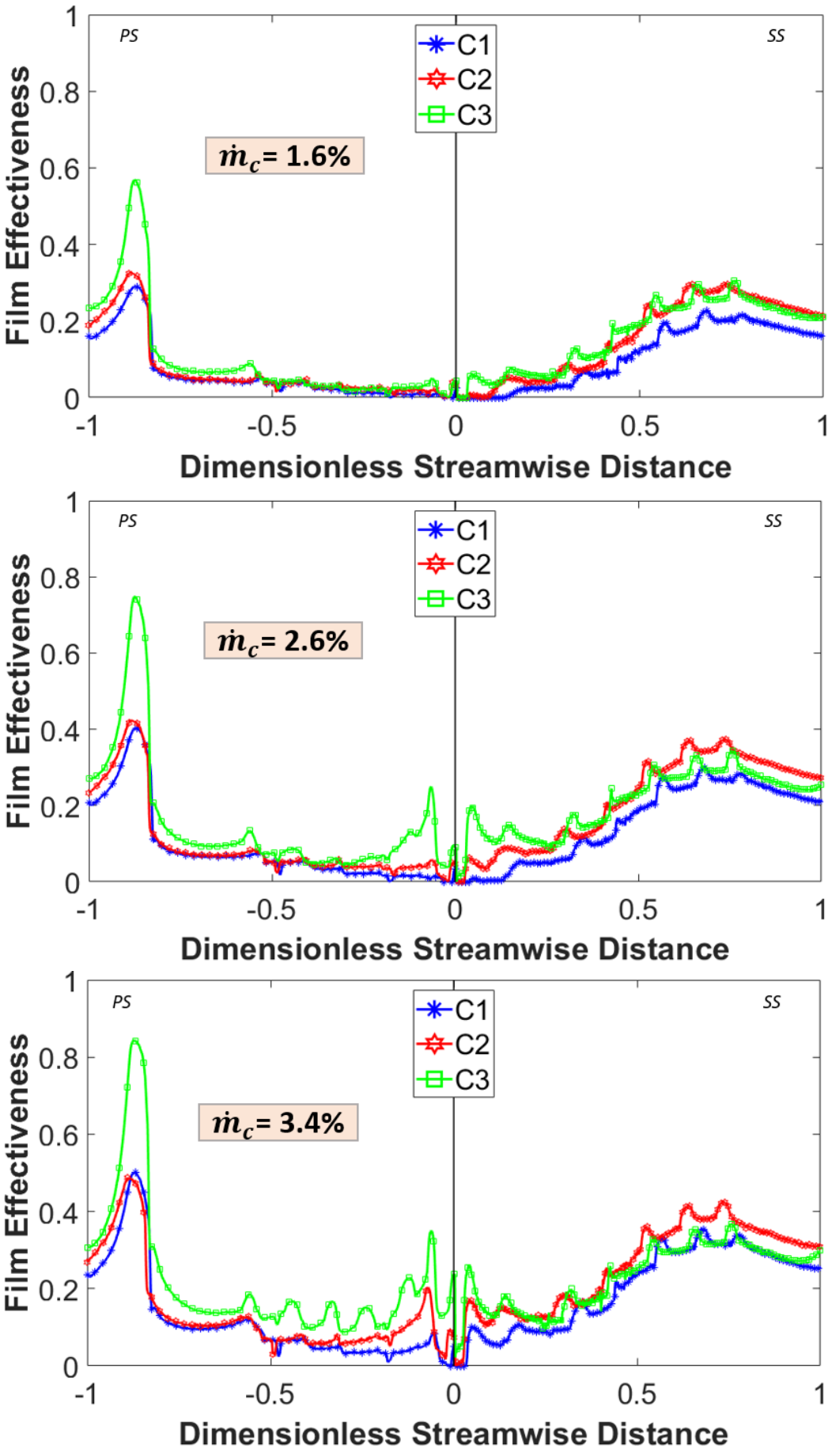

Figure 6.8: C1, C2 and C3 combined laterally-averaged film cooling effectiveness

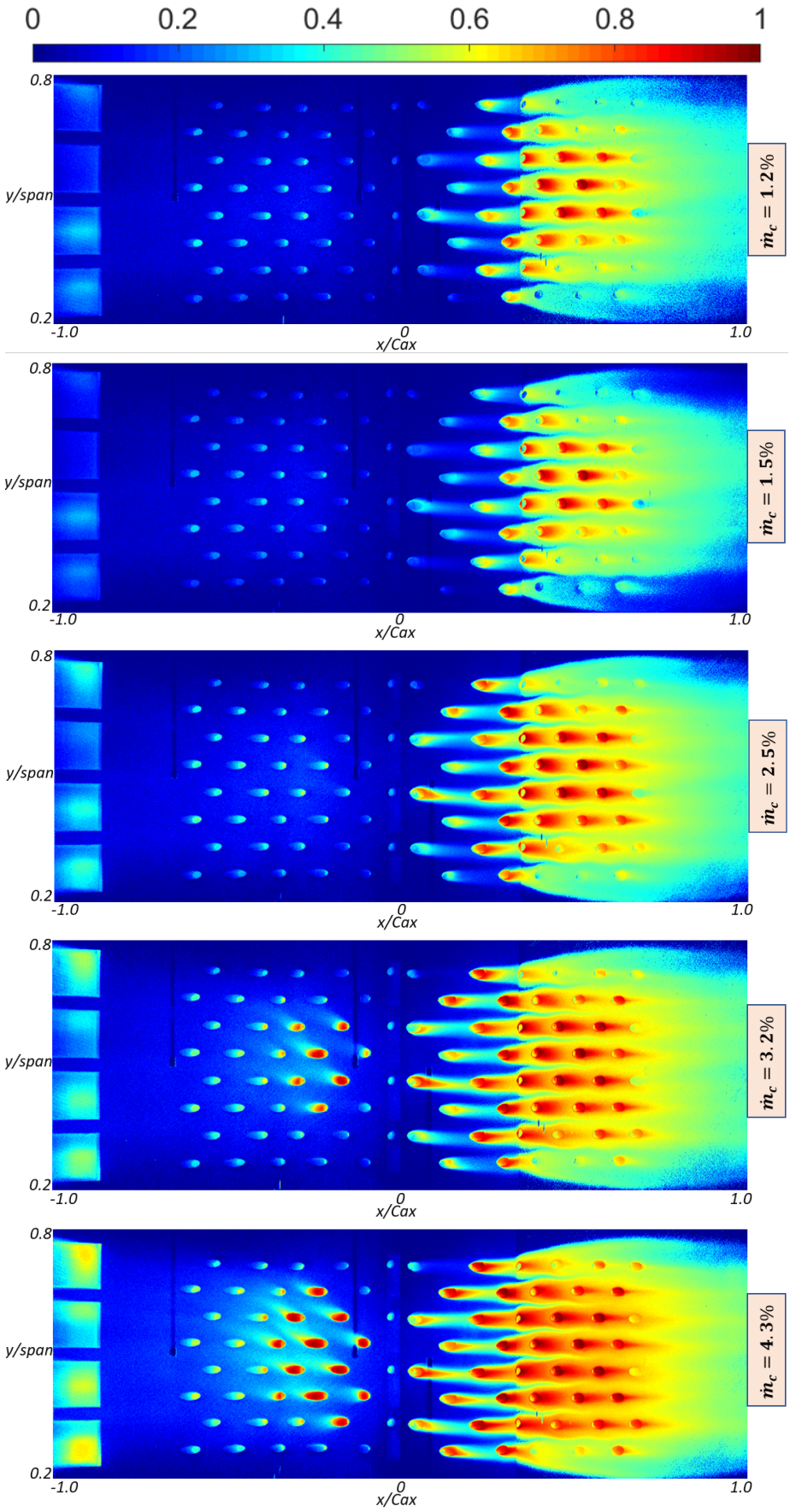

Figure 6.9: D1a film cooling effectiveness contour maps

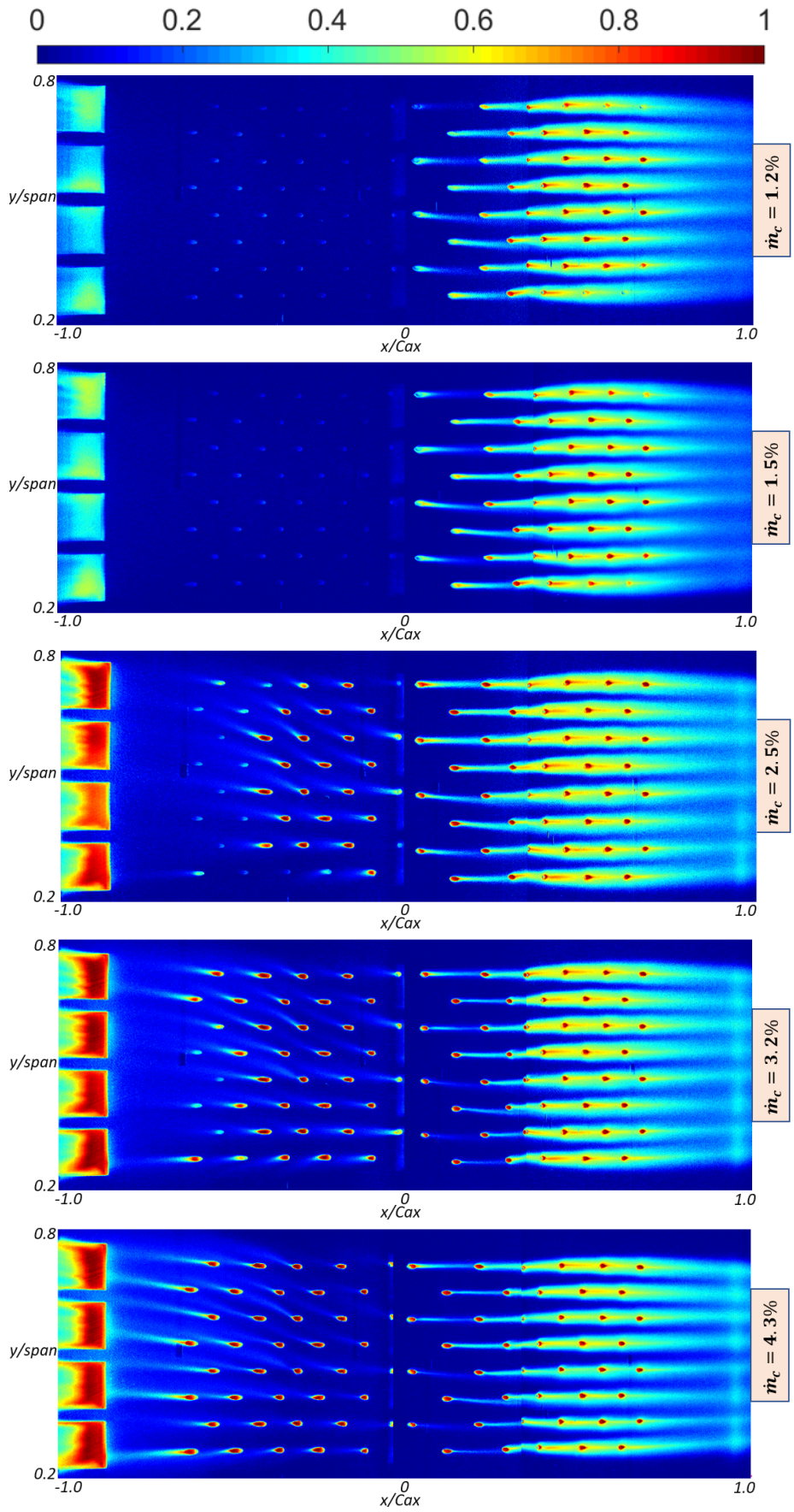

Figure 6.10: D1b film cooling effectiveness contour maps

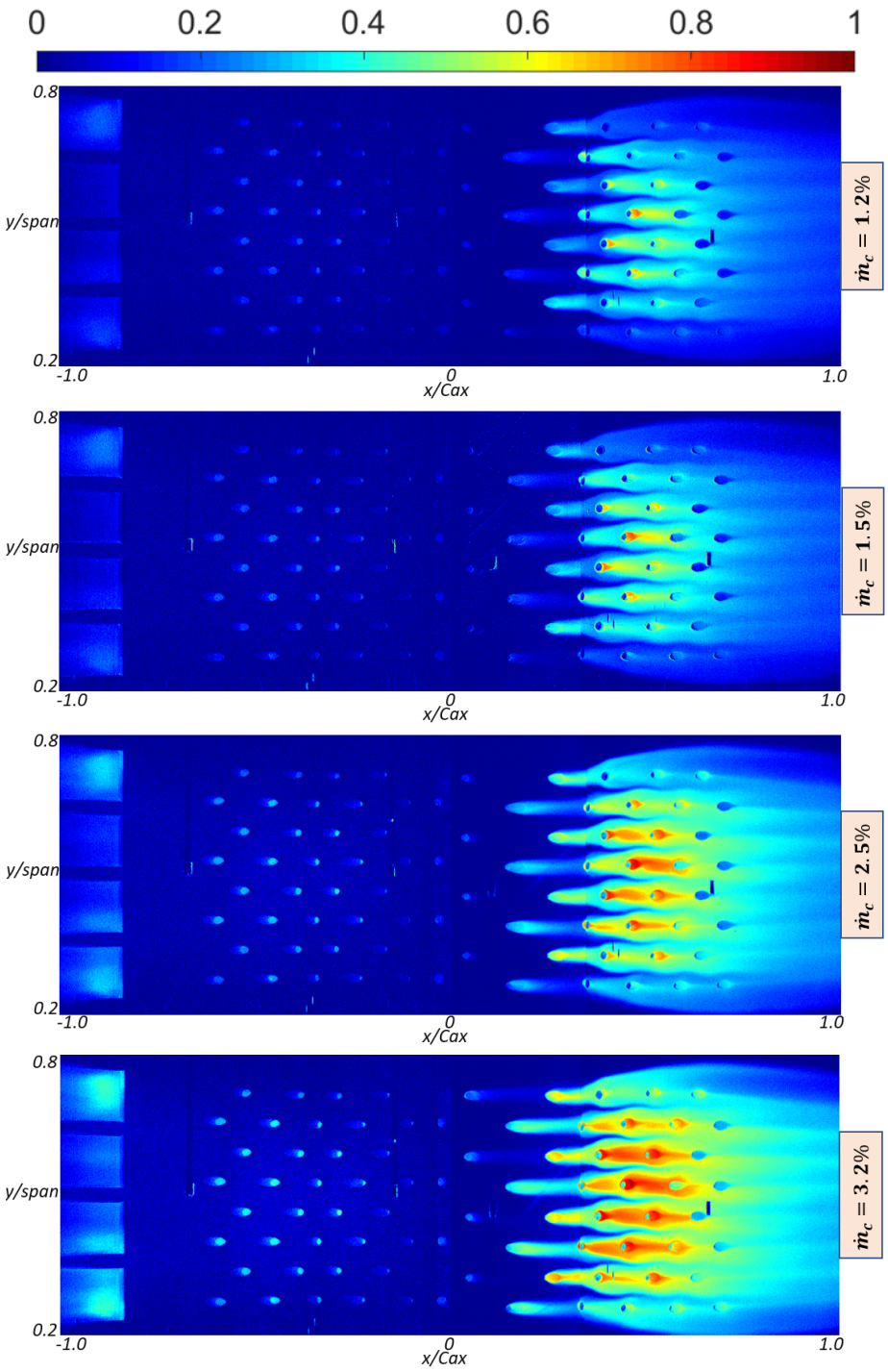

Figure 6.11: D2a film cooling effectiveness contour maps

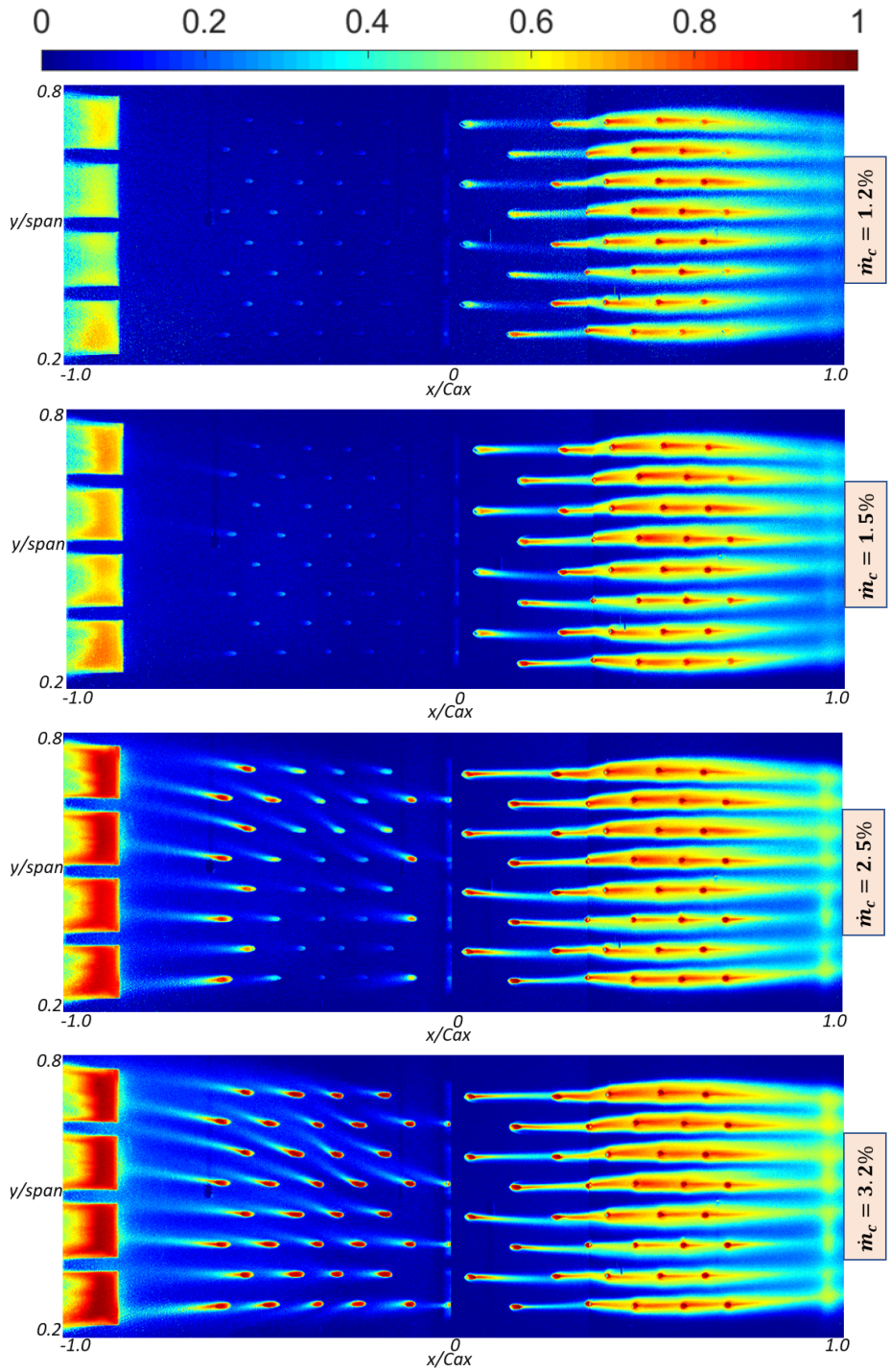

Figure 6.12: D2b film cooling effectiveness contour maps

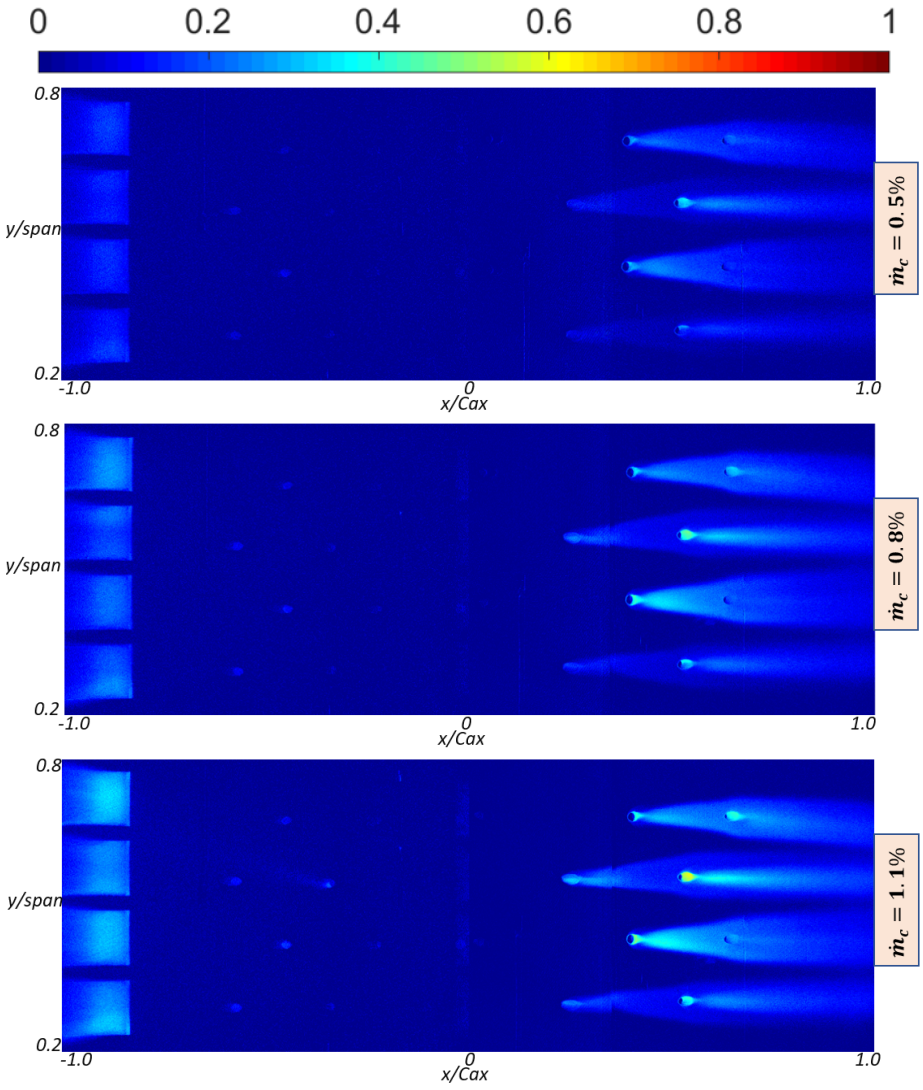

Figure 6.13: D3a film cooling effectiveness contour maps

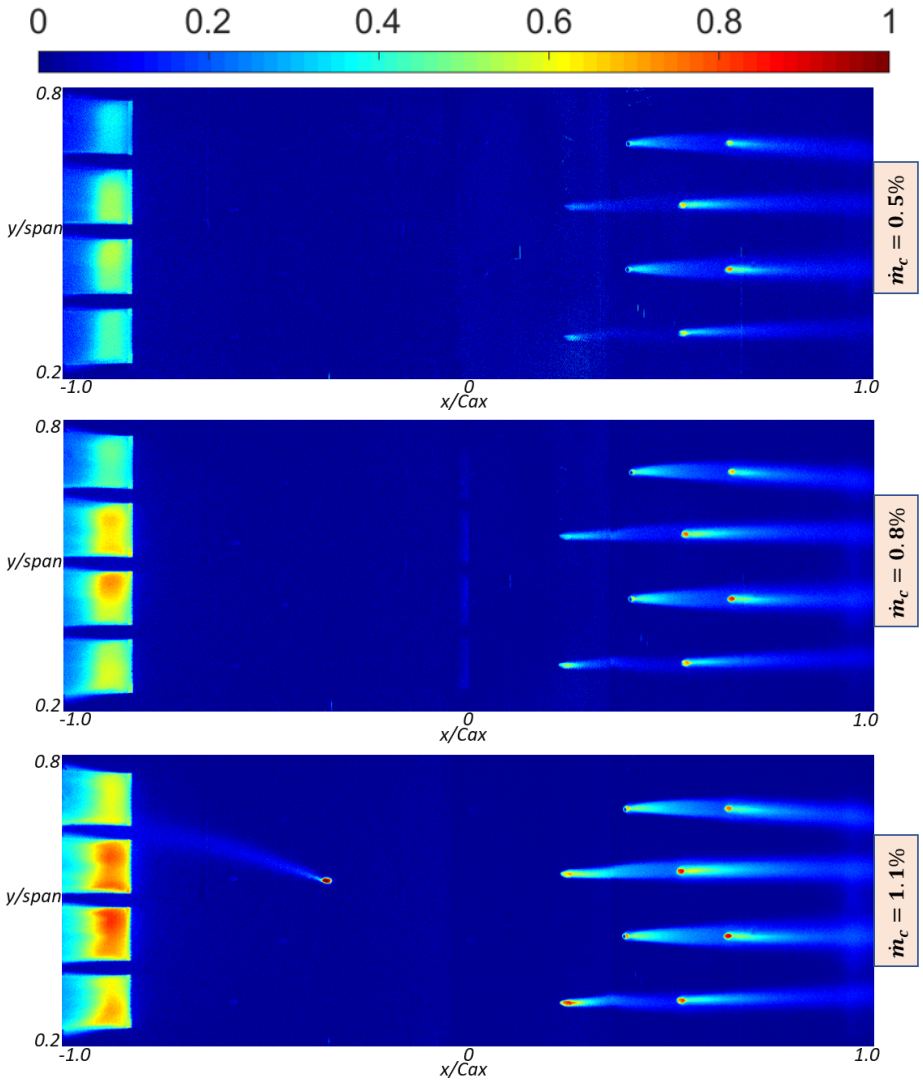

Figure 6.14: D3b film cooling effectiveness contour maps

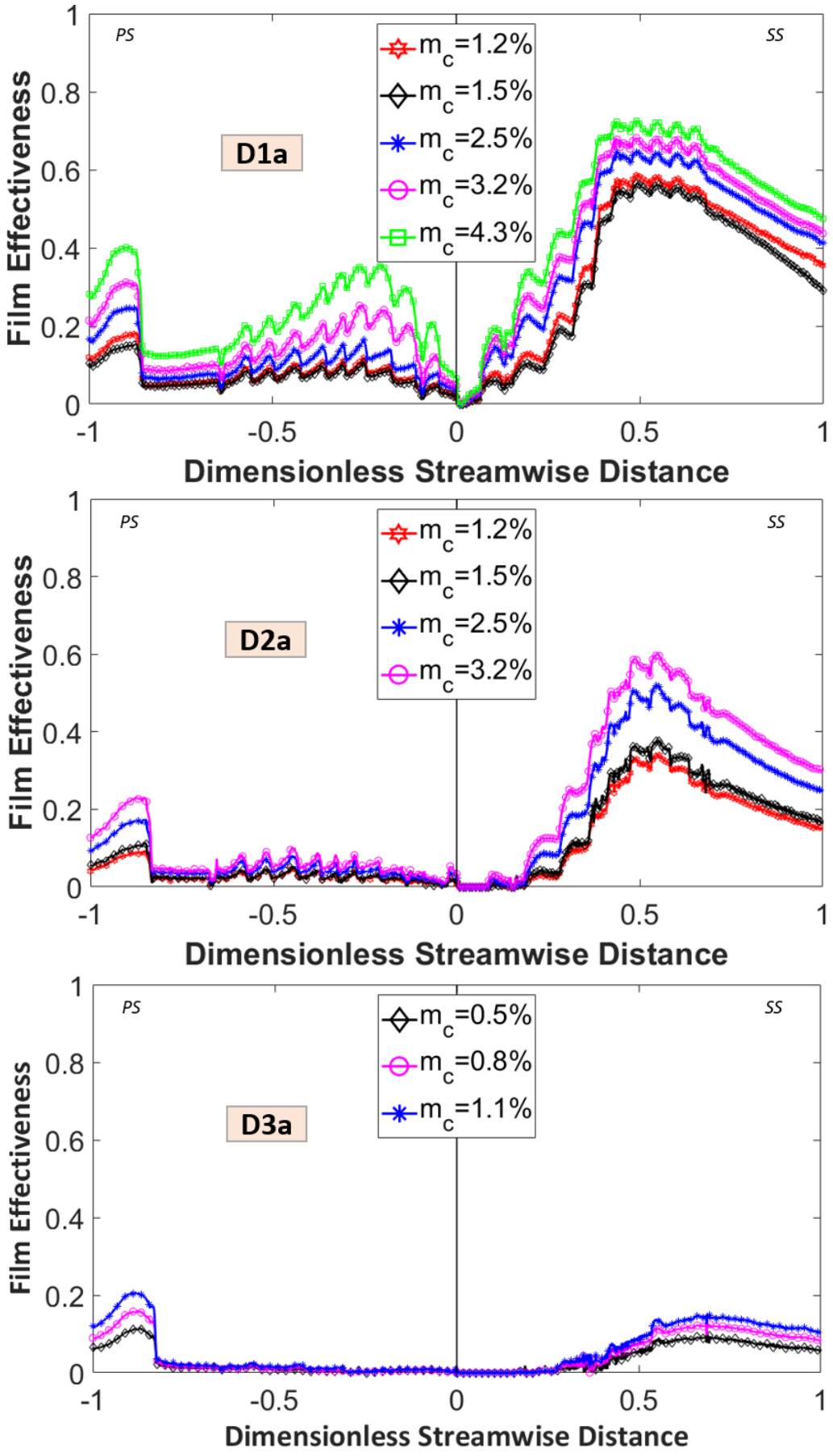

Figure 6.15: Diamond pedestal D1a, D2a and D3a individual laterally-averaged film cooling effectiveness

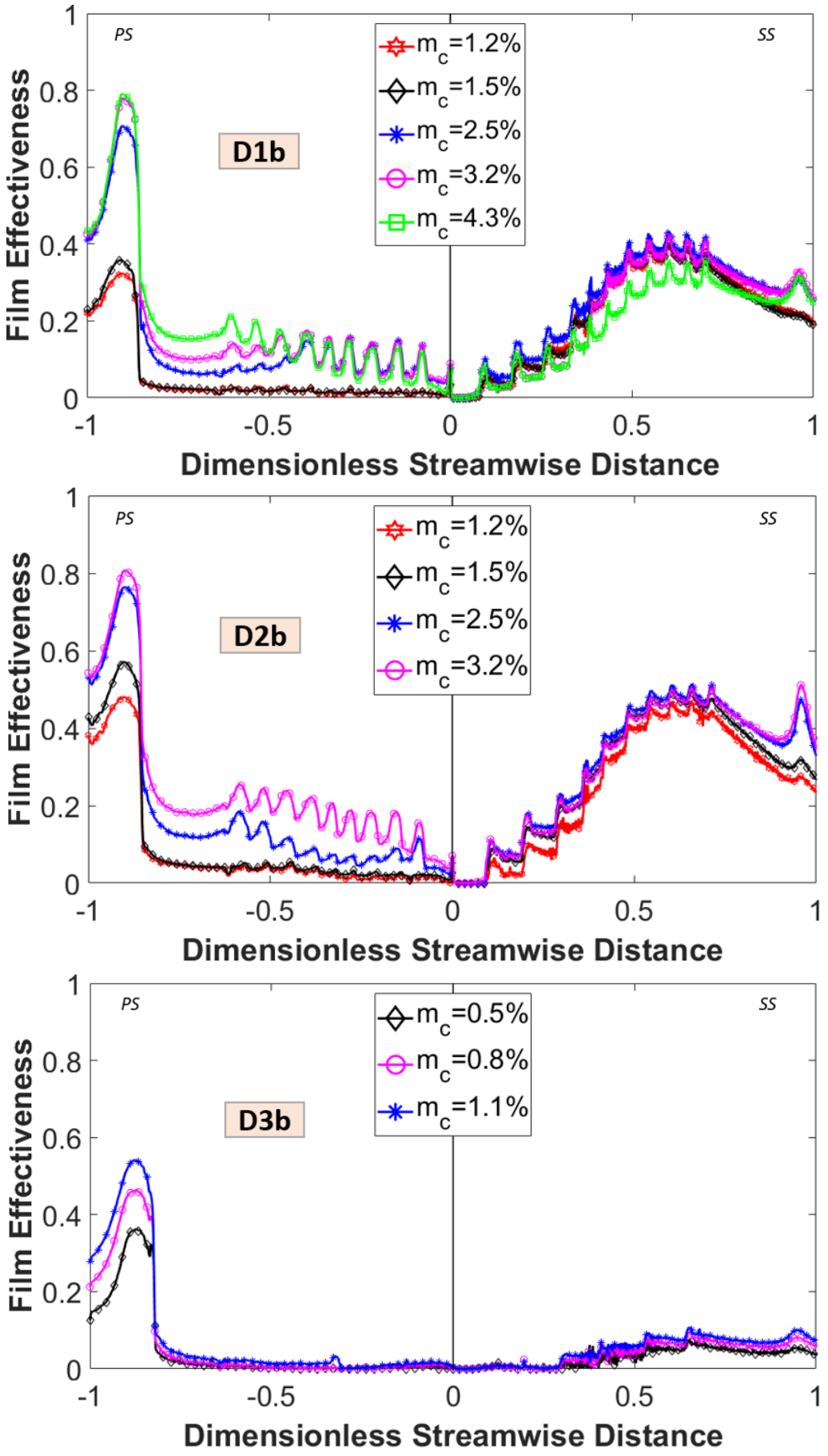

Figure 6.16: Diamond pedestal D1a, D2a and D3a individual laterally-averaged film cooling effectiveness

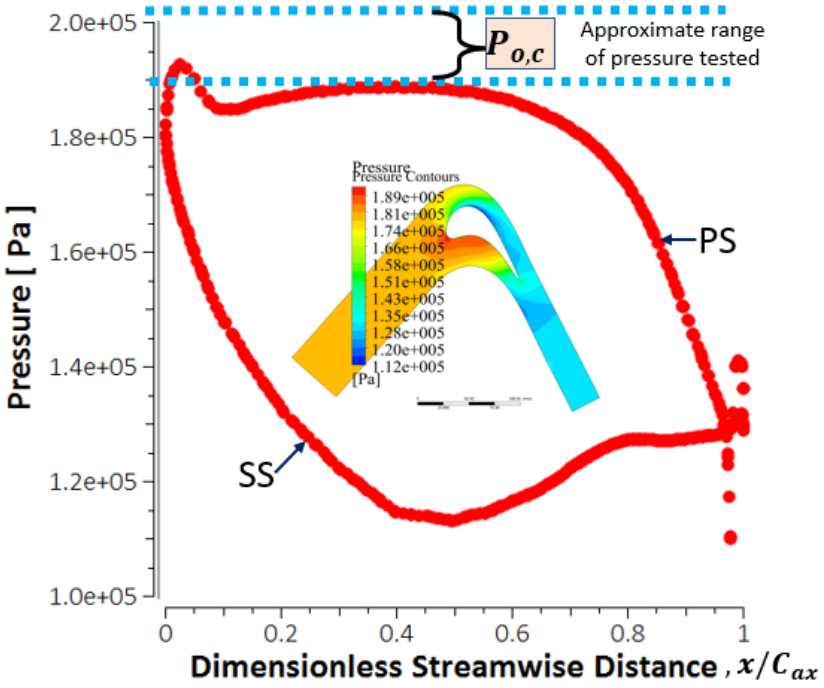

Figure 6.17: Variation of static pressure distribution, from CFD, around the aerofoil compared to the coolant supply pressure $P_{o,c}$

effectiveness at the TE compared to the rest of the pressure surface can be explained by the fact that the external static pressure at the TE is less than for the rest of the PS, see Figure 6.17. Consequently, more coolant flows out of the TE slots than for the other PS cooling holes. For all the blade designs and especially at low mass flow rates, there was hardly any film out of the PS cooling holes located on the aerofoil region with the highest external static pressure. This same observation was made by Takeishi et al. (1992), attributing it the fact that there is velocity deceleration in this zone and also that this zone has a small radius of curvature compared to the zone further downstream where the curvature approximates that of a flat plate.

The increase in laterally-averaged film cooling effectiveness levels near the TE on the suction surface side was attributed to the drop in surface temperature caused by the coolant flowing out of the TE slots. The slots are located just beneath this SS region. The coolant flowing out of the TE slots, causes temperature to decrease thus causing the evident rise in the film cooling effectiveness levels in this region. There were no surface thermocouples installed in this region during the tests and, therefore, it was not possible to account for the drop in temperature during the experiment. This means that there is some uncertainty in the

intensity ratio, $(I_{Ref} - I_B)/(I - I_B)$. The aerodynamic effects resulting from the high-speed flow around the aerofoil were accounted for during post-processing. Figure 6.18 and Figure 6.19 show the Mach number and recovery temperature (normalised by dividing recovery temperature, $T_{r,\infty}$ by the inlet total temperature, $T_{o,\infty}$) distribution around the blade respectively. Surface thermocouples were installed on the surface of the blade to record surface temperature during tests. Image intensity, I increases with decreasing temperature (Anyoji et al., 2015). Because of aerodynamic effects, surface temperature when recording I_{air} and I_{N_2} was lower than the surface temperature when recording I_{Ref}. Post processing of the images should be done at the same temperature, therefore a correction factor was applied to I_{air} and I_{N_2}. A temperature correction factor of 0.5% per K associated with the UniFIB^4 PSP (ISSI, 2012) was used.

6.7.2 Influence of Mass Flow Rates

As aforementioned, the circular pedestal C3 blade was tested at three different mass flow rates of $\dot{m}_c$=1.6%, 2.6%, and 3.4%. While C1 and C2 were tested at four different mass flow rates of $\dot{m}_c$=1.6%, 2.6%, 3.4% and five different mass flow rates of $\dot{m}_c$ = 1.6%, 2.6%, 3.4%, and 4.5% respectively. The diamond pedestal blades D1a and D1b designs were tested at five different mass flows of $\dot{m}_c$ = 1.2%, 1.5%, 2.5%, 3.2%, and 4.3%, blades D2a and D2b tested at four different mass flows of $\dot{m}_c$ = 1.2%, 1.5%, 2.5%, and 3.2%. It was only possible to test the less porous blades, D3a and D3b at only three mass flows; $\dot{m}_c$ = 0.5%, 0.8%, and 1.1%.

$$FlowFunction = \frac{\dot{m}_c \sqrt{T_{o,c}}}{P_{o,c}} \tag{6.5}$$

Generally, across all the blades, it was observed that increasing the mass flow rates and hence the blowing ratio, caused an improvement in the film performance although this improvement is more pronounced on the SS than the PS. The progressive increase in mass flow reaches a point, however, when a further increase in the mass flow rate ceased to offer significant film cooling effectiveness improvements on the SS. A case in point, where further raising mass flow rate from $\dot{m}_c$ = 4.5% to 5.5% in blade C2 caused jets to lift off resulting in

no further film effectiveness improvements, can be seen for blade C2 for which the laterally averaged effectiveness graph is presented as in Figure 6.7. Another very good example is seen in Figure 6.16 for the case of D1b where jet lift off the mid chord SS causes the film cooling effectiveness performance at the highest mass flow of $\dot{m}_c = 4.3\%$ to drop below that of the lowest mass flow of $\dot{m}_c = 1.2\%$. The PS films, however, were not found to suffer from jet lift off at high mass flow rates. In fact, the same rise in mass flow ($\dot{m}_c$ = 4.5% to 5.5%) that caused jet lift-off on the C2 and D1a SS, resulted in a significant film effectiveness improvement on their respective pressure surfaces. This lift-off is more pronounced at the transonic region of the SS not so much on the LE, the TE, and the PS.

6.7.3 Influence of Internal Geometry

As aforementioned, all nine DWEC blade designs tested here were built from the validated unit wall elements which included varying pedestal size, spacing and shape and cooling hole size and spacing, with details specified in Table 5.3. For the same spanwise and streamwise separations, bigger film holes, such as those in C2, result in a decreased dimensionless pitch and hence better film coalescing and film cover.

The more porous blades exhibited better film cooling effectiveness than the lower porosity blades. Examples of the high film effectiveness for the most porous blades - the circular pedestal blade design, C2, and the most porous diamond pedestal blade, D1a are shown in Figure 6.8 and Figure 6.15 respectively. The flow function graph, shown in Figure 6.20, was obtained by conducting flow tests; varying the pressure ratio, PR from PR = 1 to 1.6 and measuring the corresponding amount of air through the blade. Equation 6.5 was used to evaluate the flow function.

Even though PSP offered valuable insight into the film effectiveness structure on the surface of the blades, it did not give information about the blade internal geometrical structure and its possible influence on the film, internal convection and overall cooling effectiveness. In order to get an insight into the blade internal cooling and influence of the different blade cooling features on the overall cooling effectiveness, the internal convection and overall cooling effectiveness curve (refer to Figure 3.17 in Chapter 3) obtained from the novel simplified

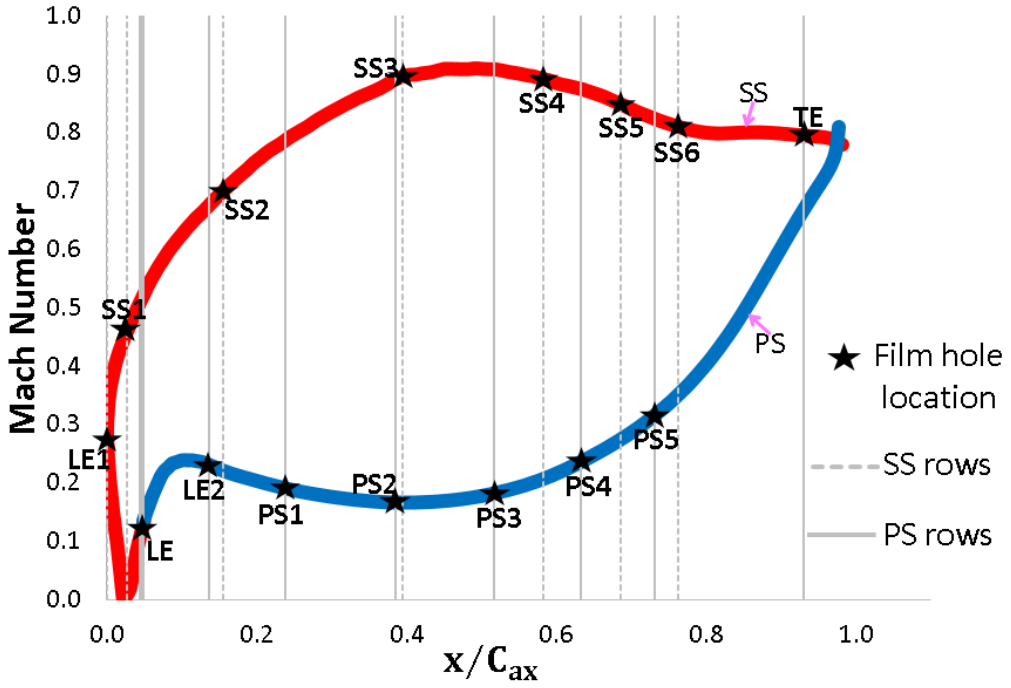

Figure 6.18: Mach number distribution on the blades obtained from CFD and using the boundary conditions presented in Table 5.1, including the streamwise hole locations

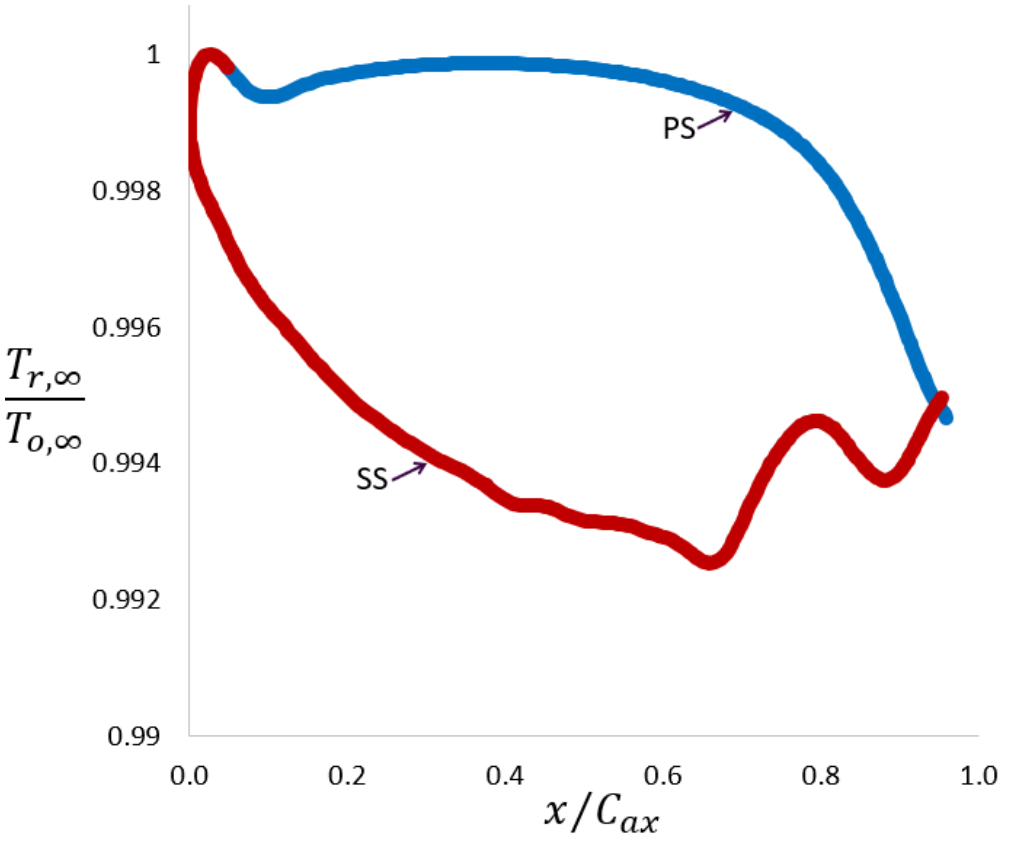

Figure 6.19: Recovery temperature distribution around the aerofoil

numerical analysis approach that has been outlined in detail in Chapter 3 was considered. As has been already mentioned in Chapter 3, it was only possible to analyse six DWEC blades

(that is C1, C2,C3, D1b, D2a, D3a) using the simplified numerical analysis approach. The unit wall element data, from Murray et al. (2017), needed for the simulations were only available for the blades C1, C2,C3, D1b, D2a and D3a. It should be noted that for any particular diamond pedestal design, the only difference between letters a and b in the name is the size of the effusion hole diameter; 2.3 mm and 1.15 mm respectively. So that D1b, for instance, has exactly the same design features as D1a except the size of the effusion hole diameter. The circular pedestals designs have circular pedestals while the diamond pedestal designs have diamond pedestals connecting the inner and outer skins in the mid-chord region of the DWEC blade.

As discussed in Chapter 3, the larger spacing between the inner and outer skins and, therefore, the length of the pedestals in C2 relative to C1 resulted in extra internal convecting surface area. The extra internal heat transfer area boosted both the internal convection and thus the overall cooling effectiveness compared to C1. The only difference between C1 and C2 is the length of the pedestal, as shown in Table 5.3. A similar observation can be made for the diamond pedestal designs - the blade with the largest internal wetted area (such as D2a) exhibited better internal convection and overall effectiveness. D2a is seen to consistently exhibit the best internal convection and overall effectiveness performance of all the five blades C1, C2,C3, D1b, D3a, across all the tested m^*.

Murray et al. (2017) experimentally and numerically studied the double-wall elements, used to build the mid chord section of the DWEC blades studied here. They found that, for the same pressure drop across the double-wall, overall effectiveness increased with the increase in the effective porosity (effective porosity is defined here as a product of C_d and outer skin porosity with porosity defined in Chapter 3). This phenomenon was attributed to the fact that, for the same pressure drop, there is more coolant flow in designs with higher effective porosities. A similar trend can be seen here. The overall effectiveness of the six blades at the same pressure drop of 0.9 bar can be ranked in the following descending order; D2a, C2, C1, D1b, C3, D3a, reflecting the effective porosities ranking, as shown in Figure 3.18 in Chapter 3.

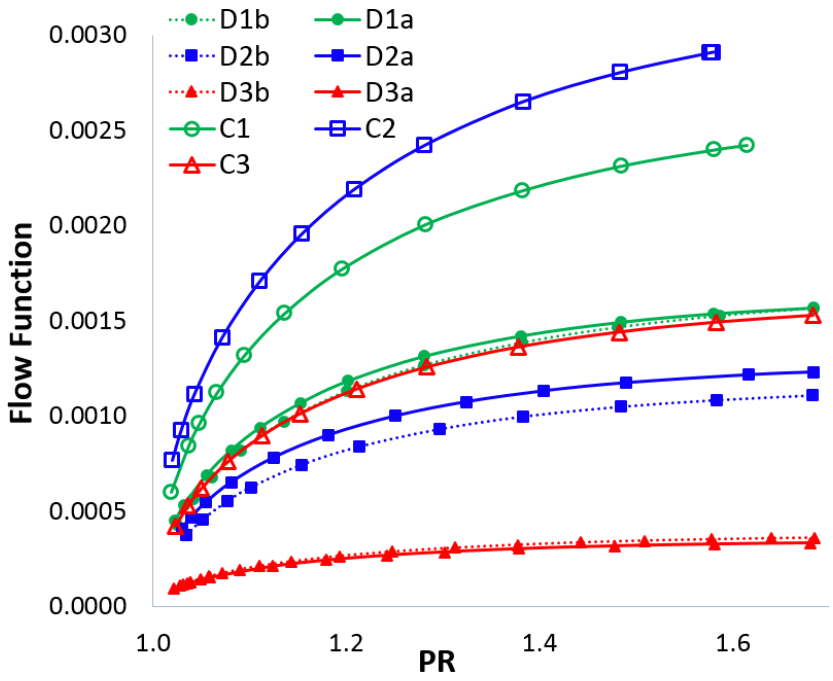

Figure 6.20: The flow function characteristics of all the 9 DWEC test blades

6.7.4 Influence of the Film Cooling Hole Size

It is natural, in effusion-cooled systems, to attempt to drive down the size of the film cooling hole with the aim of minimizing boundary layer disturbance so as to achieve transpiration-like film cover. An ideal effusion cooling is characterised by use of highly packed small-diameter (down to 0.2 mm) cooling holes (Krewinkel, 2013). This phase of the research was undertaken to investigate the influence of hole size on film cooling effectiveness.

As aforementioned, the diamond pedestals designs were configured so that it was possible to investigate the influence of film hole size on film cooling performance/distribution over the aerofoil. Three diamond pedestal designs D1a, D2a, and D3a had film cooling holes diameters equal to 2.3 mm. It should be noted that the size of the impingement holes in all the six diamond pedestal DWEC blade designs was the same ($D_i = 1.15$ mm). These three designs were replicated but with film hole diameter halved to form D1b, D2b and D3b respectively. The results from these six diamond pedestal designs were compared.

The film cooling effectiveness contour maps of the six diamond pedestal designs - D1a, D1b, D2a, D2b, D3a, D3b are presented in Figure 6.9, Figure 6.10, Figure 6.11, Figure 6.12, Figure 6.13 and Figure 6.14. In order to understand the effect of film hole size on film cooling effectiveness, laterally averaged film cooling effectiveness of all six diamond

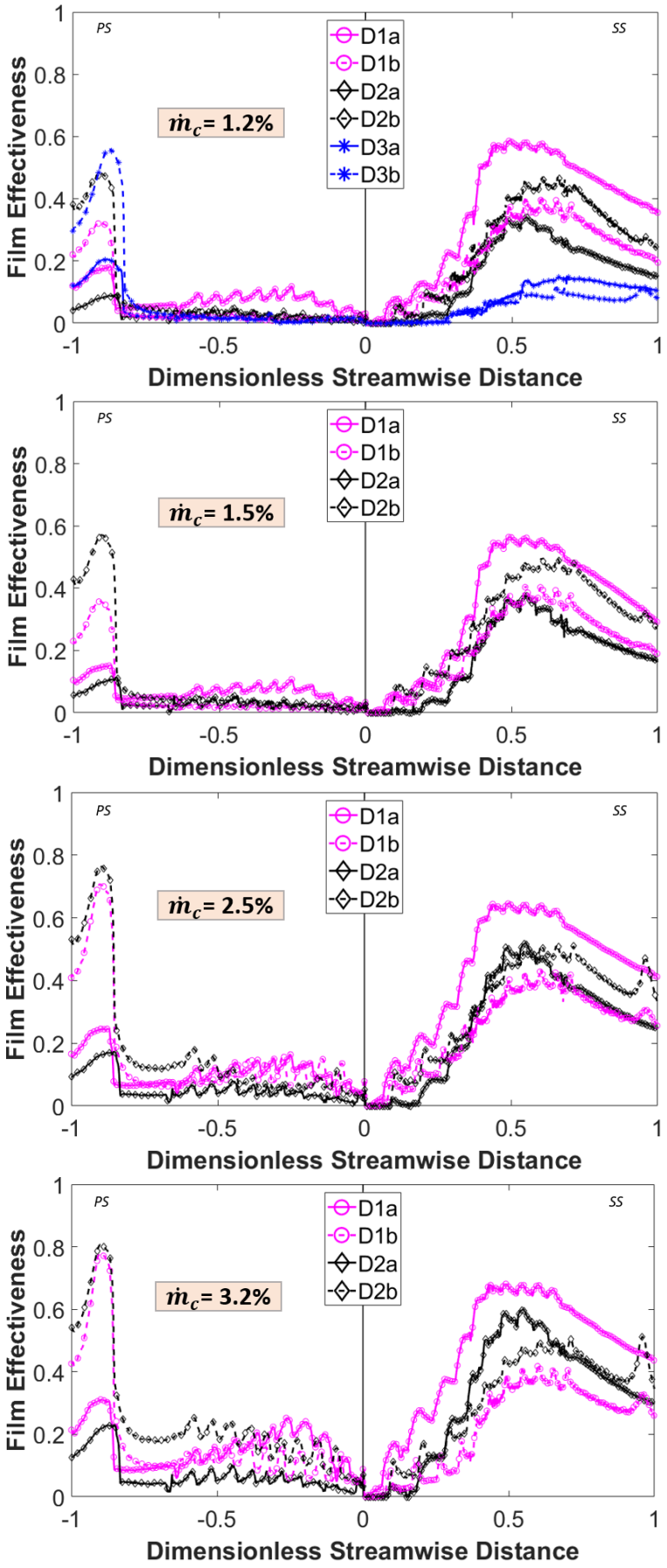

Figure 6.21: Diamond pedestal blade designs D1a, D1b, D2a, D2b, D3a and D3b combined laterally-averaged film cooling effectiveness

pedestal blades were compared at four different mass flow rates; $\dot{m}_c = 1.2\%, 1.5\%, 2.5\%$ and 3.2%, see Figure 6.21. Blades D3a and D3b were the least porous of all the six diamond pedestal designs. Therefore, it was not possible to compare D3a and D3b to the other four designs (D1a, D1b, D2a, and D2b) at higher mass flow beyond $\dot{m}_c = 1.2\%$.

On both the PS and SS and for both hole diameters, the laterally averaged film cooling effectiveness improved with the increase in coolant flows, with large film hole blade designs benefiting more than the small film hole designs. The latter seem not to improve much with increase in mass flow - especially on SS. It was interesting to note that this improvement in laterally averaged film effectiveness was significant, particularly for the designs with high effective porosity like D2a, see the case of D2a in Figure 6.21. D2a laterally averaged film cooling effectiveness levels, on the SS, is below that of D1a, D1b, and D2b at low mass flow of $\dot{m}_c = 1.6\%$ but drastically improves as the coolant flow increases and, by $\dot{m}_c = 3.2\%$ this design's laterally averaged film effectiveness is higher than D1b and D2b.

For the same streamwise and spanwise spacing, reducing the film hole size reduces the external skin porosity, and increasing the film hole size increases the external skin porosity. In the latter case, the jet exit velocities are reduced and thereby boundary layer stirring is minimized. At the same mass flow rates on the SS, the higher porosity blade designs D1a, D2a, D3a show better laterally averaged film effectiveness levels than that of lower porosity designs - D1b, D2b, D3b. The better film cooling effectiveness performance in the high porosity blades was particularly evident at high mass flow rates, see the case of $\dot{m}_c = 3.2\%$ in Figure 6.15 and Figure 6.16. The low outer skin porosity of blades D3a and D3b is responsible for an almost non-existent film coalescence causing very poor laterally averaged film cooling effectiveness. It was noted that excess bleeding of coolant through the SS is minimized if the porosity on the SS is reduced. See the individual blades laterally-averaged film effectiveness presented in Figure 6.16 where the diamond pedestal blade designs (D1b, D2b, and D3b) with low SS porosity manage to limit excessive coolant flow through the SS unlike the high porosity counterparts - D1a, D2a, and D3a which suffer excessive coolant flow through SS especially at high mass flow rates. From these results, it seems that the DWEC blade may benefit from any design that attempts to limit coolant flow through the

SS, for instance, by reducing the SS porosity and increasing PS porosity, so as to drive more coolant through the PS which is naturally challenging to film cool.

The geometric changes to the film cooling holes had a major influence, not only on film cooling effectiveness but also on overall cooling effectiveness. This is because film cooling effectiveness and internal wall cooling, and hence overall cooling effectiveness, are highly coupled. Since the temperature at exit from the internal cooling is effectively the supply temperature for the film cooling, as noted by Andrews et al. (1985).

6.8 Conclusion

The film cooling effectiveness performance over the full surface of three circular pedestal and six diamond pedestal DWEC high-pressure turbine rotor blades has been experimentally investigated using Pressure Sensitive Paint (PSP). The tests were carried out in a high-speed stationary single-blade linear cascade running at engine-representative Mach and Reynolds numbers flows. The blades were built from validated unit wall elements from Murray et al. (2017). The novel numerical simulation approach developed in Chapter 3 was also employed to obtain an insight into the internal convection and overall cooling characteristics of some of the test blades.

Extended film coolant streaks were observed on the suction surface whereas the films on the pressure surface tended to be short (relative to the chord length) and rapidly mixed out.

The presence of the passage vortices caused the coolant jet on the suction surface to be deflected towards the blade midspan while the coolant jet on the pressure surface tended to be deflected away from the midspan.

Owing to relatively higher pressure margin on the SS, the SS was easier to film cool than the PS. The SS exhibited relatively higher film cooling effectiveness levels even at low mass flow rates. It was, however, noted that the SS films started to lift off at higher mass flow rates.

The excess coolant flow through the SS is minimized if the SS porosity is reduced. Giving the implication that the DWEC blade may benefit from any design that attempts to limit the coolant flow through the SS, for instance, by reducing the SS porosity and increasing PS

porosity, so as to drive more coolant through the PS which is naturally challenging to film cool.

From the novel simplified analysis approach presented in Chapter 3, it was possible to compare the overall cooling effectiveness of some of the DWEC blades. At the same pressure drop across the double-wall, the overall cooling effectiveness was found to be directly proportional to the effective porosity - effective porosity is defined as the product of the C_d and the outer skin geometric porosity.

The valuable film effectiveness results from this study, have offered an immense insight into the design of the next generation double-wall effusion cooled turbine blades. The investigation of the influence of internal and external blade geometry on film and overall effectiveness was, however, not exhaustive. This research was aimed at an investigation of the application of a double-wall effusion cooling system in an aerofoil design. Further research is, therefore, recommended to thoroughly investigate the influence of the geometrical parameters like pedestal spacing, shape, and size, cooling holes spacing, shape and sizing on both internal cooling, film, and overall cooling effectiveness.

6.9 Summary

This chapter has reported a detailed investigation into the film cooling effectiveness of nine large scale double-wall effusion cooled rotor blades in a stationary single-blade linear cascade at engine realistic Mach and Reynolds numbers. Film cooling effectiveness measurements on a DWEC aerofoil with effusion cooling, to the best knowledge of the author, has not been reported before. The results covered the influence of coolant mass flow rate, internal geometry, and film cooling hole size on film cooling effectiveness. The investigation of the influence of double-wall cooling parameters like pedestal spacing, size, and cooling holes spacing and size on film cooling effectiveness was not exhaustive, as it was out of the scope of the current work. More research, therefore, is recommended to fully understand effect of such parameters on DWEC aerofoil cooling performance. Nonetheless, the results and observations presented in this chapter will be valuable for the design of the second-generation DWEC aerofoil.

The next chapter will summarize the whole research and make a case for the present research contributions.

Chapter 7

SUMMARY AND CONCLUSION

7.1 Summary of Major Themes and Assessment of Aims

7.1.1 Simplified 3D numerical analysis approach

A novel computationally efficient numerical analysis method for analysis of DWEC blades was developed. In this numerical analysis model, the film cooling effectiveness and the internal heat transfer coefficient predictions are obtained from a modified flat plate correlation and a validated unit wall block element respectively. Conduction through the blade is then solved using the finite element code available in ANSYS[1] Steady-State Thermal module. The numerical analysis approach makes it possible to rapidly extract key performance parameters like mass flow rates, metal effectiveness, film effectiveness, and overall effectiveness and is thus particularly useful for redesign and optimization of a DWEC aerofoil. The developed novel numerical analysis approach, compared to a fully coupled CHT simulation, reduced computational time by approximately 50 times. Therefore, it was found to be a simplified computationally efficient tool that can be used in the preliminary and optimisation stages of a DWEC turbine blade design.

The developed numerical analysis tool was used to analyse a total of six DWEC aerofoils. One of the key observations from the simplified numerical analysis is that the internal cooling was found to contribute a larger proportion to the overall cooling effectiveness of the DWEC blade. This was attributed to a very large internal surface area brought about

by a combination of impingement cooling and a large internal surface area contributed by the pedestals. The effective internal cooling performance of the DWEC blade permits the DWEC system to closely approximate that of transpiration cooling, as has been noted by Andrews and Asere (2013) and Andrews et al. (1985).

It should be noted that influence of various geometrical parameters like the cooling hole diameters, shape, and pedestal shape and size were not exhaustively investigated. To enable redesign and optimization of the DWEC aerofoils, further research is, therefore, recommended to thoroughly investigate the influence of the DWEC geometrical parameters like pedestal spacing, shape, and size, cooling holes spacing, shape and sizing on the cooling performance of the DWEC.

7.1.2 Fully coupled CFD simulations

The commercial CFD software - ANSYS[1] was used to carry out CHT simulations to further analyse and understand the DWEC aerofoil. The general conclusion was that, the isolated wall block predicted C_d, and subsequently other parameters such as mass flow rates, on the SS with reasonable accuracy but overestimated parameters on the PS - for instance of up to 71% on C_d prediction. The implication of this is that, the isolated wall block data may be used to predict aerofoil SS performance but not the PS.

In addition, it was further noted that:

- Metal effectiveness improved with the increase in the coolant inlet total pressure, and hence the mass flow rates. The LE is located at the mainstream flow stagnation point where vortices are formed that augment heat transfer and the TE has a narrow shaped geometry and is exposed to a fully turbulent hot gas path causing both the LE and the TE regions of the aerofoil to exhibit low metal effectiveness, compared to the rest of the aerofoil surfaces, for all of the test PR. Simplified analysis model and isolated wall block $\varepsilon_m - m^*$ comparison showed a drop in the metal effectiveness performance of the isolated wall block when used on the aerofoil with a varying external static pressure.

- 3D streamlines visualised using Mach number provided some information about the

[1] www.ansys.com

flow interaction on the impingement/effusion cooled midchord section of the aerofoil. Showing the impingement jet impinging on the inner walls of the outer target surface at relatively high velocity, spent jet split and vortices and spent jet interaction resulting in re-impingement.

- Blowing ratio increased with an increase in PR on both the PS and the SS. Owing to a relatively low external static pressure, and hence relatively higher pressure margin on the SS, blowing ratio of the SS holes was generally higher than that of the PS holes at any given PR. The low pressure margin on the PS made it difficult for the coolant to flow out of the PS holes particularly at low PR - it was only at the highest PR=1.25 that the coolant was able flow out of all the PS holes. On the other hand, the high pressure margin on the SS caused the coolant to flow out of the SS holes, even at the lowest PR=1.0.

- As expected, the adiabatic film cooling effectiveness improved on both the PS and the SS with an increase in PR, and hence blowing ratio. At high blowing ratios, SS exhibited low film cooling effectiveness as a result of jet lift off. Whereas on the PS, better film cooling effectiveness was evident at high blowing ratios.

- Despite the difference in density ratio between the CFD and the experiment, CFD results compared well with the experiments and were able to capture similar ε_f trends on the PS and the SS. Inability of RANS models to correctly predict coolant diffusion led to ε_f over prediction around the vicinity of the film cooling holes and over prediction of film superposition on the SS.

7.1.3 Film cooling effectiveness measurement using PSP

Film cooling effectiveness tests in a stationary high-speed single-blade linear cascade at engine representative Mach number and Re flows were carried out. The film effectiveness tests provided a valuable insight into the film performance and structure on the DWEC turbine aerofoil. Furthermore, the tests provided an insight into the influence of some of the key

parameters like the DWEC aerofoil internal structure and film hole size on the film performance.

Film cooling effectiveness tests were carried out using PSP. PSP is a mass transfer principle which is non-intrusive and free from heat conduction errors and thus capable of producing well-defined coolant traces on the test component. A total of nine (six diamond pedestal and three circular pedestal) large-scale double-wall blade designs with varying pedestal height, pedestal size, cooling hole diameter, and streamwise pitch were tested within a range of typical modern engine coolant mass flow, $\dot{m}_c$, to mainstream, $\dot{m}_g$, ratios; $0.5\% < (\dot{m}_c/\dot{m}_g) < 5.5\%$.

Extended film coolant streaks were observed on the suction surface whereas the films on the pressure surface tended to be short (relative to the chord length) and rapidly mixed out. The presence of the passage vortices caused the coolant jet on the suction surface to be deflected towards the blade midspan while the coolant jet on the pressure surface tended to be deflected away from the midspan.

Owing to relatively higher pressure margin on the SS, the SS was easier to film cool than the PS. The SS exhibited relatively higher film cooling effectiveness levels even at low mass flow rates. It was, however, noted that the SS films started to lift off at higher mass flow rates.

The excess coolant flow through the SS is minimized if the SS porosity is reduced. Giving the implication that the DWEC blade may benefit from any design that attempts to limit the coolant flow through the SS, for instance, by reducing the SS porosity and increasing PS porosity, so as to drive more coolant through the PS which is naturally challenging to film cool.

From the novel simplified analysis approach presented in Chapter 3, it was possible to compare the overall cooling effectiveness of some of the DWEC blades. At the same pressure drop across the double-wall, the overall cooling effectiveness was found to be directly proportional to the effective porosity - effective porosity is defined as the product of the C_d and the outer skin geometric porosity.

The valuable film effectiveness results from this study, have offered an immense insight

into the design of the next-generation double-wall effusion cooled turbine blades. The investigation of the influence of internal and external blade geometry on film and overall effectiveness was, however, not exhaustive. This research was aimed at an investigation of the application of a double-wall effusion cooling system in an aerofoil design. Further research is, therefore, recommended to thoroughly investigate the influence of the geometrical parameters like pedestal spacing, shape, and size, cooling holes spacing, shape and sizing on both internal cooling, film, and overall cooling effectiveness.

7.2 Conclusion

Through numerical and experimental studies, the present research has extended double-wall cooling studies that have long been conducted on flat plate geometries onto turbine-representative aerofoils. DWEC aerofoils were built from double-wall block elements that have been validated by another author. Both low porosity and high porosity circular and diamond pedestal designs were considered.

The novel simplified numerical analysis method that was developed for analyis of DWEC aerofoils was found to offer good performance approximation, particularly on the suction surface. The simplified numerical analysis, compared with CHT, reduced computational time by over 50 times and thus computationally efficient for use during preliminary design and optimization stage.

From both numerical and experiments, it was found that due to relatively low-pressure margin on pressure surface, compared to suction surface, blowing ratios on pressure surface were lower – particularly at low coolant pressure ratios, consequently making pressure surface difficult to cool. High effective porosity designs exhibited better film cooling effectiveness, than the low effective porosity counterparts, but this came at an expense of internal cooling efficiency. CFD results compared well with the experiments and were able to capture similar film cooling effectiveness trends on both the pressure surface and the suction surface. Inability of Reynolds-Averaged Navier–Stokes equations, RANS models to correctly predict coolant diffusion led to film cooling over prediction around the vicinity of film cooling holes and over prediction of film superposition on the suction surface.

The present work has successfully extended the double-wall effusion cooling research that has long been reported for flat plates to a gas turbine aerofoil. This work has contributed knowledge of the DWEC aerofoils performance including overall cooling effectiveness predictions, internal cooling effectiveness predictions and film cooling effectiveness performance measurements.

There is still much work to be done - including investigation into aerodynamic losses, weight and stresses associated with this cooling technology, to realise a practical double-wall effusion-cooled blade. The present author includes recommendations for future work in Chapter 8.

Chapter 8

RECOMMENDATIONS

The present work has presented interesting findings after numerically and experimentally studying double-wall effusion-cooling scheme for gas turbine blade application. From the literature survey conducted, there is a dearth of studies in the public domain that have investigated double-wall effusion-cooling scheme applied to an aerofoil and the present work has successfully stretched the boundaries of the double-wall cooling research. But at the same time, the study was not exhaustive. Some of the critical issues such as aerodynamic losses and the subsequent negative effect on the overall engine efficiency was not done (as it was not the focus of the current work). This chapter discusses some of the issues to be considered for further understanding of aerofoil double-wall cooling so as to pave way for optimisation with an aim of attaining a practical design that can be put into an engine. These recommendations are described in the following sections.

8.1 Explore Shaped Cooling Holes

The present author focused the research on inclined cylindrical effusion cooling holes. The double-wall cooling scheme can reap further benefits from the use of fan-shaped cooling holes especially on the outer skin. Despite some disadvantages associated with the use of fan-shaped holes, such as an increased aerodynamic mixing losses, they are generally known to cause less tendency to lift off at high blowing ratio and are associated with a higher film cooling effectiveness compared to their round hole counterparts. Bunker (2005) has provided

an excellent review of shaped cooling holes for gas turbine applications.

8.2 Optimization

The benefits of optimization in design is not debatable. The double-wall effusion cooled system has numerous parameters (such as size, shape of the pedestals and cooling holes) that when altered lead to notable changes in the cooling requirements and heat transfer in the whole system.

The double-wall blade mid-chord section is essentially made up of small unit cells. Unit cells have varying characteristics such as $\dot{m}_c$, convective efficiency, and discharge coefficient. Therefore, it is possible to engineer different unit cells that can be fitted on the different parts of the aerofoil wall depending on the aerofoil wall cooling requirements. For instance, fitting a low-mass-flow high-internal-convection unit cells on transonic flow region of the aerofoil SS where excess coolant bleeding out of the outer wall is undesirable owing to high aerodynamic losses.

By understanding optimization, (1) a relatively uniform blade temperature and hence reduced thermal stresses is realizable. (2) Coolant mass flow is optimized; by only effusing a controlled amount of coolant onto the surface (and in an accurate amount) in areas where cooling air is required. (3) Aerodynamic losses are minimized because of optimized and controlled ejection of coolant onto the surface, particularly on the suction of the aerofoil where aerodynamic losses are high.

8.3 Flow Visualisation

This work has investigated film cooling effectiveness performance and reported the results in Chapter 6. However, flow visualisation, for instance using smoke and optical techniques, could offer additional information about the mixing of the coolant and mainstream flow. This would give non-quantitative data about the mixing processes for further understanding of double-wall cooling technology.

8.4 Investigate Aerodynamic Losses

Aerodynamic loss is a big topic when it comes to full-coverage film cooling on a turbine aerofoil. Even though full-coverage film cooling results in a transpiration-like coolant film coverage on the surface of the blade, it leads to additional aerodynamic losses especially in the vicinity of the transonic flow region of the blade suction surface. The loss measurement tests would therefore investigate aerodynamic losses associated with the full-coverage film cooling on a double-wall turbine rotor blade, paving way for mass flow cooling optimization.

8.5 Investigate double-wall blade weight and the impact on turbine disc sizing

As afore mentioned in Chapter 1, gas turbine rotor disc is generally subjected to a combination of thermal load, aerodynamic load and centrifugal load - with a large proportion of centrifugal load emanating from turbine blades. Therefore, turbine rotor weight has a direct impact on the stresses experienced by the turbine rotor disc and by extension its life. An investigation should be conducted on the double-wall blade weight and the impact on gas turbine disc sizing.

8.6 Repeat simplified model analysis at other pressure ratios

For the present study, simplified analysis model in Chapter 3 considered a coolant total pressure corresponding to PR=1.00. It is recommended that numerical simulations using the developed simplified analysis tool be repeated at other pressure ratios.

8.7 Repeat the experiment at the same blowing ratios as the fully coupled CHT

The experimental and numerical data in the present study have been compared at almost similar pressure ratios, $0.98 \geq PR \leq 1.27$. Owing to difference in density ratios between the experiments and the CFD, blowing ratio was not matched. It is recommended that experiments be repeated at the same blowing ratios as those used for the fully coupled CHT.

References

Ahn, J., Schobeiri, M. T., Han, J.-C., and Moon, H.-K. (2006). Film Cooling Effectiveness on the Leading Edge Region of a Rotating Turbine Blade with Two Rows of Film Cooling Holes Using Pressure Sensitive Paint. *Journal of Heat Transfer, 128(9), 879-888*.

Amaral, S.and Verstraete, T., Van den B., R., and Arts, T. (2010). Design and Optimization of the Internal Cooling Channels of a High Pressure Turbine Blade—Part I: Methodology. *ASME J. Turbomach., 132(2), 021013*.

Ames, F. E. (1998). Aspects of Vane Film Cooling With High Turbulence: Part II—Adiabatic Effectiveness. In *ASME Journal of Turbomach. 120(4), 777-784*.

Andrei, L., Andreini, A., Facchini, B., and Winchler, L. (2014). A Decoupled CHT Procedure: Application and Validation on a Gas Turbine Vane with Different Cooling Configurations. *Energy Procedia, 45, 1087-1096*.

Andreini, A., Bonini, A., Da Soghe, R., Facchini, B., Ciani, A., and Innocenti, L. (2012). Conjugate Heat Transfer Calculations on GT Rotor Blade for Industrial Applications. Part II: Improvement of External Flow Modeling. In *ASME Paper No. GT2012-69849*.

Andrews, G. E. and Asere, A. A. (2013). Transpiration Cooling of Gas Turbine Combustion Chamber Walls. In *1st UK National Heat Transfer Conference, Leeds, I. Chem. E. Symposium Series*, number 86, pages 1047–1056.

Andrews, G. E., Asere, A. A., Gupta, M. L., and Mkpadi, M. C. (1985). Transpiration and Full Coverage Discrete Hole Film Cooling. *ASME Paper No. 85-GT-47*.

Andrews, G. E., Asere, A. A., Gupta, M. L., Mkpadi, M. C., and Tirmahi, A. (1990). Full Coverage Discrete Hole Film Cooling: The Influence of the Number of Holes and Pressure Loss. In *ASME Paper No. 90-GT-061*. American Society of Mechanical Engineers Digital Collection.

Andrews, G. E., Asere, A. A., Mkpadi, M. C., and Tirmahi, A. (1986). Transpiration Cooling: Contribution of Film Cooling to the Overall Cooling Effectiveness. *ASME Paper No. 86-GT-136*, 3.

ANSYS (2013). *ANSYS Fluent User's Guide*. ANSYS, Inc, 275 Technology Drive, Canonsburg, PA 15317.

Anyoji, M., Numata, D., Nagai, H., and Asai, K. (2015). Pressure-Sensitive Paint Technique for Surface Pressure Measurements in a Low-Density Wind Tunnel. *Journal of visualization, 18(2), 297-309*.

Astarita, T., Cardone, G., de Luca, L., and Carlomagno, G. M. (2015). Some Experimental Investigations on Gas Turbine Cooling Performed with Infrared Thermography at Federico II. *International Journal of Rotating Machinery, Paper ID. 890414*.

Baldauf, S., Scheurlen, M., Schulz, A., and Wittig, S. (2002). Correlation of Film-Cooling Effectiveness From Thermographic Measurements at Enginelike Conditions. *ASME Paper No. GT2002-30180*.

Baldauf, S., Schulz, A., and Wittig, S. (1999). High Resolution Measurements of Local Effectiveness from Discrete Hole Film Cooling. In *ASME J. Turbomach. 123(4), 758-765*.

Baldauf, S., Schulz, A., Wittig, S., and Schleurlen, M. (1997). An Overall Correlation of Film Cooling Effectiveness from One Row of Holes. *ASME Paper No. 97-GT-079*.

Battisti, L., Fedrizzi, R., and Cerri, G. (2006). Novel Technology for Gas Turbine Blade Effusion Cooling. In *ASME Paper No. GT2006-90516*.

Berhe, M. K. and Patankar, S. V. (1999). Curvature Effects on Discrete-Hole Film Cooling. *ASME J. Turbomach., 121(4), 781-791*.

Bernard, A., Brizzi, L.-E., and Bousgarbies, J.-L. (1999). Study of Several Jets Impinging on a Plane Wall: Visualizations and Laser Velocimetry Investigations. *Journal of Fluids Engineering 121(4), 808-812*.

Bohn, D. (1995). Combined Aerodynamic and Thermal Analysis of a High-Pressure Turbine Nozzle Guide Vane. *In Proceedings of the 1995 Yokohama International Gas Turbine Congress : October 22 - October 27, 1, 35-39*.

Bohn, D., Becker, V. J., and Kusterer, K. A. (1997). 3-D Conjugate Flow and Heat Transfer Calculations of a Film-Cooled Turbine Guide Vane at Different Operation Conditions. In *ASME Paper No. 97-GT-023*.

Bonini, A., Andreini, A., Carcasci, C., Facchini, B., Ciani, A., and Innocenti, L. (2012). Conjugate Heat Transfer Calculations on GT Rotor Blade for Industrial Applications: Part I—Equivalent Internal Fluid Network Setup and Procedure Description. *ASME Paper No. GT2012-6984*.

Boyce, M. P. (2011). *Gas Turbine Engineering Handbook*. Elsevier Science.

Brown, S. F. (1990). 21st Century Hot Jet Engines. *Popular Science, 236(6), 83-89*.

BSI (2005). BS EN ISO 9300:2005 - Measurement of Gas Flow by Means of Critical Flow Venturi Nozzles.

Bunker, R. S. (2005). A Review of Shaped Hole Turbine Film-Cooling Technology. *Journal of Heat Transfer 127(4), 441-453*.

Bunker, R. S. (2006). Gas Turbine Heat Transfer: Ten Remaining Hot Gas Path Challenges. *ASME J. Turbomach., 129(2), 193-201*.

Bunker, R. S. (2013). Gas Turbine Cooling: Moving from Macro to Micro Cooling. In *ASME Paper No. GT2013-94277*.

Bunker, R. S., Dees, J. E., and Palafox, P. (2014). Impingement Cooling in Gas Turbines: Design, Applications, and Limitations. *Impingement Jet Cooling in Gas Turbines, 25, 1*.

Cho, H. H. and Rhee, D. H. (2000). Local Heat/Mass Transfer Measurement on the Effusion Plate in Impingement/Effusion Cooling Systems. *ASME Journal of Turbomachinery, 123(3), 601-608*.

Cho, H. H., Rhee, D. H., and Goldstein, R. (2008). Effects of hole arrangements on local heat/mass transfer for impingement/effusion cooling with small hole spacing. *Journal of turbomachinery*, 130(4):041003.

Chowdhury, N. H. K., Zirakzadeh, H., and Han, J.-C. (2017). A Predictive Model for Preliminary Gas Turbine Blade Cooling Analysis. *ASME J. Turbomach., 139(9), 091010*.

Colban, W. F., Thole, K. A., and Bogard, D. (2010). A Film-Cooling Correlation for Shaped Holes on a Flat-Plate Surface. *ASME J. Turbomach., 133(1), 011002*.

Colladay, R. S. (1972). Analysis and Comparison of Wall Cooling Schemes for Advanced Gas Turbine Applications. Technical report, No. NASA-TN-D-6633, E-6439, NASA Lewis Research Center; Cleveland, OH, USA.

Cutbirth, J. M. and Bogard, D. G. (2001). Thermal Field and Flow Visualization Within the Stagnation Region of a Film Cooled Turbine Vane. In *ASME J. Turbomach., 124(2), 200-206*.

Denton, J. D. (1993). Loss Mechanisms in Turbomachines. *ASME Paper No. 93-GT-435*.

Dring, R. P., Blair, M. F., and Joslyn, H. D. (1980). An Experimental Investigation of Film Cooling on a Turbine Rotor Blade. *Journal of Engineering for Power, 102(1), pp. 81-87*.

Dyson, T. E., Bogard, D. G., and Bradshaw, S. D. (2012). Evaluation of CFD Simulations of Film Cooling Performance in the Showerhead Region of a Turbine Vane Including Conjugate Effects. In *ASME Paper No: IMECE2012-88386*, pages 1977–1986. American Society of Mechanical Engineers Digital Collection.

Dyson, T. E., Bogard, D. G., and Bradshaw, S. D. (2014). Evaluation of CFD Simulations of Film Cooling Performance on a Turbine Vane Including Conjugate Heat Transfer Effects. *ASME Paper No. GT2012-69107*.

Eckert, E. R. G. (1956). Engineering Relations for Heat Transfer and Friction in High-Velocity Laminar and Turbulent Boundary-Layer Flow Over Surfaces with Constant Pressure and Temperature. *Transactions of the ASME, 78(6), 1273-1283*.

Epstein, A. H. (2014). Aeropropulsion for Commercial Aviation in the Twenty-First Century and Research Directions Needed. *AIAA Journal, 52(5), 901-911*.

Esch, T. (2003). Heat Transfer Predictions Based on Two-Equation Turbulence Models with Advanced Wall Treatment. *Turbul. Heat Mass Transfer, 4, 633-640.*

Facchini, B., Magi, A., and Del Greco, A. S. (2004). Conjugate Heat Transfer Simulation of a Radially Cooled Gas Turbine Vane. *ASME Paper No. GT2004-54213*.

Folayan, C. O. and Whitelaw, J. H. (1976). The Effectiveness of Two-Dimensional Film-Cooling Over Curved Surfaces. In *American Society of Mechanical Engineers and American Institute of Chemical Engineers, Heat Transfer Conference, St. Louis, Aug. 9-11, p. 11*.

Friedrichs, S. and Hodson, H. P. (1994). The Ammonia and Diazo Surface Coating Technique for Measuring Adiabatic Film Cooling Effectiveness. In *12th Symp. on Measuring Techniques for Transonic and Supersonic Flows in Cascades and Turbomachines, The Czech Republic, Prague, 12-13 September 1994*.

Funazaki, K., Tarukawa, Y., Kudo, T., Matsuno, S., Imai, R., and Yamawaki, S. (2001). Heat Transfer Characteristics of an Integrated Cooling Configuration for Ultra-High Temperature Turbine Blades: Experimental and Numerical Investigations. *ASME Paper Number 2001-GT-148*.

Gao, Z., Narzary, D. P., and Han, J.-C. (2008). Film Cooling on a Gas Turbine Blade Pressure Side or Suction Side with Axial Shaped holes. *International Journal of Heat and Mass Transfer, 51(9-10), 2139-2152*.

Gao, Z., Narzary, D. P., and Han, J.-C. (2009). Film-Cooling on a Gas Turbine Blade Pressure Side or Suction Side with Compound Angle Shaped Holes. *ASME J. Turbomach., 131(1), 011019*, 131(1):011019.

Garg, V. K. (2000). Heat Transfer on a Film-Cooled Rotating Blade. *International Journal of Heat and Fluid Flow, 21(2), 134-145*.

Gaugler, R. E. and Lee, C.-M. (2001). The NASA Glenn Research Center General Multi-Block Navier-Stokes Heat Transfer Code. Technical report, NASA Glenn Research Center, Cleveland, Ohio, USA.

Goldstein, R. J. (1971). Film Cooling. In *Advances in Heat Transfer*, volume 7, pages 321–380. Academic press, New York, USA.

Goldstein, R. J. and Chen, H. P. (1985). Film Cooling on a Gas Turbine Blade Near the End Wall. *Journal of Engineering for Gas Turbines and Power, 107(1), 117-122*.

Gritsch, M., Schulz, A., and Wittig, S. (1998). Heat Transfer Coefficient Measurements of Film-Cooling Holes with Expanded Exits. *ASME Paper No. 98-GT-028*.

Gritskevich, M. and Hohenstein, S. (2017). Assessment of Modern RANS Models for the C3X Vane Film Cooling Prediction. *International Journal of Mechanical, Aerospace, Industrial, Mechatronic and Manufacturing Engineering, 11(6), 1160-1167*.

Gurram, N., Ireland, P. T., Wong, T. H., and Self, K. P. (2016). Study of Film Cooling in the Trailing Edge Region of a Turbine Rotor Blade in High Speed Flow Using Pressure Sensitive Paint. In *ASME Paper No. GT2016-57356*.

Han, J.-C., Dutta, S., and Ekkad, S. (2012). *Gas Turbine Heat Transfer and Cooling Technology*. CRC Press, Taylor & Francis Group.

Hay, N. Lampard, D. and Benmansour, S. (1983). Effect of Crossflows on the Discharge Coefficient of Film Cooling Holes. *Journal of Engineering for Power, 105(2), 243-248*.

Heidmann, J. D., Kassab, A. J., Divo, E. A., Rodriguez, F., and Steinthorsson, E. (2003). Conjugate Heat Transfer Effects on a Realistic Film-Cooled Turbine Vane. *ASME Paper No. GT2003-38553*.

Ho, K.-S., Liu, J. S., Elliott, T., and Aguilar, B. (2016). Conjugate Heat Transfer Analysis for Gas Turbine Film-Cooled Blade. *ASME Paper No. GT2016-56688*.

Ho, K.-S., Urwiller, C., Konan, S. M., Liu, J. S., and Aguilar, B. (2012). Conjugate Heat Transfer Analysis for Gas Turbine Cooled Stator. *ASME Paper No. GT2012-68196*.

Ho, K.-S., Urwiller, C., Konan, S. M., Liu, J. S., and Aguilar, B. (2014). Conjugate Heat Transfer Analysis for Gas Turbine Cooled Blade. *ASME Paper No. GT2014-25952*.

Holland, M. J. and Thake, T. F. (1980). Rotor Blade Cooling in High Pressure Turbines. *Journal of Aircraft, 17(6), 412-418*.

Hong, S. K., Rhee, D.-H., and Cho, H. H. (2007). Effects of Fin Shapes and Arrangements on Heat Transfer for Impingement/ Effusion Cooling with Crossflow. *Journal of Heat Transfer, 129(12), 1697-1707*.

Hylton, L. D., Mihelc, M. S., Turner, E. R., Nealy, D. A., and York, R. E. (1983). Analytical and Experimental Evaluation of the heat Transfer Distribution Over the Surfaces of Turbine Vanes. Technical report, Technical Report No. NASA-CR-168015, NAS 1.26:168015, EDR-11209, NASA, Detroit Diesel Allison; Indianapolis, United States.

Ireland, P. T., Green, N., Romero, E., and Ngetich, G. C. (2019). A Blade and a Method of Manufacturing a Blade. US Patent Number: US 2019/0323359 A1.

ISO (1991). ISO 5167-1 - Measurement of Fluid Flow by Means of Pressure-Differential Devices - Part 1: Orifice Plates, Nozzles and Venturi Tubes Inserted in Circular Cross-Section Conduits Running Full .

ISSI (2012). UniFIB Pressure Sensitive Paint Datasheet. *Innovative Scientific Solutions, Inc.*

Ito, S., Goldstein, R. J., and Eckert, E. R. G. (1978). Film Cooling of a Gas Turbine Blade. *Journal of Engineering for Power 100(3), 476-481*.

Je-Chin, H. and Akhilesh, P. R. (2010). Turbine Blade Film Cooling Using PSP Technique. *Heat Mass Transfer, 1, 1-16*.

Jiang, Y., He, L., Capone, L., and Romero, E. (2016). Investigation of Steady and Unsteady Film-Cooling Using Immersed Mesh Blocks with New Conservative Interface Scheme. *ASME Paper No. GT2016-57363*.

Kasagi, N., Hirata, M., Makino, M., Ikeyama, M., and Kumada, M. (1987). Effects of the Wall Curvature on the Full-Coverage Film Cooling Effectiveness. In *Heat Transfer and Fluid Flow in Rotating Machinery, 103-112*.

Kassab, A., Divo, E., Heidmann, J., Steinthorsson, E., and Rodriguez, F. (2003). BEM/FVM Conjugate Heat Transfer Analysis of a Three-Dimensional Film Cooled Turbine Blade. *International Journal of Numerical Methods for Heat and Fluid Flow, 13(5-6), 581-610*.

Kays, W. M. and Crawford, M. E. (1993). *Convective Heat and Mass Transfer*. McGraw-Hill, New York, USA.

Koff, B. L. (2004). Gas turbine technology evolution: A designers perspective. *Journal of Propulsion and Power, 20(4), 577-595*.

Krewinkel, R. (2013). A Review of Gas Turbine Effusion Cooling Studies. *International Journal of Heat and Mass Transfer, 66, 706-722*.

Kusterer, K., Jens, D., René, J. B., Ryota, T., Tomoki, T., and Dieter, B. (2016). Conjugate Heat Transfer Simulations for a Film Cooled Nozzle Guide Vane of a High-Efficiency, Industrial Gas Turbine. In *International Symposium on Transport Phenomena and Dynamics of Rotating Machinery Hawaii, Honolulu, April 10-15*.

Lad, B. and He, L. (2013). Use of an Immersed Mesh for High Resolution Modeling of Film Cooling Flows. *ASME Journal of Turbomachinery, 135(1), 011022*.

Langston, L. S. (1980). Crossflows in a Turbine Cascade Passage. *Journal of Engineering for Power 102(4), 866-874*.

Laschet, G. (2004). Homogenization of the Fluid Flow and Heat Transfer in Transpiration Cooled Multi-Layer Plates. *ASME Paper No. GT2003-38439*.

Laschet, G., Krewinkel, R., Hul, P., and Bohn, D. (2013). Conjugate Analysis and Effective Thermal Conductivities of Effusion-Cooled Multi-Layer Blade Sections. *International Journal of Heat and Mass Transfer 57(2), 812-821*.

Laschet, G., Rex, S., Bohn, D., and Moritz, N. (2002). 3-D Conjugate Analysis of Cooled Coated Plates and Homogenization of their Thermal Properties. *Numerical Heat Transfer: Part A: Applications, 42(1-2), 91-106*.

L'Ecuyer, M. R. and Soechting, F. O. (1985). A Model for Correlating Flat Plate Film Cooling Effectiveness for Rows of Round Holes. *Fluid Mechanics and Heat Transfer, N86-29823 21-07*.

Ledezma, G. A., Laskowski, G. M., and Tolpadi, A. K. (2008). Turbulence Model Assessment for Conjugate Heat Transfer in a High Pressure Turbine Vane Model. *ASME Paper No. GT2008-50498*.

Lefebvre, A. H. (1998). *Gas Turbine Combustion*. Hemisphere Pub. Corp.

Luo, J. and Razinsky, E. H. (2007). Conjugate Heat Transfer Analysis of a Cooled Turbine Vane Using the V2F Turbulence Model. *ASME J. Turbomach., 129(4), 773-781*.

Lynch, S. P., Thole, K. A., Kohli, A., and Lehane, C. (2011). Computational Predictions of Heat Transfer and Film-Cooling for a Turbine Blade with Nonaxisymmetric Endwall Contouring. *ASME J. Turbomach., 133(4), 041003*.

Mayle, R. E. (1991). The Role of Laminar-Turbulent Transition in Gas Turbine Engines. *ASME Paper No. 91-GT-261*.

Mendez, S., Nicoud, F., and Poinsot, T. (2007). Large-Eddy Simulation of a Turbulent Flow around a Multi-Perforated Plate. In *Complex Effects in Large Eddy Simulations*, pages 289–303. Springer Berlin Heidelberg, Berlin, Heidelberg.

Menter, F. and Esch, T. (2001). Elements of Industrial Heat Transfer Predictions. In *16th Brazilian Congress of Mechanical Engineering (COBEM), 109, p 650*.

Menter, F., Ferruira, C. J., Esch, T., and Konno, B. (2003). The SST Turbulence Model with Improved Wall Treatment for Heat Transfer Predictions in Gas Turbines. *International Gas Turbine Congress Paper No. IGTC2003-TS-059*.

Metzger, D. E. and Bunker, R. S. (1990). Local Heat Transfer in Internally Cooled Turbine Airfoil Leading Edge Regions: Part II—Impingement Cooling with Film Coolant Extraction. *Journal of Turbomachinery, 112(3), 459-466*.

Mhetras, S., Han, J.-C., and Rudolph, R. (2012). Effect of Flow Parameter Variations on Full Coverage Film-Cooling Effectiveness for a Gas Turbine Blade. *ASME J. Turbomach 134(1), 011004*.

Mick, Y., Wörz, B., Findeisen, E., Jeschke, P., and Caspary, V. (2013). Study on Relevant Effects Concerning Heat Transfer of a Convection Cooled Gas Turbine Blade Under Realistic Engine Temperature Conditions. *ASME Paper No. GT2013-94185*.

Moffat, R. J. (1988). Describing the Uncertainties in Experimental Results. *Experimental thermal and fluid science, 1(1), 3-17*.

Moritz, N., Kusterer, K., Bohn, D., Sugimoto, T., Tanaka, R., and Taniguchi, T. (2013). Conjugate Calculation of a Film-Cooled Blade for Improvement of the Leading Edge Cooling Configuration. *Journal of Propulsion and Power Research, 2(1), 1-9*.

Murray, A. V. (2019). *Advanced Gas Turbine Cooling: Double-Wall Turbine Cooling Technologies in Turbine NGV/Blade Applications*. PhD thesis, DPhil Thesis, University of Oxford.

Murray, A. V., Ireland, P. T., and Rawlinson, A. J. (2017). An Integrated Conjugate Computational Approach for Evaluating the Aerothermal and Thermomechanical Performance of Double-Wall Effusion Cooled Systems. *ASME Paper No. GT2017-64711*.

Murray, A. V., Ireland, P. T., Wong, T. H., Tang, S. W., and Rawlinson, A. J. (2018). High Resolution Experimental and Computational Methods for Modelling Multiple Row Effusion Cooling Performance. *International Journal of Turbomachinery, Propulsion and Power, 3(1), 4*.

Nam, Y., Rhee, D., and Cho, H. (2003). Heat Transfer in Impingement/Effusion Cooling System with Rib Turbulators. In *Proceedings of the International Gas Turbine Congress 2003 Tokyo, November 2-7, 2003*. Citeseer.

Narzary, D. P., Liu, K. C., Rallabandi, A. P., and Han, J. C. (2012). Influence of Coolant Density on Turbine Blade Film-Cooling using Pressure Sensitive Paint Technique. *ASME J. Turbomach., 134(3), 031006*.

Ngetich, G. C., Ireland, P. T., Murray, A. V., and Romero, E. (2019a). Study of Film Cooling Effectiveness on a Double-Walled Effusion-Cooled Turbine Blade in a High-Speed Flow Using Pressure Sensitive Paint. *ASME Paper No. GT2019-90545*.

Ngetich, G. C., Murray, A. V., Ireland, P. T., and Romero, E. (2019b). A Three-Dimensional Conjugate Approach for Analyzing a Double-Walled Effusion-Cooled Turbine Blade. *ASME Journal of Turbomachinary, 141(1), 011002*.

Polezhaev, J. (1997). The Transpiration Cooling for Blades of High Temperatures Gas Turbine. *Energy Conversion and Management Paper No. 38(10-13), 1123-1133*, (10-13).

Rallabandi, A. P., Li, S.-J., and Han, J.-C. (2010). Unsteady Wake and Coolant Density Effects on Turbine Blade Film Cooling using PSP Technique. *ASME Paper No. IHTC14-22911*.

Rhee, D. H., Choi, J. H., and Cho, H. H. (2003). Heat (Mass) Transfer on Effusion Plate in Impingement/Effusion Cooling Systems. *Journal of Thermophysics and Heat Transfer, 17(1), 95-102*.

Rogers, T. and Hersh, A. (1976). The Effect of Grazing Flow on the Steady State Resistance of Square-Edged Orifices. In *AIAA Paper No. 75-493*.

Rolls-Royce (2015). *The Jet Engine*. John Wiley & Sons.

Rowbury, D. A., Oldfield, M. L. G., and Lock, G. D. (2001). Large-Scale Testing to Validate the Influence of External Crossflow on the Discharge Coefficients of Film Cooling Holes. *ASME J. Turbomach, 123(3), 593-600*.

Sellers, J. P. (1963). Gaseous Film Cooling with Multiple Injection Stations. *AIAA Journal, 1(9), 2154-2156*.

Sharma, O. P. and Butler, T. L. (1987). Predictions of Endwall Losses and Secondary Flows in Axial Flow Turbine Cascades. *ASME Journal of Turbomachinery, 109(2), 229-236*.

Sipatov, A., Gomzikov, L., Latyshev, V., and Gladysheva, N. (2009). Three Dimensional Heat Transfer Analysis of High Pressure Turbine Blade. *ASME Paper No. GT2009-59153*.

Son, C., Gillespie, D., Ireland, P., and Dailey, G. M. (2001). Heat Transfer Characteristics of an Impingement Plate Used in a Turbine Vane Cooling System. *ASME Paper No. 2001-GT-154*.

Sweeney, P. C. and Rhodes, J. F. (1999). An Infrared Technique for Evaluating Turbine Airfoil Cooling Designs. *ASME J. Turbomach., 122(1), 170-177*.

Takahashi, T., Watanabe, K., and Sakai, T. (2005). Conjugate Heat Transfer Analysis of a Rotor Blade with Rib-Roughened Internal Cooling Passages. *ASME Paper No. GT2005-68227*.

Takeishi, K., Aoki, S., Sato, T., and Tsukagoshi, K. (1992). Film Cooling on a Gas Turbine Rotor Blade. *ASME J. Turbomach., 114(4), 828-834*.

Tianshu, L., Guille, M., and Sullivan, J. P. (2001). Accuracy of Pressure-Sensitive Paint. *AIAA Journal, 39(1), 103-112*.

Tsukamoto, K., Horiuchi, Y., Sugimura, K., and Higuchi, S. (2014). Conjugate Heat Transfer Analysis in an Actual Gas Turbine Rotor Blade in Comparison with Pyrometer Data. *ASME Paper No. GT2014-26962*.

Wadia, A. R. (1988). Advanced Combustor Liner Cooling Technology for Gas Turbines. *Defence Science Journal, 38(4), 363-380*.

Wambersie, A. (2019). *Modeling Cooling Effectiveness of Transpiration Cooled Turbine Blade*. PhD thesis, Transfer of Status Report, University of Oxford, August 2019.

Wassell, A. B. and Bhangu, J. K. (1980). The Development and Application of Improved Combustor Wall cooling Techniques. *ASME Paper No. 80-GT-66*.

Witek, L. (2006). Failure Analysis of Turbine Disc of an Aero Engine. *Engineering Failure Analysis, 13(1), 9-17*.

Wong, T. H. (2018). *Novel Cooling Design for Blade or Vane Trailing Edges*. PhD thesis, DPhil Thesis, University of Oxford.

Zecchi, S., Arcangeli, L., Facchini, B., and Coutandin, D. (2004). Features of a Cooling System Simulation Tool used in Industrial Preliminary Design Stage. *ASME Paper No. GT2004-53547*.

Appendix A

Patent Application Number GB1806542.5; An Alternative DWEC Aerofoil Manufacturing Approach

Abstract

Disclosed herein is a method of manufacturing a double walled section of an aerofoil (701) of a gas turbine engine (10), the method comprising: forming a plurality of columns (402) on an outer surface of a first structure; forming a plurality of columns (402) on a surface of each of a plurality of parts of a second structure; and forming a double walled section of an aerofoil (701) by attaching the ends of columns (402) on each part of the second structure to the ends of columns (402) on the first structure such that the first structure is an inner wall (401) of the section of the aerofoil (701) and the second structure is an outer wall (501) of the section of the aerofoil (701).

Patent Description

The present disclosure relates to the manufacture of a blade for use in a gas turbine engine. More particularly, the present disclosure is of a manufacturing technique of a blade with a double walled section. The blade may be used as one of the blades in the turbine of a gas turbine engine. There is a general need to improve known manufacturing techniques of blades. According to a first aspect there is provided a method of manufacturing a double walled section of an aerofoil of a gas turbine engine, the method comprising: forming a plurality of columns on an outer surface of a first structure; forming a plurality of columns on a surface of each of a plurality of parts of a second structure; and forming a double walled section of an aerofoil by attaching the ends of columns on each part of the second structure to the ends of columns on the first structure such that the first structure is an inner wall of the section of the aerofoil and the second structure is an outer wall of the section of the aerofoil.

The method may comprise forming a plurality of columns on the outer surface of the first

structure by imprinting the columns in its outer surface; and/or for each of the plurality of parts of the second structure, forming a plurality of columns on the surface by imprinting the columns in the surface. The method may comprise imprinting by Electrode Discharge Machining (EDM). The method may comprise performing a smoothing operation that flattens the ends of each of the columns after the columns have been formed. The method may comprise attaching the ends of columns on each part of the second structure to the ends of columns on the first structure by diffusion bonding or brazing the ends of the columns together. The method may comprise forming a plurality of columns on the outer surface of the first structure by a plurality of manufacturing operations with each manufacturing operation forming a plurality of parallel columns in a single region of the first structure; and/or forming a plurality of columns on the surface of each part of the second structure by one or more manufacturing operations with each manufacturing operation forming a plurality of parallel columns in a single region of the second structure.

In the first aspect, a section of the aerofoil may be comprised by a turbine blade or a compressor blade. In the first aspect, the turbine blade or compressor blade may be comprised by a leading-edge region, a mid-chord region and a trailing edge region; and the section of the aerofoil is the leading edge region and mid-chord region of the blade. The method may comprise attaching each part of the second structure to one or more other parts of the second structure. In the first aspect, the first structure may comprise a plurality of parts; and the method may comprise attaching each of the parts of the first structure to one or more other parts of the first structure. In the first aspect, the first structure and/or one or more parts of the second structure may be formed by casting. In the first aspect, the first structure and/or one or more parts of the second structure may comprise crystals that are directionally solidified. In the first aspect, the first structure and/or one or more parts of the second structure may be single crystal super alloys. In the first aspect, the first structure may be a walled structure with the walls providing an enclosed inner part of the section of the aerofoil and the second structure may be a walled structure with the walls enclosing the first structure, and the method may further comprise: forming one or more holes through the walls of the first structure; and forming one or more holes through the walls of the second structure, such that air in the inner part of the aerofoil can flow out of the aerofoil via the holes in the first structure and second structures.

The method may comprise positioning the holes in the walls of the first structure staggered with respect to the positioning of the holes in the walls of the second structure. According to a second aspect there is provided an aerofoil that is manufactured according to the method of the first aspect. According to a third aspect there is provided a double walled section of an aerofoil of a gas turbine engine, the double walled section of the aerofoil comprising: an inner wall with a plurality of columns protruding from its outer surface; an outer wall with a plurality of columns protruding from its inner surface; joints between the end surfaces of the columns on the inner wall and the end surfaces of the columns on the outer wall. In the third aspect, the joints may be diffusion bonds or braised connections. In the third aspect, the columns may be grouped to provide one or more interface regions; and within each of the interface regions, the joints between the ends of the columns are all in the same plane. In the third aspect, the section of the aerofoil may be comprised by a turbine blade or a compressor blade. In the third aspect, the turbine blade or compressor blade has a leading-edge region, a mid-chord region and a trailing edge region; and the section of the aerofoil is the leading edge region and mid-chord region.

According to a fourth aspect, there is provided a gas turbine engine for an aircraft comprising: an engine core comprising a turbine, a compressor, and a core shaft connecting the

turbine to the compressor; a fan located upstream of the engine core, the fan comprising a plurality of fan blades; and a gearbox that receives an input from the core shaft and outputs drive to the fan so as to drive the fan at a lower rotational speed than the core shaft; wherein one or more of the turbine and compressor comprise one or more sections of an aerofoil according to the third aspect. In the fourth aspect, the turbine may be a first turbine, the compressor may be a first compressor, and the core shaft may be a first core shaft; the engine core may further comprise a second turbine, a second compressor, and a second core shaft connecting the second turbine to the second compressor; and the second turbine, second compressor, and second core shaft may be arranged to rotate at a higher rotational speed than the first core shaft; wherein one or more of the second turbine and second compressor comprise one or more sections of an aerofoil according to the third aspect. As noted elsewhere herein, the present disclosure may relate to a gas turbine engine. Such a gas turbine engine may comprise an engine core comprising a turbine, a combustor, a compressor, and a core shaft connecting the turbine to the compressor. Such a gas turbine engine may comprise a fan (having fan blades) located upstream of the engine core.

Arrangements of the present disclosure may be particularly, although not exclusively, beneficial for fans that are driven via a gearbox. Accordingly, the gas turbine engine may comprise a gearbox that receives an input from the core shaft and outputs drive to the fan so as to drive the fan at a lower rotational speed than the core shaft. The input to the gearbox may be directly from the core shaft, or indirectly from the core shaft, for example via a spur shaft and/or gear. The core shaft may rigidly connect the turbine and the compressor, such that the turbine and compressor rotate at the same speed (with the fan rotating at a lower speed).

The gas turbine engine as described and/or claimed herein may have any suitable general architecture. For example, the gas turbine engine may have any desired number of shafts that connect turbines and compressors, for example one, two or three shafts. Purely by way of example, the turbine connected to the core shaft may be a first turbine, the compressor connected to the core shaft may be a first compressor, and the core shaft may be a first core shaft. The engine core may further comprise a second turbine, a second compressor, and a second core shaft connecting the second turbine to the second compressor. The second turbine, second compressor, and second core shaft may be arranged to rotate at a higher rotational speed than the first core shaft. In such an arrangement, the second compressor may be positioned axially downstream of the first compressor. The second compressor may be arranged to receive (for example directly receive, for example via a generally annular duct) flow from the first compressor.

The gearbox may be arranged to be driven by the core shaft that is configured to rotate (for example in use) at the lowest rotational speed (for example the first core shaft in the example above). For example, the gearbox may be arranged to be driven only by the core shaft that is configured to rotate (for example in use) at the lowest rotational speed (for example only be the first core shaft, and not the second core shaft, in the example above). Alternatively, the gearbox may be arranged to be driven by any one or more shafts, for example the first and/or second shafts in the example above. In any gas turbine engine as described and/or claimed herein, a combustor may be provided axially downstream of the fan and compressor(s). For example, the combustor may be directly downstream of (for example at the exit of) the second compressor, where a second compressor is provided. By way of further example, the flow at the exit to the combustor may be provided to the inlet of the second turbine, where a second turbine is provided. The combustor may be provided upstream of the turbine(s). The or each compressor (for example the first compressor and

second compressor as described above) may comprise any number of stages, for example multiple stages. Each stage may comprise a row of rotor blades and a row of stator vanes, which may be variable stator vanes (in that their angle of incidence may be variable). The row of rotor blades and the row of stator vanes may be axially offset from each other.

The or each turbine (for example the first turbine and second turbine as described above) may comprise any number of stages, for example multiple stages. Each stage may comprise a row of rotor blades and a row of stator vanes. The row of rotor blades and the row of stator vanes may be axially offset from each other. Each fan blade may be defined as having a radial span extending from a root (or hub) at a radially inner gas-washed location, or 0% span position, to a tip at a 100% span position. The ratio of the radius of the fan blade at the hub to the radius of the fan blade at the tip may be less than (or on the order of) any of: 0.4, 0.39, 0.38 0.37, 0.36, 0.35, 0.34, 0.33, 0.32, 0.31, 0.3, 0.29, 0.28, 0.27, 0.26, or 0.25. The ratio of the radius of the fan blade at the hub to the radius of the fan blade at the tip may be in an inclusive range bounded by any two of the values in the previous sentence (i.e. the values may form upper or lower bounds). These ratios may commonly be referred to as the hub-to-tip ratio. The radius at the hub and the radius at the tip may both be measured at the leading edge (or axially forwardmost) part of the blade. The hub-to-tip ratio refers, of course, to the gas-washed portion of the fan blade, i.e. the portion radially outside any platform. The radius of the fan may be measured between the engine centreline and the tip of a fan blade at its leading edge. The fan diameter (which may simply be twice the radius of the fan) may be greater than (or on the order of) any of: 250 cm (around 100 inches), 260 cm, 270 cm (around 105 inches), 280 cm (around 110 inches), 290 cm (around 115 inches), 300 cm (around 120 inches), 310 cm, 320 cm (around 125 inches), 330 cm (around 130 inches), 340 cm (around 135 inches), 350cm, 360cm (around 140 inches), 370 cm (around 145 inches), 380 (around 150 inches) cm or 390 cm (around 155 inches). The fan diameter may be in an inclusive range bounded by any two of the values in the previous sentence (i.e. the values may form upper or lower bounds).

The rotational speed of the fan may vary in use. Generally, the rotational speed is lower for fans with a higher diameter. Purely by way of non-limitative example, the rotational speed of the fan at cruise conditions may be less than 2500 rpm, for example less than 2300 rpm. Purely by way of further non-limitative example, the rotational speed of the fan at cruise conditions for an engine having a fan diameter in the range of from 250 cm to 300 cm (for example 250 cm to 280 cm) may be in the range of from 1700 rpm to 2500 rpm, for example in the range of from 1800 rpm to 2300 rpm, for example in the range of from 1900 rpm to 2100 rpm. Purely by way of further non-limitative example, the rotational speed of the fan at cruise conditions for an engine having a fan diameter in the range of from 320 cm to 380 cm may be in the range of from 1200 rpm to 2000 rpm, for example in the range of from 1300 rpm to 1800 rpm, for example in the range of from 1400 rpm to 1600 rpm. In use of the gas turbine engine, the fan (with associated fan blades) rotates about a rotational axis. This rotation results in the tip of the fan blade moving with a velocity Utip. The work done by the fan blades 13 on the flow results in an enthalpy rise dH of the flow. A fan tip loading may be defined as dH/Utip2, where dH is the enthalpy rise (for example the 1-D average enthalpy rise) across the fan and Utip is the (translational) velocity of the fan tip, for example at the leading edge of the tip (which may be defined as fan tip radius at leading edge multiplied by angular speed). The fan tip loading at cruise conditions may be greater than (or on the order of) any of: 0.3, 0.31, 0.32, 0.33, 0.34, 0.35, 0.36, 0.37, 0.38, 0.39 or 0.4 (all units in this paragraph being Jkg-1K-1/(ms-1)2). The fan tip loading may be in an inclusive range bounded by any two of the values in the previous sentence (i.e. the values may form

upper or lower bounds).

Gas turbine engines in accordance with the present disclosure may have any desired bypass ratio, where the bypass ratio is defined as the ratio of the mass flow rate of the flow through the bypass duct to the mass flow rate of the flow through the core at cruise conditions. In some arrangements the bypass ratio may be greater than (or on the order of) any of the following: 10, 10.5, 11, 11.5, 12, 12.5, 13, 13.5, 14, 14.5, 15, 15.5, 16, 16.5, or 17. The bypass ratio may be in an inclusive range bounded by any two of the values in the previous sentence (i.e. the values may form upper or lower bounds). The bypass duct may be substantially annular. The bypass duct may be radially outside the core engine. The radially outer surface of the bypass duct may be defined by a nacelle and/or a fan case. The overall pressure ratio of a gas turbine engine as described and/or claimed herein may be defined as the ratio of the stagnation pressure upstream of the fan to the stagnation pressure at the exit of the highest pressure compressor (before entry into the combustor). By way of non-limitative example, the overall pressure ratio of a gas turbine engine as described and/or claimed herein at cruise may be greater than (or on the order of) any of the following: 35, 40, 45, 50, 55, 60, 65, 70, 75. The overall pressure ratio may be in an inclusive range bounded by any two of the values in the previous sentence (i.e. the values may form upper or lower bounds).

Specific thrust of an engine may be defined as the net thrust of the engine divided by the total mass flow through the engine. At cruise conditions, the specific thrust of an engine described and/or claimed herein may be less than (or on the order of) any of the following: 110 Nkg-1s, 105 Nkg-1s, 100 Nkg-1s, 95 Nkg-1s, 90 Nkg-1s, 85 Nkg-1s or 80 Nkg-1s. The specific thrust may be in an inclusive range bounded by any two of the values in the previous sentence (i.e. the values may form upper or lower bounds). Such engines may be particularly efficient in comparison with conventional gas turbine engines. A gas turbine engine as described and/or claimed herein may have any desired maximum thrust. Purely by way of non-limitative example, a gas turbine as described and/or claimed herein may be capable of producing a maximum thrust of at least (or on the order of) any of the following: 160kN, 170kN, 180kN, 190kN, 200kN, 250kN, 300kN, 350kN, 400kN, 450kN, 500kN, or 550kN. The maximum thrust may be in an inclusive range bounded by any two of the values in the previous sentence (i.e. the values may form upper or lower bounds). The thrust referred to above may be the maximum net thrust at standard atmospheric conditions at sea level plus 15 deg C (ambient pressure 101.3kPa, temperature 30 deg C), with the engine static. In use, the temperature of the flow at the entry to the high pressure turbine may be particularly high. This temperature, which may be referred to as TET, may be measured at the exit to the combustor, for example immediately upstream of the first turbine vane, which itself may be referred to as a nozzle guide vane. At cruise, the TET may be at least (or on the order of) any of the following: 1400K, 1450K, 1500K, 1550K, 1600K or 1650K. The TET at cruise may be in an inclusive range bounded by any two of the values in the previous sentence (i.e. the values may form upper or lower bounds). The maximum TET in use of the engine may be, for example, at least (or on the order of) any of the following: 1700K, 1750K, 1800K, 1850K, 1900K, 1950K or 2000K. The maximum TET may be in an inclusive range bounded by any two of the values in the previous sentence (i.e. the values may form upper or lower bounds). The maximum TET may occur, for example, at a high thrust condition, for example at a maximum take-off (MTO) condition.

A fan blade and/or aerofoil portion of a fan blade described and/or claimed herein may be manufactured from any suitable material or combination of materials. For example at least a part of the fan blade and/or aerofoil may be manufactured at least in part from a composite, for example a metal matrix composite and/or an organic matrix composite, such as carbon

fibre. By way of further example at least a part of the fan blade and/or aerofoil may be manufactured at least in part from a metal, such as a titanium based metal or an aluminium based material (such as an aluminium-lithium alloy) or a steel based material. The fan blade may comprise at least two regions manufactured using different materials. For example, the fan blade may have a protective leading edge, which may be manufactured using a material that is better able to resist impact (for example from birds, ice or other material) than the rest of the blade. Such a leading edge may, for example, be manufactured using titanium or a titanium-based alloy. Thus, purely by way of example, the fan blade may have a carbon-fibre or aluminium based body (such as an aluminium lithium alloy) with a titanium leading edge. A fan as described and/or claimed herein may comprise a central portion, from which the fan blades may extend, for example in a radial direction. The fan blades may be attached to the central portion in any desired manner. For example, each fan blade may comprise a fixture which may engage a corresponding slot in the hub (or disc). Purely by way of example, such a fixture may be in the form of a dovetail that may slot into and/or engage a corresponding slot in the hub/disc in order to fix the fan blade to the hub/disc. By way of further example, the fan blades maybe formed integrally with a central portion. Such an arrangement may be referred to as a blisk or a bling. Any suitable method may be used to manufacture such a blisk or bling. For example, at least a part of the fan blades may be machined from a block and/or at least part of the fan blades may be attached to the hub/disc by welding, such as linear friction welding. The gas turbine engines described and/or claimed herein may or may not be provided with a variable area nozzle (VAN). Such a variable area nozzle may allow the exit area of the bypass duct to be varied in use. The general principles of the present disclosure may apply to engines with or without a VAN. The fan of a gas turbine as described and/or claimed herein may have any desired number of fan blades, for example 16, 18, 20, or 22 fan blades.

As used herein, cruise conditions may mean cruise conditions of an aircraft to which the gas turbine engine is attached. Such cruise conditions may be conventionally defined as the conditions at mid-cruise, for example the conditions experienced by the aircraft and/or engine at the midpoint (in terms of time and/or distance) between top of climb and start of decent. Purely by way of example, the forward speed at the cruise condition may be any point in the range of from Mach 0.7 to 0.9, for example 0.75 to 0.85, for example 0.76 to 0.84, for example 0.77 to 0.83, for example 0.78 to 0.82, for example 0.79 to 0.81, for example on the order of Mach 0.8, on the order of Mach 0.85 or in the range of from 0.8 to 0.85. Any single speed within these ranges may be the cruise condition. For some aircraft, the cruise conditions may be outside these ranges, for example below Mach 0.7 or above Mach 0.9. Purely by way of example, the cruise conditions may correspond to standard atmospheric conditions at an altitude that is in the range of from 10000m to 15000m, for example in the range of from 10000m to 12000m, for example in the range of from 10400m to 11600m (around 38000 ft), for example in the range of from 10500m to 11500m, for example in the range of from 10600m to 11400m, for example in the range of from 10700m (around 35000 ft) to 11300m, for example in the range of from 10800m to 11200m, for example in the range of from 10900m to 11100m, for example on the order of 11000m. The cruise conditions may correspond to standard atmospheric conditions at any given altitude in these ranges. Purely by way of example, the cruise conditions may correspond to: a forward Mach number of 0.8; a pressure of 23000 Pa; and a temperature of -55 deg C.

As used anywhere herein, “cruise” or “cruise conditions” may mean the aerodynamic design point. Such an aerodynamic design point (or ADP) may correspond to the conditions (comprising, for example, one or more of the Mach Number, environmental conditions and

thrust requirement) for which the fan is designed to operate. This may mean, for example, the conditions at which the fan (or gas turbine engine) is designed to have optimum efficiency. In use, a gas turbine engine described and/or claimed herein may operate at the cruise conditions defined elsewhere herein. Such cruise conditions may be determined by the cruise conditions (for example the mid-cruise conditions) of an aircraft to which at least one (for example 2 or 4) gas turbine engine may be mounted in order to provide propulsive thrust. The skilled person will appreciate that except where mutually exclusive, a feature or parameter described in relation to any one of the above aspects may be applied to any other aspect. Furthermore, except where mutually exclusive, any feature or parameter described herein may be applied to any aspect and/or combined with any other feature or parameter described herein.

Embodiments will now be described by way of example only, with reference to the Figures, in which:

- Figure 1 is a sectional side view of a gas turbine engine;
- Figure 2 is a close up sectional side view of an upstream portion of a gas turbine engine;
- Figure 3 is a partially cut-away view of a gearbox for a gas turbine engine;
- Figure 4 is a cross-section of an inner wall of a blade after pedestals have been formed on the inner wall according to an embodiment;
- Figure 5 is a cross-section of both an inner wall and a plurality of parts of an outer wall according to an embodiment;
- Figures 6A and 6B are cross-sections of a blade according to an embodiment;
- Figure 7 shows a blade according to an embodiment with a portion of the blade cut away; and
- Figure 8 is flowchart of a method according to an embodiment.

Figure 1 illustrates a gas turbine engine 10 having a principal rotational axis 9. The engine 10 comprises an air intake 12 and a propulsive fan 23 that generates two airflows: a core airflow A and a bypass airflow B. The gas turbine engine 10 comprises a core 11 that receives the core airflow A. The engine core 11 comprises, in axial flow series, a low pressure compressor 14, a high-pressure compressor 15, combustion equipment 16, a high-pressure turbine 17, a low pressure turbine 19 and a core exhaust nozzle 20. A nacelle 21 surrounds the gas turbine engine 10 and defines a bypass duct 22 and a bypass exhaust nozzle 18. The bypass airflow B flows through the bypass duct 22. The fan 23 is attached to and driven by the low pressure turbine 19 via a shaft 26 and an epicyclic gearbox 30.

In use, the core airflow A is accelerated and compressed by the low pressure compressor 14 and directed into the high pressure compressor 15 where further compression takes place. The compressed air exhausted from the high pressure compressor 15 is directed into the combustion equipment 16 where it is mixed with fuel and the mixture is combusted. The resultant hot combustion products then expand through, and thereby drive, the high pressure and low pressure turbines 17, 19 before being exhausted through the nozzle 20 to provide some propulsive thrust. The high pressure turbine 17 drives the high pressure compressor 15 by a suitable interconnecting shaft 27. The fan 23 generally provides the majority of the propulsive thrust. The epicyclic gearbox 30 is a reduction gearbox.

An exemplary arrangement for a geared fan gas turbine engine 10 is shown in Figure 2. The low pressure turbine 19 (see Figure 1) drives the shaft 26, which is coupled to a sun wheel, or sun gear, 28 of the epicyclic gear arrangement 30. Radially outwardly of the sun gear 28 and intermeshing therewith is a plurality of planet gears 32 that are coupled together by a planet carrier 34. The planet carrier 34 constrains the planet gears 32 to precess around the sun gear 28 in synchronicity whilst enabling each planet gear 32 to rotate about its own axis. The planet carrier 34 is coupled via linkages 36 to the fan 23 in order to drive its rotation about the engine axis 9. Radially outwardly of the planet gears 32 and intermeshing therewith is an annulus or ring gear 38 that is coupled, via linkages 40, to a stationary supporting structure 24.

Note that the terms "low pressure turbine" and "low pressure compressor" as used herein may be taken to mean the lowest pressure turbine stages and lowest pressure compressor stages (i.e. not including the fan 23) respectively and/or the turbine and compressor stages that are connected together by the interconnecting shaft 26 with the lowest rotational speed in the engine (i.e. not including the gearbox output shaft that drives the fan 23). In some literature, the "low pressure turbine" and "low pressure compressor" referred to herein may alternatively be known as the "intermediate pressure turbine" and "intermediate pressure compressor". Where such alternative nomenclature is used, the fan 23 may be referred to as a first, or lowest pressure, compression stage.

The epicyclic gearbox 30 is shown by way of example in greater detail in Figure 3. Each of the sun gear 28, planet gears 32 and ring gear 38 comprise teeth about their periphery to intermesh with the other gears. However, for clarity only exemplary portions of the teeth are illustrated in Figure 3. There are four planet gears 32 illustrated, although it will be apparent to the skilled reader that more or fewer planet gears 32 may be provided within the scope of the claimed invention. Practical applications of a planetary epicyclic gearbox 30 generally comprise at least three planet gears 32.

The epicyclic gearbox 30 illustrated by way of example in Figures 2 and 3 is of the planetary type, in that the planet carrier 34 is coupled to an output shaft via linkages 36, with the ring gear 38 fixed. However, any other suitable type of epicyclic gearbox 30 may be used. By way of further example, the epicyclic gearbox 30 may be a star arrangement, in which the planet carrier 34 is held fixed, with the ring (or annulus) gear 38 allowed to rotate. In such an arrangement the fan 23 is driven by the ring gear 38. By way of further alternative example, the gearbox 30 may be a differential gearbox in which the ring gear 38 and the planet carrier 34 are both allowed to rotate.

It will be appreciated that the arrangement shown in Figures 2 and 3 is by way of example only, and various alternatives are within the scope of the present disclosure. Purely by way of example, any suitable arrangement may be used for locating the gearbox 30 in the engine 10 and/or for connecting the gearbox 30 to the engine 10. By way of further example, the connections (such as the linkages 36, 40 in the Figure 2 example) between the gearbox 30 and other parts of the engine 10 (such as the input shaft 26, the output shaft and the fixed structure 24) may have any desired degree of stiffness or flexibility. By way of further example, any suitable arrangement of the bearings between rotating and stationary parts of the engine (for example between the input and output shafts from the gearbox and the fixed structures, such as the gearbox casing) may be used, and the disclosure is not limited to the exemplary arrangement of Figure 2. For example, where the gearbox 30 has a star arrangement (described above), the skilled person would readily understand that the arrangement of output and support linkages and bearing locations would typically be different to that shown by way of example in Figure 2.

Accordingly, the present disclosure extends to a gas turbine engine having any arrangement of gearbox styles (for example star or planetary), support structures, input and output shaft arrangement, and bearing locations.

Optionally, the gearbox may drive additional and/or alternative components (e.g. the intermediate pressure compressor and/or a booster compressor).

Other gas turbine engines to which the present disclosure may be applied may have alternative configurations. For example, such engines may have an alternative number of compressors and/or turbines and/or an alternative number of interconnecting shafts. By way of further example, the gas turbine engine shown in Figure 1 has a split flow nozzle 20, 22 meaning that the flow through the bypass duct 22 has its own nozzle that is separate to and radially outside the core engine nozzle 20. However, this is not limiting, and any aspect of the present disclosure may also apply to engines in which the flow through the bypass duct 22 and the flow through the core 11 are mixed, or combined, before (or upstream of) a single nozzle, which may be referred to as a mixed flow nozzle. One or both nozzles (whether mixed or split flow) may have a fixed or variable area. Whilst the described example relates to a turbofan engine, the disclosure may apply, for example, to any type of gas turbine engine, such as an open rotor (in which the fan stage is not surrounded by a nacelle) or turboprop engine, for example. In some arrangements, the gas turbine engine 10 may not comprise a gearbox 30.

The geometry of the gas turbine engine 10, and components thereof, is defined by a conventional axis system, comprising an axial direction (which is aligned with the rotational axis 9), a radial direction (in the bottom-to-top direction in Figure 1), and a circumferential direction (perpendicular to the page in the Figure 1 view). The axial, radial and circumferential directions are mutually perpendicular.

The present disclosure provides an improved method of manufacture of a blade. The blades that are manufactured according to the present disclosure can be used as the blades of any of the components of the above-described gas turbine engine 10. The blades that are manufactured according to the present disclosure may be used as either high or low pressure turbine blades. However, the blades according to the present disclosure may be used in any of the other components of the gas turbine engine, such the first or second compressor. In order to clearly present the context of the present disclosure, details of background technology are provided below.

An important property of blades in a gas turbine engine is how efficiently the blades can be cooled. Known techniques for cooling blades include transpiration cooling, as well as similar techniques such a effusion cooling and porous multi-wall cooling. Laminated multi-wall cooling schemes, in which a film is formed over at least part of the surface of the blade, are known to provide a practical implementation of these cooling schemes. The cooling schemes provide good cooling uniformity due to a series of highly distributed micro cooling channels. The heat transfer is also highly efficient as the cooling air is brought close to the outer surface of a blade.

Known multi-wall cooling blade designs with film cooling are disclosed in US6514042B2 and US5702232A. Both of these blades comprise a double wall configuration in the mid-chord region with radial feed passages on each side of the blade between the inner and outer wall. A problem with these known designs of blades is that they are difficult to manufacture. A method of manufacture is described in US5640767A. A partially-hollow blade support wall, that is formed by casting, with a desired outer profile has longitudinally-extending recesses, that are filled with channel fillers. A blade skin of a second material is then deposited, by methods comprising physical, chemical vapour deposition, thermal spraying and

plating, onto the blade support wall such that the skin conforms and is metallurgically bonded to the blade support wall. The recesses' channel filler is removed and the combination of outer blade skin and blade support wall forms a double wall blade structure with the voids in the recess creating an integral internal chamber within the double walled structure. Another known manufacturing method of double walled blades is the Shell-and-Spar approach, as disclosed in Novikov et al, 'Creation of High Efficiency Turbine Cooled Blades With Structural Electron Beam Coatings', in collection of papers Electron Beam and Gas-Thermal Coatings, pages 87 to 97. This is similar to the manufacturing method described in US5640767A.

The known manufacturing techniques of double walled blades therefore comprise additive manufacturing. A problem with this manufacturing technique is that the layering processes introduce imperfections and it is difficult to construct surfaces with intricate details and without defects.The present disclosure provides a new method of manufacturing double walled blades that avoids the problems associated with additive manufacturing processes. The blades may be effusion cooled aerofoils. The blades may be fabricated with a single crystal structure using known materials for blades. The blades may be made with intricate features, high surface quality and high mechanical strength.

The blades according to the present disclosure may be aerofoils that comprise a leading edge region, a mid-chord region and a trailing edge region. The leading edge region and mid-chord region may be constructed with double walls with the trailing edge region only having a single wall. The double wall is provided by an outer wall and an inner wall, which may alternatively be referred to as an outer skin and inner skin. The inner and outer walls are connected to each other by pedestals. A pedestal is a column. The columns can have a variety of shapes and may be linear with a substantially circular cross-section and a constant diameter along their length. The columns may alternatively be linear with a substantially square cross-section that is constant along their length. The pedestals protrude from corresponding surfaces of the inner and outer walls. The ends of the pedestals are flat and can therefore be joined together by, for example, diffusion bonding. The pedestals are effectively pin fins. The inner wall has holes through it that are referred to as impingement holes. The outer wall also has holes through it that are referred to as effusion holes. The impingement and effusion holes are positioned in a staggered arrangement with respect to each other. Accordingly, air can pass from an inner cavity of the blade, that is enclosed by the inner walls, through the impingement holes past the pedestals and out through the effusion holes. The air forms a transpiration-like film on at least part of the outer surface of the blade and is very effective at cooling the blade.

The present disclosure is described in more detail below with reference to Figures 4, 5, 6A, 6B and 7. The inner wall 401 is initially manufactured without pedestals 402 in its surface. The pedestals 402 are then formed in its surface. The initial structure of the inner wall 401 may be manufactured through casting. The cast material may be directionally solidified or single crystal super alloy.

The pedestals 402 may be formed in the surface of the initial structure of the inner wall 401 by an imprinting process that removes material from the surface. The imprinting process may be milling/spark electrode discharge machining, EDM, using a graphite/tungsten tool. The tool may be configured with an exact negative of the desired pedestal pattern and may effectively be plunged into the surface of the initial structure of the inner wall 401 in order to form an array of a plurality of pedestals 402. The pedestals 402 are therefore part of the initial structure of the inner wall 401 and protrude from the surface of the inner wall 401 due to the imprinting process removing material around the pedestals 402 from the surface.

A plurality of imprinting processes are performed over the surface of the initial structure

of the inner wall 401. Figure 4 shows the inner wall 401 after the imprinting processes have been performed. The pedestals 402 formed in each imprinting process are all aligned in the same direction. In order for pedestals 402 to be formed over the entire surface of the inner wall 401, a plurality of imprinting processes may be performed from different directions. The number of directions that the pedestals 402 are aligned in may therefore the same as the number of different directions of the imprinting processes.

After the pedestals 402 have been formed, a smoothing operation may be performed in order to flatten the tops of the pedestals 402. This may also ensure that all of the pedestals 402 have the desired height. The smoothing operation may be, for example, a grinding operation. The distance between two adjacent pedestals 402 on the inner wall 401 may be in the range 0.5mm to 1.5mm. If a pedestal 402 on the inner wall 401 has a substantially square cross-section that is constant along the length of the pedestal 402, the length of a side of the square cross-section of the pedestal 402 may be in the range 0.5mm to 1.5mm. The height of a pedestal 402 on the inner wall 401 after the smoothing operation may be in the range 0.5mm to 1.5mm.

The outer wall 501 may be initially manufactured as a structure with a plurality of separate parts. Each of the parts of the initial structure of the outer wall 501 may be initially manufactured without pedestals 402 in its surface. The pedestals 402 may then formed in a surface of each part. Each part may be manufactured through casting. The cast material may be directionally solidified or single crystal super alloy. The pedestals 402 may be formed in the surface of each part of the initial structure of the outer wall 501 by an imprinting process that removes material from the surface. The imprinting process may be milling/spark electrode discharge machining, EDM, using a graphite/tungsten tool as described above for the formation of pedestals 402 on the outer surface of the inner wall 401. The tool may be configured with an exact negative of the desired pedestal pattern and may effectively be plunged into the surface in order to form an array of a plurality of pedestals 402. The pedestals 402 are therefore comprised by the part of the initial structure of the outer wall 501 and protrude from the surface of the part due to the imprinting process removing material around the pedestals 402 from the surface.

Each part of the initial structure of the outer wall 501 may have one or more imprinting processes performed on it. Figure 5 shows the plurality parts of the initial structure of the outer wall 501 with pedestals 402 formed in a surface of each part. As described for the formation of pedestals 402 in the outer surface of the inner wall 401, the pedestals 402 formed in each imprinting process are all aligned in the same direction. Imprinting processes may be performed from different directions on the same part. After the pedestals 402 have been formed in a surface of each part of the initial structure of the outer wall 501, a smoothing operation is performed in order to flatten the tops of the pedestals 402. This may also ensure that all of the pedestals 402 have the desired height. The smoothing operation may be, for example, a grinding operation.

The distance between two adjacent pedestals 402 on the outer wall 501 may be in the range 0.5mm to 1.5mm. If a pedestal 402 on the outer wall 501 has a substantially square cross-section that is constant along the length of the pedestal 402, the length of a side of the square cross-section of the pedestal 402 may be in the range 0.5mm to 1.5mm. The height of a pedestal 402 on the outer wall 501 after the smoothing operation may be in the range 0.5mm to 1.5mm. On the inner wall 401, each group of adjacent pedestals 402 with flattened ends that are all in the same plane provides an attachment interface to the inner wall 401. On each part of the outer wall 501, each group of adjacent pedestals 402 with flattened ends that are all in the same plane provides an attachment interface to the part of the outer wall 501.

Each attachment interface to the inner wall 401 has a corresponding attachment interface on a part of the outer wall 501. Each pedestal on the inner wall 401 is therefore arranged to be attached to a corresponding pedestal on a part of the outer wall 501.

Figures 6A and 6B show cross-sections of a blade 701 according to the present disclosure. Figure 7 shows a blade 701 according to the present disclosure with a portion of the outer wall 501 cut away so as to show the pedestals 402. The trailing edge region of the blade 701 may comprise TE slots. A blade 701 according to the present disclosure is formed by attaching each of the parts of the outer wall 501 to the inner wall 401. Each part of the outer wall 501 may be attached to the inner wall 401 by joining the end surfaces of all of the pedestals 402 in the one or more interfaces of the part of the outer wall 501 and the corresponding one or more interfaces on the inner wall 401. The end surfaces of the pedestals 402 may be joined together by diffusion bonding or brazing. This technique is possible since the end surfaces of each of the pedestals 402 being joined are all flat and parallel to each other. The joints in each of the interfaces may therefore all be in the same plane. Adjacent parts of the outer wall 501 may also be directly attached to each other, such as by diffusion bonding or brazing, so that the parts of the outer wall 501 are no longer separated from each other.

As shown in Figures 6B and 7, there are impingement holes 601 through the inner wall 401 and effusion holes 602 through the outer wall 501. The initial structures of both the inner wall 401 and each part of the outer wall 501 may be made with these holes. For example, the initial structures may be cast with these holes. Alternatively, the holes may be formed in the initial structures of both the inner wall 401 and each part of the outer wall 501 after the initial structures have been manufactured. Possible advantages of the above manufacturing technique may include the pedestals 402 all being integral with either the inner or outer wall 501. The attachment of each pedestal to the wall may therefore be very strong. Another advantage may be that the outer surface of the blade 701 does not need to be altered after each part of the initial structure of the outer surface has been manufactured. The features of outer surface may therefore be made with high precision.

As explained above, a plurality of machining operations are performed in order to form pedestals 402 in the inner wall 401. Each machining operation cuts out some of the surface in order to form an interface comprising a plurality of parallel columns. Due to the non-planar shape of the inner wall 401, adjacent interfaces may not be co-linear with each other and there may be an oblique or reflex angle between adjacent interfaces. The portion of the outer surface of the inner wall 401 between any two adjacent interfaces may therefore not have any material cut away by a machining operation. There may also be a corresponding portion on one or more parts of the outer wall 501 without pedestals 402. Since there may be no pedestals 402 in these portions between interfaces, the portions may not be cooled as much as the parts of the walls with pedestals 402 and, in particular on the outer wall 501, may become hot spots. If such hot spots are too large then they overheat and degrade operation. The size of the hot spots can be reduced by increasing the number of interfaces that are formed in the inner wall 401 so that the plurality of linear interfaces more closely approximate the shape of the inner wall 401. However, increasing the number of machining operations increases the cost of manufacture. There is therefore a trade off between the number of interfaces and the cost of manufacture.

The number, shape, size and position of all of the pedestals 402, effusion holes 602 and impingement holes 601 can be varied in order to achieve minimal aerodynamic losses and to maximise the cooling of the blade 701. The position of the effusion holes 602 and impingement holes 601 may be staggered with respect to each other. Advantageously, the flow of air from inside the inner walls 401, through the impingement holes 601, past the

pedestals 402 and through the effusion holes may result in a transpiration-like film being formed on the outer surface of the blade 701 and good cooling properties. Compared to known blades, the required cooling air consumption may be reduced and efficiency may be increased. Figure 8 is a flowchart of a method of manufacturing a double walled section of an aerofoil of a gas turbine engine according to the present disclosure. In 801, the method begins. In 802, a plurality of columns are formed on an outer surface of a first structure. In 803, a plurality of columns are formed on a surface of each of a plurality of parts of a second structure. In 804, a double walled section of an aerofoil is formed by attaching the ends of columns on each part of the second structure to the ends of columns on the first structure such that the first structure is an inner wall of the section of the aerofoil and the second structure is an outer wall of the section of the aerofoil. In 805, the method ends.

Embodiments include a number of modifications and variations to the techniques as described above. For example, in addition to the outer wall 501, the inner wall 401 may also be initially formed as a plurality of separate parts that are later attached together. The pedestals 402 and parts of the outer wall 501 may be joined together by other techniques, such as welding. The imprinting processes may alternatively be performed by other techniques than EDM. For example, any of CNC milling, casting, abrasive jet machining, water jet machining, laser cutting or electronic beam machining may alternatively be used for the imprinting processes. The end surfaces of the pedestals 402 may alternatively be joined together by other techniques than diffusion bonding or brazing. For example, friction welding or adhesive bonding may be used to join the end surfaces of the pedestals 402.

It will be understood that the invention is not limited to the embodiments above-described and various modifications and improvements can be made without departing from the concepts described herein. Except where mutually exclusive, any of the features may be employed separately or in combination with any other features and the disclosure extends to and includes all combinations and sub-combinations of one or more features described herein.

Claims

1. A method of manufacturing a double walled section of an aerofoil (701) of a gas turbine engine (10), the method comprising: forming a plurality of columns (402) on an outer surface of a first structure; forming a plurality of columns (402) on a surface of each of a plurality of parts of a second structure; and forming a double walled section of an aerofoil (701) by attaching the ends of columns (402) on each part of the second structure to the ends of columns (402) on the first structure such that the first structure is an inner wall (401) of the section of the aerofoil (701) and the second structure is an outer wall (501) of the section of the aerofoil (701).

2. The method according to claim 1, wherein: forming a plurality of columns (402) on the outer surface of the first structure comprises imprinting the columns (402) in its outer surface; and/or for each of the plurality of parts of the second structure, forming a plurality of columns (402) on the surface comprises imprinting the columns (402) in the surface.

3. The method according to claim 2, wherein imprinting is performed by Electrode Discharge Machining (EDM).

4. The method according to any preceding claim, further comprising performing a smoothing operation that flattens the ends of each of the columns (402) after the columns (402)

have been formed.

5. The method according to any preceding claim, wherein attaching the ends of columns (402) on each part of the second structure to the ends of columns (402) on the first structure comprises diffusion bonding or brazing the ends of the columns (402) together.

6. The method according to any preceding claim, wherein forming a plurality of columns (402) on the outer surface of the first structure is performed by a plurality of manufacturing operations with each manufacturing operation forming a plurality of parallel columns (402) in a single region of the first structure; and/or wherein forming a plurality of columns (402) on the surface of each part of the second structure is performed by one or more manufacturing operations with each manufacturing operation forming a plurality of parallel columns (402) in a single region of the second structure.

7. The method according to any preceding claim, wherein the section of the aerofoil (701) is comprised by a turbine blade (701) or a compressor blade (701).

8. The method according to claim 7, wherein the turbine blade (701) or compressor blade (701) comprises a leading-edge region, a mid-chord region and a trailing edge region; and the section of the aerofoil (701) is the leading edge region and mid-chord region of the blade.

9. The method according to any preceding claim, further comprising attaching each part of the second structure to one or more other parts of the second structure.

10. The method according to any preceding claim, wherein the first structure comprises a plurality of parts; and the method comprises attaching each of the parts of the first structure to one or more other parts of the first structure.

11. The method according to any preceding claim, wherein the first structure and/or one or more parts of the second structure are formed by casting.

12. The method according to any preceding claim, wherein the first structure and/or one or more parts of the second structure comprises crystals that are directionally solidified.

13. The method according to any preceding claim, wherein the first structure and/or one or more parts of the second structure are single crystal super alloys.

14. The method according to any preceding claim, wherein the first structure is a walled structure with the walls providing an enclosed inner part of the section of the aerofoil (701) and the second structure is a walled structure with the walls enclosing the first structure, wherein the method further comprises: forming one or more holes (601) through the walls of the first structure; and forming one or more holes (602) through the walls of the second structure, such that air in the inner part of the aerofoil (701) can flow out of the aerofoil (701) via the holes in the first structure and second structures.

15. The method according to claim 14, wherein the positioning of the holes (601) in the walls of the first structure is staggered with respect to the positioning of the holes (602) in the walls of the second structure.

16. An aerofoil (701) that is manufactured according to the method of any of claims 1 to 15.

17. A double walled section of an aerofoil (701) of a gas turbine engine (10), the double walled section of the aerofoil (701) comprising: an inner wall (401) with a plurality of columns (402) protruding from its outer surface; an outer wall (501) with a plurality of columns (402) protruding from its inner surface; joints between the end surfaces of the columns (402) on the inner wall (401) and the end surfaces of the columns (402) on the outer wall (501).

18. The section of an aerofoil (701) according to claim 17, wherein the joints are diffusion bonds or braised connections.

19. The section of an aerofoil (701) according to claim 18, wherein the columns (402) are grouped to provide one or more interface regions; and within each of the interface regions, the joints between the ends of the columns (402) are all in the same plane.

20. The section of an aerofoil (701) according to claim 19, wherein the section of the aerofoil (701) is comprised by a turbine blade (701) or a compressor blade (701).

21. The section of an aerofoil (701) according to claim 20, wherein the turbine blade (701) or compressor blade (701) has a leading-edge region, a mid-chord region and a trailing edge region; and the section of the aerofoil (701) is the leading edge region and mid-chord region.

22. A gas turbine engine (10) for an aircraft comprising: an engine core (11) comprising a turbine (19), a compressor (14), and a core shaft (26) connecting the turbine to the compressor; a fan (23) located upstream of the engine core, the fan comprising a plurality of fan blades; and a gearbox (30) that receives an input from the core shaft (26) and outputs drive to the fan so as to drive the fan at a lower rotational speed than the core shaft; wherein one or more of the turbine (19) and compressor (14) comprise one or more sections of an aerofoil (701) according to any of claims 17 to 21.

23. The gas turbine engine according to claim 22, wherein: the turbine is a first turbine (19), the compressor is a first compressor (14), and the core shaft is a first core shaft (26); the engine core further comprises a second turbine (17), a second compressor (15), and a second core shaft (27) connecting the second turbine to the second compressor; and the second turbine, second compressor, and second core shaft are arranged to rotate at a higher rotational speed than the first core shaft; wherein one or more of the second turbine and second compressor comprise one or more sections of an aerofoil (701) according to any of claims 17 to 21.

Fig 1

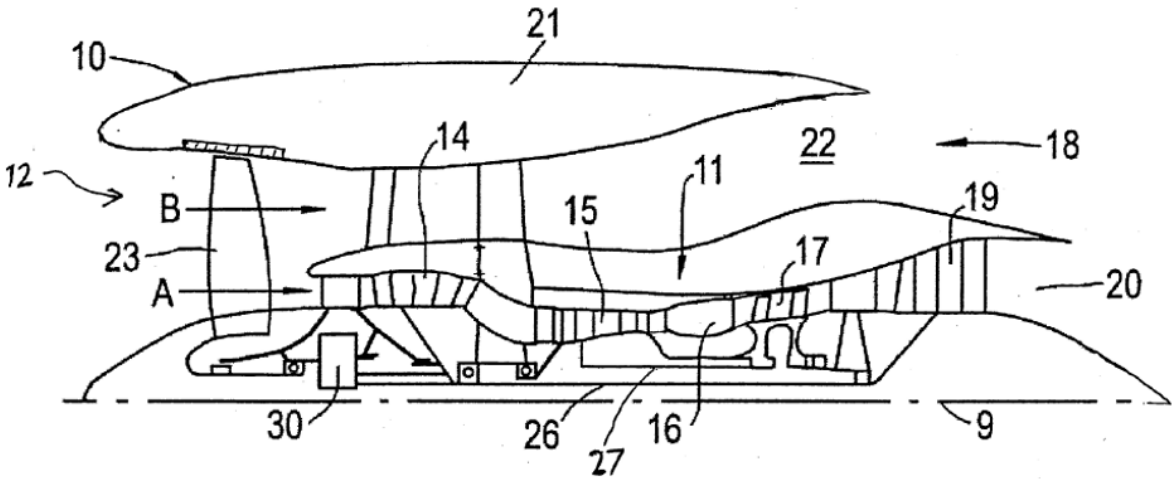
21
10
14
22
18
12
11
B
15
19
23
17
A
20
30
26
16
9
27

Fig 2

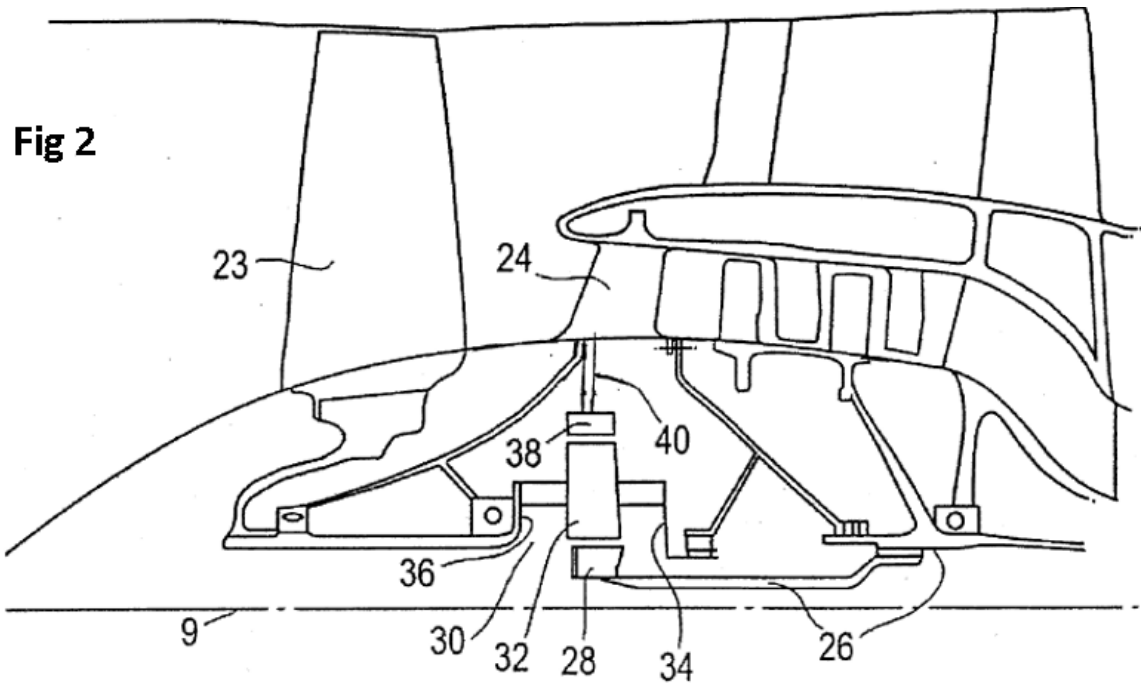
23
24
40
38
36
9
30
32
28
34
26

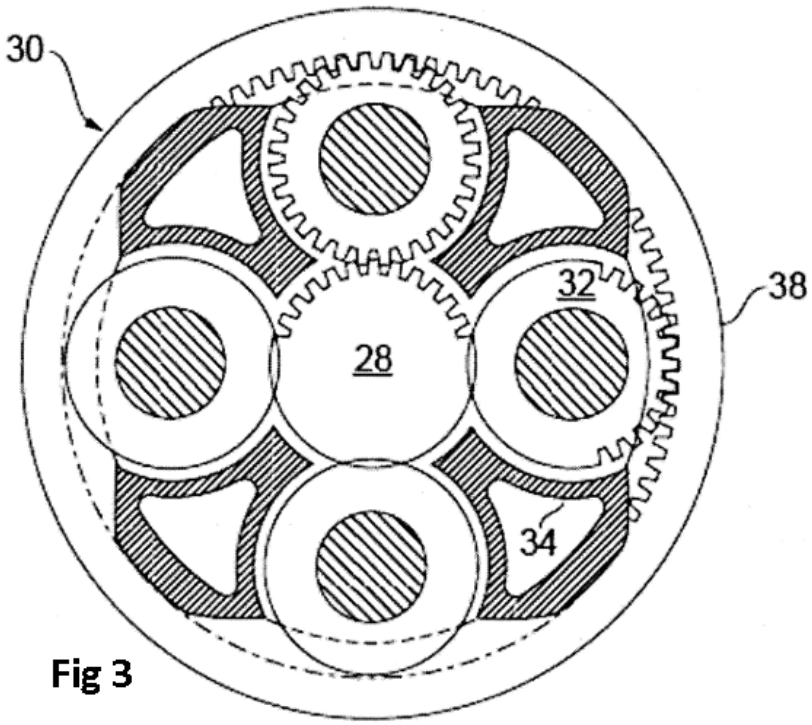

Fig 3

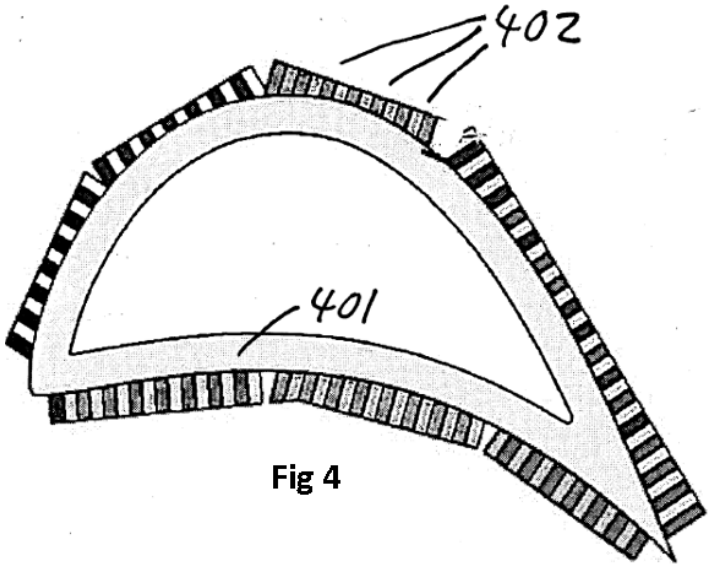

Fig 4

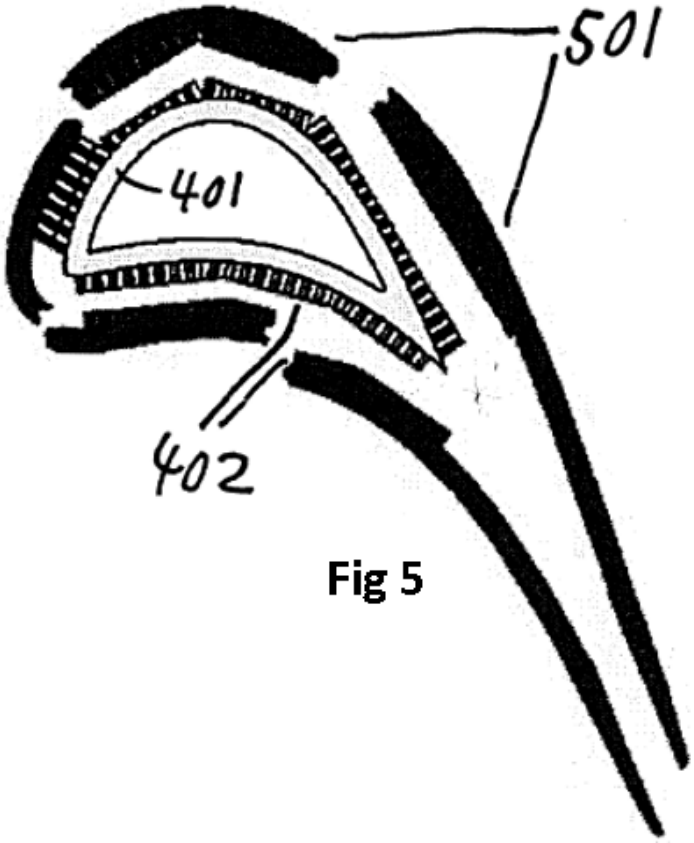

Fig 5

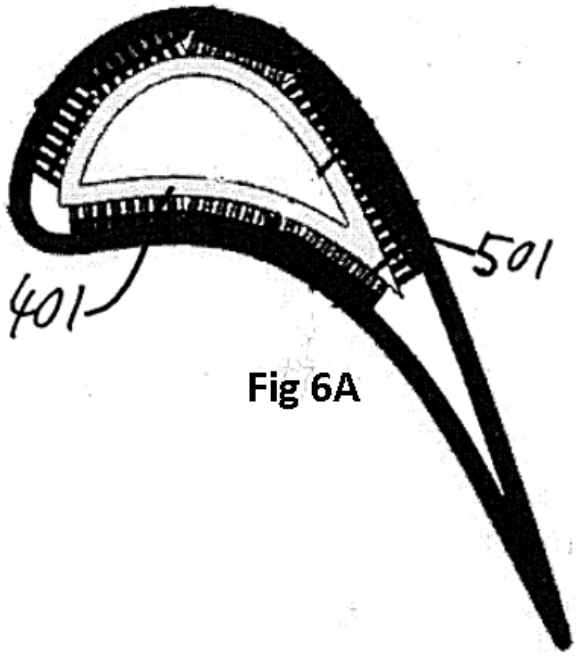

Fig 6A

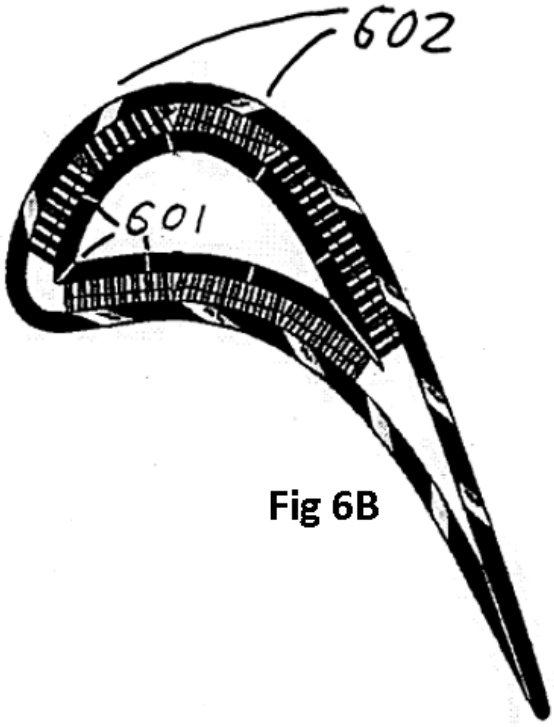

Fig 6B

Fig 7

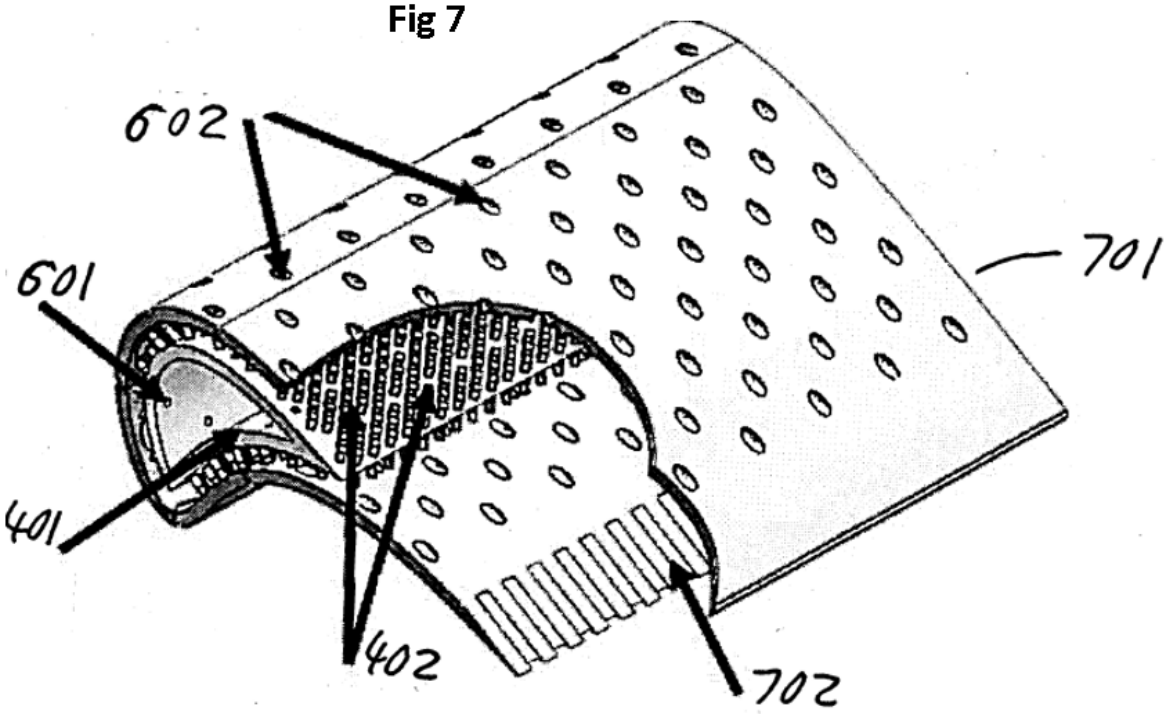
602
601
701
401
402
702

Fig 8

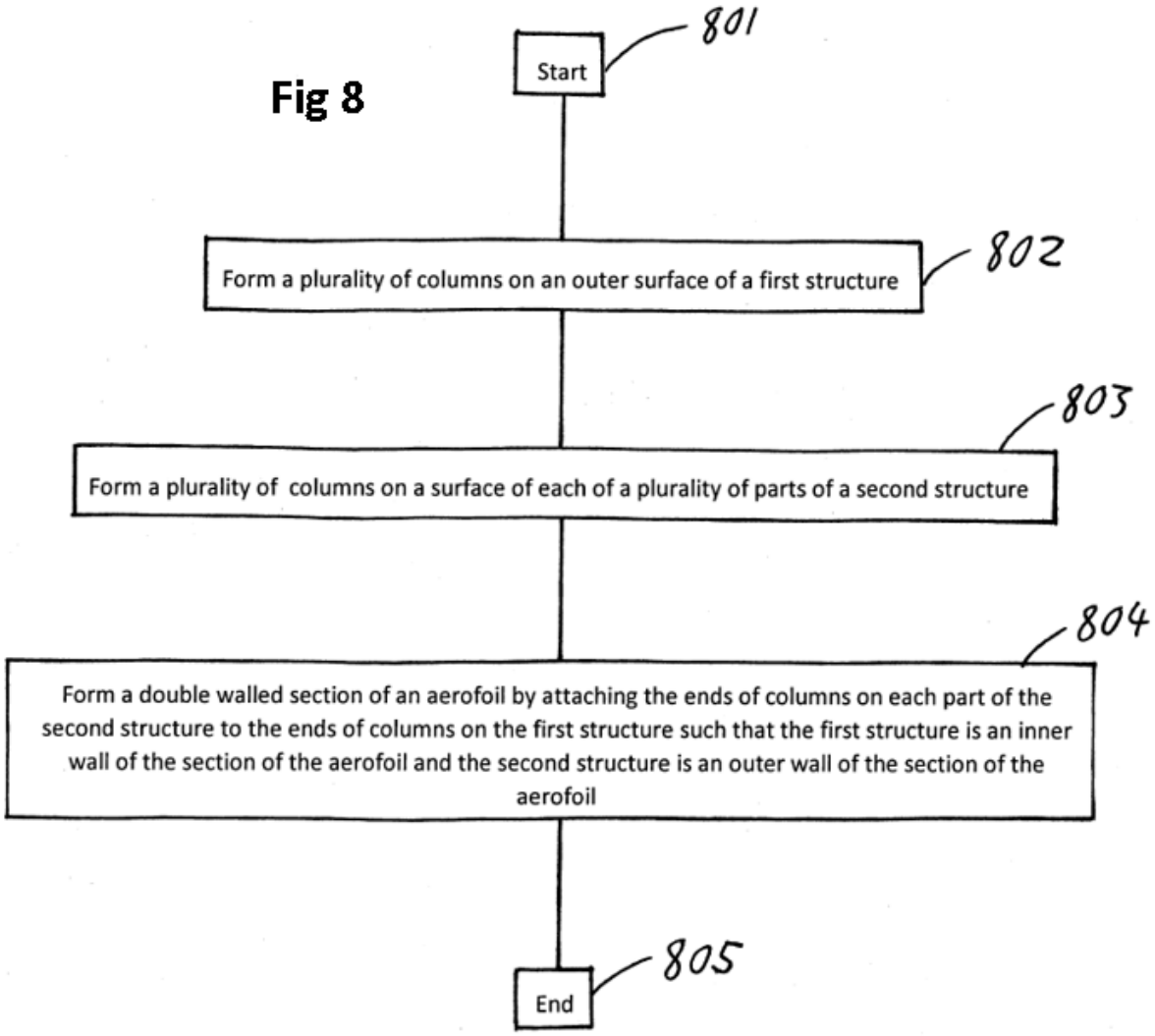
801
Start
802
Form a plurality of columns on an outer surface of a first structure
803
Form a plurality of columns on a surface of each of a plurality of parts of a second structure
804
Form a double walled section of an aerofoil by attaching the ends of columns on each part of the second structure to the ends of columns on the first structure such that the first structure is an inner wall of the section of the aerofoil and the second structure is an outer wall of the section of the aerofoil
805
End

Appendix B

A section of the MATLAB Code Used for Evaluating Aerofoil Metal Temperature

```
clear all;
clc;

%% CONSTANT PARAMETERS
%Specify the constant parameters for mainstream gas and coolant
Cp_coolant = 1107.327;%[J/(Kg.K)]-Coolant specific heat capacity
Cp_gas = 1286;%[J/(Kg.K)]- Mainstream gas specific heat capacity
K_hotair = 0.083;%[W/(m.K)]- Mainstream gas thermal conductivity
Pr_gas = 0.7;%[Pr]
dynamic_viscosity_gas = 60*10^-6;%[kg/(m.s)]
dynamic_viscosity_coolant = 37.96*10^-6;%[kg/(m.s)]
Toc = 811; %[K]-Coolant inlet temperature
T_g = 2200; %[K]- Mainstream inlet temperature
m_g = 1.77; %[kg/s] - Mainstream mass flow rate
rec_factor = (Pr_gas)^(1/3);%[-]- Recovery factor
chord_length = 33.81;%[mm]
gamma = 1.4;%[-]
R = 287;%[J/Kg]
R_stagnation = 2.4/1000;%[m]- Radius of the aerofoil stagnation region
L = 0.001;%[m]- Thickness of the aerofoil wall
D = 1; % [mm]- Film hole diameter
dia = D/1000;  radius = dia/2; % Film hole diameter and radius
area_hole = pi()*(radius^2);
cd = 0.54;%%using without cross flow case
phi = pi()/6;%[rad] - Film cooling hole inclination to the mainstream
%%Specify the C2 wall block element features
wetted_area_block =  0.0000863911;%[m^2]
ext_surf_area = 0.0000246073;%[m^2]
area_scale = wetted_area_block/ext_surf_area;%[-]
htc_ext_ave = 4506.75;%[W/(m^2.K)]- HTC average on the aerofoil

%% IMPORT PRESSURE VALUES ON THE AEROFOIL FROM ANSYS CFD
absolute_press = xlsread('stat_total_pressure_ss.xlsx');
```

```
stat_press = xlsread('stat_total_pressure_ss.xlsx');
total_press = xlsread('stat_total_pressure_ss.xlsx');
x_index = (absolute_press(:,2))*1000;
y_index = (absolute_press(:,3))*1000;
x_index_sorted = sort(x_index);

%% IMPORT SS BLADE COORDINATES STORED IN THE 'blade_coords' EXCEL SHEET
BladeCoords = xlsread('blade_coords.xlsx','sheet2','U2:V124');
x_vector = BladeCoords(:,1);
y_vector = BladeCoords(:,2);
no_coords_x =length(x_vector);
no_coords_y =length(y_vector);
nPoints_x = no_coords_x;
nPoints_z = 120;
for i = 1:no_coords_x-1
    delx(i) = x_vector(i+1)- x_vector(i);
    dely(i) = y_vector(i+1)- y_vector(i);
    s(i)= sqrt(delx(i).^2+dely(i).^2);
end
    s_len1 = cumsum(s);
    s_first = 0;
    s_len= [s_first;s_len1(1:end-1)];

for i = 1:nPoints_x
    if i<=8
        P_static(i) = mean (P_static1((find((abs(x_index - x_vector(i))<0.0001) ...
            & y_index <1))));
        P_total(i) = mean (P_total1((find((abs(x_index - x_vector(i))<0.0001) &...
            y_index <1))));
    elseif 9<i && i<=18
        P_static(i) = mean (P_static1((find((abs(x_index - x_vector(i))<0.0001) &...
            y_index >1))));
        P_total(i) = mean (P_total1((find((abs(x_index - x_vector(i))<0.0001) & ...
            y_index >1))));
        else
        P_static(i) = mean (P_static1((find((abs(x_index - x_vector(i))<0.0001)))));
        P_total(i) = mean(P_total1((find((abs(x_index - x_vector(i))<0.0001)))));
    end
end

%% USE THE TEMPERATURE AND PRESSURE VALUES TO EVALUATE OTHER PARAMETERS
for i=1:nPoints_x
 for k=1:nPoints_z
 mach_g(i)= sqrt((2/(gamma-1))*(((P_total(i)/P_static(i))^((gamma-1)/gamma))-1));
 Tg_static(i)= T_g*((P_static(i)/P_total(i)))^((gamma-1)/gamma);
 Tg_recovery(i,k)= Tg_static(i)+ rec_factor*(T_g-Tg_static(i));
 Tg_recovery1(i)= Tg_static(i)+ rec_factor*(T_g-Tg_static(i));
 T_diff(i) = Tg_recovery(i)-Tg_static(i);
 velocity(i) = mach_g(i).*sqrt(gamma*R.*Tg_static(i));
 density(i)= (P_abs(i))/(R*Tg_static(i));
 x_axis(i) = (i-1)/(nPoints_x-1);
 Re_g(i) = (velocity(i)*density(i)*s_len(i))/dynamic_viscosity_gas;
 end
end
T_gr = mean(Tg_recovery1);

%% EVALUATE HTC AROUND THE AEROFOIL (USING EQUATION 3.10)
htc_ext_stagnation_point =(Pr_gas^0.4)*0.93*(K_hotair/R_stagnation)*...
```

```
((velocity(1).*density(1)*R_stagnation)/(dynamic_viscosity_gas))^(0.5);%LE HTC
for i = 1:nPoints_x
    for im = 1:nPoints_x-1
      mass_flux(i) = density(i).*velocity(i);
      mass_flux_dx(im) = ((mass_flux(im+1)+mass_flux(im))/2000)*...
          (abs(s_len(im+1)-s_len(im)));
      mass_flux_int = (cumsum(mass_flux_dx)).^(0.2);
      stanton_number(i) = (0.0287*Pr_gas^(-0.4)*dynamic_viscosity_gas^0.2)...
          /(mass_flux_int(i));
      htc_ext(i) = Cp_gas*stanton_number(i).*mass_flux(i);
    end
end

z_dist = 10; %Spanwise hole distance
no_holes_pr_n_st = 7;%Staggered + primary holes
pr_holes_z = 4; %Number of holes in one row in spanwise direction
no_holes_x = 4; %Number of holes in one row in streamwise direction

%% IMPORT EXCEL DATA
%varible thermal diffusivity, X_decay and Z_(1/2)
%interpolated from the data shown Appendix A.1 of this thesis
epsilon_n_xdecay = xlsread('x_decay_n_epsilon.xlsx','D13:K22'); %Import
%Imports grid points where film holes are located
hole_location = xlsread('inner_curve','sheet2','F4:F10');
%Import Re, convective efficiency, internal HTC data of C2 wall block ...
%element stored in 'C2-data' excel sheet
Re_block = xlsread('C2-data.xlsx','N2:N5');
convec_eff_block = xlsread('C2-data.xlsx','L2:L5');
htc_block = xlsread('C2-data.xlsx','m2:m5');

%% IMPORT TEMPERATURE VALUE FROM SOLID CONDUCTION SOLUTION IN ANSYS THERMAL MODULE
Tm = 1505.5;%Current Tm
Tm2 = 1600;%Previous Tm
Tm_deviation =(abs(Tm - Tm2)/(Tg_r - Toc))*100;
Delta_P = 0.9*10^5;
z_dim = z_dist*no_holes_z;
for i = 1:no_coords_x-1
    for in = 1:length(x_vector_ic)-1
    delx(i) = x_vector(i+1)- x_vector(i);
    dely(i) = y_vector(i+1)- y_vector(i);
    s(i)= sqrt(delx(i).^2+dely(i).^2);
   end
end

%% BUILD GRID ON THE AEROFOIL SURFACE
% Build grid; distance between the grid points
for i = 1:nPoints_x-1
        dx(i) = s(i);
end
dz = z_dim/(nPoints_z-1);
dx_ave = mean(dx);
dz_ave = mean(dz);
istepz = nPoints_z/no_holes_z;

%% POSITIONS OF THE PRIMARY HOLES IN THE GRID
%Let the identity of the primary grid point called 'idP'
idpx = hole_location(1:2:end);
idsx = hole_location(2:2:end-1);
```

```
for j = 1:no_holes_z
    for i = 1:no_holes_x
        idP_x(i,j) = idpx(i);
        idP_z(i,j) = round((j-1)*istepz+1);
    end
end
idpz = idP_z(1,:);
idsz = idS_z(1,:);

%% POSITIONS OF THE STAGGERED HOLES IN THE GRID
%Let the identity of the primary grid point called 'idS'
for j = 1:no_holes_z-1
    for i = 1:no_holes_x-1
        idS_x(i,j) = idsx(i);
        idS_z(i,j) = round((j-1)*istepz+1+istepz/2);
    end
end
for i = 1:nPoints_x
    for ic = 1:no_coords_x_ic
          for j = 1:nPoints_z
        x(i,j) = sum(dx(1:(i-1)));
        z(i,j) = dz*(j-1);
          end
    end
end

%% BUILD PRIMARY HOLES
for kx = 1:no_holes_x
for j = 1:nPoints_z
    for i = idP_x(kx):nPoints_x
    idhx = idP_x(kx,1);
    idhz = idP_z(kx,1);
    lenmin = abs(z(i,j)-z(idhx,idhz));
    for kz = 2:no_holes_z
        len = abs(z(i,j)-z(idhx,idP_z(kx,kz)));
        if len < lenmin
            lenmin = len;
            idhz = idP_z(kx,kz);
        end
    end
lenx = abs(x(i,j)-x(idhx,idhz));
lenz = abs(z(i,j)-z(idhx,idhz));
   Poc_pr(kx) = P_static_pr(kx)+Delta_P;
   P_ratio_pr(kx) = P_static_pr(kx)/Poc_pr(kx);
   T_ratio_pr(kx) = (P_ratio_pr(kx))^((gamma-1)/gamma);
   T_static_pr(kx) = (P_ratio_pr(kx))^((gamma-1)/gamma)*Toc;
   rho_static_pr(kx) = P_static_pr(kx)/(287*T_static_pr(kx));
   Mach_pr(kx) = sqrt((2/(gamma-1))*((1/T_ratio_pr(kx))-1));
   if  Mach_pr(kx)> 1
       Mach_pr(kx)=1;
   else
        Mach_pr(kx) =   Mach_pr(kx);
   end
   a_pr(kx) = sqrt(gamma*287*T_static_pr(kx));
   Uc_pr(kx) = Mach_pr(kx).*a_pr(kx);
   m_flow_ideal_pr(kx) = area_hole*Uc_pr(kx).* rho_static_pr(kx);
   m_flow_actual_pr(kx) = m_flow_ideal_pr(kx)*cd; %Equation 3.2
   uc_exit_pr(kx) = m_flow_actual_pr(kx)/(density_pr(kx)*area_hole);
```

```
208
209   m_hole_ave_pr(kx) = m_flow_actual_pr(kx)/mdot_ave_per_hole;
210   Re_pr(kx) = ((m_flow_actual_pr(kx)/area_hole)*dia)/dynamic_viscosity_coolant;
211   convec_eff_blade_pr(kx) = interp1(Re_block,convec_eff_block, ...
212       (2*Re_pr(kx)),'linear','extrap');
213   Tce_pr(kx) = Toc + convec_eff_blade_pr(kx)*(Tm - Toc); %Equation 3.8
214   htc_int_pr(kx) = ((m_flow_actual_pr(kx)/2)*Cp_coolant*...
215       convec_eff_blade_pr(kx))/ext_surf_area; %Equation 3.3
216
217   M_P(kx) = (m_flow_actual_pr(kx)/area_hole)/(velocity_pr(kx)*density_pr(kx));
218   epsilon_h_P(kx) = interp1(epsilon_n_xdecay(8,:),epsilon_n_xdecay(9,:)...
219       ,M_P(kx),'linear','extrap'); %Thermal diffusivity
220   xdecay_P(kx) = interp1(epsilon_n_xdecay(8,:),epsilon_n_xdecay(10,:),...
221       M_P(kx),'linear','extrap'); %X_decay
222   Z_Half_P(kx) = interp1(epsilon_n_xdecay(1,:),epsilon_n_xdecay(2,:),...
223       M_P(kx),'linear','extrap')*D;%Z_(1/2)
224
225 %Film effectiveness evaluation from Equation 3.5
226 etaTemp(kx,i,j)=(M_P(kx).*velocity_pr(kx).*exp(-0.693*((lenz/Z_Half_P(kx))^2)))...
227    /(8*(epsilon_h_P(kx))*((lenx/D)+xdecay_P(kx)));
228      if kx == 1
229      eta(i,j) = etaTemp(kx,i,j);
230      end
231     end
232 end
233 end
234
235 %% CALCULATE COOLANT EXIT TEMPERATURE, T_c,ex (EQUATION 3.8)
236 %Determine Tce at every hole location
237 Tce1(1:2:end) = Tce_pr;
238 Tce1(2:2:end-1) = Tce_st;
239 idx(1:2:end) = idpx;
240 idx(2:2:end-1) = idsx;
241 idz(1:2:end) = idpz;
242 idz(2:2:end) = idsz;
243 for i = 1:nPoints_x
244    for kx = 1:length(idx)-1
245     for j = 1:nPoints_z
246      if x_vector(idx(kx)) <= x_vector(i) && x_vector(i) < x_vector(idx(kx+1));
247          Tce(i,j) = Tce1(kx);
248      elseif x_vector(i) >= x_vector(idx(end))
249          Tce(i,j) = Tce1(end);
250      end
251     end
252    end
253 end
254
255 %% CALCULATE ADIABATIC WALL TEMPERATURE, T_aw (USING EQUATION 3.9)
256 for j = 1:nPoints_z
257     ip = 1;
258     for jh = 1:no_holes_z-1
259         limbot = idS_z(1,jh)-int8(istepz/4);
260         limup  = idS_z(1,jh)+int8(istepz/4);
261         if j>=limbot && j<=limup
262             ip = 0;
263         end
264     end
265     upEffect = 0;
```

```
    for i = 1:nPoints_x
        if (ip==1 && i>=idP_x(2))||(ip==0&&i>=idS_x(2))
            upEffect = 1;
        end
        if upEffect == 0
          Taw(i,j) = Tg_recovery(i,j)- eta(i,j).*(Tg_recovery(i,j)-Tce(i,j));
        else
            if ip == 1
                prevh = 1;
                for ih = 2:no_holes_x-1
                    if i >= idP_x(ih,1)
                        prevh = ih;
                    end
                end
                jh = 1;
                Tawup = Taw(idP_x(prevh,jh)-1,j);
            else
                for xx = 1:length(idpx)-1
                    istepx(xx) = idpx(xx+1)-idpx(xx);
                     ih(xx) = int8(i/istepx(xx));
                         if ih > no_holes_x-1
                      ih = no_holes_x-1;
                         end
                end
                prevh = 1;
                for ih = 2:no_holes_x-1
                    if i >= idS_x(ih,1)
                        prevh = ih;
                    end
                end
                jh = 1;
                Tawup = Taw(idS_x(prevh,jh)-1,j);
            end

            Taw(i,j) = Tce(i,j)*eta(i,j)+(1.-eta(i,j))*Tawup;
        end
    end
end

%% EXPORT MATLAB DATA TO ANSYS STEADY STATE THERMAL MODULE
%%External HTC
y = repmat(y_vector,1,nPoints_z);
x_final = repmat(x_vector,1,nPoints_z);
htc_ex1 = repmat(htc_ext,1,nPoints_z);
X = x_final(:);
Y = y(:);
Z = z(:);
TAW = Taw(:);
htc_extern = htc_ex1(:);
Mat_ext = [X,Y,Z,TAW,htc_extern];
csvwrite('SS_ext1a.csv',Mat_ext);

%%Internal HTC
y_ic = repmat(y_vector_ic,1,nPoints_z);
x_ic = repmat(x_vector_ic,1,nPoints_z);
X_ic = x_ic(:);
Y_ic = y_ic(:);
Z_ic = z_ic(:);
```

```
T_cool = repmat(Toc,no_coords_x_ic,nPoints_z);
T_coolant = T_cool(:);
htc_int = repmat(htc_blade_int,1,nPoints_z);
htc_internal = htc_int(:);
Mat_int = [X_ic,Y_ic,Z_ic,T_coolant,htc_internal];
csvwrite('SS_int1.csv',Mat_int);
```

Appendix C

Film Effectiveness Parameter Variation with Streamwise Pitch and Blowing Ratio (from Murray et al. (2018))

S_x = 2.0	M	0.3	0.4	0.4	0.6	0.7	0.8	1.0	1.1
	α_t	3.8	3.6	2.8	2.4	2.1	2.0	1.9	2.0
	x_{decay}	2.3	3.0	4.5	7.0	10.5	13.0	17.0	19.0
S_x = 5.7	M	0.3	0.4	0.4	0.6	0.7	0.8	1.0	1.1
	α_t	4.6	3.8	2.7	2.7	2.4	2.2	2.0	2.3
	x_{decay}	2.2	3.3	7.0	7.0	10.5	13.0	18.0	18.3
S_x = 10.0	M	0.3	0.4	0.4	0.6	0.7	0.8	1.0	1.1
	α_t	5.5	4.0	2.6	3.1	2.8	2.4	2.1	2.5
	x_{decay}	2.1	3.7	10.0	7.0	10.5	13.0	19.2	17.5
	M	0.4	0.6	0.9	1.0	1.2	1.4	1.7	2.0
	$Z_{1/2}/D$	0.8	0.8	0.7	0.7	0.6	0.6	0.5	0.4